



Boonruang, Arjin (2021) *Fabrication and characterisation of microultrasound array transducers*. PhD thesis.

<http://theses.gla.ac.uk/82631/>

Copyright and moral rights for this work are retained by the author

A copy can be downloaded for personal non-commercial research or study, without prior permission or charge

This work cannot be reproduced or quoted extensively from without first obtaining permission in writing from the author

The content must not be changed in any way or sold commercially in any format or medium without the formal permission of the author

When referring to this work, full bibliographic details including the author, title, awarding institution and date of the thesis must be given

Enlighten: Theses

<https://theses.gla.ac.uk/>  
[research-enlighten@glasgow.ac.uk](mailto:research-enlighten@glasgow.ac.uk)

# **Fabrication and Characterisation of Microultrasound Array Transducers**



**By**  
**Arjin Boonruang**

*A Thesis submitted in fulfilment of the requirements  
for the degree of Doctor of Philosophy*

*Centre for Medical and Industrial Ultrasonics  
James Watt School of Engineering  
College of Science and Engineering  
University of Glasgow  
December 7, 2021*

# Declaration of Authorship

I, Arjin Boonruang, hereby declare that this thesis entitled, “**Fabrication and Characterisation of Microultrasound Array Transducers**”, submitted to University of Glasgow for the degree of Doctor of Philosophy represents my own original research. It has been composed by me and all references cited have been consulted by me. It has not been previously submitted for any other degree in this university or any other university.

Signed: Arjin Boonruang

Date: December 7, 2021

# Abstract

High frequency or microultrasound array transducers ( $\mu$ US) made by 1-3 piezocomposites, operating at frequencies beyond 20 MHz, have become attractive since they provide extended imaging depth of field generated from electronic scanning with high image resolution, and better acoustic impedance matching between the transducers and medium. However,  $\mu$ US arrays are much less available commercially than users would like due to difficulties in manufacture and economic production. Key aspects in the development of  $\mu$ US arrays lie in alternative approaches to establish the microscale composite structures, array elements and electrical interconnects. This thesis thus presents fabrication processes for  $\mu$ US arrays made with 1-3 connectivity randomised and diced piezocomposites.

The first part of the thesis involves the fabrication of the microscale 1-3 piezocomposites for  $\sim$ 30 MHz  $\mu$ US arrays. A promising technique based on a gel-casting method associated with micromoulding was used to create innovative 1-3 randomised  $\text{Pb}(\text{Zr}_{0.52}\text{Ti}_{0.48})\text{O}_3$  (PZT) ceramic piezocomposites with arbitrary, randomised pillar cross-sections, providing capability to reduce extraneous modes effectively. In addition, a commercial method based on a dice-and-fill technique was modified to manufacture diced piezocomposites from PZT ceramic and relaxor  $\text{PbIn}_{1/2}\text{Nb}_{1/2}\text{O}_3 - \text{PbMg}_{1/3}\text{Nb}_{2/3}\text{O}_3 - \text{PbTiO}_3$  (PIN-PMN-PT; PIMNT) single crystal materials to compare electrical and functional properties.

Another challenge addressed was microfabrication of array elements with one wavelength pitch ( $\sim$ 50  $\mu\text{m}$ ), made by photolithography based on a bilayer lift-off process. Satisfactory edge definition and high yield of electrically continuous tracks in 20 element arrays were achieved by careful process optimisation. The delicate processes in releasing the thin composite arrays and wax removal after lapping to the required thickness were proved as the most challenging steps in  $\mu$ US array fabrication. They must be carefully controlled to maintain the yield of active elements since the composites experience harsh environmental cycling during fabrication.

Each of three completed composite array coupons was incorporated into an additively manufactured housing with a printed plastic handle. The prototype devices were driven with an ultrasound research array controller to assess their functional properties. It was shown that the novel randomised piezocomposites can potentially be used for  $\mu$ US array applications and gel casting allied with micromoulding offers a cost-effective and viable route to wafer-scale fabrication.

# Acknowledgement

I am sincerely grateful to my advisor Prof. Sandy Cochran for giving me the opportunity to carry out a Ph.D under his supervision, and for his continuous support, patience, motivation, enthusiasm and valuable knowledge throughout my Ph.D studies. His valuable guidance and immense support enlightened me throughout my research and this thesis writing.

I would also like to express my great appreciation to Prof. Tim Button, my first supervisor in the University of Birmingham, for all his support and invaluable insight, guidance in both academic work and life balance, and all his generous help before and after his retirement.

I would like to extend my appreciation to Dr Steven Neale and Dr Alex Moldovan, my second supervisors, for their timely guidance, technical assistance and advice on microfabrication and electrical solutions of the transducer systems in the James Watt Nanofabrication Centre. Their expertise helped me get through some difficult times during this research.

I am deeply thankful to Dr. Yongqiang Qiu, Dr. Rachael McPhillips, Dr. Tanikan Thongchai and Dr. Bongkot Hararak for their valued advice and mentorship during the start of my project with my endless questions, as well as their immense help in encouraging me to adapt to a new environment and thesis writing.

I also thank my colleagues and friends from the Functional Materials Group at the University of Birmingham, the Centre for Medical and Industrial Ultrasonics at the University of Glasgow, and Amin Rigi from the University of Edinburgh, for their company, encouragement and support in both my academic and personal life.

I would also like to acknowledge The Royal Thai Government, the Ministry of Science and Technology, and the Thailand Institute of Scientific and Technological Research for providing research funding and resources.

Finally, and most importantly, I would like to express my sincere love and gratitude to my parents, Boonruang and Panyadaeng families. My parents for their endless love and encouraging me to never give up. My son and husband for the moral support and raising our child while I was far from home for over 4 years in doing my Ph.D. Without their sacrifices, I would never have come this far.

# Table of Contents

Declaration of Authorship.....	ii
Abstract.....	iii
Acknowledgement.....	iv
Table of Contents.....	v
List of Figures.....	ix
List of Tables.....	xiv
List of Terms.....	xv
Chapter 1 Introduction.....	1
1.1. High Frequency Ultrasound for Medical Imaging.....	1
1.2. Motivation and Objectives.....	2
1.3. Contributions to Knowledge.....	3
1.4. Thesis Structure.....	4
1.5. Publications and Conference Submissions.....	6
Chapter 2 Functional Background.....	7
2.1. Introduction.....	7
2.2. Medical Imaging Modalities.....	7
2.3. Basics of Ultrasound Imaging.....	10
2.3.1. Ultrasound Waves.....	10
2.3.2. Ultrasound Operation.....	11
2.3.3. Interaction of Ultrasound Waves.....	12
2.4. Functional Properties of Ultrasound Transducers.....	15
2.5. 1D Microultrasound Array Transducer.....	18
2.5.1. Structure of Piezoelectric Medical Ultrasound Probes.....	19
2.6. Principle of piezoelectricity.....	22
2.6.1. Piezoelectric effects.....	22
2.6.2. Piezoelectricity and Ferroelectricity.....	22
2.6.3. Electrical impedance spectroscopy.....	25
2.7. Piezoelectric Materials for Medical Imaging.....	27
2.7.1. Specific Requirements.....	27
2.7.2. Pb-based Piezoelectric Ceramics.....	27
2.7.3. Relaxor PT-based Piezoelectric Single Crystal.....	28
2.7.4. Piezoelectric Polymers.....	29
2.7.5. Piezoelectric Composite.....	30
2.7.6. Spurious Resonance Modes.....	31
2.7.7. Design Considerations for 1-3 Piezocomposite $\mu$ US Transducers.....	32

2.8.	Summary .....	36
Chapter 3	Microultrasound Array Fabrication .....	38
3.1.	Introduction.....	38
3.2.	1-3 Piezocomposite Manufacture for $\mu$ US Transducers .....	39
3.2.1.	Dice and Fill .....	41
3.2.2.	Interdigital Pair Bonding .....	43
3.2.3.	Micromachining .....	44
3.2.4.	Viscous Polymer Processing .....	46
3.2.5.	Gel Casting .....	48
3.3.	Array Element Fabrication.....	53
3.3.1.	Mechanical and Laser Machining .....	53
3.3.2.	Photolithography .....	54
3.3.3.	Discussion.....	59
3.4.	Interconnection.....	60
3.4.1.	Isotropic Conductive Adhesive .....	60
3.4.2.	Anisotropic Conductive Adhesive.....	61
3.4.3.	Wire Bonding .....	62
3.5.	Summary .....	63
Chapter 4	Research Methods.....	65
4.1.	Introduction.....	65
4.2.	1-3 Piezocomposite Fabrication.....	66
4.2.1.	1-3 Randomised Piezocomposites .....	67
4.2.2.	1-3 Diced Piezocomposites .....	71
4.3.	Surface Preparation of Composites.....	75
4.4.	Photolithography .....	77
4.5.	Thinning, Releasing and Wax Removal .....	80
4.6.	Poling .....	81
4.7.	Characterisation Techniques .....	82
4.7.1.	Characterisation of Gel-Cast Material.....	82
4.7.2.	Surface Characterisation.....	85
4.7.3.	Microstructure Characterisation .....	86
4.8.	Interconnect, Transducer Packaging, and Cabling.....	87
4.9.	Transducer Functional Testing.....	93
4.9.1.	Dielectric Measurement.....	93
4.9.2.	Electrical Impedance Spectroscopy .....	94
4.9.3.	Electrical Continuity .....	94
4.9.4.	Pulse-echo Response Measurement .....	95

4.10.	Finite Element Analysis .....	96
4.11.	Summary .....	98
Chapter 5	Composite Fabrication.....	100
5.1.	Introduction.....	100
5.2.	Material Characterisation for 1-3 Randomised Composites .....	101
5.2.1.	Powder Characterisation.....	101
5.2.2.	Slurry Characterisation .....	106
5.2.3.	Characterisation of Green and Sintered Samples .....	109
5.2.4.	Electrical Properties of Bulk Gel-cast PZT Ceramics and Randomised Composites.....	114
5.3.	Material Characterisation for 1-3 Diced Composites .....	116
5.3.1.	Single pitch Dicing .....	116
5.3.2.	Double pitch Dicing .....	117
5.3.3.	Electrical Properties of Diced Composites.....	118
5.4.	Surface Characterisation .....	120
5.4.1.	Surface Profile .....	120
5.4.2.	Surface Roughness .....	122
5.5.	Summary .....	125
Chapter 6	Microfabrication .....	128
6.1.	Introduction.....	128
6.2.	Microfabrication of Array Element Patterning .....	128
6.2.1.	Development Process I: LOR3A .....	129
6.2.2.	Development Process II: LOR10A.....	137
6.3.	Releasing and Wax Removal .....	144
6.4.	Summary .....	147
Chapter 7	Functional Characterisation .....	149
7.1.	Introduction.....	149
7.2.	Electrical Continuity .....	150
7.3.	Electrical Impedance Measurements .....	152
7.3.1.	1-3 Piezocomposite with 20 Array Elements .....	152
7.3.2.	20 Element $\mu$ US Array Transducers .....	157
7.4.	Pulse-echo Response.....	158
7.5.	Summary .....	163
Chapter 8	Conclusions and Recommendations for Future Work.....	166
8.1.	Conclusions .....	166
8.1.1.	Fabrication of the 1–3 Piezocomposites.....	166
8.1.2.	Microfabrication based on Photolithography .....	168

8.1.3.	Functional Properties of $\mu$ US Array Transducers .....	169
8.2.	Recommendations for Future Work.....	170
8.2.1.	$\mu$ US Array Transducers with the Addition of a Matching Layer.....	170
8.2.2.	Miniaturising the $\mu$ US Array Transducer Probe .....	171
	References .....	173
	Appendix I.....	190
	Appendix II .....	191
	Appendix III.....	192

# List of Figures

Figure 2.1 Schematic diagram of basic US imaging in A and B mode scanning. ....	12
Figure 2.2 An example of a B-mode image showing part of the profile of a foetus imaged by a 2.5 MHz Aloka system (Hitachi Aloka Medical, Ltd., Tokyo, Japan).....	12
Figure 2.3 Schematic illustration of an US beam generated by a single element transducer, SET.....	15
Figure 2.4 Schematic illustration of (a) axial and (b) lateral resolutions of two objects. ....	16
Figure 2.5 Schematic illustration of axial resolution of two objects resolved by (a) low frequency and (b) high frequency transducers. ....	16
Figure 2.6 Schematic diagram of (a) electronic scanning (b) focusing of 1-D linear arrays. ....	19
Figure 2.7 Structure of a commercial array transducer for biomedical imaging. ....	19
Figure 2.8 Schematic illustration of piezoelectric effects (a) direct and (b) converse piezoelectric effects.....	22
Figure 2.13 Two-dimensional model of non-centrosymmetric crystal materials. ....	23
Figure 2.10 Crystallographic structure of perovskite $ABO_3$ unit cell of PZT (a) cubic, (b) tetragonal and (c) rhombohedral with polarisation reversal, showing polarisation directions of [001] and [111], respectively. ....	24
Figure 2.11 A typical characteristic plot of electrical impedance magnitude and phase as function of frequency for poled piezoelectric materials.....	26
Figure 2.12 Schematic diagram of (a) 2-2 and (b) 1-3 composites.....	31
Figure 2.13 Simulated electrical impedance magnitude and phase of the 1-3 connectivity PZT ceramic piezocomposite with a periodic repetition of square pillars. ....	31
Figure 2.14 Schematic illustration of the spurious modes on the surface of 1-3 piezocomposite with a periodic repetition of square pillars in two dimensions. ....	32
Figure 2.15 Influence of volume fraction of piezoelectric material on (a) elastic stiffness constant, $C_{33D}$ ; dielectric constant, $\epsilon_{33S}$ ; thickness-mode electromechanical coupling coefficient, $k_{eff}$ , and acoustic impedance, $Z_a$ and of 1-3 piezoelectric composites fabricated with an active element or piezoelectric material based on PIMNT, PZ54 or PZT5H and an epoxy filler based on Epofix (Struers Ltd. UK).....	34
Figure 2.16 Randomised composite pattern (reprinted from <i>Ref.</i> [92]). ....	36
Figure 2.17 Simulated electrical impedance magnitude and phase of the 1-3 randomised composite with the pattern shown in Figure 2.16. ....	36
Figure 3.1 (a) Bristle block structure of 1-3 piezocomposite material surrounded by (b) passive polymer material. ....	39
Figure 3.2 Schematic procedure for the dice-and-fill technique for manufacturing 1-3 composites for single element transducers. ....	41
Figure 3.3 Schematic procedures for 1-3 composite fabrication by interdigital pair bonding (adapted from <i>Ref.</i> [8]). ....	44
Figure 3.4 Chemical structure of (a) hydantoin resin, $C_{11}H_{16}N_2O_4$ , (b) ethylene glycol diglycidyl ether, $C_8H_{14}O_4$ , and (c) Bis (3-aminopropyl) amine, $C_8H_{14}O_4$ . ....	51
Figure 3.5 SEM images of (a) $60^\circ$ tilted view of green ceramic pillars with arbitrary geometries and (b) top view of ceramic pillars (reprinted from <i>Ref.</i> [50]). ....	52
Figure 3.6 Illustration of the fabrication process of (a-d) soft mould and (e-l) a 1-3 randomised piezocomposite for a SET, using a gel casting method associated with micromoulding (adapted from <i>Ref.</i> [50]). ....	52

Figure 3.7 (a) Electrical impedance magnitude and phase (Reprinted from <i>Ref. [95]</i> ) (b) Electrical impedance magnitude (Reprinted from <i>Ref. [50]</i> ) measured from 1-3 connectivity randomised piezoelectric composite transducers. ....	53
Figure 3.8 Schematic illustration of basic photolithographic process. ....	55
Figure 3.9 Schematic illustration of the photolithographic process based on different photoresists.....	57
Figure 4.1 Outline fabrication process flow for $\mu$ US composite transducer arrays. ....	66
Figure 4.2. Photograph of the Logitech PM5 lapping machine. ....	75
Figure 4.3 SEM micrographs of (a)-(b) a sintered gel cast sample and (c)-(d) a diced ceramic piezocomposite. ....	77
Figure 4.4 Designs of array elements with fanout for (a) diced composites and (b) randomised composites.....	78
Figure 4.5 Optical micrographs of mark references used for (a) diced and (b) randomised composites at magnification of 20x. ....	78
Figure 4.6 Equipment set-up for contact poling using a power supply of 5 kV and silicone oil heated by a hotplate. A guard was used in front of the hotplate during the poling process. ....	82
Figure 4.7. (a) The custom corona poling equipment for non-contact poling of 1-3 composites (b) the assembly for holding a sample in place using a silica ring and copper plate. (reprinted from <i>Ref. [50]</i> ). ....	82
Figure 4.8 An overview of Cabline <sup>®</sup> -VS (a) plug (b) receptacle and (c) set (I-PEX Inc., Kyoto, Japan). ....	87
Figure 4.9 An expanded view of the complete composite transducer assembly and components, with an independent ground wire represented as a braided tinned Cu shield used in the final prototype.....	89
Figure 4.10 Photographs of the 20-element composite $\mu$ US transducer array prototypes...92	92
Figure 4.11 Photographs of (a) 20-channel custom-made cables (b) a 20-way receptacle soldered onto a breakout board. ....	93
Figure 4.12 (a) Experimental set-up with an impedance analyser and (b) a probe measurement on a fanout pad.....	94
Figure 4.13 (a) A Summit 12000 probe station, (b) microprobes and (c) element measurement.....	95
Figure 4.14 Experiment setup for measuring the pulse-echo response.....	95
Figure 4.15 Onscale 3D models of (a) a sample of 1-3 piezocomposite material with pillar width of 25 $\mu$ m and (b) a miniaturised transducer with assigned components in a water load with boundary conditions as indicated.....	97
Figure 5.1 The particle size distribution curves of (a) as-received PZT powder (batch no. 2008) and (b) milled PZT powder after 48 hr vibro milling. ....	102
Figure 5.2 Microstructures of (a) as-received PZT powder with batch no.2008 and (b) the same powder after vibro milling for 48 hr. ....	103
Figure 5.3 The particle size distribution curves of PZT powder with batch no. 2002 of (a) as-received powder and milled PZT powder after (b) 24 hr, (c) 36 hr and (d) 39 hr milling time.....	104
Figure 5.4 Microstructures of (a) as-received PZT powder with batch no.2002 and (b) milled PZT powder after 39 hr vibro-milling.....	105
Figure 5.5 XRD patterns of as-received and sintered PZT disc at 1200°C, prepared from 1.24 $\mu$ m powder from the batch no 2008.....	105

Figure 5.6 Variation of viscosity curves as (a) a function of shear rate and (b) a function of time of slurries comprising PZT5H powders milled for various times and with constant 48 vol% solid loading and 30 wt% resin content.....	109
Figure 5.7 A green PZT sample, prepared by gel casting from 48 vol% solid loading in 30 wt% resin with 1 wt% Dispex AA4040 and solvent, after demoulding and drying.....	111
Figure 5.8 SEM images showing (a, c) surface and (b, d) fracture microstructures of (a, b) bulk-green body samples and (c, d) sintered samples obtained from milled PZT5H powder with 48 vol% solid loading and 30 wt% resin content.....	112
Figure 5.9 SEM micrographs of typical (a-c) green and (d-f) sintered bristle-block PZT samples derived from the gel casting technique with 48 vol% solid loading of (1.24- $\mu\text{m}$ powder) in 30 wt% resin content.....	113
Figure 5.10 SEM micrograph showing exposed surfaces with defects in 1-3 randomised ceramic composites. ....	114
Figure 5.11 The electrical impedance magnitude and phase of 1-3 randomised PZT piezocomposites with operating frequencies of (a) 30.3 MHz, and (b) 36.2 MHz. ....	116
Figure 5.12 Optical micrographs showing examples of collapsed pillars in the PZT ceramic diced at (a) 36 $\mu\text{m}$ , (b) 37 $\mu\text{m}$ and (c) 38 $\mu\text{m}$ pitches. ....	117
Figure 5.13 Optical micrograph showing a top view of a test sample of diced PZT ceramic piezocomposite (after pillar exposure) made with single pitch dicing to produce 38 $\mu\text{m}$ pillar pitch. ....	117
Figure 5.14 Optical micrographs showing top views of (a) diced ceramic sample and (b) diced single crystal composite (after pillar exposure) made with a double pitch dicing method to produce 38- $\mu\text{m}$ pillar pitch.....	118
Figure 5.15 Experimental electrical impedance magnitude and phase of 1-3 (a) diced ceramic and (b) diced single crystal composites.....	119
Figure 5.16 Maximum displacement in Y-axis (YDMX) showing lateral vibration of spurious modes observed in (a) diced ceramic and (b) diced single crystal composites with the composite structure of 38 $\mu\text{m}$ pitch.....	120
Figure 5.17 Surface profiles in the composite area of (a) randomised ceramic, (b) diced ceramic and (c) diced single crystal piezocomposites measured after polishing. ....	121
Figure 5.18 Surface profiles at the interfaces between the composite area and the fan-out epoxy of (a) randomised ceramic, (b) diced ceramic and (c) diced single crystal piezocomposites measured after polishing.....	122
Figure 5.19 Optical micrographs of surfaces after polishing of 1-3 (a-b) randomised composite, (c-d) diced ceramic composite and (e-f) diced single crystal composite.....	123
Figure 5.20 Three-dimensional optical profiler images of (a – b) randomised ceramic, (c – d) diced ceramic and (e – f) diced single crystal piezocomposite surfaces (magnification 50 x). Images (a, c, and e) are the composite surfaces, images (b, d and f) are the interface regions between the composite area and the fan-out epoxy.....	124
Figure 6.1 SEM micrographs showing the undercut geometry of the LOR3A/S1818 bilayer resist profiles on Si substrates baked on a hot plate with varying baking time (a) 5, (b) 6, (c) 7, and (d) 8 min.....	131
Figure 6.2 Undercut width generated with a constant developing time of 160 sec as a function of baking time. ....	131
Figure 6.3 Optical micrographs of bilayer LOR3A/S1818 resists on Si substrates with varying LOR3A baking time at (a) 5, (b) 6, (c) 7, and (d) 8 min.....	132
Figure 6.4 SEM micrographs showing bilayer LOR3A/S1818 resists on Si substrates (a) a cross-section with an average S1818 width of $14.46 \pm 0.06 \mu\text{m}$ and (b) overview of bilayer resist profiles baked at 150 °C for 5 min.....	133

Figure 6.5 Optical micrographs of the 50- $\mu\text{m}$ array elements with fan-out patterned on a Si substrate with the baking conditions of 150 $^{\circ}\text{C}$ / 5 min. Linewidth after development: $35.04 \pm 0.56 \mu\text{m}$ ; element traces after lift-off: $34.52 \pm 0.56 \mu\text{m}$ .	133
Figure 6.6 Optical micrographs of (a-b) bilayer LOR3A/S1818 resist profiles on epoxy substrates made with the LOR3A baking condition at 150 $^{\circ}\text{C}$ for 5 min and (c-d) the 50- $\mu\text{m}$ element pitch patterned Ti/Au array elements with fan-out after lift-off in 1165 stripper.	134
Figure 6.7 Optical images of bilayer LOR3A/S1818 resist profiles established on surfaces of 1-3 (a) randomised ceramic (b) diced ceramic and (c) diced single crystal composites.	135
Figure 6.8 Optical micrographs of 50- $\mu\text{m}$ pitch Ti/Au array elements with fan-out patterned on surfaces of 1-3 (a) randomised ceramic (b) diced ceramic and (c) diced single crystal piezocomposites using a LOR3A/S1818 bilayer resist profile with the LOR3A baking conditions of 150 $^{\circ}\text{C}$ /5 min.	136
Figure 6.9 Optical micrographs of LOR10A/S1818 bilayer resist profiles established on Si substrates with LOR10A spin speeds of (a) 3000, (b) 4000, and (c) 6000 rpm.	139
Figure 6.10 SEM micrographs showing thickness of LOR10A as a function of spinning speed of (a) 3000, (b) 4000, and (c) 6000 rpm.	140
Figure 6.11 SEM micrographs showing a cross-section of (a) bilayer LOR10A/S1818 resist profile with the spin condition of 4000 rpm for 30 sec and (b) 500 nm metal film deposited on the bilayer resist pattern.	140
Figure 6.12 Microscopic images of epoxy substrates with a bilayer resist spun at 4000 rpm for 30 rpm.	142
Figure 6.13 Optical micrographs of 20 array 500 nm thick Ti/Au elements established on epoxy surfaces using a LOR10A/S1818 bilayer resist process with and lift-off carried out in (a) 1165 and (b) SVC-14 removers.	142
Figure 6.14 Optical micrographs of LOR10A/S1818 bilayer resist profiles established on the surfaces of 1-3 (a) randomised composite (b) diced ceramic composite and (c) diced single crystal composite.	143
Figure 6.15 Optical micrographs of 20 array 500 nm thick Ti/Au electrodes established using a LOR10/S1818 bilayer resist process metal established on surfaces of 1-3 (a) randomised composite (b) diced ceramic composite and (c) diced single crystal composite.	144
Figure 6.16 Optical micrographs of composite array samples derived from process 1, showing (a-b) cracking on array elements and (c) a discontinuous trace.	145
Figure 6.17 Optical microscopes of composite array samples derived from process 2, illustrating (a) cracking at a corner of an element trace, and (b-c) discontinuous traces at interfaces between fan-out pads and traces.	146
Figure 6.18 Optical micrographs of composite samples, presenting discontinuous traces caused from peeling in Process 3.	146
Figure 6.19 Optical micrographs composite samples with flawless array elements derived from Process 4.	146
Figure 7.1 Calculated resistance, $R$ , for individual elements of the (a) randomised composite, (b) diced ceramic composite, and (c) diced single crystal 1 composites; continuous element - $R < 100 \Omega$ , partial continuity - $100 < R < 10^6 \Omega$ , and discontinuous element - $R > 10^6 \Omega$ .	151
Figure 7.2 Optical microscope images of element arrays patterned on (a-b) randomised composite fabricated by the BLO Process I, (c-d) diced ceramic composite fabricated by the BLO Process II, and (e-f) diced single crystal composite 1 fabricated by the BLO	

Process I, illustrating typical examples of damages electrodes on each type of composite. .....	152
Figure 7.3 Repaired elements of (a) randomised composite and (b) diced single crystal composite 2. ....	153
Figure 7.4 Experimental measurements of electrical impedance magnitude (left) and phase (right) of 20 array elements patterned on (a-b) randomised composite, (c-d) diced ceramic composite, (e-f) diced single crystal composite 2. ....	154
Figure 7.5 Measurements of the resonance ( $f_r$ ) and anti-resonance ( $f_a$ ) frequencies and $k_{eff}$ for functional elements in (a) randomised composite, (b) diced ceramic composite, and (c) diced single crystal composite 2.....	156
Figure 7.6 Experimental measurements of (left) electrical impedance magnitude and (right) phase measured from 20 elements connected to microcoaxial cable for (a-b) TX1-RM, (c- d) TX2-PZ, and (e-f) TX3-PIMNT $\mu$ US array transducers. ....	158
Figure 7.7 Pulse-echo response of elements (a) 3, (c) 11, (c) 13, and (d) 20 from TX1-RM with $f_c$ of 27 MHz. ....	161
Figure 7.8 Pulse-echo response of elements (a) 2, (b) 7, (c) 12, and (d) 14 from TX2-PZ with $f_c$ of 30 MHz. ....	161
Figure 7.9 Pulse-echo response of elements (a) 3, (c) 5, (c) 13, and (d) 19 from TX3- PIMNT with $f_c$ of 23 MHz.....	162
Figure 7.10 FEA modelled pulse-echo response of SETs made with (a) diced ceramic composite and (b) diced single crystal composite with structures identical to those made experimentally in the present works.....	162
Figure 7.11 B-scan images of a quartz flat imaged by (a) TX1-RM, (b) TX2-PZ, and (c) TX3-PIMNT $\mu$ US array transducers. ....	163
Figure 8.1 FEA modelled pulse-echo response of SETs made with the diced single crystal composites with an identical composite structure to the experimental structure in the present work (a) without a matching layer and (b) with a matching layer. ....	171
Figure 8.2 A virtual prototype of a proposed 30 MHz $\mu$ US array with a probe with small cross-section. It comprises (a) the 1–3 piezocomposite with 20 array elements, (b) the extra epoxy, cut using the laser cutting technique, (c) flexible circuits aligned to match with the elements and connected with ACA, and (d) the addition of a backing layer cast in place to secure the electrical joints. ....	172

# List of Tables

Table 2.1 Comparison of routine medical imaging modalities. ....	8
Table 2.2 Acoustic wave velocity and acoustic impedance of body tissues. ....	13
Table 2.3 Properties of piezoelectric materials for US transducer. ....	29
Table 2.4 The acoustic, piezoelectric and electromechanical properties of 1-3 piezocomposites used for virtual prototyping $\mu$ US linear arrays. ....	34
Table 4.1 List of prototypes of $\mu$ US transducer arrays and their applications. ....	65
Table 4.2 Raw materials for the preparation of gel casting PZT suspension. ....	68
Table 4.3 Fabrication process for a 1-3 randomised piezocomposite based on a gel casting method. ....	69
Table 4.4 Geometrical parameters for a 1-3 piezocomposite operating at $\sim 30$ MHz. ....	72
Table 4.5 Dicing program parameters for production of 1-3 piezocomposite fabricated from PZT piezoceramic and PIMNT single crystal materials. ....	72
Table 4.6 Fabrication process for 1-3 diced piezoceramic composite based on a single pitch dicing method. ....	73
Table 4.7 Fabrication process for 1-3 diced single crystal composite based on a double pitch dicing method. ....	74
Table 4.8 Surface preparation conditions established for 1-3 piezocomposites using a Logitech PM5 Lapping Machine. ....	76
Table 4.9 Fabrication process of the generic steps in a bilayer lift-off process. ....	79
Table 4.10 Parameters for composite release and wax removal after lapping. ....	81
Table 4.11 Process diagram of interconnect for $\mu$ US composite transducer arrays. ....	90
Table 4.12 FEA model parameter set for 1-3 diced piezocomposite material made with the dice-and-fill technique for $\mu$ US linear arrays. ....	97
Table 5.1 Summary of particle size and specific surface area of the as-received and milled PZT powders. ....	104
Table 5.2 Measurement of viscosity and idle time of the slurries made with milled PZT powders. ....	108
Table 5.3 Electrical properties of bulk gel cast samples and 1-3 randomised composites. .....	115
Table 5.4 Electrical properties of 1-3 diced piezocomposites. ....	119
Table 6.1 Process flow of bilayer lift-off process for Si, epoxy and composite substrates based on LOR3A/S1818 resist. ....	129
Table 6.2 Process flow of bilayer lift-off process for Si, epoxy and composite substrates based on LOR10A/S1818 resist. ....	138
Table 7.1 Mean resonance and centre frequencies, and effective coupling coefficient of 1-3 piezocomposites. ....	155
Table 7.2 Characteristics and properties of $\mu$ US array transducers made with 1-3 randomised ceramic, diced ceramic, and diced single crystal piezocomposites. ....	159

# List of Terms

## Abbreviations

AC	Alternating Current Circuit
ACA	Anisotropic Conductive Adhesive
AR	Aspect Ratio
ASIC	Application-Specific Integrated Circuit
BCZT	$0.5\text{Ba}(\text{Zr}_{0.2}\text{Ti}_{0.8})\text{O}_3 - 0.5(\text{Ba}_{0.7}\text{Ca}_{0.3})\text{TiO}_3$
BET	Brunauer–Emmett– Teller Analyser
BLO	Bilayer Lift-off
BW	Bandwidth
CT	Computed Tomography
DMSO	Dimethyl Sulfoxide
DRIE	Deep Reactive Ion Etching
EGDGE	Ethylene Glycol Diglycidyl Ether
FDA	The United States Food and Drug Administration
FEA	Finite Element Analysis
FPCB	Flexible Printed Circuit Boards
ICA	Isotropic Conductive Adhesive
IPA	Isopropyl Alcohol
IPB	Interdigital Pair Bonding
LOR	Lift-off Resist
MAM	Methacrylamide
<i>MEMS</i>	Micro-Electro-Mechanical-Systems
MHz	Megahertz
MPa	Mega Pascal
MPB	Morphotropic Phase Boundary
MRI	Magnetic Resonance Imaging
NDT	Non-Destructive Testing
NMP	1-Methyl-2 Pyrrolidinone
NVP	N-Vinylpyrrolidone
PbO	Lead Oxide
PbZrO <sub>3</sub>	Lead Zirconate
PC-MUT	Piezocrystal Micromachined Ultrasonic transducers
PDMS	Polydimethylsiloxane
PET	Positron Emission Tomography
PIMNT	$\text{PbIn}_{1/2}\text{Nb}_{1/2}\text{O}_3 - \text{PbMg}_{1/3}\text{Nb}_{2/3}\text{O}_3 - \text{PbTiO}_3$
<i>PL</i>	Pulse Length
PMGI	Polydimethylglutarimide
PSD	Particle size distribution

PVB	Polyvinyl Butyral Binder
PVDF	Polyvinylidene Difluoride
PZT	$\text{Pb}(\text{Zr}_{0.52}\text{Ti}_{0.48})\text{O}_3$
RF	Radio Frequency
RM	Randomised Composite
RPM	Revolutions Per Minute
SEM	Scanning Electron Microscopy
SET	Single Element Transducer
SSA	Specific Surface Area
TX	Transducer
US	Ultrasound
VF	Volume Fraction
vol%	Volume percent
VPP	Viscous Polymer Processing
wt%	Weight percent
XRD	X-ray Diffraction
ZrO <sub>2</sub>	Zirconium Dioxide

## Symbols

$A$	Area
$C$	Capacitance
$d$	Depth
$d_{33}$	Piezoelectric charge coefficient
$\epsilon_0$	Permittivity of free space $\approx 8.85 \times 10^{-12}$ F/m
$\epsilon_r$	Relative permittivity
$f$	Frequency
$f_a$	Antiresonance frequency
$f_r$	Resonance frequency
$h$	Thickness
$I_{\text{SPTA}}$	Spatial-Peak Temporal-Average Intensity
$K$	Stiffness
$k_{33}$	Electromechanical coupling coefficient in ro mode
$k_p$	Planar electromechanical coupling coefficient
$k_t$	Thickness electromechanical coupling coefficient
$L$	Inductance
$R$	Resistance
$r$	Density
$R_A$	Axial Resolution
$R_a$	Surface roughness
$R_L$	Lateral Resolution

$R_X$	Reflection coefficient
$T$	Time delay
$T_C$	Curie Temperature
$T_G$	Glass transition
$T_R$	Room Temperature
$T_X$	Transmission coefficient
$X$	Reactance
$X_C$	Capacitive reactance
$X_L$	Inductive reactance
$\eta$	Viscosity
$\lambda$	Wavelength
$v$	Wave velocity
$\tau$	Shear stress
$\dot{\gamma}$	Shear rate

# Chapter 1 Introduction

## 1.1. High Frequency Ultrasound for Medical Imaging

Ultrasound (US) is extensively used in routine clinical diagnostics because of its excellent safety and wide availability of ultrasound frequencies. It is well-known as a non-invasive technique that does not have any biological side effects [1], as opposed to other medical imaging modalities e.g., computed tomography (CT), magnetic resonance imaging (MRI), and positron emission tomography (PET). US also has the other advantages of being a real-time imaging modality and providing low-cost imaging and portability. In contrast, CT and MRI systems are high cost, up to \$1 million, and involve time-consuming processes.

Regarding the wide availability of US systems, they have been categorised according to ranges of ultrasound frequency. US medical imaging with low operating frequencies ranging from 3-10 MHz is typically used for obstetrics, cardiology, vascular and surgical imaging to visualise objects down to approximately 1 mm in size [2], [3]. To meet the requirements for a wider range of clinical applications, high-frequency US transducers with operating frequencies beyond 10 MHz have been developed to improve resolution for imaging near subsurface structures such as in dermatology, intravascular diagnosis, ophthalmology, and US capsule endoscopy applications [4], [5]. The spatial resolution of an US transducer is principally dependent on the frequency of the device. A higher frequency gives a shorter ultrasound wavelength allowing better resolution to distinguish adjacent objects located near to each other, by distance in the order of micrometres, e.g., 50  $\mu\text{m}$  at 30 MHz.

In consequence, the clinical demand for high frequency microultrasound ( $\mu\text{US}$ ) array devices has been increasing, but few commercial manufacturers worldwide, only such as FUJIFILM Visualsonic, Verasonics, and Novosound, have been intensively focused on  $\mu\text{US}$  array development so far. It is an undeniable fact that progress toward development of  $\mu\text{US}$  arrays based on 1-3 piezocomposite materials has been developed slowly due to difficulties in manufacturing and the need to find a cost-effective approach [6]–[12]. One of the challenges to address is the limitation of fabrication techniques to achieve microscale composite structures suitable for operating at high frequencies. For example, a 1-3 piezocomposite  $\mu\text{US}$  array operating at 30 MHz needs  $\sim 25 \mu\text{m}$  pillar width,  $\sim 10 \mu\text{m}$  of inter-pillar spacing, and a pillar height of  $\sim 50 \mu\text{m}$  to maintain an aspect ratio (pillar height-to-width ratio) of two to produce adequate pulse response [13]. Another challenge in their development lies in the need for microscale array element electrodes, which should be

ideally based on half of the ultrasound wavelength in tissue ( $\lambda/2$ ) to minimise grating lobes, which can cause ghost images [1]. This means that an element pitch less than 50  $\mu\text{m}$  is required for 30 MHz  $\mu\text{US}$  imaging.

## 1.2. Motivation and Objectives

This thesis aims to demonstrate the fabrication processes for 30 MHz  $\mu\text{US}$  arrays with 20 elements based on three types of 1-3 piezocomposites. The main purpose of using composite material is due to its greater effective electromechanical coupling factor,  $k_{eff}$  (0.6-0.9), and low acoustic impedance ( $Z_a \sim 15 \text{ MRayl}$ ) for having better acoustic impedance matching to tissue than bulk piezoelectric materials. These two factors improve the transducer's capability in transmission and reception. The 1-3 connectivity piezocomposite has higher  $k_{eff}$  since this connectivity allows the piezoelectric pillars to oscillate along their length more effectively. While the low  $Z_a$  allows more acoustic energy to be transmitted to the tissue by reducing acoustic mismatch at the transducer/tissue interface. For this reason, strong transmission pulses are generated, thereby, returning echoes with high amplitude, indicating improved transducer sensitivity and bandwidth. However, it comes at the potential expense of the formation of spurious modes coupled to the fundamental thickness mode resonances, resulting in transducer performance being degraded. In addition, existing  $\mu\text{US}$  arrays based on piezocomposites have demonstrated their capabilities in US imaging. However, they have limitations in terms of proper routes to manufacture the microscale structures of piezocomposite materials and cost-effectiveness also remains a difficulty.

Considering these challenges, the objectives of the work described in this thesis are as follows:

- To address promising techniques to fabricate microscale 1-3 piezocomposite structures for  $\mu\text{US}$  arrays by gel casting associated with micromoulding and by modified dicing methods;
- To demonstrate the capabilities of 1-3 randomised piezocomposites with arbitrary pillar geometries and spacing to reduce the spurious modes which are often found in 1-3 diced piezocomposites with repetitive and symmetrical structures;
- To develop micromachining techniques by manipulating machining parameters suitable for multiple production of 1-3 diced piezocomposites for operation at high frequencies;

- To enhance transducer performance, in term of sensitivity and bandwidth, by using different types of piezoelectric materials with optimised piezoelectric and electromechanical properties;
- To develop microfabrication processes suitable for establishing fine-scale array elements on the surfaces of the 1-3 piezocomposites: and
- To demonstrate the functional properties and acoustic performance of three type of 1-3 piezocomposites and 20 element ~30 MHz  $\mu$ US arrays.

### **1.3. Contributions to Knowledge**

In realising the objectives listed in Section 1.2, this thesis presents the following contributions to knowledge established during this PhD research:

- Understanding of the study of the effect of particle size distribution on rheology behaviour and gelation time in suspensions for the gel casting technique [14].
- Demonstration of a fabrication process for 1-3 randomised PZT piezocomposites with micro-scale pillars of arbitrary horizontal cross-section using a novel technique of gel casting associated with a soft micromoulding technique [14]. A study of the development and optimisation of dicing programs to establish the minimum pillar pitch of 38  $\mu$ m for 1-3 connectivity piezocomposites, along with demonstration of fabrication processes for 1-3 piezocomposites based on commercially available PZ54 ceramic and PIMNT single crystal materials, suitable for operation at 30 MHz [15].
- Study and optimisation of surface preparation processes to minimise material thickness variation, thus providing 1-3 piezocomposites with surface roughness values in the range of 23-28 nm [15].
- Development and optimisation of a bilayer lift-off (BLO) photolithography process applied for establishment of 50- $\mu$ m element pitch, 20 element arrays with fan-out pads on 1-3 piezocomposites. Achievement of increasing yield of active elements relied on the quality of a metal layer deposited on composite substrates. Metal layers of Ti/Au with a total thickness of 500 nm are highly recommended to use to overcome thickness variation on the composite surfaces and to improve shape uniformity and continuity of array elements. This was achieved by using a LOR10A resist as a primary photoresist in the BLO process, which allowed the deposited metal thickness to be increased by 41.8%. This facilitated clean lift-off processing for smooth and

neat edges of the array elements and creation of the thicker metal layers on the composite surfaces than those using LOR3A resist [16], [17].

- Achieved methods to release and dissolve wax after lapping the composite arrays to the required thickness, while maintaining yield and avoiding the formation of cracks in the array elements. The conventional process, using 50 °C to release the composite arrays from a glass carrier and solvent cleaning, e.g., IPA and acetone, induced electrode discontinuity from epoxy deformation. This was because the arrays were exposed to harsh environments during the cycles of lapping and photolithography, leading to epoxy inclusion in the composite arrays becoming more sensitive to temperature and chemical solvents. Instead, immersion in an Ecoclear solution at room temperature was found here to be an appropriate method to release the composite arrays and maintain the quality of the array elements.
- First establishment of a 1-3 randomised piezocomposite for manufacturing a prototype 20 element  $\mu$ US array and demonstration of its capability in reducing spurious modes and its performance in US imaging [14], [15], [17], [18].
- Manufacture of three prototype  $\mu$ US arrays that incorporated 20 elements, made with PZT-5H, semi-hard PZT, and PIMNT piezocomposites with frequencies up to 32 MHz, equivalent to commercial transducers. The design of array elements with fanout pads allowed composite arrays to be interconnected and secured within a 21 mm diameter additively manufactured probe to the rear of the device with the electrical ground facing forwards for direct contact with tissue. Most elements showed themselves to be operational via primary measurements of impedance characteristics and electrical continuity, as well as pulse-echo tests for determining the acoustic performance of the devices [17].

## 1.4. Thesis Structure

This thesis is focused on  $\mu$ US array manufacture, particularly the materials and processes to which they are subject, with demonstration of success through functional and performance measures.

Chapter 2 provides an overview of the functional background behind this work, including US waves for US imaging, the basic structure of piezoelectric US probes, functionality of  $\mu$ US linear arrays, piezoelectric materials, and requirements for  $\mu$ US fabrication. In addition,

Chapter 3 reviews past and recent research in  $\mu$ US fabrication, focusing on 1-3 piezocomposite manufacture, array element fabrication and interconnection.

Chapter 4 discusses the fabrication processes to produce 1-3 randomised piezocomposites via a gel casting method and 1-3 diced piezocomposites using a modified dice-and-fill method. These processes are followed by surface preparation, array element patterning via a bilayer lift-off process based on photolithography, investigation of achievable methods for wax removal after lapping to the required thickness, and poling. Interconnects and transducer packaging are also described to demonstrate feasibility, along with prototypes of  $\mu$ US transducer arrays made with 1-3 piezocomposites. In addition, functional characterisation of the composites, as well as transducer testing are also described.

Chapter 5 presents the basic characterisation tests and measurements required for each type of 1-3 piezocomposite material. Results such as particle size distribution, rheology behaviour, green strength, density, and electrical properties of gel cast ceramic are reported to demonstrate the capability of gel casting in producing microscale structures of 1-3 randomised piezocomposites. The outcomes of manipulating dicing parameters for 1-3 diced PZT ceramic and PIMNT single crystal piezocomposites and their primary electrical properties are described. Finally, the surface roughness and profile of the three types of composites are discussed.

Chapter 6 describes microfabrication processes based on photolithography. A bilayer lift-off process was developed suitable for array element patterning on the composite substrates. The delicate processes in releasing the thin composite arrays from a glass carrier and wax removal after lapping to the required thickness are explored as means to control the yield of active array elements, since the composite experiences harsh environmental cycles during production.

Chapter 7 examines the electrical and acoustic characterisation of the three manufactured  $\mu$ US transducer arrays made with 1-3 piezocomposites. Electrical continuity identifies the active elements and electrical impedance spectroscopy characteristics provide informative data to assess functional properties of composite arrays and transducers. Pulse-echo responses are standard tests to demonstrate overall transducer performance.

Chapter 8 presents the conclusions drawn from the work presented in this thesis. The discussion highlights the various accomplishments and challenges experienced throughout the project and future work and further development that could potentially be carried to improve the devices and achieve further imaging objectives.

## 1.5. Publications and Conference Submissions

### Journal papers in preparation

1. A. Boonruang, T. Thongchai, Y. Jiang, C.E.M. Demore, S. Neale, A. Moldovan, T.W. Button, S. Cochran, Progress towards wafer-scale fabrication based on gel casting technique for 1-3 randomised piezocomposite microultrasound transducers, intend to submit in Journal of the European Ceramic Society, In progress [14].
2. A. Boonruang, C.E.M. Demore, A. Moldovan, T.W. Button, S. Cochran, Fabrication of 30 MHz microultrasound linear arrays based on 1-3 randomised and diced piezocomposites, intend to submit in IEEE Transactions on Ultrasonics, Ferroelectrics, and Frequency Control, In progress [17].

### Conference Proceedings

1. A. Boonruang, T. Thongchai, T.W. Button, S. Cochran, “Microfabrication of 1-3 composites with photolithographically defined electrode patterns for kerfless microultrasound arrays”: Poster Presentation at IEEE International Ultrasonics Symposium (IUS2019), Glasgow, UK, 6<sup>th</sup>-9<sup>th</sup> October 2019 [15].
2. A. Boonruang, A. Moldovan, T.W. Button, S. Cochran , IEEE International Ultrasonics Symposium (IUS2021), “Design and characterisation of a  $\mu$ US linear array based on randomised piezocomposite”: Poster Presentation: Virtual Conference organised by IEEE IUS2021, 11<sup>th</sup> -16<sup>th</sup> September 2021 [18]

### Conference presentations

1. A. Boonruang, T.W. Button, S. Cochran, “Progress Towards Piezocomposite Materials for Microultrasound Medical Arrays”: Poster Presentation at 48<sup>th</sup> Ultrasound Industry Association Symposium (UIA48), Toronto, Canada, 15<sup>th</sup>-17<sup>th</sup> April 2019.
2. A. Boonruang, T. Thongchai, T.W. Button, S. Cochran, “Fabrication and characterization of randomised 1-3 composite for micro-US array for biomedical imaging”: Poster Presentation at 7<sup>th</sup> International Symposium on Integrated Functionalities (ISIF 2019), Dublin, UK, 12<sup>th</sup>-14<sup>th</sup> August 2019.
3. A. Boonruang, A. Moldovan, T.W. Button, S. Cochran, “Progress towards Cross Talk Suppression in Microultrasound Arrays based on Randomized and Diced 1-3 Piezocomposites”: Poster Presentation with **Winning Poster Competition** at Piezoelectrics for End Users XI (PIEZO2021), Virtual Conference organised by University of Sassari, Italy, 21<sup>st</sup>-24<sup>th</sup> February 2021.

# Chapter 2 Functional Background

## 2.1. Introduction

Clinical US imaging is the most frequently used imaging modality because it allows non-invasive diagnosis and timely intervention, compared to other imaging modalities. An overview, capabilities, as well as introduction to use of each diagnostic imaging method are given in Section 2.2. To interpret US images, a basic understanding of the physical principles, US waves, and interaction of the waves in relation to the generation of US images are essential. These concepts are described in Section 2.3. The performance of US transducers can be determined by various parameters as listed in Section 2.4. The operating principle of ultrasonic linear array transducers and their basic components and functions are presented in Section 2.5. Section 2.6 describes piezoelectricity which is well known as an inherent characteristic in an active material or element used in US transducers. The active element is the most important part in the transducers because its function is to produce and receive US waves. It is often made of 1-3 piezoelectric composite because it provides an enhanced electromechanical coupling factor and low acoustic impedance compared to monolithic materials. However, a pitfall of this composite material remains in unwanted modes which can cause artifacts in biomedical images. Piezoelectric materials and specific requirements suited for using in US transducers are given in detail in Section 2.7. Finally, the chapter is ended by describing a promising design to tackle the problem of unwanted modes.

## 2.2. Medical Imaging Modalities

Medical imaging is a non-invasive method for imaging inside the body to characterise tissue, identify and diagnose abnormalities, and to guide interventional tools. The generic concept of a medical imaging system is that it uses energy generated from different sources which can pass through and interact with tissue. The signals generated from the interaction of energy at different levels are detected, then employed to create an image [19]. Medical imaging techniques have extended from diagnosis to intervention and from two-dimensional, 2D, images to three-dimensional, 3D, volumes to obtain high detail and precise geometrical structure of organs. Existing imaging modalities include X-ray radiography, computed tomography, CT, magnetic resonance imaging, MRI, positron emission tomography, PET, and US. Occasionally, these methods are used cooperatively for the benefit of the patient, however each of them has their own strengths and drawbacks. Table 2.1 shows a comparison of main characteristics for these techniques.

Table 2.1 Comparison of routine medical imaging modalities.

		X-ray	CT	MRI	Nuclear medicine	US
<b>Source</b>		X-rays	X-rays	Magnetic field & radio frequency	Radiotracer Positron radiation	Acoustic waves
<b>Imaging quality</b>	<b>Image resolution</b>	1 mm	<1 mm	1 mm	1 cm	0.3-3 mm
	<b>View</b>	Global view of interest, except tissue	Global view of Veins	Global view of interest	Global view of interest	Global view of interest, except veins
<b>Safety</b>	<b>Ionizing effect</b>	Low	High	Very low	High	Very low
	<b>Heat effect</b>	Very low	Very Low	Low	Low	Low
<b>System availability</b>	<b>Real-time</b>	Yes	No	No	No	Yes
	<b>2D/3D</b>	2D	2D slice/3D cross-section	2D	2D	2D/3D
	<b>Examination time</b>	Short	Medium	Long	Long	Short
	<b>Cost</b>	Low	High	High	High	low
	<b>Portability</b>	No	No	No	No	Yes

X-ray radiography and CT are based on ionizing electromagnetic radiation which is differentially absorbed by amounts according to the organs' densities in the body so that an image of the organs can be distinguished and recognisable [20]. Dense structures, such as bone, are easily imaged as they absorb the radiation and show as bright regions in the radiograph, whereas soft tissues may be difficult to image because the radiation passes through the fluids and the soft tissue easily leading to poor soft tissue contrast [19]. However, a contrast agent is occasionally used to improve contrast resolution of certain tissues in the body, appearing distinctively in the image for clear recognition and visualization e.g., blood vessels [20]. Conventional X-ray equipment generates 2D images, whilst CT produces 3D image using spiral scanning in which the machine rotates continuously around the body to acquire volume data for visualization [19]. Thus, X-ray imaging is usually used for detecting tumours, fractures in bones, and lesions within the abdomen. Although it offers speedy acquisition and highly detailed information, it is expensive and lacks a real time capability. Owing to the use of the contrast agent, the patient may be uncomfortable because the contrast materials enter the body by swallowing, rectal administration, or injection. In addition, clinicians must take precautions due to the exposure to ionizing radiation generated using

these imaging techniques, with the radiation potentially causing negative biological effects to living tissue as the number of exposures increases over a patient's lifetime [19].

MRI uses a combination of magnetic field and radio frequencies, RF, to visualise 3D images with excellent contrast in soft tissues. This technology is based on the interaction of RF energy in the electromagnetic spectrum being absorbed and emitted by protons in the tissues [21]. Most soft tissues are rich in free protons which are highly sensitive to RF signals. Consequently, this method is currently the primary imaging modality for most joint, brain, spinal pathology, and other soft tissues, which are difficult to image in both X-ray and CT imaging systems because of their poor soft tissue contrast. However, MRI produces loud noise, thus, earplugs, or headphones are needed to endure the noise. Other drawbacks of this modality include long acquisition time and relatively high cost in terms of equipment and examination [21].

PET is an advanced imaging technique used in nuclear medicine which uses a gamma camera device to detect the proton emission from a radiotracer injected into specific organs in the patient. The camera produces an image by capturing photons and converting them to the light and to a voltage signal, respectively. PET is used to locate tumours and it allows screening of the entire body [21]. To date, it is used with CT or MRI to combine the functional image with enhanced image resolution because its resolution to distinguish adjacent objects is limited to approximately 1 cm [21]. A disadvantage of PET imaging is that the radiation dose is very high.

US is sound waves with high frequencies (from 20 kHz up to gigahertz), above the frequency range detectable by human hearing (up to 20 kHz). The transducer is typically used to emit a series of US signals into the tissue, which reflect at the boundaries between dissimilar tissues and organs within the patient's body and return to the transducer. The intensity of the reflected waves (also known as echoes) is then electrically converted into a grey-scale image [21]. US is well-known as the safest form of medical imaging because it is a non-ionizing form of transmitted energy, e.g., it does not use harmful radiation, and does not have any known biological side effects as long as high intensities are not used [1], [22]. The maximum permitted intensity or spatial-peak temporal-average intensity,  $I_{SPTA}$ , stated by the United States Food and Drug Administration, FDA, should not exceed  $720 \text{ mW/cm}^2$  because  $I_{SPTA}$  determines the rise of temperature in tissue produced by the US probe [22], [23]. US provides real-time imaging which allows guidance of interventional procedures such as biopsies. Further benefits over other imaging modalities include its relatively low cost in terms of ease

of access to patients, speed of examination, low equipment cost. Also, it does not require any special infrastructure.

## 2.3. Basics of Ultrasound Imaging

### 2.3.1. Ultrasound Waves

As stated previously, US is sound waves beyond the audible range, >20 kHz. The sound can also be called a mechanical wave because the sound wave propagates through the medium by particle or molecular vibration. The sound wave can be described by frequency, wavelength, and wave velocity. The frequency,  $f$ , is the number of waves passing per second. The wavelength,  $\lambda$ , is the distance travelled in one complete wave cycle. The wave velocity,  $v$ , is the speed of sound travelling through the medium. Regarding Eq. 2.1, the velocity is dependent on the density,  $\rho$ , and the bulk modulus,  $K$ , where  $K$  is the measure of resistibility of the medium to the externally applied forces (i.e., the ratio of volumetric stress to volumetric strain). It varies in different media e.g., the average value for most human tissue is approximately 1540 m.s<sup>-1</sup>, while air and bone are 330 and 4000 m.s<sup>-1</sup>, respectively.

$$v = \sqrt{K/\rho} \quad \text{Eq. 2.1}$$

The frequency is inversely proportional to the wavelength as expressed in Eq. 2.2. This means the shorter the wavelength, the higher the frequency.

$$\lambda = \frac{v}{f} \quad \text{Eq. 2.2}$$

Several types of wave propagation exist in a medium e.g., longitudinal waves, transverse waves and Lamb waves [24]. For US imaging, longitudinal and transverse waves are mostly considered. The particle motion in the former is parallel to the direction of the wave propagation. In the latter, the particles vibrate perpendicular to the direction of the wave propagation. Longitudinal waves can be generated in liquid and solid because the waves propagate through the atomic structure or particles by a series of compressions and rarefactions. However, the waves travel faster in solid because their molecules are in closer proximity than those in liquid or gas. Consequently, they propagate in soft tissue with low speed because the tissue acts as a liquid [1]. Surface or Rayleigh waves propagate along the surface of materials with a depth of approximately one wavelength. The surface waves create ellipsoidal displacement on the surface because they comprise both longitudinal and transverse motion. For Lamb waves, the particle movement is similar to ellipsoidal displacement in surface waves, however, Lamb waves exist in materials of limited depths (plates) and penetrate them to a depth of a few wavelengths.

### 2.3.2. Ultrasound Operation

This section presents the basic principles of US image formation based on a pulse – echo response, which is usually displayed through a B-mode or brightness mode system [25].

A series of US waves are generated by a transducer and travel into the tissues of interest, where they reflect at boundaries and scatter at small dissimilarities within tissues, resulting in echoes. The echoes return to the transducer, where the pulses were generated and are detected. They are then converted into electrical signals which are used to form an image. Each echo is represented as a feature in the B-mode image. Additionally, the elapsed time between the emission of the pulses and the reception of the echoes can be calculated to quantify the distance between the transducer and an organ, corresponding to the position of the target within the body [26]–[28]. The measurement of the time delay,  $T$ , is expressed in Eq. 2.3, where the depth is represented as  $d$ , and  $v$  refers to the wave velocity in a medium. The factor of two represents the sound waves travelling to the target and returning to the transducer.

$$d = \frac{vT}{2} \quad \text{Eq. 2.3}$$

In US imaging, an amplitude scan, called an A-mode signal, is the simplest scanning mode and is a 1D measurement in which the series of sound waves are transmitted in one direction. It is usually displayed as a graph of the amplitude of the echoes from the boundaries (on the Y-axis) versus the travelling time (X-axis), known as the time domain, as illustrated in Figure 2.1. This mode is most widely employed in non-destructive testing, NDT, to detect flaws or changes in materials. Additionally, it is often used to determine transducer performance from the reflected echoes by transforming signal from the time to frequency domain, shown as a graph of the amplitude against frequency. A B-scan is a brightness mode image based on a 2D measurement. Each point displayed in the image has a different brightness which represents the amplitude of the returning echo, depending on its intensity as shown in Figure 2.2.

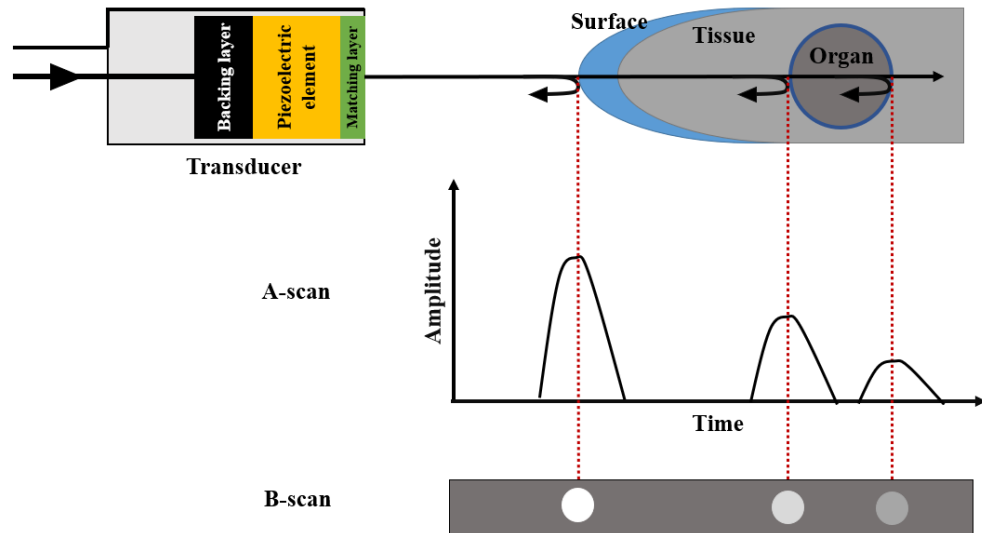


Figure 2.1 Schematic diagram of basic US imaging in A and B mode scanning.



Figure 2.2 An example of a B-mode image showing part of the profile of a foetus imaged by a 2.5 MHz Aloka system (Hitachi Aloka Medical, Ltd., Tokyo, Japan).

### 2.3.3. Interaction of Ultrasound Waves

Various interactions happen when US waves travel through a material or medium. Generally, only a small fraction of the waves could be transmitted into the deeper structure and the waves will be increasingly attenuated by refraction, scattering and absorption as the depth that the waves travel increases [29]. The remainder is reflected at boundaries between two materials with different properties, and they are called reflected waves or echoes. The relevant property is known as acoustic impedance,  $Z_a$ , which is a measure of the resistance of waves passing through a medium.  $Z_a$  is defined by the relationship between the density,  $\rho$ , of the material and the wave velocity in the material,  $v$ , as expressed in Eq. 2.4 and shown in Table 2.2.

$$Z_a = \rho \cdot v$$

Eq. 2.4

Table 2.2 Acoustic wave velocity and acoustic impedance of body tissues.

Substance	$\rho$ (g/m <sup>3</sup> )	$v$ (m/s)	$Z_a$ (10 <sup>6</sup> kg/m <sup>2</sup> s)
Air	1.3	330	0.00043
Blood	1060	1570	1.59
Bone	1908	4000	7.8
Fat	925	1450	1.38
Brain	1025	1540	1.58
Muscle	1075	1590	1.7

### Reflection, transmission, and refraction

Reflection of the US waves occurs when there is a difference in  $Z_a$ . A strong echo will be produced when two materials have a large difference in  $Z_a$ ; conversely, a weak echo will be generated if the difference in  $Z_a$  is small. However, the remainder of the US energy will continue to propagate through the next medium. Thus, the greater the difference in  $Z_a$ , the stronger the intensity of the incident waves that are reflected, measured as the magnitude of the echo. In soft tissue, most tissues have similar  $Z_a$ ; thus the magnitude of echo at a boundary is relatively small [30]–[32]. However, the interface between soft tissue and bone has a large difference in  $Z_a$ , so that a strong echo is generated, producing a high contrast US image.

For pulse-echo imaging technique, the same transducer is usually employed as an US wave transceiver; consequently, relevant boundaries are perpendicular to the US waves (angle of incidence is zero or normal angle) [32], [33]. For normal incidence, the magnitude reflection coefficient,  $R_x$ , is calculated by Eq. 2.5, where  $Z_1$  and  $Z_2$  are the acoustic impedances of the two media, respectively.

$$R_x = \left( \frac{Z_2 - Z_1}{Z_2 + Z_1} \right)^2 \quad \text{Eq. 2.5}$$

The remainder of the US waves is transmitted into the next medium when the values of  $Z_a$  for the two media are similar. A measure of the transmission wave at normal angle of incidence, known as the transmission coefficient,  $T_x$ , can be determined using Eq. 2.6 [33].

$$T_X = 1 - R_X = \frac{4Z_1Z_2}{(Z_1 + Z_2)^2} \quad \text{Eq. 2.6}$$

However, the direction of transmitted waves propagated through the next medium deviates from the incident waves because of the change in the wave velocity of the medium [34]. This effect is called refraction. Besides, the wavelength is also changed according to the difference in the wave velocities in the two media. The refracted angle is determined by Snell's law as follows:

$$\frac{\sin\theta_t}{\sin\theta_i} = \frac{v_1}{v_2} \quad \text{Eq. 2.7}$$

where  $\theta_i$  is the angle of the incidence,  $v_1$  is the wave velocity in the first medium,  $\theta_t$  is the angle of the refraction, and  $v_2$  is the wave velocity in the second medium. According to Eq. 2.7, the angular deviation of the refracted beams is proportional to the difference in the wave velocity in the two media. Thus, the refracted beams may cause artifacts in US images. For this reason, the US probe should be close to perpendicular to the structure of interest to minimise the angle of incidence [25].

### **Attenuation**

As US waves propagate through material, the energy intensity in the wave is lost to the material by several processes e.g., reflection, scattering, and absorption [32]. This loss of intensity is called attenuation. The intensity of the acoustic wave becomes increasingly attenuated as the depth of penetration increases. Reflection is categorized as one cause of attenuation since the intensity of the echo is proportional to the difference in  $Z_a$  as described above. Scattering occurs when acoustic energy encounters a material whose dimensions are smaller than the US wave. Thus, the wave is scattered in different directions other than its original direction, resulting in a reduction of echo intensity [32]. The greatest cause of attenuation in the body is absorption, which is the process in which the acoustic energy is converted into heat. In this case, the heat arises from molecular oscillation in tissue produced by the acoustic pulse [31]–[33].

In soft tissue, the amount of attenuation is proportional to the frequency of US and penetration [32], [34]. It can also be specified in terms of an attenuation coefficient,  $\alpha$ , in the units of decibel, dB, per centimetre, cm. Thus, a high frequency US wave will be more attenuated than a lower frequency one because the former has a short wavelength, and consequently provides high resolution. For this reason, high frequencies are preferentially

employed for imaging superficial structures e.g., in ophthalmology, dermatology and intravascular imaging [34].

## 2.4. Functional Properties of Ultrasound Transducers

The quality of US images is strongly dependent on the parameters of the transducer performance, including axial and lateral resolution and sensitivity. It is thus worth to mention the parameters before describing transducer components and their function.

### Imaging Resolution

The quality of biomedical images is dependent on the operating frequency and the spatial resolution of a transducer. Spatial resolution can be divided into axial resolution and lateral resolution and is the ability of the US transducer to distinguish between two adjacent objects in tissue [35]. Generally, an US beam comprises three regions: the near field zone, the focal point zone and the far field zone [36] as presented in Figure 2.3. The near field zone is located close to the transducer face, where the beam profile converges towards the focal zone where the beam is greatly focused. The far field is the zone beyond the focal zone, with a divergent beam profile and loss of US intensity [36].

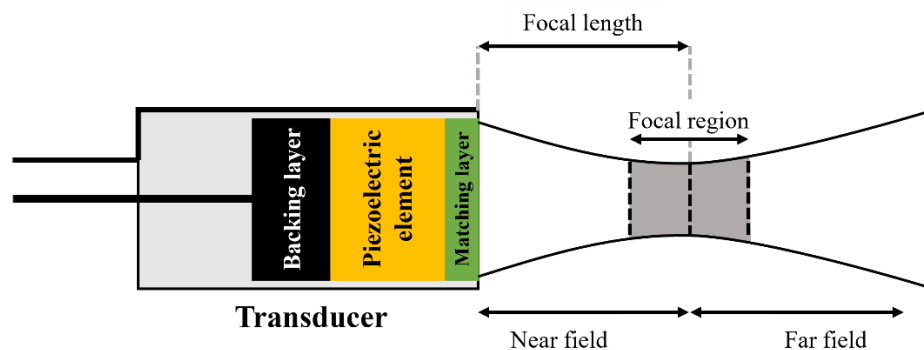


Figure 2.3 Schematic illustration of an US beam generated by a single element transducer, SET.

### Axial Resolution

Axial resolution,  $R_A$ , expresses the ability to differentiate two targets located close to each other along the direction of wave propagation, as displayed in Figure 2.4 (a), thus, it is also known as longitudinal resolution. The axial resolution is typically determined by the spatial pulse length,  $PL$ , of the pulse-echo response of the transducer and the acoustic velocity,  $v$ , in the medium, which can be expressed in Eq. 2.8 [35], [37].

$$R_A = \frac{1}{2} \nu PL$$

Eq. 2.8

Better axial resolution requires a short pulse, which can be provided by using a high frequency transducer and a damping material (backing layer) to reduce the number of cycles or reverberations. However, this comes at the expense of reducing the penetration depth of US waves because high frequencies and pulses which have lost energy to a backing layer are easily absorbed by tissue. Figure 2.5 illustrates the characteristics of transmitted pulses from low and high frequency transducers and their ability to resolve two adjacent targets. A high frequency transducer with a shorter pulse achieves better axial resolution than a low frequency one.

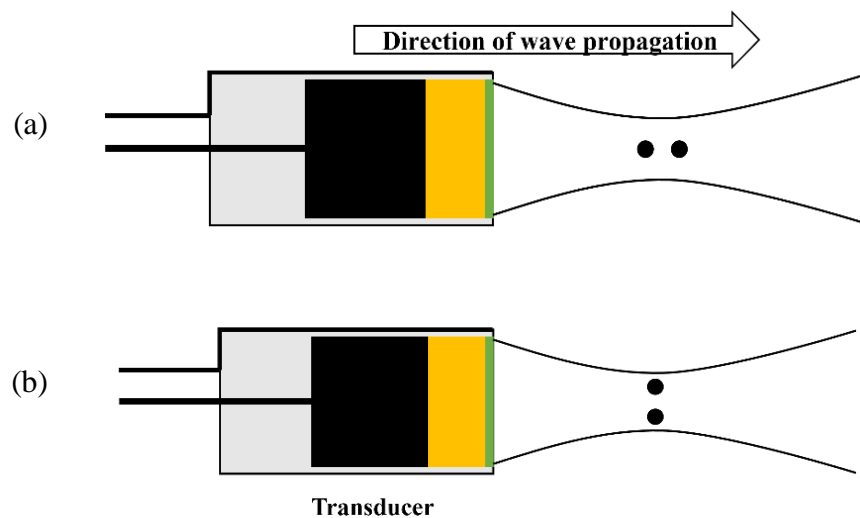


Figure 2.4 Schematic illustration of (a) axial and (b) lateral resolutions of two objects.

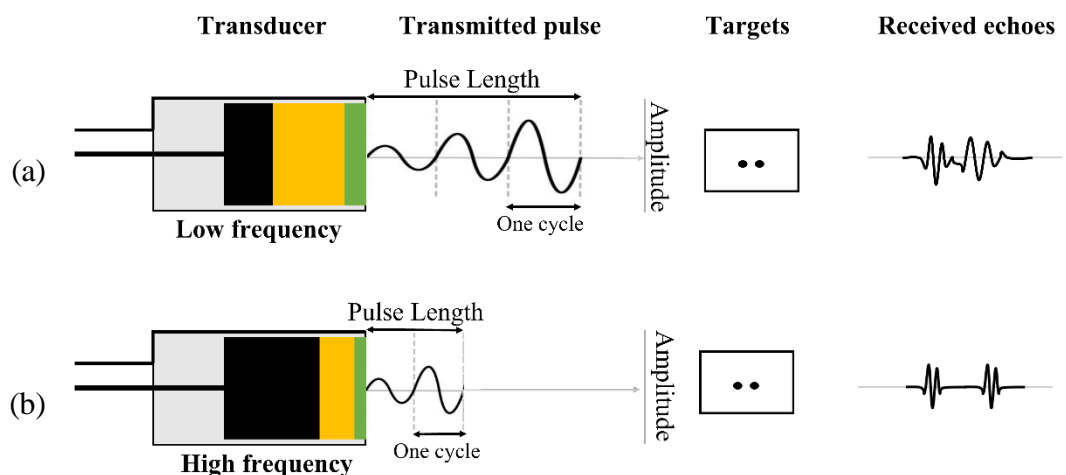


Figure 2.5 Schematic illustration of axial resolution of two objects resolved by (a) low frequency and (b) high frequency transducers.

## Lateral Resolution

Lateral resolution,  $R_L$ , is the ability to distinguish two close targets perpendicular to the direction of the US beam as presented in Figure 2.4 (b).  $R_L$  is dependent on depth of imaging [35]. Also, transducers provide effective focusing and high  $R_L$  in near field zone because the structures are scanned by a convergent beam which can only focus within this region. Meanwhile,  $R_L$  in the tissues beyond the near field zone or focal length deteriorates because they are scanned with a divergent beam with low echo intensity [35] as shown in Figure 2.3. Thus, the longer the focal length, the better the lateral resolution. The focal length of transducers can be determined as follows [35]:

$$\text{Focal length} = \frac{\text{aperture diameter}^2}{4 \times \text{wavelength}} \quad \text{Eq. 2.9}$$

According to Eq. 2.9, a short wavelength and large aperture are required to increase the focal length. Short wavelength can be achieved by fabricating a high frequency transducer assembled with a highly damping backing material to reduce the number of reverberations of the active element. The aperture of a transducer is described as the transducer diameter. For the SETs, the aperture size is equivalent to the width of an active element, while for array transducers, the aperture is the overall dimension of all active elements that work together.

In US imaging,  $R_A$  is more often used than  $R_L$  because  $R_L$  is heavily affected by the depth of imaging and width of the US beam as mentioned previously. However,  $R_L$  of the array can be enhanced by electrically focusing via time delays. By altering the time sequence, the array allows flexibility in focusing at different depths [38].

## Sensitivity

Sensitivity is the ability of a transducer to detect small targets at definite locations in the medium, which is determined by the magnitude of the amplitude in the echo response [39], [40]. Greater sensitivity can be achieved by employing piezoelectric materials with high electromechanical coupling coefficient, high volume fraction of piezoelectric material, matching and backing layers with a lower  $Z_a$  than the piezoelectric materials in order to enhance the transmitted pulses and the echo response [41]–[44]. All these factors are described in Section 2.5.1.

## 2.5. 1D Microultrasound Array Transducer

To explain the data acquisition in a B-scan system, the six elements of the linear array shown in Figure 2.6 are used as an example. To produce the left B-mode scan line in the final display, the left element is initially excited, and the same element receives echoes. Then, the second element from the left is pulsed, and the echoes are received by this element. This will continue line-by-line as a sequence until the last element is excited to complete the last scanned line shown in the display. Generally, the scan lines correspond to the number of elements in the array, and the field of view is similar to the physical length of the linear array aperture [45].

In a 1D array, active elements are usually rectangular in shape and arranged in a straight line along the x-axis as shown in Figure 2.6. The array provides 2D images where subgroups of the elements are excited to produce a transmitted pulse, and subsequently receive the echo with the same elements. Image formation by this array type produces a rectangular image format.

Typically, the active elements in an array system are individually connected to electrical circuits and are mechanically and electrically isolated from their neighbours. The distance between the centres of two adjacent elements is called the pitch, and the spacing between the elements is known as the kerf [46]. In structural transducer design in relation to array operation, the element pitch is usually designed to be approximately one wavelength,  $1\lambda$ , to minimise side lobes, which consist of low-intensity acoustic beams located near the main beam [6], [47]. The side lobes appear when the pitch is much larger than a half-wavelength,  $\lambda/2$ , because several beams are sent out, instead of one primary beam being transmitted. Ideally, it should be equal to the half-wavelength to produce one main beam travelling to the tissue. With this arrangement, the side lobes will no longer exist to cause artefacts in US imaging [1]. However, the element pitch and kerf based on  $\lambda/2$  is difficult to achieve due to the limitation of tools to fabricate extremely fine dimension of element and kerf.

The array provides three advantages over SETs. Firstly, focusing can be varied as a function of depth by altering the timing sequence for each depth of focus. Secondly, it allows electronic control by which active elements are sequentially scanned along the x-axis. Lastly, according to electronic scanning, high frame rates of 160 frames/sec can be achieved, depending on maximum image depth and number of elements in the array [38], [40], [45], [48].

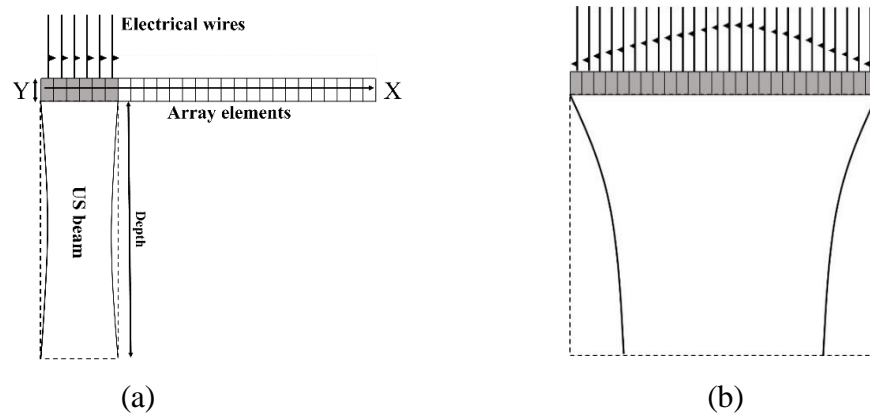


Figure 2.6 Schematic diagram of (a) electronic scanning (b) focusing of 1-D linear arrays.

### 2.5.1. Structure of Piezoelectric Medical Ultrasound Probes

Generally, the principal components of a SET are similar to those of array transducers, except that each element in the arrays is isolated to act as a SET. An overview of the structures and functions is presented in this section. Figure 2.7 shows features and components in a commercial array transducer. The basic transducer comprises the principal components as follows:

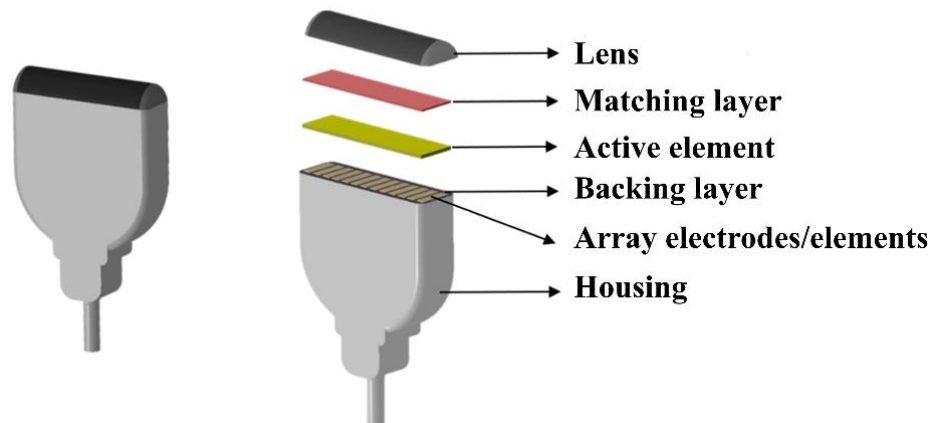


Figure 2.7 Structure of a commercial array transducer for biomedical imaging.

#### Active element

The active element is the most important part of an US transducer. It is usually made of piezoelectric material which generates and receives US waves. 1-3 piezocomposite material is the extensively used in medical US imaging because of its two main advantages. Firstly, it provides an excellent electromechanical coupling coefficient in thickness mode,  $k_t$ , which is a measure of the conversion efficiency between acoustic and electrical energy in the material. The greater the coupling coefficient, the better the transducer performance, expressed as broad bandwidth and high sensitivity. This is because the 1-3 composite with high  $k_t$  enables to produce strong transmission of US waves [41], [42]. Secondly, it has low

$Z_a$  leading to better acoustic matching between the transducer and the medium because the low  $Z_a$  also improves transmission of US waves to the human body [49]. Widely used piezoelectric materials for manufacturing 1-3 composite transducers include soft PZT,  $\text{Pb}(\text{Zr}_{(1-x)}\text{Ti}_x)\text{O}_3$ , type ceramics and relaxor Pt-based material, e.g.,  $\text{Pb}(\text{In}_{1/2}\text{Nb}_{1/2})\text{-Pb}(\text{Mg}_{1/3}\text{Nb}_{2/3})\text{-PbTiO}_3$ , PIN-PMN-PT or PIMNT, single crystals because they possess excellent piezoelectric properties.

There have been attempts to use lead-free piezoelectric material, e.g., BCZT ( $0.5\text{Ba}(\text{Zr}_{0.2}\text{Ti}_{0.8})\text{O}_3 - 0.5(\text{Ba}_{0.7}\text{Ca}_{0.3})\text{TiO}_3$ , 0.5BZT-0.5BCT, as alternative piezoelectric materials, to replace the Pb-based materials because of the risks in using lead-based material. Unfortunately, single element transducers, SETs, made from Pb-free materials provide lower coupling coefficient e.g.  $k_t$  of 0.43, which is poorer than that of Pb-based materials by a significant amount e.g. 53% for PZT with  $k_t$  of 0.76 [50].

### **Backing layer**

In transducers for biomedical imaging, the backing layer of absorbing material is generally made of a mixture of an epoxy resin and tungsten powder. The purpose of this layer is to support the thin layer of an active element and reduce reverberation. A backing layer with  $Z_a$  identical in value to that of the active element enables to produce a short  $PL$  because it will absorb energy and produce a short transmission pulse, so that better axial resolution and broad bandwidth can be achieved. However, less acoustic energy is emitted, leading to decreased transducer's sensitivity [44], [51], [52]. Alternatively, a backing material with a lower  $Z_a$  than that of the active material can improve sensitivity because less energy is absorbed into the backing layer and, consequently, penetration depth is increased. Unfortunately, to achieve good sensitivity, spatial resolution must be sacrificed because of the production of a long wavelength [43], [51]. Therefore, a compromise between resolution and sensitivity is required.

The backing layer should have high attenuation or a high absorption coefficient to absorb acoustic energy from internal reverberation [51]. The optimal composition of backing materials used for medical US imaging has been well studied by Webster [43]. It was found that tungsten-loaded epoxy ranging from 15 - 30 % volume fraction obtains  $Z_a$  of 6 - 10 MRayl, which is lower than that of composite,  $Z_a \sim 15$  MRayl, and attenuation of 30-35 dB/mm. Besides, a mixture to satisfy these conditions provides good flowability for ease of casting in the manufacturing process.

### **Matching layer**

The matching layer is used to improve the efficiency of energy transmission from the active element to the target medium, e.g., tissue, by reducing their difference in  $Z_a$ . A large acoustic mismatch between two media results in most of the acoustic energy being lost by attenuation through reflection at the transducer faces, leading to few acoustic waves being transferred to the medium, as previously described in Section 2.3.3. Thus, the acoustic mismatch at the interface should be reduced to enhance the acoustic energy transferred across the interfaces. This can be achieved by using a matching layer with intermediate acoustic impedance, compared to that of the material and the medium, to minimise the acoustic mismatching across the interface, leading to more transmission power being transmitted [43]. The required  $Z_a$  can be calculated in relation to the acoustic impedance of the active element and the load as follows:

$$Z_a = \sqrt{Z_{active\ element} Z_{load}} \quad \text{Eq. 2.10}$$

Additionally, a specific thickness of matching layer corresponding to a quarter wavelength,  $\lambda/4$ , at the transducer's operating frequency enhances the intensity of the acoustic energy transmitted into tissue [53], [54]. However, for high frequency or microultrasound transducers,  $\mu\text{US}$ , it is difficult to establish a matching layer with the required thickness based on the wavelength and the acoustic impedance because the thickness is typically on the order of a few microns,  $\sim 18\ \mu\text{m}$  for 30 MHz. Especially in the case of array transducers, any variation in fabricating the thickness, either by machining e.g., precise lapping or using a bond line layer greater than  $1\ \mu\text{m}$  in thickness to attach a stacked matching layer, can significantly degrade the transducer performance by causing variation in the signal response across the elements [53].

### **Transducer housing**

The transducer housing is typically made of a hard material e.g., stainless steel or plastic. The housing contains the whole assembly including the active element, matching layer, backing layer, array electrodes or elements and interconnects, such as flexible PCBs. It protects the electrical components inside from the outside environment.

## 2.6. Principle of Piezoelectricity

### 2.6.1. Piezoelectric Effects

Most biomedical US transducers employ piezoelectric materials to generate and convert US waves into electronic signals for imaging. The specific characteristic of change of dimension or production of an electric field of the material is known as the piezoelectric effect. The property of the materials that enables the generation of an electric charge proportional to the applied mechanical stress is denoted as the direct effect, Figure 2.8 (a). Conversely, the property of the materials undergoing a change in dimensions when they are subjected to an electric field is called the converse effect, Figure 2.8 (b). The equations that describe these effects are as follows [55]:

$$D = dE + \varepsilon^T E \quad \text{Eq. 2.11}$$

$$S = s^E T + dE \quad \text{Eq. 2.12}$$

where  $D$  is the electric displacement (or polarisation),  $T$  is the stress,  $E$  is the electric field,  $S$  is the strain,  $d$  is a piezoelectric coefficient,  $s^E$  represents the material compliance under short-circuit conditions, and  $\varepsilon^T$  represents the dielectric constant of piezoelectric materials without clamping.

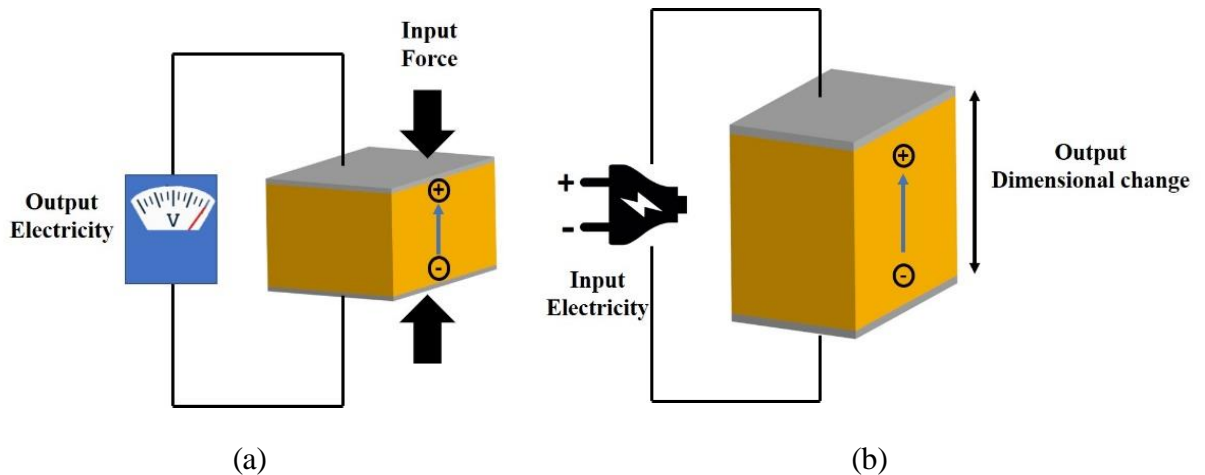


Figure 2.8 Schematic illustration of piezoelectric effects (a) direct and (b) converse piezoelectric effects.

### 2.6.2. Piezoelectricity and Ferroelectricity

Materials consist of many three-dimensional crystallographic units, called the unit cell, repeated throughout their entirety. In general, there are seven crystal systems in crystalline materials: triclinic, monoclinic, orthorhombic, tetragonal, rhombohedral, hexagonal and cubic, which are classified by the symmetry of the unit cell [56]. Regarding crystallographic

symmetry, crystal materials can be categorised into 32 crystal classes [55]. Among these groups, they are divided into two types: centrosymmetric and non-centrosymmetric. In centrosymmetric classes with and/or without an applied force, there is no net polarisation ( $P = 0$ ) because the effective centres of the cations and anions in the unit cell coincide. For the non-centrosymmetric classes, which lack a centre of symmetry in the unit cell, the net polarisation ( $P > 0$ ) is produced by negative ion displacement when a force is applied, as presented in Figure 2.9 [57]. Only 20 of these non-centrosymmetric classes possess a polarisation which is proportional to an applied stress, known as piezoelectric. 10 of these groups are pyroelectric. The pyroelectric groups have a permanent polarisation which is dependent on temperatures. For instance, the net polarisation in the crystal increases with increasing the temperature but it reduces to zero when the temperature rises beyond its Curie temperature,  $T_C$ , at which a material loses its pyroelectricity. All pyroelectric materials exhibit the piezoelectric effect, but not all piezoelectric materials are pyroelectric.

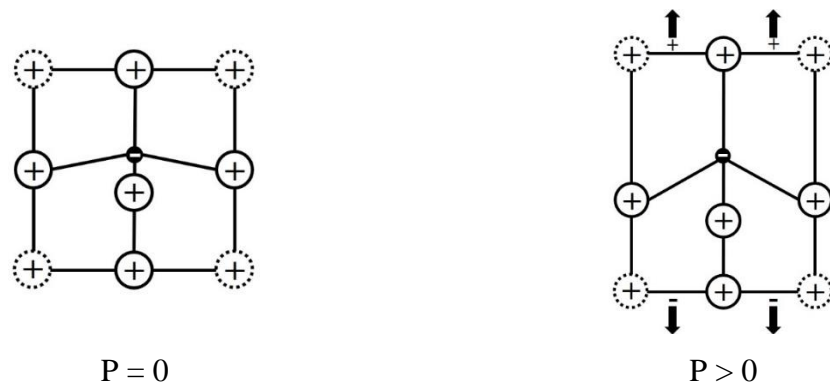


Figure 2.9 Two-dimensional model of non-centrosymmetric crystal materials.

As mentioned previously, piezoelectricity, with its reversible transduction effect between mechanical and electrical energy, is exhibited only in non-centrosymmetric materials. The characteristics of materials which exhibit the piezoelectric effect rely on polarisation, e.g., electric dipoles generated from a net movement of positive and negative ions [55] as illustrated in Figure 2.10 (b) - (c). For those materials to exhibit piezoelectricity, the polarisation can be induced by external stress and /or an applied electric field.

From the crystallographic classification, ferroelectric materials are a subset of piezoelectric materials [55]. They possess spontaneous polarisation and permanent dipoles in the unit cell structure, indicating a material which possesses electrical polarisation in the absence of an external electric field. The dipoles can be reversed by an applied electric field. There are four types of ferroelectric ceramics that can be subdivided from ferroelectric materials. The group with the  $ABO_3$  perovskite structure is the most important for various applications, e.g.

sensors, generators, and transducers, because the materials in it possess superior dielectric, ferroelectric and piezoelectric properties [55].

The unit cell of lead zirconate titanate, PZT, is usually used to represent the  $ABO_3$  perovskite structure, where the six coordinated oxygen,  $O^{2-}$ , anions are located at the face centres of the cubic or pseudo cubic unit cell and linked to each other as an octahedral cage. The A-sites at the corner of the unit cell are filled by  $Pb^{2+}$  ions and the B-sites within the oxygen cage are occupied by  $Zr^{4+}$  and  $Ti^{4+}$  ions as shown in Figure 2.10 (a), which represents the material at temperatures above its  $T_C$ . In this cubic form the structure is centrosymmetric and thus paraelectric (not piezoelectric). As the material is cooled below the  $T_C$ , a number of structural changes occur into tetragonal, orthorhombic and rhombohedral forms at progressively lower temperatures. Red arrows indicate a spontaneous polarisation in a particular crystallographic direction. The tetragonal crystallographic structure has six polarisation directions in a family of equivalent directions of  $\langle 001 \rangle$  in the unit cell, including  $[100]$ ,  $[100]$ ,  $[010]$ ,  $[010]$ ,  $[001]$ ,  $[001]$  directions. While the rhombohedral crystallographic structure has eight polarisation directions along body diagonal in a family of equivalent directions of  $\langle 111 \rangle$ , including  $[111]$ ,  $[111]$ ,  $[111]$ ,  $[111]$ ,  $[111]$ ,  $[111]$ ,  $[111]$ ,  $[111]$ . The application of an appropriate electric field or mechanical stress can cause the direction of polarisation to be reversed, so the materials display ferroelectric behaviour.

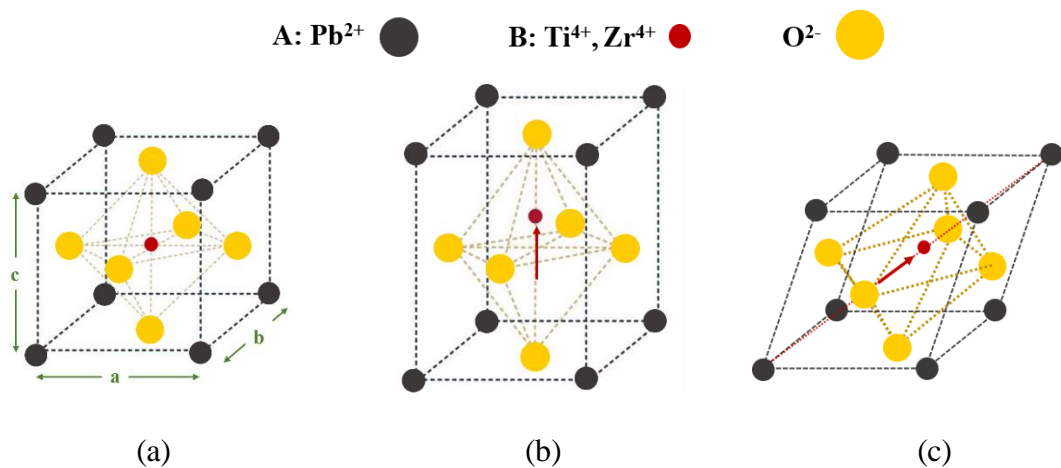


Figure 2.10 Crystallographic structure of perovskite  $ABO_3$  unit cell of PZT (a) cubic, (b) tetragonal and (c) rhombohedral with polarisation reversal, showing polarisation directions of  $[001]$  and  $[111]$ , respectively.

Generally, in polycrystalline materials under their natural condition, the individual dipoles are randomly oriented, cancelling their overall effect and thus resulting in a net zero dipole. In order to become piezoelectrically active, a high-voltage direct current electric field is applied while the material is heated to a temperature below the  $T_C$ . This procedure, known

as poling, aligns the random dipoles in the material and renders it to display bulk piezoelectric properties [58]. The higher temperature eases the mobility of domain walls; hence, the dipoles are more easily reoriented along crystallographic directions close to that of the electric field. After the poling process, the dipoles remain at least partially aligned, producing a net dipole or polarisation [55], [59].

### 2.6.3. Electrical Impedance Spectroscopy

Electrical impedance,  $Z$ , is one of the key properties of piezoelectric materials, indicating their resonance frequencies. It is always measured with an alternating current circuit, AC, and affects the relative phase of the voltage and current. It is composed of a real part, resistance,  $R$ , and an imaginary part, reactance,  $X$ . Thus, the electrical impedance of the materials can be expressed by the impedance magnitude,  $|Z|$ , and phase,  $\theta$ , as follows:

$$|Z| = \sqrt{R^2 + X^2} \quad \text{Eq. 2.13}$$

$$\theta = \arctan\left(\frac{X}{R}\right) \quad \text{Eq. 2.14}$$

In a circuit with fixed resistance, capacitance and inductance,  $R$  is constant and does not vary with frequency, but  $X$  is frequency dependent. The reactance comprises an inductive reactance,  $X_L$ , and a capacitive reactance,  $X_C$ , and is expressed as:

$$X = X_L - X_C \quad \text{Eq. 2.15}$$

$X_L$  and  $X_C$  are calculated as follows:

$$X_L = 2\pi fL \quad \text{Eq. 2.16}$$

$$X_C = \frac{1}{2\pi fC} \quad \text{Eq. 2.17}$$

where  $L$  is the inductance, and  $C$  is the capacitance.

In the impedance spectroscopy of piezoelectric materials, the capacitive reactance is a significant property as it relates to the permittivity of the unpoled materials. In a high frequency US transducer, materials with a high permittivity are preferred because the electrical impedance of the device is inversely proportional to the permittivity of the piezoelectric material [60] as described in Eq. 2.18:

$$C = \frac{A\varepsilon_r\varepsilon_0}{h} \quad \text{Eq. 2.18}$$

where  $A$  is the electrode area of the active element,  $h$  is the thickness of the substrate,  $\epsilon_0$  is the permittivity or dielectric constant of free space,  $\epsilon_0 \approx 8.85 \times 10^{-12}$  F/m, and  $\epsilon_r$  is the relative permittivity of the material. Thus, unpoled materials with high permittivity, and high volume fraction of piezoelectric material enable improved electrical matching and minimise electric noise between the device, cabling, and standard instruments, which generally have an impedance matching the  $50 \Omega$  impedance of the cabling [49], [61].

Electrical impedance spectroscopy is a tool used for evaluating the electrical impedance magnitude and phase of a sample of piezoelectric material as a function of frequency, as shown in Figure 2.11.

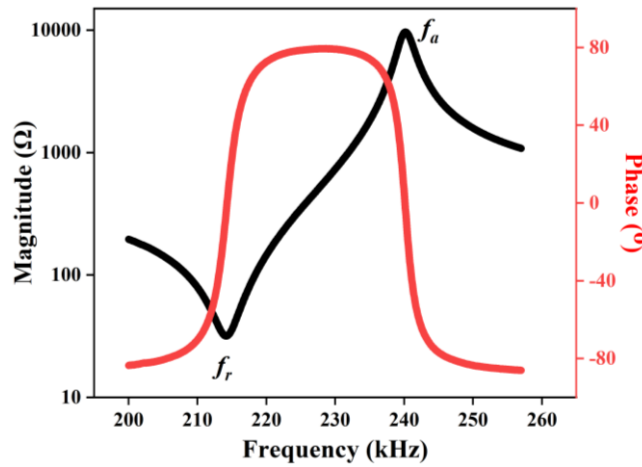


Figure 2.11 A typical characteristic plot of electrical impedance magnitude and phase as function of frequency for poled piezoelectric materials.

Electrical impedance spectra can be used to determine  $f_r$ , the resonance frequency, and  $f_a$ , the antiresonance frequency, of the sample, as well as other harmonics and unwanted resonances.  $f_r$  is the frequency at which the material impedance has a minimal magnitude and a phase closed to  $-90^\circ$ , and  $f_a$  is the frequency at which the material impedance has a maximum magnitude and a phase closed to  $90^\circ$  [62]. Additionally, these resonance frequencies are often employed to calculate the effective electromechanical coupling coefficient in the thickness mode ( $k_{eff}$ ) of the piezoelectric elements as follows [63]:

$$k_{eff} = \sqrt{\frac{\pi}{2} \cdot \frac{f_r}{f_a} \cdot \tan\left(\frac{\pi}{2} \cdot \frac{f_a - f_r}{f_a}\right)} \quad \text{Eq. 2.19}$$

## 2.7. Piezoelectric Materials for Medical Imaging

### 2.7.1. Specific Requirements

To maximise the performance of an US transducer for medical use, a compromise is necessary between its dielectric, elastic, and piezoelectric properties. The crucial factors that need to be considered for the active element selection are summarised as follows [41], [42], [49]:

- The  $k_t$  or  $k_{eff}$  should be high, as close as possible to 1, to achieve broad bandwidth and high sensitivity of US transducers.
- The acoustic impedance should be similar to that of human tissue ( $\sim 1.5 \times 10^6$  kg/m<sup>2</sup>s) to maximise the intensity of the transmitted acoustic waves and of the received echoes.
- High relative permittivity,  $\epsilon_r$ , is desirable for better electrical matching between the transducers and imaging instrumentation circuits as mentioned in Section 2.6.3.
- Mechanical and dielectric losses should be minimised to reduce the heat generated by energy conversion of the materials.

### 2.7.2. Pb-based Piezoelectric Ceramics

Pb(Zr<sub>0.52</sub>Ti<sub>0.48</sub>)O<sub>3</sub>, PZT, piezoceramic is the most extensively used in medical imaging transducers among the other available piezoelectric materials [55], [64]. Particularly, PZT with a morphotropic phase boundary, MPB, composition is usually found at the ratio composition of PbZrO<sub>3</sub>:PbTiO<sub>3</sub> 52%:48%. This composition has high electromechanical coupling coefficient, piezoelectric constant and dielectric permittivity because it has two coexisting phases of rhombohedral and tetragonal crystal structures [59]. The coexisting phases provide more possible polarisation states as described in Section 2.6.2. The more polarisation states, the better the electrical properties of the materials because there are more possibilities of the dipole moment to be aligned along the polarisation directions when an external electric field is applied. In addition, PZT is relatively low cost and widely commercially available. Furthermore, it offers a relatively high  $T_C$ , allowing utilization at relatively high temperature.

The properties of PZT can be easily tailored to meet the requirements for a wide range of applications by means of donor and acceptor doping [55], [59]. Donor additives, e.g., ions with higher charge than that of the replaced ions, are compensated by cation vacancies to

maintain the stability of the unit cell structure. For instance,  $\text{La}^{3+}$  and  $\text{Nb}^{5+}$  ions substitute into the A- and B-site  $\text{Pb}^{2+}$  and  $\text{Zr}^{4+}$  ions, respectively. This compensation enhances domain reorientation and hence PZT ceramic produced with donor additives, known as soft PZT, offers high remanent polarisation, permittivity and electromechanical coupling factors [55]. In contrast, in hard PZT, oxygen vacancies are created to increase the stability through acceptor dopants such as  $\text{Fe}^{3+}$  replacing the  $\text{Zr}^{4+}$  or  $\text{Ti}^{4+}$  ions. Domain reorientation is restricted by these oxygen vacancies. Consequently, hard PZT provides low dielectric constants, low dielectric losses and poor coupling factor [55]. For the reasons outlined above, soft PZT is more desirable for use as the active element in high frequency US transducers for biomedical imaging.

Standard commercial soft PZT material is divided into two types, PZT5A and PZT5H. PZT5H is commonly used due to its high electromechanical coupling coefficient and dielectric permittivity [65]. Unfortunately, the PZT ceramics have a high acoustic impedance (34 MRayls, as shown in Table 2.3) which results in high transmission and reception losses generated by the large difference in acoustic impedance between tissue and the active element. It is also brittle, and this may lead to difficulty in machining it e.g., for focused transducers.

### 2.7.3. Relaxor PT-based Piezoelectric Single Crystal

Among piezoelectric materials, the relaxor lead titanate (PT)-based family in single crystal form is the most attractive group for fabricating high frequency US transducers because it can be used to produce transducers with broad bandwidth and high sensitivity. The binary phase,  $\text{Pb}(\text{Mg}_{1/3}\text{Nb}_{2/3})\text{O}_3\text{-PbTiO}_3$ , PMN-PT, and the ternary phase  $\text{Pb}(\text{In}_{1/2}\text{Nb}_{1/2})\text{-Pb}(\text{Mg}_{1/3}\text{Nb}_{2/3})\text{-PbTiO}_3$ , PIN-PMN-PT or PIMNT, are extensively used in biomedical imaging. They exhibit higher electromechanical coupling coefficients, including,  $k_t \sim 0.59$  and  $k_{33} \sim 0.9$ , than PZT materials. Where  $k_t$  denotes electromechanical coupling coefficient in thickness mode used in a thin and wide plate and  $k_{33}$  represents electromechanical coupling coefficient thickness mode but it is used in a tall and thin rod or pillar [66]. In addition, piezoelectric charge coefficient or  $d_{33} > 1500$  pC/N, which is a measure of induced polarisation when the material is subjected to an electric field, is greater compared with other piezoelectric materials [67]–[69]. These electrical properties are observed at the MPB, at the composition of  $\text{PbTiO}_3 \sim 35\%$ , with the existence of the rhombohedral phase.

An advantage of the ternary PIMNT single crystal is that it has a higher Curie temperature,  $T_C \sim 200$  °C, than that of the binary phase,  $T_C \sim 130$  °C [69]. Therefore, it is considered

preferable to use because it is less susceptible to degradation during transducer fabrication. However, the main drawbacks of single crystals lie not only in high  $Z_a$  as listed in Table 2.3 but also in fragility and brittleness, leading to difficulties in micromachining the materials [70], [71].

#### 2.7.4. Piezoelectric Polymers

In terms of transducer manufacturing, polyvinylidene difluoride, PVDF, is an alternative piezoelectric material with notable properties suitable for use in a wide range of medical imaging applications. It provides benefits in different aspects over other piezoelectric materials, including low cost of manufacture, high mechanical flexibility for fabricating transducers with spherical curvature for beam focusing, and extremely low  $Z_a$ , ~4 MRayl [72]. However, it has poor efficiency in US wave transmission because of its low coupling factor and low dielectric constant as illustrated in Table 2.3.

Nevertheless, it is an excellent choice for US receivers and can be used for high frequency US transducers for applications including imaging the skin and the gastrointestinal tract in the frequency range 25 – 100 MHz. This is because it has high receive sensitivity, a broadband response and low  $Z_a$ , which facilitates matching to water and tissue, as well as providing a short wavelength, to give good spatial resolution [72]–[74].

Table 2.3 Properties of piezoelectric materials for US transducer.

Property	PZT5H ceramic	PZ54 ceramic	PIMNT single crystal	PVDF polymer
<b>Dielectric constant; <math>\epsilon_{33}^S</math></b>	1250	1460	965	6
<b>Piezoelectric constant; <math>d_{33}</math> (pC/N)</b>	593	285	1500	33
<b>Electromechanical coupling coefficient; <math>k_{33}</math></b>	0.75	0.70	0.90	N/A
<b>Thickness electromechanical coupling coefficient; <math>k_t</math></b>	0.50	0.48	0.59	0.3
<b>Longitudinal velocity; <math>v</math> (m/s)</b>	3900	N/A	4550	2200
<b>Acoustic impedance; <math>Z_a</math> (MRayl)</b>	34	34	36.5	3.9
<b>Curie Temperature; <math>T_C</math> (°C)</b>	210	225	200	N/A
<b>Flexibility</b>	Poor	Poor	Poor	Excellent
<b>Reference</b>	[69]	[75]	[69], [76]	[72]

### 2.7.5. Piezoelectric Composite

As described above, there are inherent limitations in the use of single-phase piezoelectric materials. Piezoelectric composites (piezocomposites) were developed to overcome the restrictions of the single-phase materials, particularly in high  $Z_a$ . A piezocomposite is a combination of two different materials, including an active phase, usually piezoelectric material and a passive phase, usually an epoxy resin. The purpose of the passive phase is to reduce  $Z_a$  of the single phase to be close to media e.g., water and tissue,  $\sim 1.5 \text{ MRayl}$ . It also introduces greater attenuation because of absorption by the epoxy inclusion [77].

The composite concept, with various connectivity patterns, e.g., 0-0, 0-1, 0-2, 0-3, 1-3, 2-2, was developed by Newnham [78] and has been widely used in a number of applications e.g., medical imaging transducers and energy harvesting. 1-3 and 2-2 connectivity patterns, as shown in Figure 2.12, are commonly used as an active element for US transducers [6], [79]–[82]. The 1-3 composites consist of ceramic rods or pillars embedded in a passive polymer phase, whereas 2-2 composites comprise of planks of active phase and polymer phase placed side-by-side. Owing to the continuous active phase in a 2-2 composite, it possesses high  $\epsilon_r$  of  $\sim 900\text{-}1000$  [81], which is greater than that of a typical 1-3 composite,  $\epsilon_r \sim 300$  [50]. However, the 2-2 configuration is physically weak since the strength is based on adhesion between each plank and polymer. Thus, detachment might occur if the plank and passive phase are not completely bonded [79]. For a 1-3 composite, the physical strength is increased because the polymer phase continuously surrounds each pillar along its length. In addition, it possesses a higher coupling factor over other connectivity patterns because the material oscillates and generates US waves through the thickness of the pillars, which is parallel to the poling direction [66], [83]. The better coupling factor results in improved sensitivity and broader bandwidth, which can be manipulated to produce transducers with better spatial resolution [29], [52]. In addition, the decreased acoustic mismatch between the active element and tissue is also evident in 1-3 composite because its acoustic impedance is reduced to approximately  $15 \text{ MRayl}$  due to the inclusion of the polymer [41].

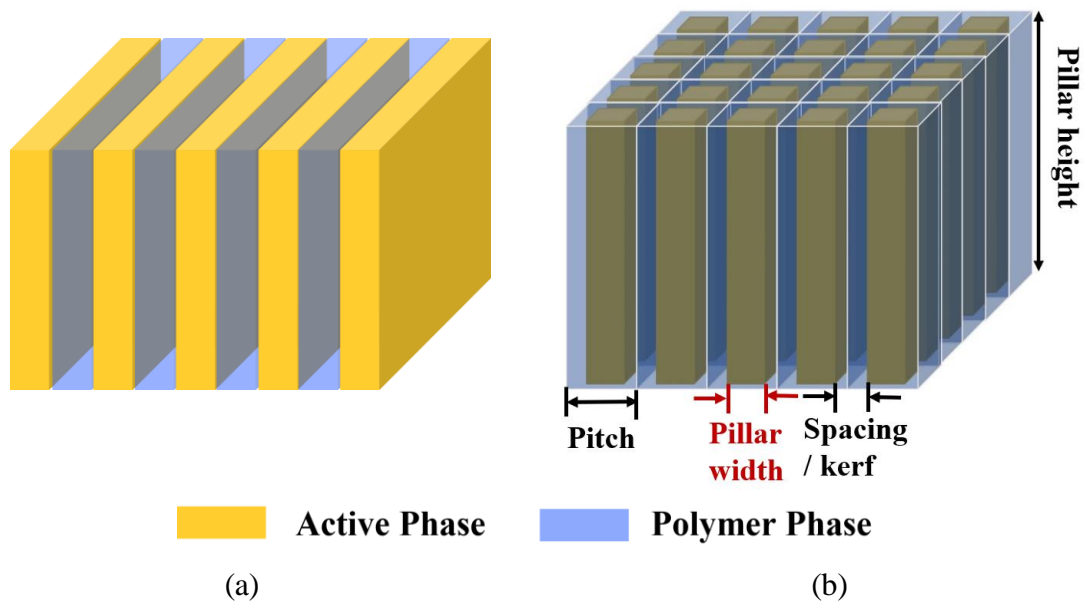


Figure 2.12 Schematic diagram of (a) 2-2 and (b) 1-3 composites.

### 2.7.6. Spurious Resonance Modes

Spurious or lateral modes are unwanted resonances, which arise from lateral reflections of US waves in the periodic structure of composites [41], [84]. These modes can interfere with the thickness resonance frequencies of the materials as shown in Figure 2.13. This results in a reduction of the transmission energy, leading to deterioration of transducer performance [85]. There are two types of such modes, of which  $f_{L1}$  is based on wave propagation parallel to the pillar width whilst  $f_{L2}$  is based on wave propagation in the diagonal direction of the pillar as demonstrated in Figure 2.14. Their frequencies are expressed in

Eq. 2.20 – 2.21, where  $v_{phase}$  is the phase velocity of Lamb waves, which is typically 95% of the shear velocity [86].

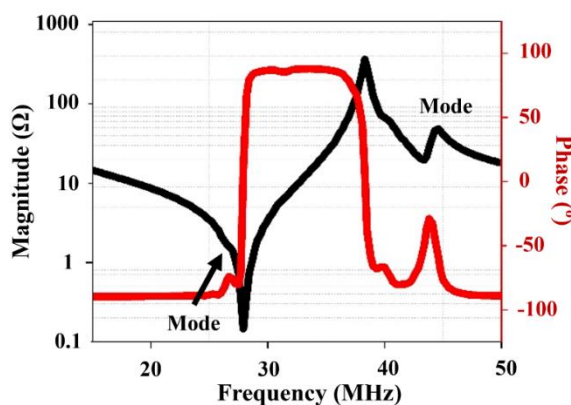


Figure 2.13 Simulated electrical impedance magnitude and phase of the 1-3 connectivity PZT ceramic piezocomposite with a periodic repetition of square pillars.

$$f_{L1} = \frac{v_{phase}}{x} \quad \text{Eq. 2.20}$$

$$f_{L2} = \frac{\sqrt{2}v_{phase}}{x} \quad \text{Eq. 2.21}$$

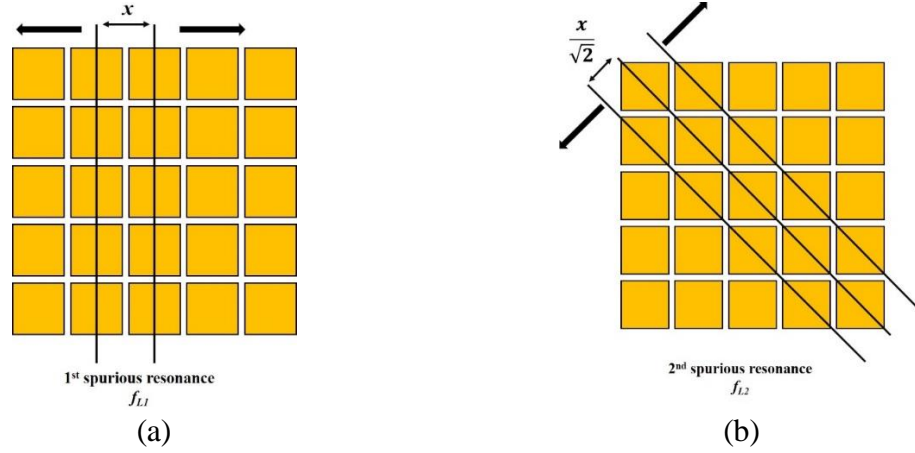


Figure 2.14 Schematic illustration of the spurious modes on the surface of 1-3 piezocomposite with a periodic repetition of square pillars in two dimensions.

### 2.7.7. Design Considerations for 1-3 piezocomposite $\mu$ US Transducers

#### Requirements

For  $\mu$ US transducers, challenges lie in fabrication of the ultrafine features of the 1-3 piezocomposite, in the order of a few micrometres, to limit the unwanted modes arising from the lateral periodicity of the pillars [41]. The requirements of the 1-3 composite structure suitable for  $\mu$ US transducer are summarised as follows:

- The operating frequency of US transducers,  $f$ , is defined by thickness of the active element. The pillar height is assumed equivalent to the thickness of the active element,  $h$ , which is typically set to  $\lambda/2$ , because the fundamental resonance frequency occurs when the thickness of the element is equal to a half-wavelength [87]. Hence, Eq. 2.2 can be rewritten to be Eq. 2.22 to describe the relationship between  $f$  and  $h$ . To achieve high frequencies,  $h$  should be small.

$$h = \frac{v}{2f} \quad \text{Eq. 2.22}$$

- As  $f$  defines the pillar height, the width of the pillar is subsequently determined by the aspect ratio,  $AR$ , of the pillar height-to-width as expressed in Eq. 2.23.  $AR$  should be higher than two to keep the ideal shape of the pulse response [82] and three to raise the magnitude of  $k_{eff}$  dominant over the spurious modes [88]. Thus, the geometry of the pillar should be tall and thin, giving high  $AR$ .

$$AR = \frac{\text{Pillar height}}{\text{Pillar width}} \quad \text{Eq. 2.23}$$

- The inter-pillar spacing or kerf, should be smaller than the thickness of the active element and pillar width, typically around half wavelength, to eliminate unwanted modes, e.g., spurious or lateral modes, by pushing them beyond the fundamental mechanical resonance frequency [41], [85].
- Volume fraction,  $VF$ , of piezoelectric materials up to 40% is required to maintain high electromechanical coupling coefficient and increased transducer's capability in transmission and reception [41], [82].  $VF$  is related to pillar width and kerf as described in Eq. 2.24.

$$VF = \frac{\text{Pillar width}^2}{(\text{Pillar width} + \text{kerf})^2} \quad \text{Eq. 2.24}$$

The mechanical and piezoelectric properties of 1-3 piezocomposites can be tailored by altering  $VF$  of the piezoelectric materials as displayed in Figure 2.15. The results presented in Table 2.4 have been calculated based on the equations given in [41] (Appendix I). The independent parameters of the materials used in this thesis, including a semi-hard  $\text{Pb}(\text{Zr}_{0.52}\text{Ti}_{0.48})\text{O}_3$ , PZT (PZ54, Meggitt AS, Kvistgaard, Denmark) and soft PZT5H (TRS610HD, TRS Technologies, Japan) piezoceramics, and PIN-PMN-P, e.g., PIMNT29 (X4, Technologies Inc, Pennsylvania, USA), are also listed in Appendix I.

With regards to the results of the 1-3 piezocomposite fabricated from the piezoelectric materials used in this present work as illustrated in Table 2.4 and Figure 2.15, it can be summarised that a compromise between the properties must be considered to meet the requirement for  $\mu\text{US}$  transducers with high operating frequency.

- $k_{eff}$  is increased at a certain  $VF$  of piezoelectrical material in the range of 20 – 80%. At small  $VF$ , the  $k_{eff}$  value is low because the ceramic or single crystal pillars are clamped by the large amount of polymer phase. The decrease of  $k_{eff}$  at high  $VF$  is attributed to the stiffening effect of adding more piezoelectric materials, hence, a planar mode is dominant over the thickness mode [41].
- $Z_a$  is reduced by 50%, providing better energy transmission by minimising acoustic mismatch between the load and the transducer.
- Permittivity is decreased because of the inclusion of epoxy. This may lead to poor electrical matching between the transducer and instrumentation circuitry.

- Ideally,  $VF$  should be as high as possible to maintain a high  $k_{eff}$  value. In practice, the  $VF$  is limited by manufacturing processes, particularly in  $\mu$ US transducers.

Table 2.4 The acoustic, piezoelectric and electromechanical properties of 1-3 piezocomposites used for virtual prototyping  $\mu$ US linear arrays.

1-3 piezocomposite made of	$\overline{C}_{33}^D$ ( $\times 10^{10}$ N/m <sup>2</sup> )	$\overline{\epsilon}_{33}^S$ (F/m <sup>2</sup> )	$k_{eff}$	$Z_a$ (MRayl)
PZT5H (40 VF%)	6.55	472	0.76	15.88
PZ54 (43 VF%)	5.34	609	0.66	14.60
PIMNT (43 VF%)	5.56	301	0.84	15.14

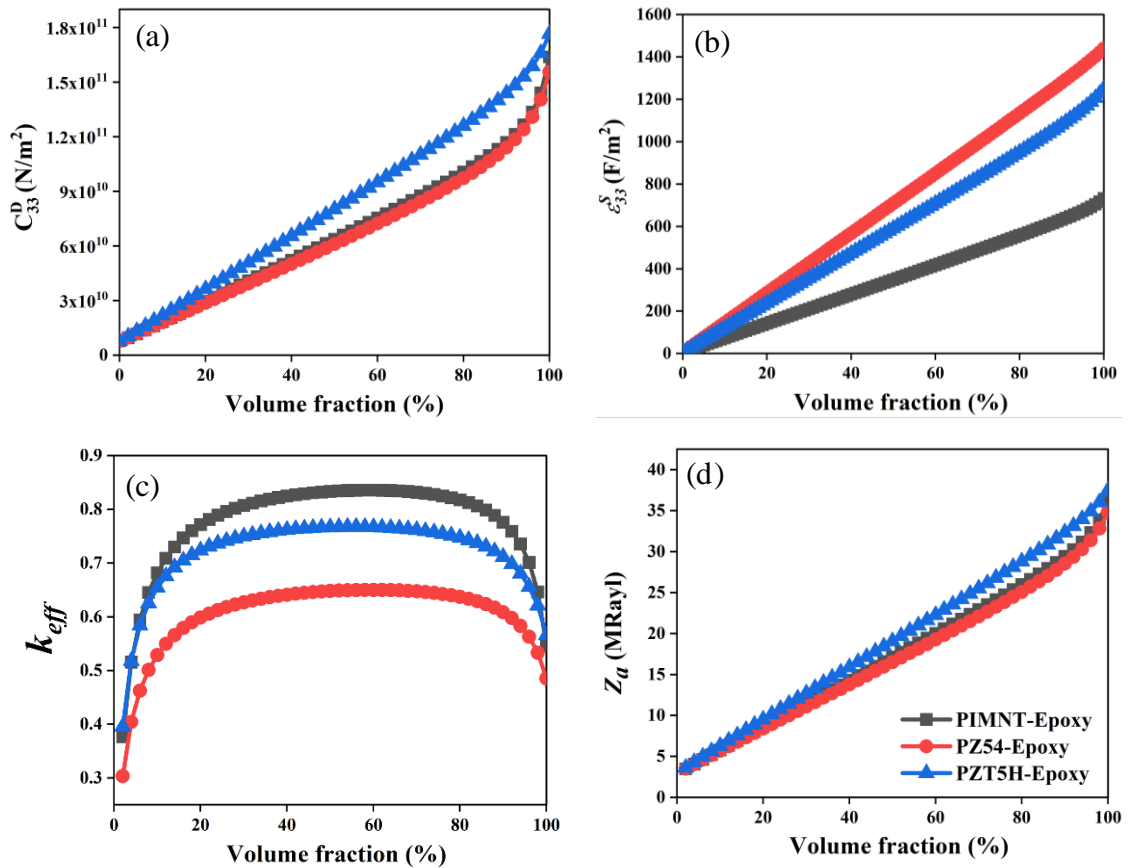


Figure 2.15 Influence of volume fraction of piezoelectric material on (a) elastic stiffness constant,  $C_{33}^D$ ; dielectric constant,  $\epsilon_{33}^S$ ; thickness-mode electromechanical coupling coefficient,  $k_{eff}$ , and acoustic impedance,  $Z_a$  and of 1-3 piezoelectric composites fabricated with an active element or piezoelectric material based on PIMNT, PZ54 or PZT5H and an epoxy filler based on Epofix (Struers Ltd. UK).

## Randomised Piezocomposite Design

As discussed above, the micro scale structure, comprising extremely small pillar and kerf dimensions, of 1-3 connectivity piezocomposites is required to minimise the spurious modes. Another approach to reduce the modes has been employed, by means of increasing the level of geometrical complexity in the piezocomposite structure [89]–[91]. This concept is used to push the modes beyond the operating frequencies because there is less US waves being reflected and coupled at the face of pillars. Unfortunately, the  $AR$  of these composites remains lower than two, resulting in low  $k_{eff}$ . In addition, these approaches come at cost of the difficulty in fabrication and a prolonged process, which are described in detail in Section 3.2.

In the last decade, a novel arbitrary piezocomposite design, as depicted in Figure 2.16, manipulating a distribution of pillar geometries, dimensions, and separations, namely a randomised pattern, was first developed and proposed by Démoré et al. [93]. The pattern provides a  $VF$  of the active piezoelectric materials of 40%. It was also studied and reported in the literature [50], [93]–[95]. Simulation of electrical impedance characteristics of the 1-3 piezocomposite with a randomised pattern by finite element analysis shows that the randomised pattern has capability in separating the modes from the resonance frequencies effectively as shown in Figure 2.17.

So far, the novel randomised pattern has been successfully employed to fabricate 1-3 randomised piezocomposites, with  $k_{eff}$  between 0.68 and 0.78, for high-frequency SETs, by using a gel-casting method associated with micromoulding [50], [94], [95]. Thus, the 1-3 composite with a randomised pattern merits further development to enhance the efficiency of  $\mu$ US array transducers. The use of this pattern is expected to reduce the spurious modes which typically appear and cause problems in array transducers. Generally, most cases of arrays face this issue because the modes arise from the wave propagation in the underlying substrate with the composite structure perpendicular to the direction of the wave propagation along the array elements [96]

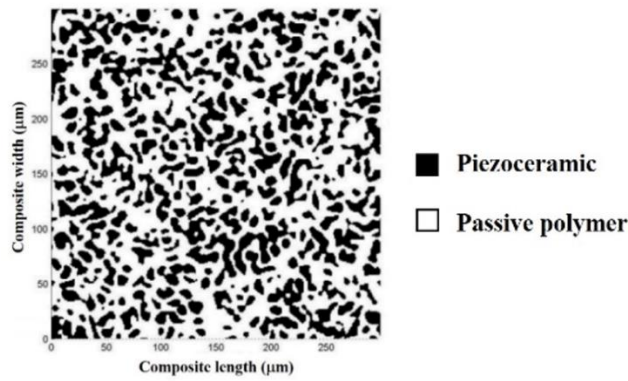


Figure 2.16 Randomised composite pattern (reprinted from *Ref.* [92]).

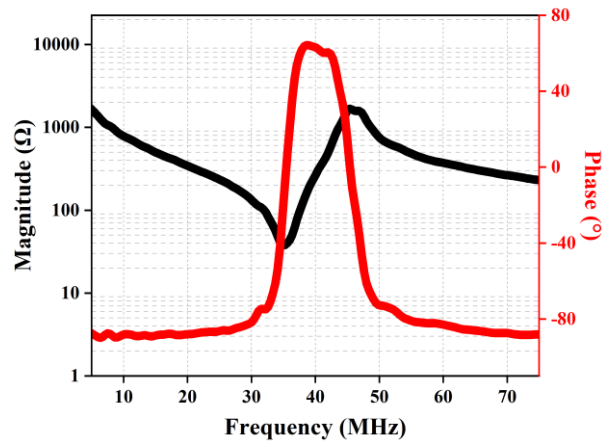


Figure 2.17 Simulated electrical impedance magnitude and phase of the 1-3 randomised composite with the pattern shown in Figure 2.16.

## 2.8. Summary

This chapter provided functional background of medical US imaging. The basic principles of US imaging and the interactions between the US waves and tissues were described. The basic components in US transducers for biomedical imaging and their function were discussed, with the aim to achieve high performance US transducers. Image resolution is dependent on the operating frequency of US transducers at the expense of shallow depth penetration and low sensitivity.

Key factors and material properties which influence the performance of the transducers were also addressed. The 2-2 and 1-3 connectivity composites are the most extensively used as an active element in transducers, to produce and receive the US waves. However, the physical strength of the former is poorer than the latter due to the possibility of detachment of adhesive layer between active phase planks, whereas the 1-3 connectivity pattern seems tougher since the pillars are embedded in the polymer phase. However, the pitfall of the 1-3 composite remains in the production of the unwanted modes, which reduces the transducer

performance. Thus, the novel randomised pattern was suggested to overcome the restriction of the classical 1-3 composite with repetitive and symmetrical structure. In addition, its capability in minimising the modes was shown. Thus, it is then proposed here as a promising means to minimise the unwanted modes in 1-3 composites for  $\mu$ US arrays.

# Chapter 3 Microultrasound Array Fabrication

## 3.1. Introduction

In the manufacturing of  $\mu$ US array transducers, various innovative technologies and methods have been developed and utilised, e.g., development of single element transducers and multi-element arrays with microscale dimensions that are able to meet the requirements of high-resolution biomedical imaging, where short pulse length,  $PL$ , high sensitivity, and broad bandwidth,  $BW$ , are needed to visualise detailed structures of soft tissues over wide frequency ranges.

As mentioned in Chapter 2, the active material of an US transducer is essential for the generation and reception of US waves for biomedical US imaging. Typically, it is made of piezocomposite material, of either the 1-3 connectivity considered in this thesis, or 2-2 connectivity. This is to gain increased electromechanical coupling coefficient,  $k_{eff}$ , compared to monolithic piezoelectric materials, which leads to enhanced sensitivity and bandwidth. The acoustic impedance is also lower, which is desirable for better acoustic matching to tissue.

Difficulties in manufacturing such materials for  $\mu$ US transducers include high processing cost due to the need for advanced technologies, e.g., composite fabrication and microfabrication defining fine array elements, and the need for delicate processes to achieve ultra-fine 1-3 composite structures. To date, there has been progressive development in manufacturing the composite structure for  $\mu$ US devices, which is described in detail in Section 3.2, as such US arrays are routinely used for preclinical research and specialised medical applications [97].

In  $\mu$ US arrays, another significant challenge lies in creating fine array elements. An element pitch of  $\sim 25 \mu\text{m}$  is needed when using the  $\mu$ US arrays operating with  $f > 30$  MHz, in order to minimise the side lobes which can degrade the transducer's capability in transmission and reception, resulting in poor quality of a biomedical image [1]. A literature review of the techniques employed to develop and manufacture these fine array elements, along with their advantages and disadvantages is provided in Section 3.3.

For *in-vivo* examination, e.g., endoscopy or intravascular imaging, fine electrical interconnects play an important role in the miniaturisation of  $\mu$ US devices and the manufacturing of reduced-scale US probes. However, reducing the dimensions of the

interconnections comes at the expense of electrical interference generated by the small gap between adjacent array elements. Additionally, the increased array complexity associated with  $\mu$ US inevitably leads to time consuming development process and higher prices of the given devices. Approaches developed to achieve reliable electrical interconnections for prototype  $\mu$ US arrays are described in Section 3.4 and conclusions regarding the means of fabrication for  $\mu$ US linear arrays relevant to this thesis are summarised in Section 3.5.

### 3.2. 1-3 Piezocomposite Manufacture for $\mu$ US Transducers

Generally, a 1-3 piezocomposite structure such as those considered here are based on a bristle block (set of piezoelectric pillars) diced from a bulk piezoelectric wafer. These pillars made of piezoelectric material are then encapsulated within a passive polymer as presented in Figure 3.1.

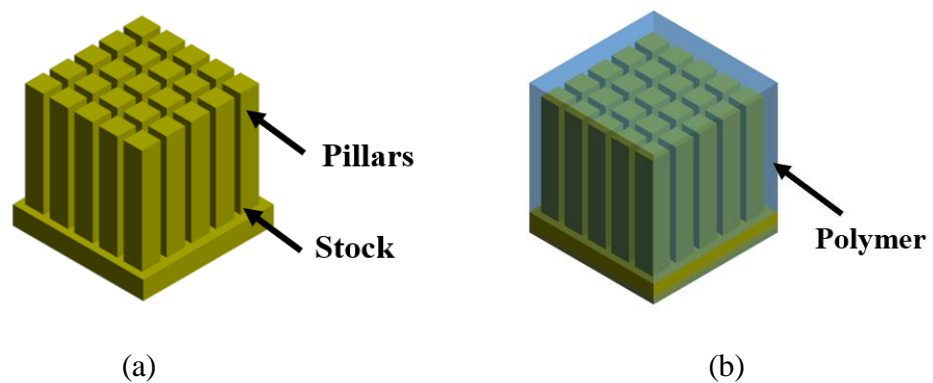


Figure 3.1 (a) Bristle block structure of 1-3 piezocomposite material surrounded by (b) passive polymer material.

A major concern in 1-3 piezocomposite fabrication for  $\mu$ US array transducers with high operating frequencies, in the range 20-50 MHz, lies in the generation of spurious lateral modes. These are influenced by pillar dimensions, pillar-to-pillar spacing and the array element pattern, as discussed in Section 2.7.6 [89]. The modes couple with fundamental thickness-mode resonance frequencies, leading to degradation of the transducer's transmission and reception performance. The spurious lateral modes can be suppressed by means of fine-spatial scale 1-3 piezocomposite structures [41], the use of a soft polymer [88], [98], and a random distribution of pillar geometry and spacing [89], [99], [100].

Firstly, Smith and Auld [41] described an approach to minimise the effect of the lateral modes by using the design of a 1-3 piezocomposite structure with fine-spatial scale, with  $AR > 3$  [6], [82], as previously described in Section 2.7.7. Secondly, with the use of a soft setting polymer as a passive polymer in the composite, spurious modes were reduced by the

influence of attenuation and phase cancellation due to poor surface dilation quality. Attenuation originates from shear loss mechanisms in the polymer, which are influenced by a reduced shear velocity by 65% compared to a hard setting polymer [98]. Poor surface dilation quality comes from the difference in Poisson's ratios of the ceramic and polymer components [101], resulting in phase cancellation. This is caused by the decoupling between ceramic and polymer leading to isolated pillar displacement: the ceramic and polymer vibrate in different phases, or even in antiphase, producing the phase cancellation. However, a benefit is that the pillars vibrate independently with low lateral clamping leading to their thickness mode efficiently dominating over the spurious modes [88].

Soft polymers are particularly undesirable in 1-3 piezocomposite manufacturing for  $\mu$ US transducers because of their several drawbacks. Their high pre-cure viscosities (980 -1800 mPa/s for CY208/HY956 and polyurethane) inhibit the flow of the polymer mixture into the microchannels, which may cause the formation of air-filled defects (bubbles) in the composite structure. Also, a prolonged curing process is necessary for full curing, which then provides economic issues [102], [103]. Especially, the soft polymer increases the difficulties in fabrication e.g., lapping to thickness and polishing [104]. For the reasons set out, hard set polymers, e.g., Epofix (Struers, UK) and CY1301/HY1300 (Robner, UK) epoxy resins, are more extensively used because of their low pre-cure viscosities (550 mPa/s for Epofix and 600 mPa/s for CY1301/HY1300), short curing process [105], [106] and ease of post-cure fabrication.

Finally, another method to avoid spurious modes is to use a randomly distributed pillar geometry and spacing, described in Section 2.7.7 [89], [99], [100]. These strategies decouple the modes from the thickness mode resonances, increasing the effectiveness of the transducer.

Another benefit of fine-scale 1-3 piezocomposite is to generate the effective electromechanical coupling coefficient with an increased  $k_{eff}$ , compared to that of the thickness mode,  $k_t$ , of plate piezoelectric materials [88], owing to the benefit of the high  $AR$  of the piezoelectric material. The incorporation of the polymer material enhances acoustic matching to biological tissue by reducing  $Z_a$  of the active material, e.g., from more than 30 MRayl for a bulk material to 15 MRayl for a composite. These merits are however dependent on the  $VF$  of the piezoelectric phase in the overall composite as described previously in Section 2.7.7, Figure 2.15 [41].

To date, a number of alternative techniques, including the dice-and-fill method [6], [89], [90], [107]–[109], interdigital pair bonding [8], [110], [111], laser machining [9], [112], [113], viscous polymer processing, and gel casting have been developed for fabricating either fine-spatial scale or a variety of pillar geometries in 1-3 composite structures that are suitable for  $\mu$ US. The processes and capabilities along with pros and cons are discussed below.

### 3.2.1. Dice and Fill

The dice-and-fill method is the industry standard for manufacturing piezocomposites because it is a precise and simple method and allows mass production [11], [12], [114]. Figure 3.2 shows the basic procedure of the dice-and-fill method. A piezoelectric wafer is diced using a mechanical dicing saw in two orthogonal directions to create a bristle-block of pillars on the remaining stock. Subsequently, the diced wafer is backfilled with a passive phase, which mostly consists of an epoxy resin. The stock and the excess polymer are then removed to expose the piezoelectric pillars and to attain the desired thickness by means of lapping. Finally, the surface of the 1-3 composite sample is electroded with a conductive metal layer.

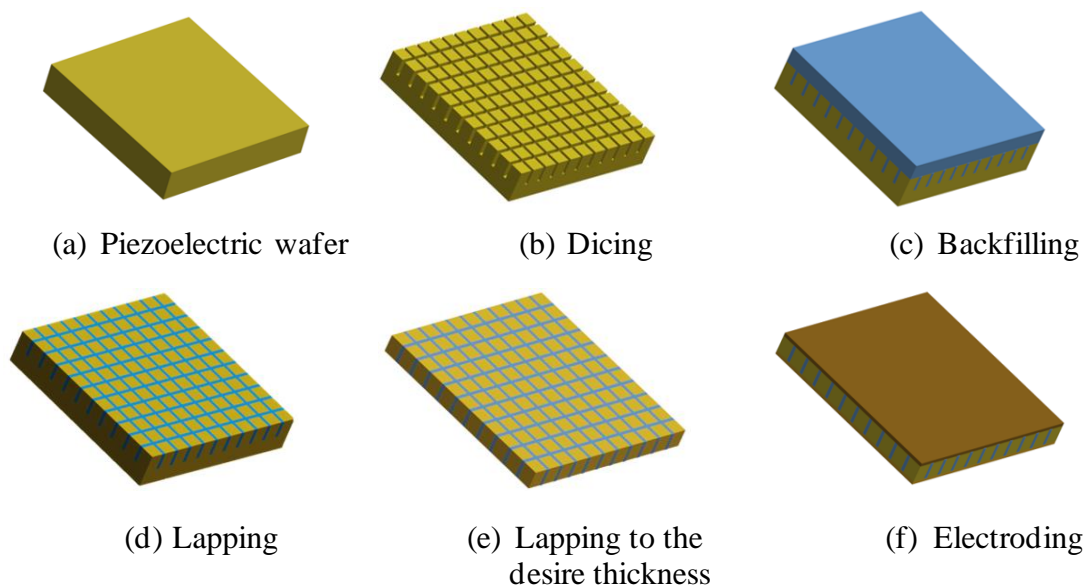


Figure 3.2 Schematic procedure for the dice-and-fill technique for manufacturing 1-3 composites for single element transducers.

The design of the piezocomposite structure based on this technique is however restricted by the availability of appropriate dicing blades, which can have nominal blade thicknesses as low as 10  $\mu$ m. To minimise the effect of spurious modes, this technique has been developed to fabricate sufficiently fine-scale 1-3 piezocomposites with various pillar geometries and pseudo-random pillar distribution. For instance, a 1-3 piezocomposite device with an

operating frequency of 30 MHz should ideally be designed with  $\sim 25$   $\mu\text{m}$  pillar width,  $\sim 10$   $\mu\text{m}$  spacing, and a pillar height of  $\sim 50$   $\mu\text{m}$ , providing  $AR$  of two to produce an adequate pulse [82].

Brown et al. [6] fabricated fine 1-3 composites with a  $VF$  of only 25%, which were used for a 40-MHz linear array. The piezocomposite with a pillar width of 20  $\mu\text{m}$  was made on a thin layer of ceramic stock,  $< 5$   $\mu\text{m}$ , on which the array elements were patterned by a photolithography process. Soft epoxy (Epofix 1232, Electron Microscopy Sciences, Hatfield, PA) was employed as the passive phase to reduce the spurious modes by damping pillar-to-pillar vibration across the composite. However, it was reported that the composites short circuited during high voltage poling because the epoxy has a relatively low dielectric breakdown which could not endure the voltage applied.

Subsequently, the same research group proposed the fabrication of a 1-3 piezocomposite with triangular pillars to reduce the effect of the lateral modes [89], [90]. The triangular pillar composite showed a relatively flat impedance magnitude response, broader resonant frequency characteristics, and increased bandwidth compared to that of a similar square pillar composite. It was claimed that the triangular pillar geometry of the pillars enabled suppression of the spurious modes by spreading their energies over the fundamental thickness mode and breaking the direction of lateral vibration across pillar-to-pillar periodicities because the parallel faces of adjacent pillars no longer existed [98].

In 2012, Yang et al. [107] employed the strategy of geometric complexities in pillars to reduce the interference in  $\mu\text{US}$  linear array transducers by investigating different pillar geometries, including square, triangular and pseudo-random pillars. The overall performance of the transducer fabricated from pseudo-random pillars exceeded that of the other transducers, including the fact that the lateral resonances appeared far from the fundamental thickness resonance frequencies. The transducer also had higher  $\epsilon_r$ ,  $\sim 493$  at 10 MHz and  $\sim 520$  at 15 MHz and  $k_{eff}$  of 0.62 at 10 MHz and  $k_{eff}$  of 0.61 at 15 MHz, compared to the other two transducers made with square and triangular pillar geometries. Additionally, the transducer made with pseudo-random pillars provided lower electrical cross coupling between elements -31.8 dB at 15 MHz, compared with 26.3 and 29.6 dB for the other two transducers, respectively. It was argued that the high level of geometric complexity in the pillars enabled a more efficient spread of the acoustic energy in all lateral directions within the composites and reduced the cross coupling between array elements.

Another approach to achieve the sufficiently fine scale of the 1-3 piezocomposite based on the dice-and-fill method is a double-pitch dicing method. This was developed for both low and high frequency transducers by using PZT-5H and (K,Na)NbO<sub>3</sub>-based piezoelectric ceramics as the active materials in the composites [108], [115]. This alternative method also has potential benefits for fabricating fragile fine-scale 1-3 single crystal piezocomposites for  $\mu$ US transducers. This is because single crystal piezoelectric materials are more brittle and fragile than piezoceramics due to their low fracture toughness and high internal stresses, leading to imperfections in the pillars as a result of chipping and cracking during the dicing process [70], [116], [117].

Although there has been success in fabricating fine scale 1-3 composites for  $\mu$ US transducers either by conventional or modified dicing methods, it cannot be denied that these methods have the significant drawback of being highly time-consuming. In addition, the pillar aspect ratios and material volume fractions are restricted by the thinnest dicing blades available.

### **3.2.2. Interdigital Pair Bonding**

Interdigital pair bonding, IPB, is a modification of the dice-and-fill method. It was originally developed in 1999 for fabrication of 2-2 piezocomposites for 26 MHz  $\mu$ US transducers, and was further adapted for the development of 1-3 composites in 2001 by Liu et al. [8], [110], [111]. Figure 3.3 presents the process diagram for manufacturing 1-3 composites with the IBP technique. Four plates of piezoelectric materials are firstly diced, followed by backfilling epoxy into the kerfs after carefully mating the diced plates, which produces the desired separation. Epoxy curing is then carried out under a dry nitrogen environment for 48 hr. After fully curing, the sample is lapped to expose the diced 2-2 composite as shown in Figure 3.3 (d). The two pieces of 2-2 composites are then diced perpendicular to the first cut series, followed by mating, epoxy filling and lapping as shown in Figure 3.3 (f-g) to form the 1-3 structure.

It is claimed that this process provided relatively high-volume fraction, 81.5-90%, of piezoelectric materials by reducing the kerf size in the range of 4-12  $\mu$ m, which results in high  $k_{eff}$  of 0.64-0.72. More importantly, the spurious modes were pushed away from the fundamental thickness modes. This was attributed to a benefit of the ultrafine kerf, which could potentially avoid the generation of the spurious modes, resulting in pure fundamental thickness mode resonances [8], [111]. For this reason, the IBP technique has been proposed as an alternative method for manufacturing high frequency transducers. However, it is time consuming, particularly due to manual mating of the plates and due to the long epoxy curing

time. In addition, there is a risk of non-uniformity of kerfs owing to manual mating. Consequently, it is considered unlikely to be implemented in industrial manufacturing processes for mass production.

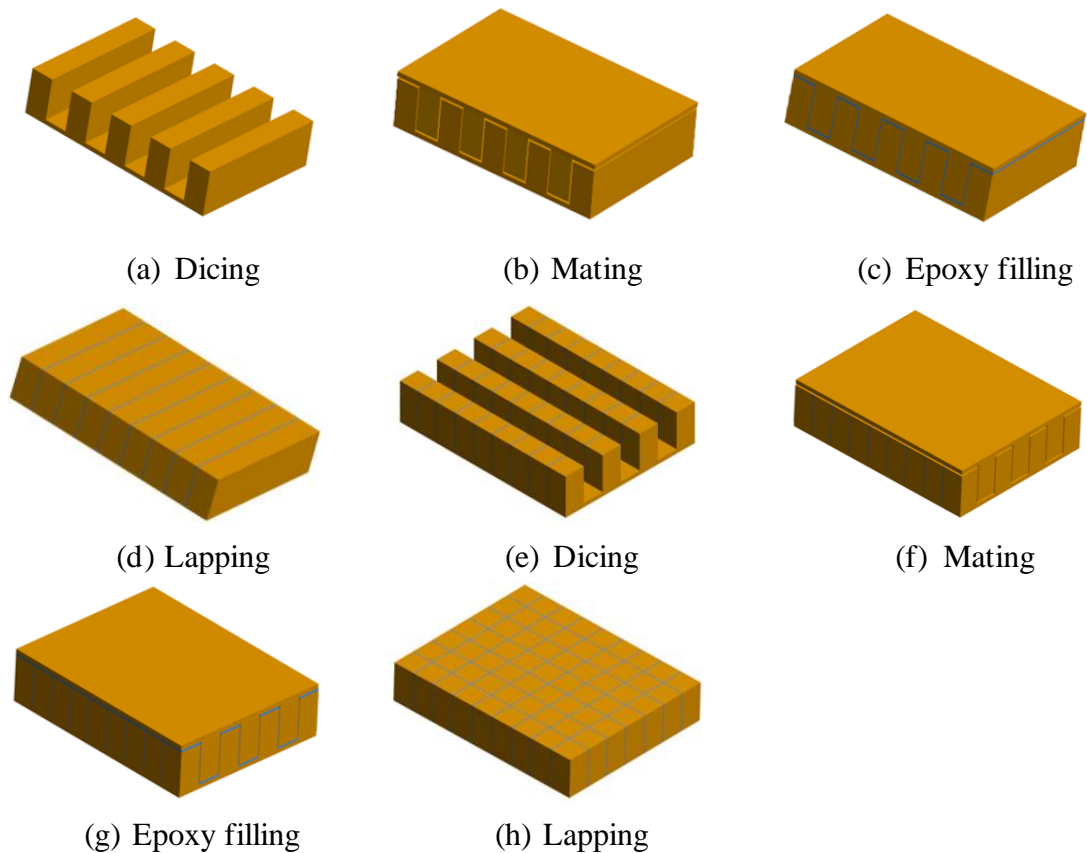


Figure 3.3 Schematic procedures for 1-3 composite fabrication by interdigital pair bonding (adapted from *Ref.* [8]).

### 3.2.3. Micromachining

Micromachining refers to techniques for fabricating three-dimensional microstructures. It is well known as the basis of micro-electro-mechanical-systems, MEMS, technology [118]. Regarding the trend towards miniaturisation, micromachining is currently gaining importance in the fabrication of micro-electronic parts in various fields, particularly in medical equipment. Since 2001, micromachining techniques, e.g., photolithographic etching and laser machining, have been employed as promising methods for the fabrication of 1-3 piezocomposites from single crystal materials for high performance single element and array  $\mu$ US transducers. Interestingly, an outstanding benefit of this alternative method is the possibility of extremely fine kerfs in the range 5 - 10  $\mu\text{m}$ , for  $\mu$ Us arrays [112], [119], with less pillar chipping and microcracking, which is difficult to achieve with the dice-and-fill method for single crystal materials because of their typical weaknesses, as described in

Section 3.2.1. The sufficiently fine separation of pillars potentially decouples the lateral modes from the fundamental thickness mode as presented in literatures [9], [119].

Photolithography technology associated with the deep reactive ion etching, DRIE, technique is an example of a micromachining processes that can be applied for piezoelectric transducer manufacturing. It involves chemical etching accompanied by ionic bombardment. Molecules of an inert gas, usually argon, are broken into ions by using a radio frequency power source. The ions are then accelerated towards a substrate where they eject the molecules of the substrate surface, thereby etching the material [120].

A generic process of this method is illustrated in a literature [119]. It relies on a piezoelectric plate coated with chrome-gold as an electroplating seed layer before the photolithography process. A positive photoresist is then deposited on the surface as a sacrificial mask by the photolithography process, including resist coating, baking, UV exposure, and lift-off, which will be described further in Section 3.3.2. A metal layer used as a hard mask is then electroplated and created as a negative of the sacrificial mask, followed by the removal of the photoresist, while the hard mask remains on the substrate. Then the sample is subjected to DRIE to create the bristle block structure. Subsequent steps employed in the composite fabrication include epoxy filling, lapping and electroding.

The fine structure of the composites can be formed by designing a fine dimension of the mask openings. This technique was used to manufacture 1-3 piezocomposites with 15  $\mu\text{m}$  pitch, a kerf width less than 6  $\mu\text{m}$ , and  $VF$  of the piezoceramics up to 50%. The active material employed in the manufacturing process was single crystal and the fabricated devices could reach operating frequencies up to 40 MHz. These included; 40 MHz piezocrystal micromachined ultrasonic transducers, PC-MUTs, with 30% sensitivity and 100% bandwidth [119], [121] and a 50 MHz annular array transducer with 90% bandwidth and an axial resolution of 20 ns [122].

A disadvantage of this method is that a slow etching rate is needed in order to achieve vertical sidewalls and reduce damage to the bristle blocks, for instance; etching rates of 6.25 and 10.25  $\mu\text{m/h}$  required for PZT piezoceramic and PMN-PT piezocrystal piezoelectric materials, respectively [123].

Laser micromachining has also been employed to fabricate fine-scale composites by optimizing parameters of the incident laser energy and cutting rate to create extremely fine kerfs ranging from 5–10  $\mu\text{m}$  and element pitch between 30 and 70  $\mu\text{m}$  for  $\mu\text{US}$  linear and annular transducers with operating frequencies over 30 MHz [9], [112], [113]. This technology is highly capable of dicing the fine-scale bristle-block structure for the composite material with less microcracking as the kerf ablation is a noncontact process. In addition to the aforementioned advantage, no significant depoling of the piezoelectric material occurred due to control of the laser beam energy [9], [124]. Consequently, this method has been identified as an alternative to the etching processes. More importantly, it is environmentally friendly manufacturing technique, though laser micromachining systems are expensive.

Both the processes are promising for the fabrication of fine-scale piezocomposites with piezocrystal materials; however, some limitations must also be considered. DRIE produces pollution due to the use of toxic and corrosive gaseous etchants [125], [126]. More importantly, the need for specialized equipment results in high production cost. In relation to laser micromachining, this is a time-consuming process due to the need for low power to avoid degrading the piezoelectric materials and again, the equipment is expensive.

### **3.2.4. Viscous Polymer Processing**

Viscous polymer processing, VPP, originated from the lost mould technique [127], [128]. The latter was further developed to relax limitations from previous practices in term of cost efficiency and to achieve a high spatial scale of 1-3 composites for high frequency transducers.

A lost Si mould method was initially developed for a microrod array with a feature size of 50  $\mu\text{m}$ . In this method, holes of the mould with 3- $\mu\text{m}$  diameter and *AR* over 15 was successfully made by DRIE. However, the piezoelectric ceramic was chemically contaminated by the production of lead and pyrochlore phases due to the interaction between the ceramic and the Si mould during heating. In addition, structural bending was found caused by the difference between the thermal expansion coefficients of the Si mould and the PZT material [129]. Subsequently, a lost polymer mould method was developed to resolve the previous contamination. Drawbacks however persisted, e.g., the mould removal step by a plasma etching process was a time-consuming process due to a slow etching rate, e.g., 0.25  $\mu\text{m}/\text{min}$  in order to achieve vertical sidewalls of pillars and shape uniformity [130], [131]. Thus, the VPP was then further developed to achieve macro-defect-free structure

ceramics in a cost-effective process by using polymer moulds with mould removal by chemical dissolution.

A generic procedure of VPP is presented in a literature [128]. It involves fine ceramic powders (particle size  $\sim 1 \mu\text{m}$ ) mixed with selected plasticizers, additives, and solvent. After mixing via high shear twin-roll milling, a VPP ceramic paste with high viscosity ( $\sim 10^5 \text{ Pa}\cdot\text{s}$  at a shear rate of  $5\text{-}10 \text{ s}^{-1}$ ) is obtained [132]. The paste is then calendered to form a tape with a typical thickness of the order of 1 mm [82]. The tape is pressed into a polymer mould and subsequently dried to form a hard, green ceramic, comprising fine scale pillars on a stock [13], [132]. After chemical dissolution of the mould, the green sample then has the additives burned out and is sintered, followed by epoxy infiltration, and curing to obtain the 1-3 composite.

The new VPP technique demonstrated its advantages over the previous systems. Firstly, it is a near net-shape technique which enabled it to prepare the fine scale ceramic segment and spacing down to  $4 \mu\text{m}$  as well as to achieve a high  $AR \sim 10$  [93], [132]. Secondly, it provides relatively high green strength, e.g., bend strength of 130 MPa [132], to maintain shape integrity after mould removal. The high green strength was attributed to homogenous paste and a macro-defect-free structural body due to the use of a high molecular weight polymer Polyvinyl butyral binder, PVB, and a high shear stress during mixing [133], [134]. The use of PVB facilitates the ceramic powder mixing with the other components because the hydroxyl groups of the PVB are adsorbed onto the powders through hydrogen bonding. This results in the production of a homogeneous VPP paste [134]. The action of high shear twin-roll milling also promotes paste homogeneity because agglomerates in the powder are largely broken down by the high shear stress, resulting in reduced macro-sized defects in the final ceramic [127], [128], [134]. Finally, it was also claimed that the shape integrity of the green bodies still retained after chemical mould dissolution because the dissolving solution did not affect the binder system in the green pillars [13], [128].

Although VPP was claimed as a cost-effective method and a viable technique for producing 1-3 piezocomposites with fine structures for US transducer applications, the spurious modes remained and were shown near the thickness resonances when fabricating transducers operating at high frequencies ( $>30 \text{ MHz}$ ). This was attributed to the regularity in pillar orientation [93], [135], [136] and coupling between spurious modes and the fundamental thickness mode when the thickness of the active material was close to that of the pillar width and spacing [41], as described in Section 2.7.7.

### 3.2.5. Gel Casting

Gel casting, also known as a near net shape forming technique, was initially developed in the 1980s by Omatete's team at Oak Ridge National Laboratory in the USA to tackle challenges in complex shape forming for advanced ceramic processing [137]. The generic process of gel casting involves dispersing ceramic powders in a solution containing a monomer, crosslinker, initiator and, catalyst to form a relatively low viscosity slurry. Following this, the slurry is cast into a desired mould, and left to gel as the monomer solution is polymerised in-situ and crosslinked to form a strong 3D polymer network structure in which the dispersed ceramic particles are held by the network within the mould. After drying, and demoulding the green sample is sintered to remove the binders.

The greatest influential factor of this technique relies on high solid loading of the ceramic powder and low viscosity of slurry. The solid loading should be typically at least 50% volume fraction, to minimise drying and sintering shrinkages in order to avoid any imperfections, e.g., warpage and cracking induced by internal stress, as well as to obtain homogeneity of microstructure [137]–[139]. The viscosity should be less than 1 Pa.s at a shear rate of  $100 \text{ s}^{-1}$ , close to normal environment values during casting for having good fluidity of the slurry [50], [140], [141]

In the early stage of process development, the mechanism of gelation relied on the free radical polymerisation of two organic monomers. A major problem in this type of mechanism is surface exfoliation of the compacted green compact sample, which can lead to e.g., cracking induced by internal stress which is generated from rapid solvent evaporation (drying shrinkage). This phenomenon is usually found on the surface of the green sample because the free radicals in the monomers are sensitive to reaction with oxygen if the process is carried out in air. Thus, the gelation process must be take place in an enclosed chamber, either maintaining high humidity,  $> 90\%$ , or flowing with  $\text{N}_2$  inert gas to minimise the internal stress and decrease the drying time [142], [143]. However, this comes at the expense of high production cost and process complexity. Furthermore, most monomers contain acrylamide, which is a neurotoxin, leading to reluctance to use in many industries [139], [142]. Thus, they were replaced by low toxicity monomers, e.g., methacrylamide, MAM, and N-vinylpyrrolidone, NVP [144].

The gel casting process was further developed by including self-hardening polymers, thermosetting or water soluble epoxies and hardener, in the gelling system in order to allow the process to proceed in an air atmosphere [141], [145]. The polymerisation of the self-hardening process relies on a ring-opening or nucleophilic addition reaction, which is not

inhibited by oxygen in the air [95], [145]. This reaction proceeds through the epoxide group of the epoxy resin reacting with the active hydrogen of an amine hardener. The mechanism of nucleophilic polymerisation is divided into three main stages, which are well described in a literature [50]. As part of the first and second steps, hydrogens of the first and second amine groups react with the epoxide group sequentially to form a secondary amine and a tertiary amine, respectively. In the last step, the formed hydroxyl compound and the residual amine react with the epoxide group; thereby, branching of these reactions proceeds further, resulting in the formation of the 3D network.

This alternative approach produces samples with a relatively high green strength and density by using a variety of epoxy monomers as gelling agents, improves water solubility and lowers the viscosity for a good flowability of the suspension [140], [141], [145]. Among the monomers, ethylene glycol diglycidyl ether, EGDGE, has the lowest viscosity, 20 mPa.s and high-water solubility. However, some problems with this monomer exist in terms of its relatively low green strength, 17 MPa, and the irritation risk it poses to skin and eyes [140], [141]. It can be also noticed that the time consuming nature of the self-hardening gel casting process is a drawback, particularly the drying step, as it is carried out at room temperature,  $T_R$ , to allow the solvent to evaporate slowly with less cracking and warpage of the sample [50], [95], [139].

Nevertheless, the gel casting method has a number of useful characteristics compared with other forming techniques, e.g., injection moulding and, slip and pressure casting as well as VPP. Its benefits are summarised below:

- Relatively low shear viscosity, of which 45 - 48 vol% solid loading in slurries provides  $< 1$  Pa.s [50], [95], compared to VPP paste,  $\sim 10^5$  Pa.s [132], consequently easing the manufacturing process of complex-shaped parts in many industries, e.g., turbine engines and the automotive industry [137]. As a result of the good flowability of the suspension, it can be fully filled into fine scale and complex mould cavities, which is beneficial for manufacturing 1-3 piezocomposite with a variety of shapes.
- High-quality ceramics, e.g., with homogeneous microstructure and high flexural strength, are produced because the gel casting is based on colloidal processing that can control particle interaction and increase the homogeneity of particle packing in the wet stage [141].
- Minimal imperfections are evident in the ceramic microstructure because the gel casting method is flexible in the choice of monomer systems to allow alteration of

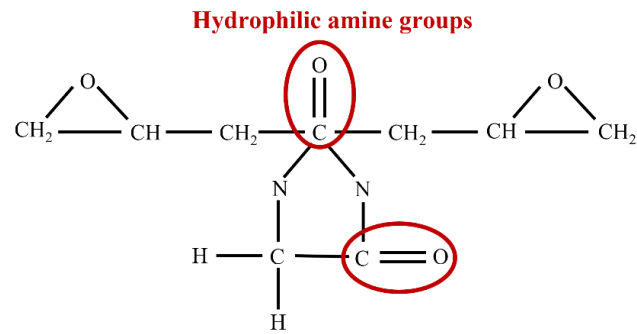
solid loading with respect to the viscosity of the solution, which leads to uniform shrinkage and less defects [127].

- Production costs for advanced ceramics are reduced as the master mould can be reused.

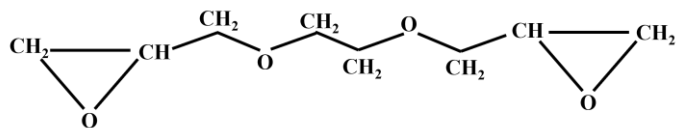
For these reasons, the gel casting method is considered an attractive and feasible technique to fabricate the fine-scale structure of 1-3 composites for  $\mu$ US transducers for biomedical imaging devices used in this present work.

In 2013, Jiang [95] reported the feasibility of merging gel casting with micromoulding to create 1-3 composites with random pillar geometry and spacing as mentioned in Section 2.7.7, called a randomised composite, for 30 MHz single element transducers. It was found that a suspension with 45 vol% solid loading of PZT powder and 40 wt% EGDGE, resin content provided a slurry of low viscosity,  $<2$  Pa.s, and produced green ceramics with relatively high green strength, 35 MPa. This allowed the slurry to fill the mould cavities and provided strength to the sample, enabling it to withstand the later process steps more easily.

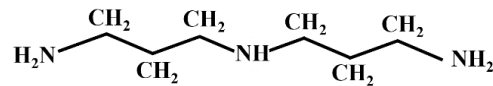
In term of disadvantages, however, EGDGE causes irritation to the skin and eyes. Therefore, Hydantoin epoxy resin has replaced this component due to its nontoxicity. In addition, it has higher water solubility owing to the strong hydrophilic amine groups, as shown in Figure 3.4 (a) [141]. Whereas the chemical structure of EGDGE resin composes of hydrocarbon (CH) groups, which are categorised as hydrophobic polymers. This epoxy resin was first studied as an EGDGE substitute in an alumina powder system, where the results showed a significant higher strength of the green body compared to that of the EGDGE resin [141]. Hydantoin epoxy resin was then used to produce a low viscosity slurry,  $<1$  Pa.s, and green ceramic sample with a relatively high green strength,  $\sim 48$  MPa from a slurry comprising of PZT powder with 48 vol% solid loading, 30 wt% Hydantoin resin content, and Bis(3-aminopropyl) amine as a curing agent [50]. Figure 3.4 (c) shows the chemical structure of the curing agent. The low viscosity potentially aided the slurry to be fully filled into the complex mould cavities with the arbitrary feature dimensions of 2-50  $\mu$ m. Additionally, *AR* of 33 (Figure 3.5) was obtained after demoulding, which is beneficial for relaxing limitations in the subsequent steps.



(a) Hydantoin resin



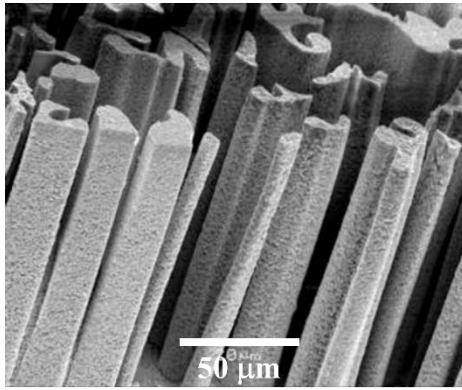
(b) Ethylene glycol diglycidyl ether, EGDGE



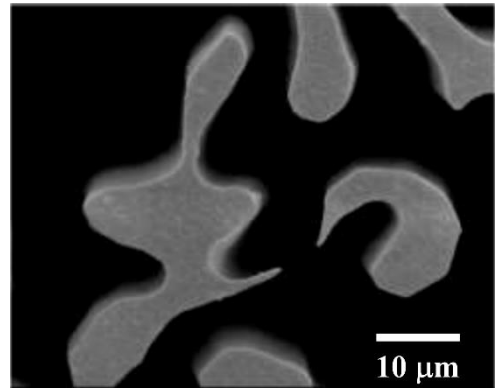
(c) Bis (3-aminopropyl) amine

Figure 3.4 Chemical structure of (a) hydantoin resin,  $C_{11}H_{16}N_2O_4$ , (b) ethylene glycol diglycidyl ether,  $C_8H_{14}O_4$ , and (c) Bis (3-aminopropyl) amine,  $C_8H_{14}O_4$ .

The generic process of manufacturing 1-3 randomised piezocomposites based on the gel casting method can be divided into two parts. The first part is the fabrication of a soft polydimethylsiloxane, PDMS, mould replicated from a silicon master mould with the randomised pattern as depicted in Figure 3.6 (a-d). The master mould was also fabricated by DRIE which is given in detail in [95]. The second part is to fabricate the bristle block pillars, followed by epoxy backfilling for fabrication of the 1-3 composite, as demonstrated in Figure 3.6 (e-l). Interestingly, the SETs made with 1-3 randomised piezocomposites evaluated in two case studies [50], [95] demonstrated the capability of the randomised design to eliminate spurious modes from the thickness resonance modes by providing clean electrical impedance magnitude and phase plots as illustrated in Figure 3.7 for both Pb-based and Pb-free piezoelectric ceramic materials. This represents an improvement compared to composites made with the dice-and-fill method [6], [89], [90].



(a)



(b)

Figure 3.5 SEM images of (a) 60° tilted view of green ceramic pillars with arbitrary geometries and (b) top view of ceramic pillars (reprinted from *Ref.* [50]).

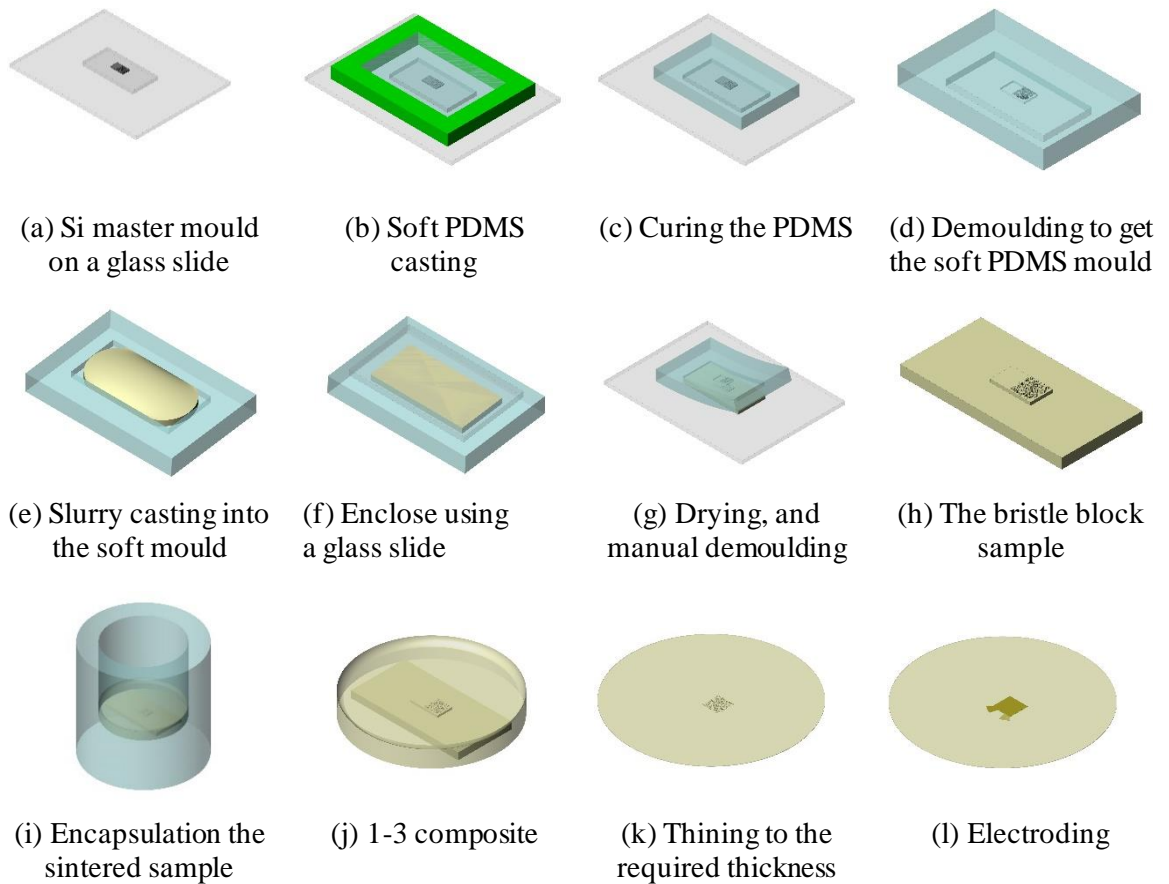


Figure 3.6 Illustration of the fabrication process of (a-d) soft mould and (e-l) a 1-3 randomised piezocomposite for a SET, using a gel casting method associated with micromoulding (adapted from *Ref.* [50]).

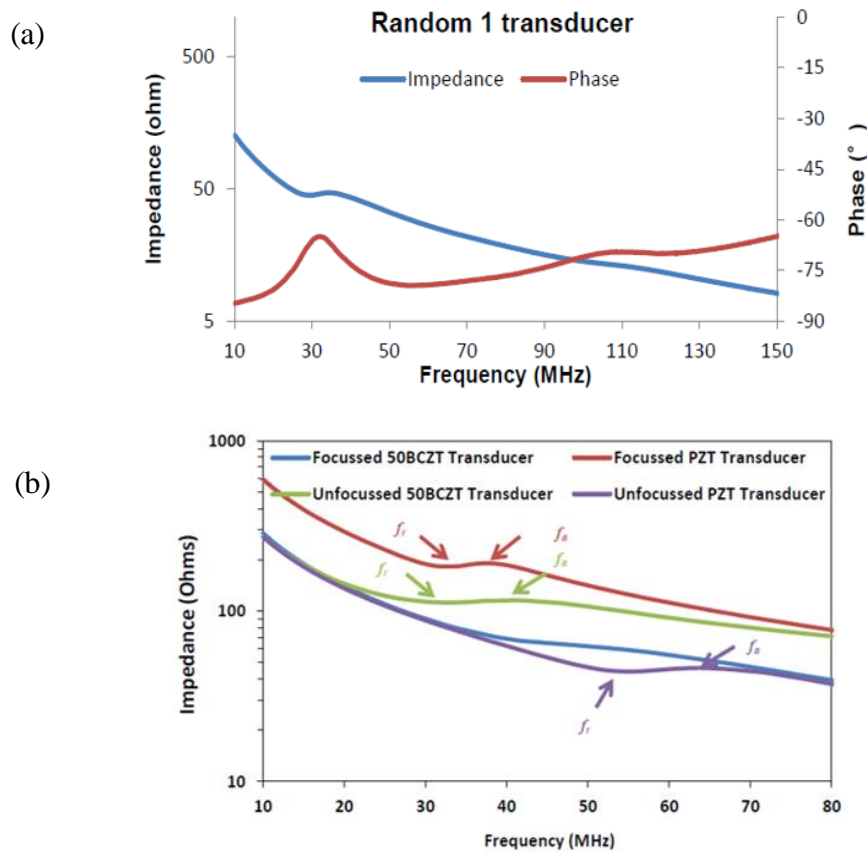


Figure 3.7 (a) Electrical impedance magnitude and phase (Reprinted from *Ref. [95]*) (b) Electrical impedance magnitude (Reprinted from *Ref. [50]*) measured from 1-3 connectivity randomised piezoelectric composite transducers.

### 3.3. Array Element Fabrication

Elements for array transducer applications have been previously applied either directly on the composite surface or on a thin stock layer. Techniques such as scratch dicing [12], [147], [148], mechanical laser dicing [80], laser micromachining [9], and photolithography [6], [112], [149], [150] were assessed as part of the work described here. The advantages and disadvantages of each method, as well as their feasibility for  $\mu$ US array development were considered.

#### 3.3.1. Mechanical and Laser Machining

Dicing and mechanical scratch dicing methods are the simplest and most cost effective method and they have been widely employed to establish elements for array transducers with operating frequencies less than 15 MHz [12], [80], [147], [148]. A desired thickness of gold is deposited onto the composite substrates. The separate array elements are created by mechanical dicing on the surface of the element using a dicing saw. A series of gaps were made across the surface of the element to define independent array elements. However, the edges of the elements across the composite surface are rougher and the kerfs narrower than

the ones established on an epoxy layer as presented in a literature [12]. It was argued that this potentially results from the cut being performed through two different types of materials (element and epoxy).

It is clear that this machining technique would be challenging when considering the small feature dimensions required for high frequency arrays; for instance, a 30 MHz linear array has 50  $\mu\text{m}$  element pitch for wavelength spacing. The finest dimension attainable for scratch dicing the array elements is restricted by the minimum size of commercially available dicing blades, which are currently a nominal 10  $\mu\text{m}$  (Disco Ltd, Tokyo, Japan), producing 13- $\mu\text{m}$  kerf.

Laser micromachining has been used for separating the array elements of a kerfless array, and thus overcome the restriction of the saw blade width in the mechanical dicing method [9]. As mentioned in Section 3.2.3, this technique is beneficial for the extremely fine kerf of the 1-3 composite structure, ranging from 5 to 10  $\mu\text{m}$ , by controlling the incident laser parameters. Additionally, it is a noncontact process, and thus, produces a smoother element edge, with less damage likely to be obtained on the composite surface. Lukacs et al. [9] took these advantages to manufacture 30 MHz  $\mu\text{US}$  linear arrays with a pitch of 74  $\mu\text{m}$  and kerf width of 8  $\mu\text{m}$  between elements. However, for piezocomposite materials, control parameters such as power intensity need to be carefully considered because the epoxy phase may be damaged by heat generated from the laser.

### **3.3.2. Photolithography**

Photolithography is well known as a microfabrication process, and is universally used to create conductor and insulator films for complex circuitry of integrated electronic circuit, IC, devices in the semiconductor and electronics industries [151]–[153]. It involves an optical lithographic method of transferring a pattern from a photomask onto a photoresist layer, known as light-sensitive material, coated onto a substrate. This can be achieved via aligning the mask onto the coated substrate, followed by the substrate being exposed to UV radiation to change resist solubility. In development step, the exposed resist is dissolved in a developer, resulting in a 3D profile of resist being developed on the substrate. A selected material, typically gold for conductor films, is then deposited along the exposed region, followed by a lift-off process to remove the photoresist in an inorganic solvent.

Photolithography considered here is based on a bilayer lift-off process, BLO, comprising of two photoresists to form a bilayer profile on a substrate. The top photoresist initially dissolves in a solvent. The underlying resist is subsequently developed to produce bilayer

re-entrance with an undercut, as illustrated in Figure 3.8. A major benefit of the bilayer resist profile with the undercut is to facilitate the lift-off process. This is because it creates discontinuity between the resist and the deposited metal layer, allowing solvent to penetrate through these re-entrances. This facilitates dissolution of the resists. Besides, it offers relatively neater and smoother edges of the metal film, as well as less chance of film detachment, because of more contact area between the film and substrate, than the single layer lift-off process [154]. In addition, the lift-off process is compatible with various substrates, especially for composite and polymer substrates. This is because the substrates comprising polymer are sensitive to etchants or solvents if they are subjected to prolonged etching processes.

The basic BLO process used in IC fabrication is illustrated in Figure 3.8 and sequentially described in detail as follows:

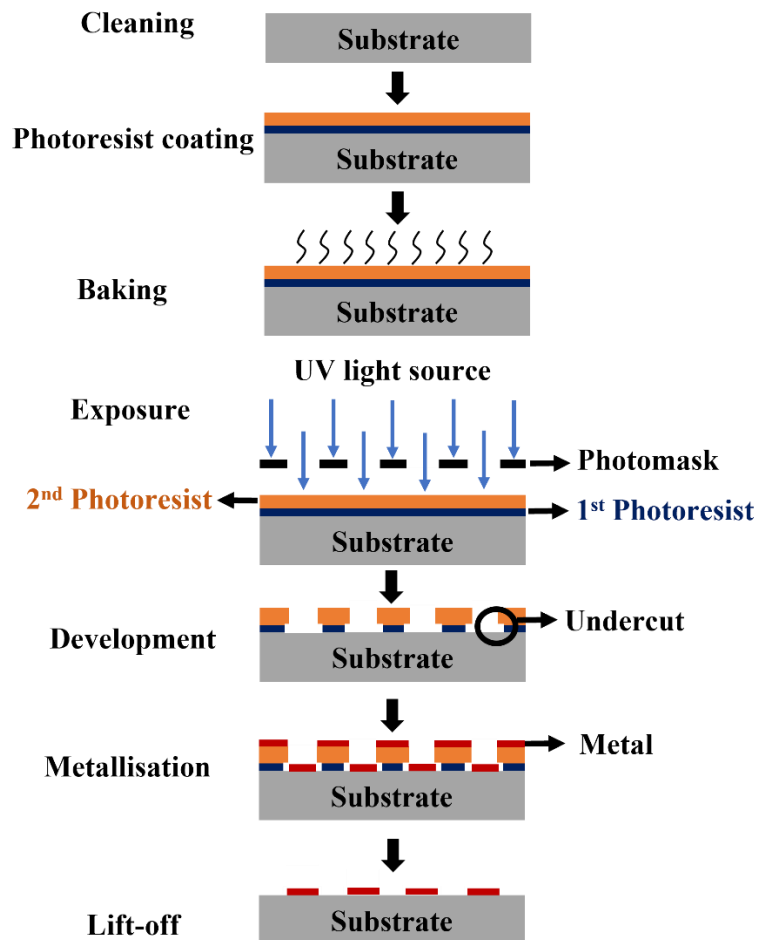


Figure 3.8 Schematic illustration of basic photolithographic process.

### Substrate Preparation

Prior to use, a substrate must be sufficiently flat, clean and dry in order to provide good adhesion for the photoresist. Typically, substrate preparation is accomplished by substrate

cleaning and dehydration. As part of the cleaning process, the substrate is chemically cleaned with solvents to remove contamination, e.g., organic, or inorganic impurities, which can be in the form of particles or films. Dehydration is employed to remove water or moisture by baking either in an oven or on a hotplate at temperatures of 200 – 400 °C for up to 60 min. The impurities must be eliminated because they cause defects in the final resist pattern and delamination of the resist can appear because of poor adhesion and linewidth control [153].

### **Photoresist Coating**

A thin and uniform photoresist layer is typically applied on a substrate by spin coating. The film thickness and uniformity can be well-controlled by choosing appropriate spin conditions with respect to the viscosity of the resist [153]. Typically, it is suggested that the resist film should be thicker than a metal film by 25-33 % for clean lift-off processing [16]. Photoresist in liquid form comprises solid components, e.g., polymer, sensitizers and additives, dissolved in a solvent. The solvent plays an important role in the coating step to aid the photoresist spreading evenly by centrifugal force during the first second of the spin cycle. Then it fully evaporates during the remainder of the spin cycle, thus producing a uniform film.

### **Bake of Photoresist**

The photoresist is usually baked on a hotplate because it is convenient for a short baking time [153]. The main purpose of the soft bake is to improve the resist adhesion to the substrate by removing residual solvents from the resist, as well as, to avoid resist contamination while transferring to the exposure step. In addition, it prevents resist dissolution when multiple resist coatings are required because the primary resist dries before the secondary resist is applied [153], [155]. Baking conditions such as time and temperature control development time, undercut rate, and overhang width.

Under-baking the resist leads to poor adhesion since the solvent does not evaporate properly from the mixture, causing resist delamination during the development process. Conversely, a prolonged baking time leads to a decrease in the resist photosensitivity because photosensitizers may decompose, and polymerisation of the photoresist is induced by the overheat, resulting in increased difficulty for dissolution of the exposed resist [153]. Furthermore, the undercut rate is mostly dependent on the baking temperature, although other conditions e.g., exposure and development times are also influential. Thus, the higher the baking temperature, the lower the undercut rate [16].

## Exposure of Photoresist

The photomask is aligned over the coated substrate, followed by the substrate being exposed to UV radiation passing through the mask. The UV radiation induces a photoreaction of the resist, which results in an alteration of the resist solubility. Depending on the photoresist type, UV exposure can induce different characteristics of the resist solubility, as shown in Figure 3.9. UV light exposure of positive resists leads to the exposed region becoming soluble in a developing solution. Negative resists have the opposite developing characteristics, where the exposed area becomes insoluble. Positive resists, are the most extensively employed in IC fabrication due to their greater resolution capability, meaning that much smaller features are achievable [156]. In addition, exposure time is related to the resist thickness. Generally, a thicker resist requires greater exposure time [155].

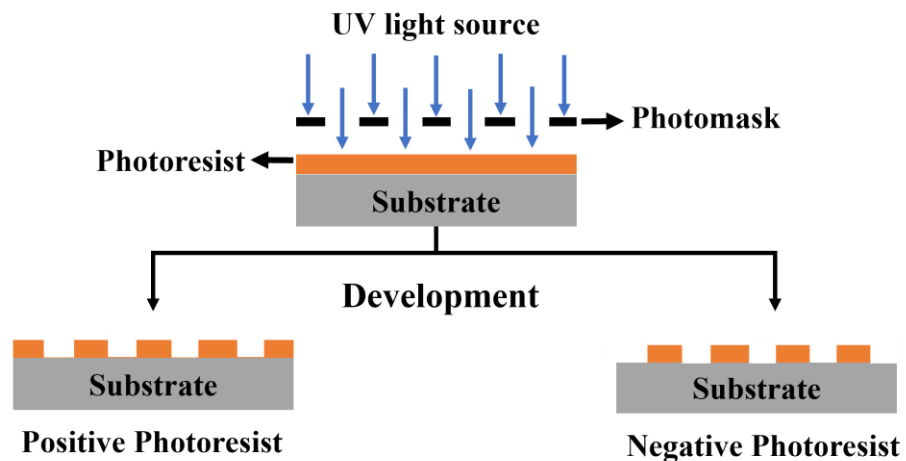


Figure 3.9 Schematic illustration of the photolithographic process based on different photoresists.

## Resist Development

The exposed region of a positive or the unexposed region of a negative resist is dissolved in a developer solvent, producing the final 3D resist structure, known as a scarified photoresist mask, on the substrate. Development is one of the most critical steps in the photolithography process because it controls the accuracy of the open window of the exposed resist (linewidth control). This step is influenced by the previous processes, including baking and exposure conditions. However, it is also affected by the resist thickness. A larger thickness requires prolonged developing time [157].

## Metallisation

Electron beam (E-beam) evaporation and/or sputtering are often used to deposit the metallic conductor layer over the developed resist. Gold, Au, is usually the metal of choice in IC

devices due to its low resistivity of  $2.4 \mu\Omega/\text{cm}^{-1}$ , offering high electrical conductivity, corrosion resistance, chemical inertness, and high compatibility with Pb-soldered material for interconnection [158], [159]. Unfortunately, one aspect of Au is undesirable because it is well known that Au films have poor adhesion to various substrates. Thus, two or more layers of additional components, e.g., Cr, Ti, Pt, Pd, etc., are usually used to promote adhesion between the substrates and the Au film [158], [160], [161]. There is a drawback with each of these additions which is a formation of unwanted reactions on the Au surface, which affects the overall properties. For instance, oxidation of Cr through diffusion up to the Au surface to form  $\text{Cr}_2\text{O}_3$  layer in the Cr-Au system and interdiffusion of Ti-Au to form  $\text{TiAu}_2$  when heating over  $250^\circ\text{C}$ . In addition, the electrical conductivity for Cr/Au is poorer than that of Ti/Au systems [162]. Thus, the latter system is preferable to use as an adhesion layer. Furthermore, three or four component, Au/x/Cr or Ti, where x represents third and fourth components, are needed to minimise the diffusion [158], [161], but it also increases production costs.

Regarding the E-beam evaporation, the electron beam is generated from a filament, and subsequently hits the metal target to evaporate it under a high vacuum environment from  $\sim 10^{-6}$  Torr to  $10^{-9}$  Torr [163], [164]. For the sputtering technique, it can be performed by energetic ion bombardment of the metallic target where the ions are accelerated by an electric field in a vacuum,  $<5$  mTorr. These molecules move towards and strike on the substrate to form a thin film [163], [164]. In IC fabrication, the E-beam evaporation is more extensively used since it provides high quality of the thin film e.g., purity, uniformity and high complexity of circuitry rather than the sputtering process [163].

### **Lift-off process**

Following metallisation, the substrate is then subjected to a lift-off process to strip the scarified mask in strippers or removers, leaving only the deposited metal pattern on the substrate surface. Stirring and elevated temperatures are usually recommended to use during the lift-off process because they accelerate the dissolution rate of the photoresist mask. However, the temperature should not exceed a flash point of the removers [155]. For example; a 1165 remover which contains 90-99% 1-methyl-2 pyrrolidinone, NMP, has a the flash point of  $88^\circ\text{C}$ , and a SVC-14 remover which contains 60% dimethyl sulfoxide, DMSO, for has a flash point of  $90^\circ\text{C}$  [165], [166]

### 3.3.3. Discussion

Due to its capabilities in transferring complex electrode patterns in a range of sizes from  $\mu\text{m}$  to nm scale onto electronic devices, a photolithography-based process has been proposed as a promising method to define the extremely fine element patterns for  $\mu\text{US}$  arrays. More importantly, it potentially produces more reliable and accurate thin film structures of elements than other techniques, e.g., dicing, printed electronics, etc.

Only a few studies have demonstrated the feasibility of applying photolithography as part of an US fabrication process for biomedical imaging. Brown et al. [6] and Bezanson [150] successfully created fine array elements with a fan-out for 40-MHz linear and phased array transducers using a standard lift-off process based on the photolithography technique, where the fan-out is an area where the electrodes are extended into larger area pads to facilitate the bonding of the interconnect wires. The process demonstrated its capabilities in defining the 38-40  $\mu\text{m}$  element-to-element pitch of the element arrays with uniform edge definition since the elements were created on thin stock layers of piezoelectric composite materials. This issue has been the subject of considerable debate because the value of  $k_{eff}$  value may be attributed to this thin layer. Ideally, the fine array elements should be patterned directly onto the surface of the 1-3 composite to achieve the ideal  $k_{eff}$ , which originates from the thickness resonances of the pillars in the composite.

Some researchers have driven further development in defining the fine array elements on composite surfaces. Bernassau [149] and Demore et al. [167] demonstrated the benefit of a bilayer lift-off process based on photolithography to directly establish the extremely fine array elements with extended fan-out features on the surface of 1-3 piezocomposites for 30 and 100 MHz linear array transducers.

The bilayer lift-off process possesses significant advantages which contribute to better element resolution, which is controlled by the undercut of the bilayer resist profiles. Additionally, the selected photoresist, polydimethylglutarimide, PMGI, does not require additional steps such as for exposure or development, which reduces the complexity of the process [155], [168]. To produce fine element  $\mu\text{US}$  arrays with more reliable and better edge definition on a composite surface, these researchers strongly recommended to improve environmental resistance, e.g., chemical and heat resistance, and surface roughness of the composite by curing the epoxy at elevated temperatures. In addition, surface planarisation combined with polishing should be implemented prior to the microfabrication process due to a thickness variation as a result of dissimilarities in the elastic characteristics of the two

materials in the piezocomposite [169]. Consequently, sufficiently fine array elements with 15 and 50  $\mu\text{m}$  element pitches were attainable.

Nonetheless, electrical impedance characteristics of the transducers, especially the 100 MHz device with an element pitch of 15  $\mu\text{m}$ , could not be observed because of the extremely fine lateral dimensions ( $\sim 7.5$ ) of the element aligned along a diagonally oriented line of pillars and the low effective volume fraction of piezoelectric material underneath the individual elements. In addition, it was argued that some elements were located on the epoxy, which resulted in a total absence of the thickness mode resonances. However, this problem could be avoided by rotating the array elements to maximise the volume fraction of piezoelectric material underneath each element [96], [170]. This solution is not only beneficial for eliminating spurious modes by disrupting the periodicity of the pillar orientation but also avoiding misalignment of the elements with lines of pillars.

Despite the work to date, there have been limited attempts to implement these alternative techniques into manufacturing  $\mu\text{US}$  arrays for biomedical imaging. Therefore, the work described in this thesis explores the bilayer lift-off process to create fine element arrays and the mean of rotating the arrays relative to lines of pillars to maximise the effective volume fraction of piezoelectric material underneath the elements. The rotation should, of course, only be an issue for the diced composite arrays as, in the randomised composite, the effective volume fraction of piezoceramic should be independent of electrode position and orientation.

### **3.4. Interconnection**

The interconnection of the  $\mu\text{US}$  array elements to the driving electronics has proved to be the most challenging stage in the development of such devices because this is limited by the fine scale of the  $\mu\text{US}$  array elements. Three methods of realising the electrical interconnections have been explored using flexible printed circuit boards, FPCB, incorporated with (a) isotropic conductive adhesive, ICA, conducting in three dimensions, (b) anisotropic conductive adhesive, ACA, conducting in the z-direction only, and (c) wire bonding. These are described in the sections that follow.

#### **3.4.1. Isotropic Conductive Adhesive**

Conductive Ag epoxy is categorised as an ICA and is now widely used as a replacement for Pb-based solder in IC fabrication because it is a lead-free adhesive. Generally, it consists of a suspension of silver flakes and powders in epoxy adhesive [171]. In terms of its functional properties compared to soldering, it offers a low temperature curing option to avoid thermal

damage to circuit components. Additionally, owing to the conductive particles being held together by an adhesive, it provides a more robust electrical joint with low volume shrinkage when it is fully hardened [172]. For these reasons, it has been claimed as a cost-effective method for the fabrication of SETs because it could be simultaneously employed as a backing layer for acoustic damping and as a mechanical support for the active materials and signal wires [135], [169], [173].

Ag epoxy has also been applied to interconnects for an array transducer. This technique was previously used successfully in the assembly of miniaturised transducers with operating frequencies up to 15 MHz through incorporation with a FPCB [12]. The technique involved manually aligning the element tracks on the FPCB, then securing them in place with tape before applying the Ag epoxy between the two, as illustrated in a literature [12]. The ICA was hardened via curing at a specific temperature, typically less than 60 °C to avoid depoling of the active materials, and then separate electrode element connections for each element were established by dicing through the ICA at appropriate intervals. However, the width of the separation is dependent on the commercial availability of blades and, consequently, this technique is restricted when applied to higher frequencies because of the limited smallest blade width. Additionally, it is susceptible to misalignment during the handling steps, e.g., manual alignment, fixing in place and curing. There is also potential for the flexible circuit to detach during the through dicing procedure. Therefore, an additional adhesive had to be applied to secure adhesion between the FPCB and the array elements.

In another procedure for manufacturing  $\mu$ US arrays [149], [167], the silver epoxy was used to make the connections between element pads which were patterned on a thin layer of piezoelectric material and copper wire soldered to the external connectors. The design of the pads with fan-out features increased the strength of the electrical joints of the wire assemblies and allowed functional testing of the composite with fine pitch array elements. However, these fan-out features were exceedingly large to be suitable for conducting biological testing on the surface of or inside the body, where small features are to be imaged.

### **3.4.2. Anisotropic Conductive Adhesive**

ACAs are employed as an alternative for solder interconnection in electronics packaging, particularly smart cards, liquid crystal displays, and flip chip packaging. The ACAs provide unidirectional electrical conductivity in the vertical direction, e.g., Z-axis. ACAs have a low volume loading of conductive particles, typically 5-20 VF%, dispersed in an adhesive. Directional connectivity in the Z-axis can be induced while the lateral connectivity, in the X

and Y axes, is minimised or fully prevented. Conventional ACAs are interposed between two substrate surfaces before mechanical interconnects are established while heat and pressure are applied simultaneously, until the conductive particles fully bridge the two substrates. The bonding and electrical quality of the ACAs are dependent on numerous factors e.g., temperature and time of both the bonding and curing processes, alignment accuracy, pressure distribution, uniformity of the applied ACAs on the substrate surface, and substrate planarity and stiffness [174].

Advantages of ACAs over conventional soldering include that the materials are more environmentally friendly than Pb-based solder and the method allows realisation of fine-pitch bonds,  $\leq 40 \mu\text{m}$ , which leads to a reduction in final package dimensions. The process uses lower temperatures for curing, 70 - 150 °C, whereas soldering requires temperatures more than 200 °C and thus cannot be used with thermally sensitive substrates. ACA also reduces processing cost with less equipment needed [12], [175], [176].

Regarding the capability of ACAs for fine-pitch bonding, those associated with flip-chip bonding have been proposed as an alternative method for establishing reliable interconnects in high frequency transducers for medical applications [12], [149]. Vertical interconnects of a stack of the 1-3 piezocomposite and a silicon wafer could be achieved by connecting electroplated Au bumps with the ACA with Au fillers between each substrate [149]. This technique was employed for the development of 15 MHz linear arrays, by bonding a FPCB with diced composite on which with array elements with a 100  $\mu\text{m}$  pitch had been established by the scratch dicing method [12]. However, this work did not succeed due to the non-uniformity of the ACA caused by its relatively high viscosity; consequently, the process could not be made repeatable.

Substrate stiffness is also an important issue in the development of high frequency transducers since a piezocomposite material with a thickness less than 100  $\mu\text{m}$  is usually required. This may allow deformation during mechanical bonding, leading to poor joint quality through misalignment and non-uniformity of the pressure distribution. However, it was suggested that these assemblies could be achieved with less deformation of the piezocomposite layer when thick composites were processed in order to tolerate the temperature during bonding [12].

### **3.4.3. Wire Bonding**

Wire bonding through fan-out pads has been shown as a viable means of realising interconnection with array elements. Brown et al. [6] demonstrated the feasibility of wire

bonding for a 256-element linear array operating at 40 MHz. 25  $\mu\text{m}$  Al wires were precisely bonded between the bonding pads on the composite and the FPCB. Based on wire bonding technology, Bezanson [150] proposed a novel technique of realising interconnects for a 64 element array by bonding 15  $\mu\text{m}$  Al wires from the bonding pads to solid vias on a multilayer FPCB that were exposed through dicing.

Whilst this is an interesting technique, it has a specific disadvantage. Generally, the ground side of the active element is positioned as a front face in commercial linear transducers, whilst the elements and interconnects are secured inside a housing. However, it has been consistently shown that if the elements and interconnects of these assembled linear arrays are positioned on opposite sides, additional adhesive is required to secure the interconnects. This can potentially affect the accuracy of image processing since the front face of the transducer cannot come into direct, close contact with human tissue due to the uneven surface of the adhesive layer.

### **3.5. Summary**

The design and development processes for the fabrication of fine scale 1-3 piezocomposites, kerfless array elements, and interconnects for  $\mu\text{US}$  arrays have been reviewed in this chapter. This review was conducted to support the development and optimisation of microfabrication processes based on a foundation of previous fabrication techniques and technical knowledge for the design and construction of  $\mu\text{US}$  arrays.

Owing to numerous advantages of gel casting over the other methods in 1-3 composite fabrication, gel casting associated with the micromoulding technique is potentially a viable route to fabricate randomised piezocomposites for suppressing interference in  $\mu\text{US}$  linear array transducers. This is addressed and reported a possibility for  $\mu\text{US}$  arrays in this thesis for the first time. Furthermore, the modified dice-and-fill method based on double pitch dicing can also enable the production of multiple devices of 1-3 diced piezocomposites with microscale manufacturing.

Photolithography based on a bilayer lift-off process is reported as a promising method to define microscale array elements with high quality on a substrate for array devices. However, surface planarisation and polishing is highly recommended to be performed prior to microfabrication to improve surface roughness due to dissimilarities in the elastic properties of the active and passive phases in the composites. To achieve reliable functional properties of the array devices made with the diced composite, the array elements should be patterned

at an angle with respect to lines of pillars of the underlying substrate derived from diced composite. Whereas this does not apply to randomised composite owing to the random distribution of pillars and spacing in the composite itself.

Among possible interconnect solutions, the ICA such as Ag epoxy adhesive is a cost-effective method and enables the production of a robust electrical joint. In addition, the design of array element patterns with fan-out pads may reduce the difficulty in creating the electrical interconnect in  $\mu$ US arrays. Thus, the Ag epoxy adhesive is chosen for creating reliable interconnect between each element through fan-out pads and small cables for  $\mu$ US arrays which are fabricated in this present work.

All these techniques are further developed and optimised for the fabrication of the three  $\mu$ US arrays based on 1-3 randomised ceramic, diced ceramic and diced single crystal piezocomposites. The feasibilities and productivities of these development processes are also investigated and reported in Chapter 5-7.

# Chapter 4 Research Methods

## 4.1. Introduction

The work described in this section was demonstrated through the production of three  $\mu$ US arrays, with frequencies over 25 MHz, capable of operation with a commercial research array controller. These three arrays are presented in Table 4.1 and the fabrication process flow for their manufacture is illustrated in Figure 4.1.

Table 4.1 List of prototypes of  $\mu$ US transducer arrays and their applications.

Transducer array	Piezoelectric material	Probe configuration
<b>TX1-RM</b> 30 MHz transducer arrays	1-3 randomised ceramic <sup>1</sup> piezocomposite	Forward facing transducer with rear surface array elements
<b>TX2-PZ</b> 32 MHz transducer arrays	1-3 diced PZ54 <sup>2</sup> ceramic piezocomposite	
<b>TX3-PIMNT</b> 27 MHz transducer arrays	1-3 diced PIMNT <sup>3</sup> single crystal piezocomposite	

<sup>1</sup> TRS 610C powder, TRS Technologies Inc, Pennsylvania, USA

<sup>2</sup> PZ54 ceramic, TRS Technologies Inc, Pennsylvania, USA

<sup>3</sup> PIMNT single crystal, Meggitt Ferroperm, Kvistgaard, Denmark

Section 4.2 gives the details of 1-3 piezocomposite fabrication using different piezoelectric materials and methods. 1-3 randomised piezocomposites were fabricated by using a method combining gel casting with micromoulding to produce the composite structure with arbitrary features in the range 2-50  $\mu$ m, proving random *AR*, in the range 1-25. Devices with 1-3 connectivity ceramic and single crystal piezocomposites were also produced for comparison, using modified dice-and-fill techniques to manufacture the structure with square pillar shapes of order of 38- $\mu$ m pillar pitch, producing *AR* value around two.

Thickness variation is usually found in composites due to the dissimilarity of its two constituent materials, the piezoelectric material and polymer material [177]. Piezocomposite surface preparation is thus required to modify surface prior to patterning 20 array elements with 50- $\mu$ m pitch on the composites. For this reason, processes of surface preparation are discussed in Section 4.3. The generic steps of a bilayer lift-off process for array element fabrication are discussed in Section 4.4. After lapping to the required thickness, the studies of material release and wax removal to maintain yield of active elements are described in Section 4.5, followed by poling for unpoled materials as given in Section 4.6.

Characterisation methods for functional properties for the 1-3 composite SETs are described in Section 4.7. Fabrication processes of interconnect, transducer packaging, and cabling are presented in Section 4.8. However, measurements of electrical impedance spectra and continuity of the composite arrays must be carried out to determine  $k_{eff}$  and identify active and passive elements of the 1-3 composite arrays before transducer packaging, and these are thus described in Section 4.9. A basic test based on pulse-echo response was used to determine the performance of the  $\mu$ US arrays, which is also shown in this section. Finally, the performance of transducers made with different 1-3 piezocomposite materials based on practical works were also investigated by means of finite element analysis via the Onscale tool as presented in Section 4.10.

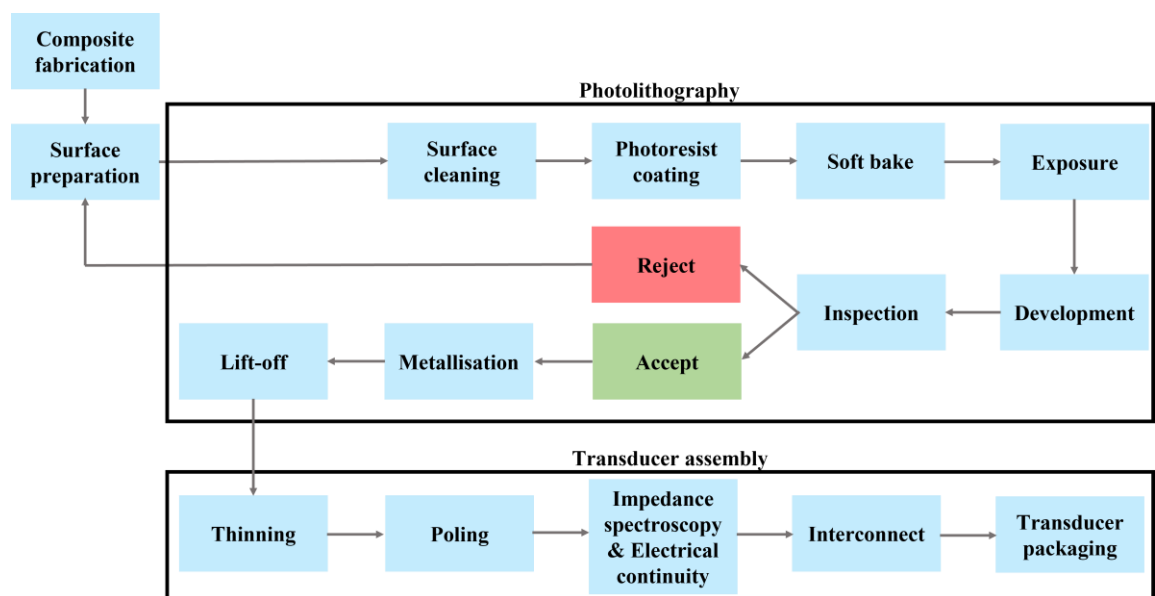


Figure 4.1 Outline fabrication process flow for  $\mu$ US composite transducer arrays.

Standard or established processes and characterisation methods that have been used in the work are presented and discussed in this chapter only, whereas any new process developments that have been made are discussed further in subsequent chapters.

## 4.2. 1-3 Piezocomposite Fabrication

The three transducers TX1-RM, TX2-PZ and TX3-PIMNT were made with 1-3 randomised PZT5H ceramic, diced PZ54 ceramic, and diced PIMNT single crystal piezocomposites, respectively. Each piezocomposite was fabricated using a different method as described below.

### **4.2.1. 1-3 Randomised Piezocomposites**

The fabrication of 1-3 randomised piezocomposite material was previously studied to validate and optimise each part of the process, with the aim to use the material for operation at the high frequencies required for  $\mu$ US.

Fabrication of silicon master moulds with a randomised pattern was previously considered by Jiang [95] using microfabrication techniques based on deep dry etching of 3-inch single crystal (<100>) silicon wafers at the Scottish Microelectronics Centre (SMC), University of Edinburgh. The optimisation of milling of piezoelectrically soft PZT powders (PZT-5H, TRS 610C, TRS Technologies, USA), the rheology of gel casting slurries, and subsequent processes were reported in detail by Thongchai [50].

Further details of the fabrication of randomised piezocomposites for  $\mu$ US arrays are provided in this thesis as follows:

#### **Powder Preparation**

A commercial soft PZT powder (PZT-5H, TRS 610C, batch no. 2002 and no. 2008, TRS Technologies, USA) with density  $7.95 \text{ g cm}^{-3}$  was milled using a custom made vibro-milling machine (Model M.18, Sweco Europe S.A., Belgium). Two batches of the as-received PZT powder were used in this present work since the first batch was exhausted.

Prior to the milling process, suspensions were prepared by adding 250 g of the powder and 200 g of zirconia balls with 5- and 10-mm diameter into 300 ml of distilled water in a polyethylene bottle. The as-received PZT powder batch no. 2008 exhibited a bimodal particle size distribution with particle population centred at 18 and  $2.5 \mu\text{m}$  and was therefore milled by the vibro-milling machine for 48 hr since this condition was optimised to produce a mean particle size of  $1.2 \mu\text{m}$  for minimising the viscosity of the casting slurry as reported in detail by Thongchai [50]. The as-received PZT powder batch no. 2002 also exhibited a bimodal particle size distribution with particle populations centred at  $2.15 \mu\text{m}$  and  $15 \mu\text{m}$  and was also vibro-milled. The milling times of 24, 36, 39 hr were varied to investigate to determine which one is suitable for producing a mean particle size of  $1.2 \mu\text{m}$  after milling, to match that of the previous batch. The milled suspensions were dried for 12 hr using a freeze drier (Edwards Modulyo Freeze dryer, Labconco Corp., Kansas City, USA), followed by sieving using a vibratory sieve shaker, through 63 and  $36 \mu\text{m}$  mesh stainless-steel drum sieves.

## Slurry Preparation

A 48 vol% of solid loading of the milled PZT powder in 30 wt% resin with other additives and solvent was employed in this study as shown in Table 4.2. This condition was developed through an optimisation of gel casting slurry to provide maximum green strength as reported by Thongchai [50]. Hydantoin epoxy resin was used, recognised as a new gelling agent chosen to produce high strength and density of green body samples. This is because it possesses excellent water solubility, allowing higher solid loading in the gelling system by retaining a high uniformity of particle distribution [141]. Bis(3-aminopropyl) amine was used as the cross-linker. In addition, Dispex AA4040 was used as an additive to aid the powder dispersion in the solution.

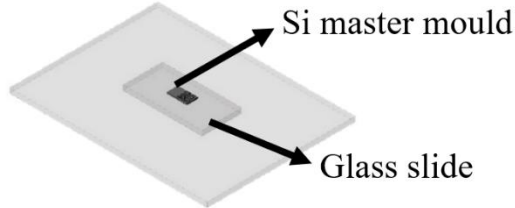
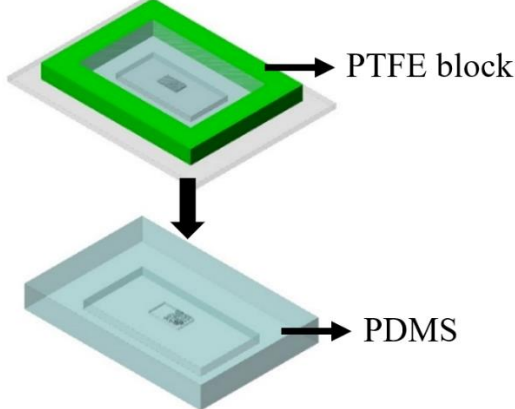
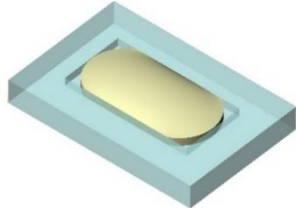
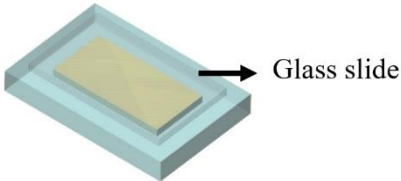
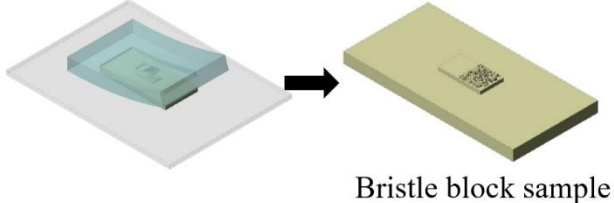
Table 4.2 Raw materials for the preparation of gel casting PZT suspension.

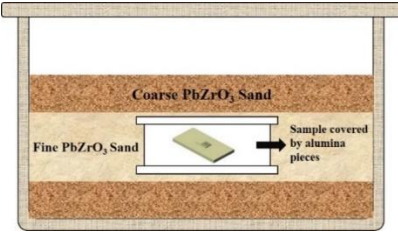
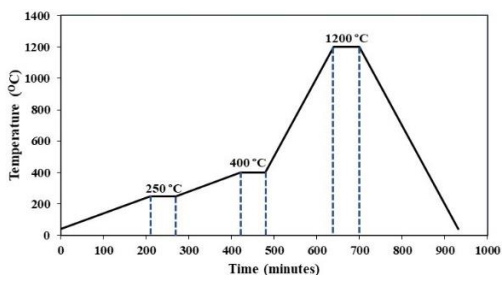
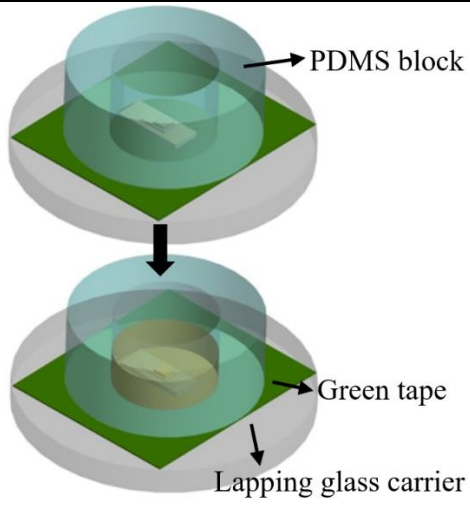
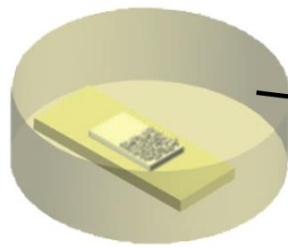
Material	Function	Details	Quantity
Milled PZT	Powder	Mean particle size of 1.2 $\mu\text{m}$	36.2 g
Distilled water	Solvent	-	3.5 g
Dispex-AA4040	Dispersant	BASF, Germany	0.362 g
Hydantoin	Epoxy monomer	Hubei, Xitai Chemical, China	1.5 g
Bis (3-aminopropyl) amine	Hardener	Sigma-Aldrich, Germany	0.07 g

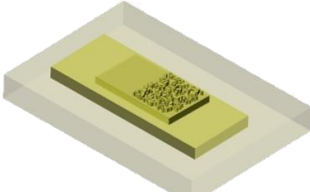
1.5 g of the Hydantoin resin was mixed with 3.5 g of distilled water, in a premix solution step, and stirred in a beaker using a magnetic stirrer until it became homogeneous. 0.362 g of Dispex-AA4040 was added and the suspension was poured into a 60 ml polyurethane container with 25 g of 4.8-mm diameter zirconia balls. 36.2 g of the milled PZT powder was added in three steps, adding one third of the total amount during each step to aid the premixing. The first two steps were carried out by mean of a magnetic stirrer on a hotplate at room temperature,  $T_R$ , following by a ball-milling process for 2 hrs with a rotation speed of 70 rpm in the final step, to mix the powder into the solution effectively. The mixture was then sieved with a strainer to separate the solution from the zirconia balls. Prior to casting, 0.07 g of the hardener was added and stirred for another 3 min.

The fabrication of 1-3 randomised piezocomposites is presented as process diagram in Table 4.3.

Table 4.3 Fabrication process for a 1-3 randomised piezocomposite based on a gel casting method.

Process step	Diagram
<p>A. A silicon master mould with a randomised pattern is attached on a glass slide by melting wax for ease of handling [50].</p>	 <p>The diagram shows a grey rectangular silicon master mould with a small black patterned area on its surface. This mould is placed on a larger, light grey rectangular glass slide. Arrows point from the labels 'Si master mould' and 'Glass slide' to their respective parts in the diagram.</p>
<p>B. The master mould is placed in a plastic petri dish and surrounded by a Teflon block to form a mould. A mixture of PDMS: Sylgard Silicone Elastomer 184 and Sylgard Curing Agent 184 (Dow Corning Corporation Ltd., UK) with a weight ratio of 10:1 is manually mixed in a beaker, followed by de-gassing in a vacuum desiccator until most of the bubbles disappeared. It is then slow poured from one corner of the dish into the mould. Curing at room temperature, <math>T_R</math>, for 24 hr is needed. Prior to demoulding, drying in an oven (Lenton Thermal Designs, UK) at 50 °C for 6 hrs is required to ensure that the PDMS mould is sufficiently dried [50].</p>	 <p>The diagram illustrates two stages. In the first stage, a green rectangular Teflon block is placed around a grey silicon master mould which is sitting on a light grey glass slide. An arrow points from the label 'PTFE block' to the green block. In the second stage, the Teflon block and glass slide are removed, leaving a light blue rectangular PDMS mould in the petri dish. An arrow points from the label 'PDMS' to the mould.</p>
<p>C. A PZT slurry made with A 48 vol% of solid loading in 30 wt% resin with other additives and solvent is then cast into the PDMS mould. After casting, a glass slide was placed on top, then gently pressed, followed by degassing for 3 min to ensure that the slurry is fully filled into the mould cavities. A gel film is created after 3 min due to the high-water volatility at the top surface. It must be removed before refilling the slurry until the slurry is fully filled into the mould. The total time of these two steps must be controlled, depending on the idle time of gel hardening [50].</p>	 <p>The diagram shows a light blue rectangular PDMS mould with a yellowish slurry being poured into it from a small container. The slurry is filling the central cavity of the mould.</p>
<p>D. Drying. A glass slide is placed on top of the slurry surface to prevent the sample from bending, which would otherwise result in difficulties in keeping the sample planar during the lapping step later in the process [50]. Drying is carried out in <math>T_R</math> for 24 hrs, followed by drying on the oven at 40 °C for another 24 hrs to ensure that the sample was completely dried before manually demoulding.</p>	 <p>The diagram shows a light blue rectangular PDMS mould with a yellowish slurry inside. A light grey rectangular glass slide is placed on top of the slurry. An arrow points from the label 'Glass slide' to the glass slide.</p>
<p>E. Demoulding is usually carried out beginning from one corner of the PDMS mould to prevent the breakage of pillars [50]. However, this step is dependent on the operator's skill and experience. The sample is then characterised via a scanning electron microscopy, SEM, to measure pillar dimension for estimating AR after demoulding.</p>	 <p>The diagram shows two stages of demoulding. On the left, a light blue rectangular PDMS mould is being lifted away from a light grey surface. An arrow points to the right, where a yellowish rectangular bristle block sample is shown, which has been successfully removed from the mould. The label 'Bristle block sample' is placed below the final product.</p>

Process step	Diagram
<p>F. The bristle-block green samples are covered by alumina pieces to prevent the damage of the pillars from the outside environment. The covers samples are then placed in an alumina crucible and buried in fine and coarse PbO-doped ZrO<sub>2</sub> sands as shown. Finally, the crucible is covered and placed in a muffle furnace (Serial No. 3967, Lenton Furnaces, UK) for sintering. The PbO-doped ZrO<sub>2</sub> (PbZrO<sub>3</sub>) sand provides a lead rich atmosphere to prevent lead-loss from the sample during sintering [50].</p>	 <p style="text-align: center;"><b>Bristle-block PZT specimens buried by fine and coarse PbZrO<sub>3</sub> sands in an alumina crucible</b></p>
<p>G. Organic burnout and sintering. Before sintering, the burnout process is separately processed at two temperatures, 250 and 400 °C with a ramp rate of 1°C/min and dwell time of 1 hr for each temperature to ensure that the resin and polymers are completely decomposed from the sample [50]. Following this, the ramp rate is increased to 5 °C/min for sintering at 1200 °C for 1 hr. The burnout and sintering profile of the PZT green samples is shown. The sample is then again characterised via a SEM to measure pillar dimension for estimating AR after sintering.</p>	 <p style="text-align: center;"><b>The burn-out and sintering profile of PZT green sample</b></p>
<p>H. Encapsulation. The sintered sample is placed on a glass carrier covered with tape and surrounded by a PDMS block to form a mould. The glass carrier ensures the sample is level in the mould and the tape prevent the sample becoming stuck to the carrier during subsequent processing. A mixture of Epofix resin and hardener (Struers, UK) in a weight ratio of 25:3 g is mixed and then degassed for 5 min and left into <math>T_R</math> for another 5 min to remove bubbles. The mixture is then slowly poured into the mould from one side of the container to prevent air entrapment in the inter pillar spacings. The assembly is intermittently degassed with total duration of 20 min to remove microbubbles, then left in <math>T_R</math> for 20 min allowing surface bubbles to disperse.</p>	
<p>I. Epoxy curing at elevated temperatures from 40-60 °C is firstly applied with ramp rate of 1 °C/min, this was followed by holding the temperature at 60 °C for 2 hr. The curing at elevated temperatures is required to enhance the heat and chemical resistance of the composite by increasing the crosslink density to raise the glass transition temperature of the epoxy [178], [179]. After heat curing, the sample is cooled down to <math>T_R</math> in the oven for another 24 hr to ensure that the epoxy was completely cured. Then a block of the randomised composite is removed from the mould as shown.</p>	

Process step	Diagram
<p>J. The overall dimension of the epoxy coupon (diameter of 20 mm) must be reduced by sawing to approximately 11 x 12 mm<sup>2</sup> to provide sufficient area for the fan-out electrode whilst allowing the pressure on the composite area during lapping and polishing to be maximized.</p>	 <p>1-3 randomised PZT5H piezocomposite</p>

#### 4.2.2. 1-3 Diced Piezocomposites

This section describes preparation of composite material for the fabrication of  $\mu$ US arrays with an operating frequency of  $\sim 30$  MHz using a modified dice and fill method to establish a fine scale 1-3 connectivity structure from different piezoelectric materials.

Owing to the availability of a semi hard PZT ( $\text{Pb}(\text{Zr}_{0.52}\text{Ti}_{0.48})\text{O}_3$ , PZ54, Ferroperm, Kvistgaard, Denmark) piezoceramic, it was employed in a preliminary study to investigate the optimisation of dicing parameters, before carrying out a similar process using single crystal material which is exceptionally fragile and brittle [70], [180]. The parameters established for the PZT were used as a baseline and modified to suit the single crystal, PIMNT ( $\text{PbIn}_{1/2}\text{Nb}_{1/2}\text{O}_3 - \text{PbMg}_{1/3}\text{Nb}_{2/3}\text{O}_3 - \text{PbTiO}_3$ , PIN-PMN-PT, X4, TRS Technologies, PA, USA) to fabricate a high-performance transducer with broad bandwidth and better sensitivity than can be achieved with piezoceramic.

The dicing saw was a DAD3320 (Disco, Tokyo Japan) with a hub diamond blade (ZHZZ series, Disco, Tokyo, Japan). The sample of material was held by adhesive tape (Universal tape, Loadpoint Ltd, Wilts, UK) attached onto a dicing frame and mounted on a vacuum chuck.

#### Dicing Parameters

In 1-3 piezocomposites for operation at 30MHz  $\mu$ US, the final thickness, defining the pillar height, is approximately 50  $\mu\text{m}$ . The  $VF$  of the active element or material and  $AR$  are both important parameters of the composite. To achieve high transducer performance  $VF \geq 40\%$  and  $AR \geq 3$  are acceptable, as described in Section 2.7.7. However, in practice, these two parameters are defined by the minimum thickness of the dicing blade available commercially nominal 10  $\mu\text{m}$  blade thickness, producing a 13  $\mu\text{m}$  kerf. As described in Section 2.7.7, the thickness of the piezoelectric material required can be determined by Eq. 2.22. Consequently, the required thickness of the 1-3 piezocomposite for 30MHz  $\mu$ US is

approximately 50  $\mu\text{m}$ . Thus, the parameters given in Table 4.4, were evaluated based on this thickness and the 13  $\mu\text{m}$  kerf using Eq. 2.22 -2.24.

Table 4.4 Geometrical parameters for a 1-3 piezocomposite operating at  $\sim 30$  MHz.

<b>Pillar height (<math>\mu\text{m}</math>)</b>	<b>Kerf (<math>\mu\text{m}</math>)</b>	<b>Pillar width (<math>\mu\text{m}</math>)</b>	<b>VF (%)</b>	<b>AR</b>	<b>Pitch (<math>\mu\text{m}</math>)</b>
50	13	17	32.11	2.94	30
50	13	20	36.73	2.50	33
50	13	23	40.82	2.17	36
50	13	24	42.07	2.08	37
50	13	25	43.28	2.00	38

### Dicing Method

A 1 mm thick plate of PZ54 ceramic was used for a preliminary study to investigate optimisation of the single pitch dicing process at 38- $\mu\text{m}$  pillar pitch. Prior to achieve the 38- $\mu\text{m}$  pillar pitch with high yield of survival pillars, several trails were performed in order to optimise dicing parameters, e.g., pillar pitch and feed speed, which were then chosen as a compromise between dicing time and yield of survival pillars. After the dicing process was validated with the piezoceramic, a 700  $\mu\text{m}$  thick plate of PIN- PMN-PT single crystal was then processed using a double pitch dicing method with a 76- $\mu\text{m}$  pillar pitch which produced the single crystal composite with the desired 38  $\mu\text{m}$  pitch. The final dicing parameters of 1-3 diced piezocomposites fabricated using ceramic and single crystal piezoelectric materials were validated as presented in Table 4.5. Owing to the dicing and curing processes involving many steps, this is presented as a process diagram shown in Table 4.6. and Table 4.7 for PZ54 ceramic and PIMNT single crystal piezoelectric materials.

Table 4.5 Dicing program parameters for production of 1-3 piezocomposite fabricated from PZT piezoceramic and PIMNT single crystal materials.

<b>Parameter</b>	<b>PZ54 ceramic</b>		<b>PIMNT Single crystal</b>	
	<b>Pass 1</b>	<b>Pass 2</b>	<b>Pass 1</b>	<b>Pass 2</b>
<b>Blade kerf size (mm)</b>	0.013	0.013	0.013	0.013
<b>Cut depth (mm)</b>	0.150	0.170	0.110	0.130
<b>Pitch (mm)</b>	0.038	0.038	0.076	0.076
<b>Feed rate (mm/s)</b>	0.200	0.200	0.100	0.100
<b>Spindle speed (rpm)</b>	20,000	20,000	20,000	20,000

Table 4.6 Fabrication process for 1-3 diced piezoceramic composite based on a single pitch dicing method.

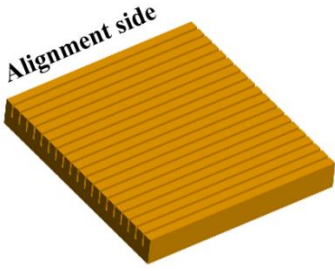
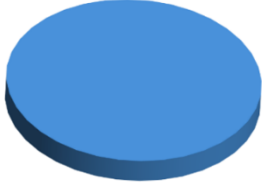
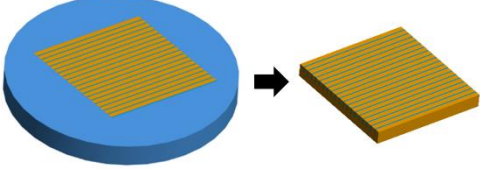
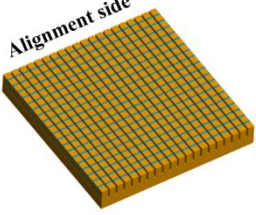
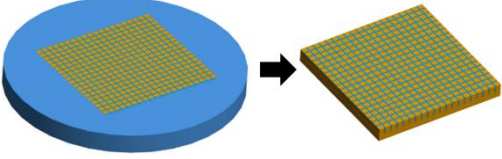
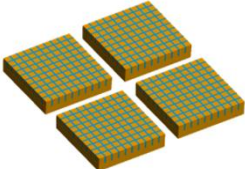
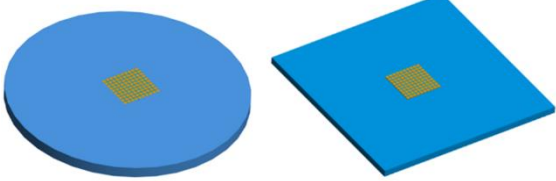
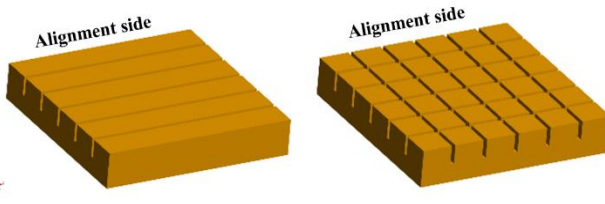
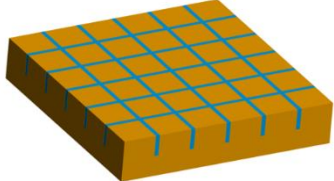
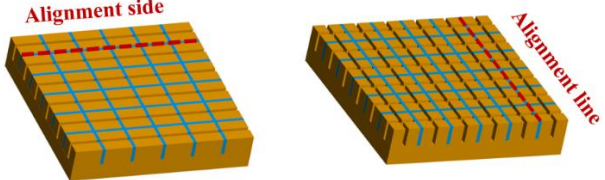
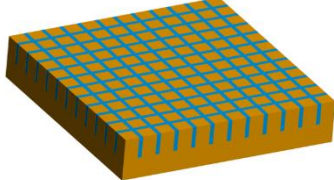
Process step	Diagram
<p>A. Vertical dicing. A plate of PZ54 piezoelectric ceramic with a size of <math>10 \times 10 \times 1 \text{ mm}^3</math> is mounted onto a dicing frame with adhesive tape. Prior to dicing in a vertical direction, a saw blade is firstly aligned at one side of the sample in order to create the first series of cuts parallel to an edge of a sample. The first series of cuts is made using a <math>10\text{-}\mu\text{m}</math> blade at <math>38 \mu\text{m}</math> pitch to produce a series of grooves in a vertical direction. The grooves are generated via a kerf width of <math>13 \mu\text{m}</math>. The cut depth is <math>150 \mu\text{m}</math>.</p>	
<p>B. Encapsulation. The diced ceramic is filled using Epofix epoxy. The height of the Epofix above the ceramic surface should be higher than 2 mm in order to ensure that the Epofix spreads sufficiently into all areas of the ceramic plate. The entire assembly is cured at <math>60^\circ\text{C}</math> for 2 hr as explained in Table 4.3(H).</p>	
<p>C. Lapping. The epoxy is lapped to expose the diced ceramic surface using suspensions of alumina varying in size from 20 to <math>3 \mu\text{m}</math>. Any extra epoxy surrounding the diced ceramic is cut away using the dicing saw.</p>	
<p>D. Horizontal dicing. The alignment is made with one side of the sample. It is then turned perpendicular to the second series to produce <math>38\text{-}\mu\text{m}</math> pillar pitch using the same procedure as the first series but the cut depth for the second series is <math>170 \mu\text{m}</math>. When the composite is flipped over to the stock layer side for lapping or thinning to the required thickness, the deeper cut depth is used as a mark to change a lapping condition, as given in Section 4.3 to avoid overlapping.</p>	
<p>E. Encapsulation using the same procedure as step B.</p>	
<p>F. Lapping is again carried out to expose the diced ceramic surface using suspensions of alumina varying in size from 20 to <math>3 \mu\text{m}</math>. Any extra epoxy surrounding the diced ceramic is cut using the dicing saw.</p>	
<p>G. The sample is cut into plates of size <math>2 \times 2 \text{ mm}^2</math>.</p>	
<p>H. After separation, the sample undergoes a third encapsulation in Epofix epoxy. This is followed by lapping to expose the composite surface. Any extra epoxy is cut away using the dicing saw leaving a match with the dimensions of the element pattern with fanout (<math>12 \times 12 \text{ mm}^2</math>) prior to lapping to expose the pillars and polishing to improve surface roughness.</p>	
<div style="display: flex; justify-content: space-around; align-items: center;"> <div style="display: flex; align-items: center;">  Piezoelectric material         </div> <div style="display: flex; align-items: center;">  Epoxy resin         </div> </div>	

Table 4.7 Fabrication process for 1-3 diced single crystal composite based on a double pitch dicing method.

Process step	Diagram
<p>A. Vertical dicing. Prior to dicing in a vertical direction, a saw blade is firstly aligned at one side of the sample in order to create the first series of cuts parallel to an edge of a sample. After finished the vertical lines, the alignment is made with one side of the sample at which it is parallel to the vertical lines, then it is turned perpendicular to the vertical lines. The first series of cuts in two orthogonal directions are made with 76-<math>\mu\text{m}</math> pitch and a cut depth of 110 <math>\mu\text{m}</math>.</p>	
<p>B. Encapsulation as described in Table 4.3(H).</p>	
<p>C. Lapping to expose the composite surface and cutting away an extra epoxy surrounding the composite as described in Table 4.6 (C).</p>	
<p>D. Prior to dicing the second series in two orthogonal directions, the saw blade is aligned from the first filled kerf of the first series in order to maintain the second series of cuts parallel to the first cuts. Then the saw blade starts to dice in the vertical direction before dicing in the horizontal direction. However, in the second series, the blade is started at the interpillar positions of the first series to produce 76-<math>\mu\text{m}</math> pillar pitch. The cut depth of this series is 130 <math>\mu\text{m}</math>.</p>	
<p>E. Encapsulation using the procedure as step B.</p>	
<p>F. Lapping to expose the composite surface and the extra epoxy is also removed as explained in step D.</p>	
<p>G. The sample is cut to a size of 2<math>\times</math>2 mm<sup>2</sup>, followed by the third encapsulation, lapping, and cutting the extra epoxy as described in Table 4.6 (Steps G and H)</p>	

### Encapsulation and curing

The encapsulation in this section is divided into two parts, for composite fabrication and the epoxy coupon added prior to photolithography for obtaining space for the element pattern with fan-out.

These steps were also carried out using a 25:3 g ratio of Epofix resin and hardener. Centrifugation with a speed of 2000 rpm for 3 min via a compact centrifuge (SciSpin One centrifuge, Sciquip, Shropshire, UK) was used to remove any air bubbles instead of degassing because the bubbles were faster removed. It was then slowly poured from one

corner into the sample placed at the centre of a PDMS mould to avoid trapping air in between the pillars. The assembly was intermittently degassed for a total duration of 20 min to remove bubbles and to ensure the epoxy fully filled into the cavities and interpillar spaces. This step is not necessary during addition of the epoxy coupon or fan-out epoxy because the interpillar spaces were already filled. The sample was left at  $T_R$  for 20 min before curing in an oven with the elevated temperatures as mentioned previously in Table 4.3 (I).

### 4.3. Surface Preparation of Composites

#### Lapping and Polishing

This section describes the method used to reduce the thickness and prepare the surface of the 1-3 composites. As indicated in Table 4.3 (J), before embarking on these processes, it is important to optimise the size of the epoxy coupon in order to improve the efficiency of material removal. The area of the epoxy coupon must be reduced to maximise the pressure applied onto the composite area during lapping onto the composite area, which is approximately  $2 \times 2 \text{ mm}^2$ . However, the overall size of the epoxy coupon must be based on the size of the full array electrode elements, including fanout, which is approximately  $12 \times 12 \text{ mm}^2$ .

Quartz wax (Logitech, Glasgow, UK) was melted on a glass carrier at  $60 \text{ }^\circ\text{C}$  prior to adhering the sample. The entire assembly was then pressed by a bonding jig to fix the sample in place whilst the wax cooled down and hardened. Lapping was carried out using a Logitech PM5 lapping machine (Logitech, Glasgow UK), and a photograph of the set-up is displayed in Figure 4.2. A lapping jig holds the material sample facing downwards against a lapping plate, and the plate rotates at a controlled speed with a controlled load while an abrasive slurry drops consistently onto the plate and is pushed between the lapping plate and the surface of the material sample.

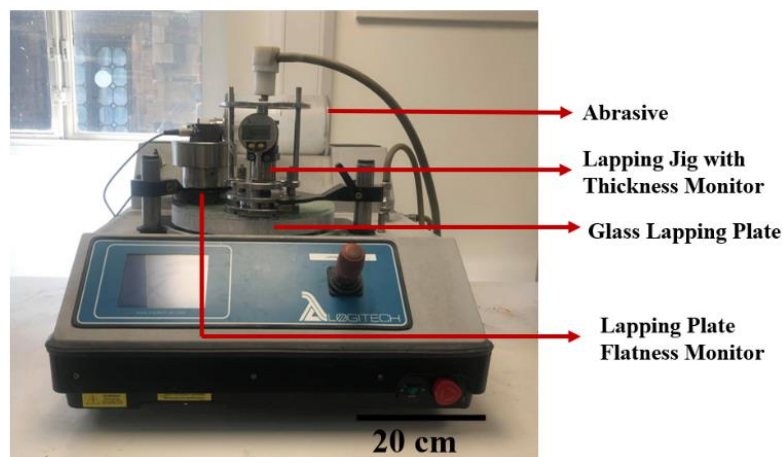


Figure 4.2. Photograph of the Logitech PM5 lapping machine.

Table 4.8 details the surface preparation steps used for 1-3 piezocomposites. Figure 4.3 shows overall thickness of the pillars and stock layers in a sintered sample with thickness of 1.3 mm fabricated by the gel casting method, and a diced piezoceramic composite with thickness of 0.8 mm. The SEM images showing overall thickness help an operator to prevent overlapping during the lapping process since the operator can estimate the remaining thickness of the excess epoxy before pillar exposure. A grooved iron plate was initially used for a greater material removal rate to remove the excess epoxy with thickness of 3 mm over the pillar surface in the first two steps. When the excess epoxy is lapped to 100  $\mu\text{m}$  thick before approaching the pillar surface, a glass plate is then employed to gradually expose the pillar surface in the third step. The abrasive particles used in this work were alumina powder (J-MAC Tech ltd, Glasgow UK) and vary in size from 3 to 20  $\mu\text{m}$ . In the photolithography process, the smoothness of the material surface controls the definition of the fine array elements. Thus, a final polishing step is necessary to improve the surface roughness. Polishing was also accomplished using this machine with alkaline colloidal silica suspension (SF1, Logitech Ltd, Old Kilpatrick, UK) on a polyurethane plate (Logitech, Glasgow UK) at a speed of 40 rpm, for a total duration of 1 hr and a load of 750 g.

Table 4.8 Surface preparation conditions established for 1-3 piezocomposites using a Logitech PM5 Lapping Machine.

Step	Lapping			Polishing
	1	2	3	4
<b>Abrasive</b>	20- $\mu\text{m}$ $\text{Al}_2\text{O}_3$	9- $\mu\text{m}$ $\text{Al}_2\text{O}_3$	3- $\mu\text{m}$ $\text{Al}_2\text{O}_3$	SF1
<b>Plate</b>	Grooved Cast Iron	Grooved Cast Iron	Glass (No Groove)	Polyurethane
<b>Rotational speed (rpm)</b>	30	30	15	30
<b>Load (g)</b>	Dependent on requirement of a remove rate			750
<b>Duration time</b>	Dependent on thickness of the extra epoxy above composite area			1 hr

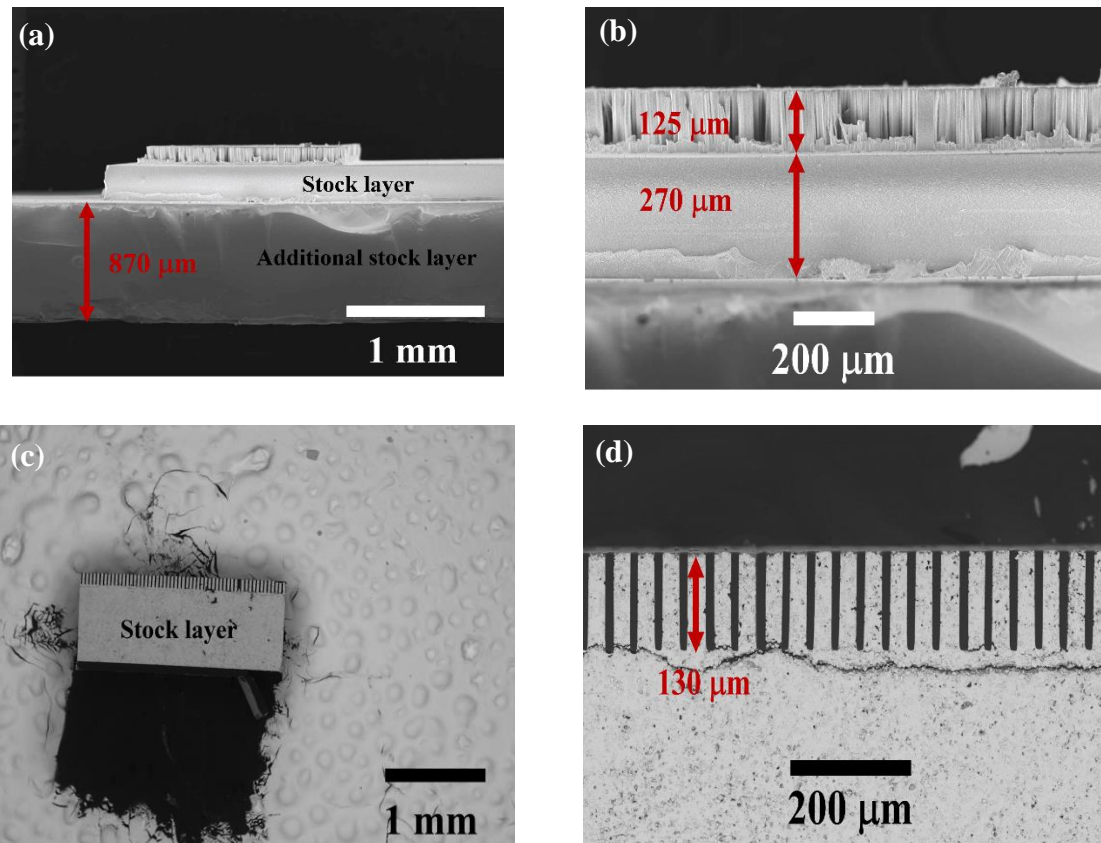


Figure 4.3 SEM micrographs of (a)-(b) a sintered gel cast sample and (c)-(d) a diced ceramic piezocomposite.

#### 4.4. Photolithography

Photolithography based on a bilayer lift-off process was employed to create 50- $\mu\text{m}$  element pitch with a pattern incorporating 20 array elements and an extended fan-out to bonding pads for interconnect as presented in Figure 4.4. Two patterns were designed to accommodate the different dimensions of the composite areas, which are approximately  $1.3 \times 1.3 \text{ mm}^2$  for the 1-3 randomised ceramic composites and  $2 \times 2 \text{ mm}^2$  for the 1-3 diced ceramic and single crystal composites. Thus, the element lengths for the diced composites were slightly longer than those for the randomised composites (2 mm vs 1.4 mm).

The linewidth of the arrays, trace, and space, forming the array elements in the middle part of the patterns were constantly defined as 35 and 15  $\mu\text{m}$ , respectively in both patterns. These dimensions provided an element pitch based on one wavelength, which was assumed to be sufficient to maintain the transmitted pulses while minimising side lobes.

In order to ensure the linewidths and element traces corresponding to the dimensions of patterns in the photomasks, they were characterised under optical microscope (Nikon Eclipse LV150, Nikon, Japan, resolution 100 nm). Marks alongside the middle part were used as a standard reference in each measurement. Five linewidths of a bilayer resist profile and

element traces were measured by using an ImageJ processing program (National Institutes of Health, USA). Lengths of the mark references are 500 and 100  $\mu\text{m}$  for the patterns of diced and randomised composites, respectively, as presented in Figure 4.5.

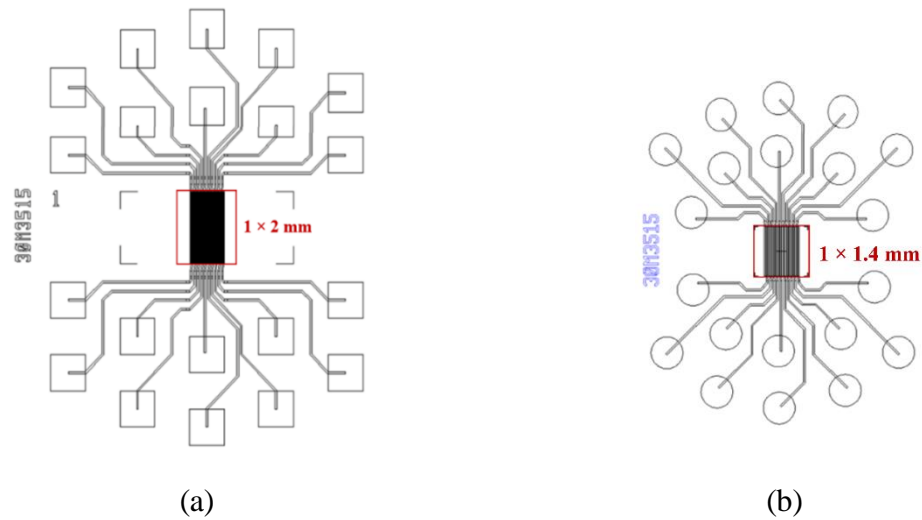


Figure 4.4 Designs of array elements with fanout for (a) diced composites and (b) randomised composites.

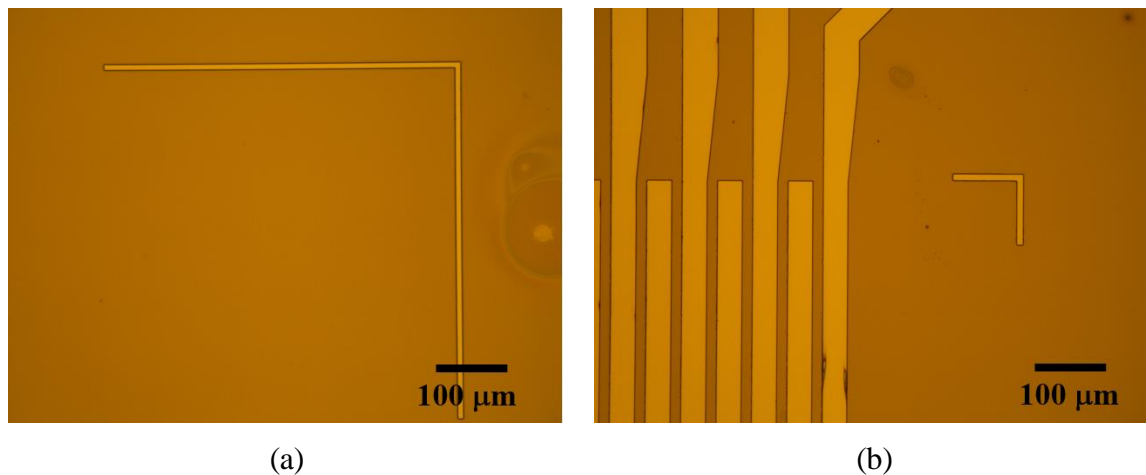
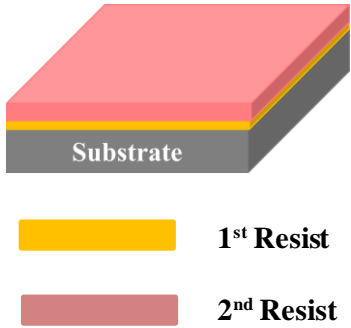
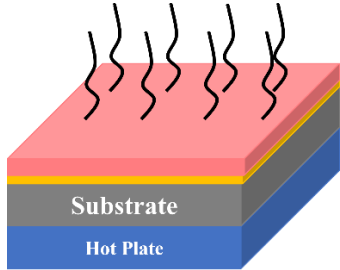
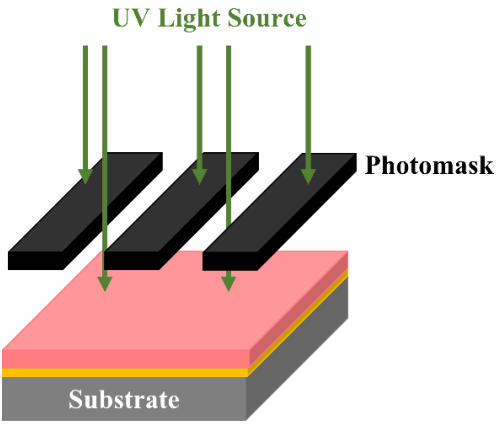
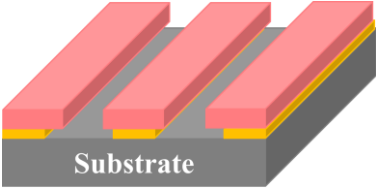


Figure 4.5 Optical micrographs of mark references used for (a) diced and (b) randomised composites at magnification of 20x.

For establishment of a bilayer resist on a substrate, two types of photoresists are employed, including lift off resists, LOR; LOR3A and LOR10A, used as a primary resist, and S1818 used as a secondary resist, respectively. The LO3A and LOR10A provide resist thicknesses in ranges 0.3-0.6 and 2.7-6  $\mu\text{m}$ , respectively, whereas the S1818 provide the thickness in range 1.4-2.7  $\mu\text{m}$  [157], [181]. Table 4.9 outlines the generic procedures and basic steps of a bilayer lift-off process adopted for the substrates used in this present work. The validation and optimisation for each substrate are described in detail in Chapter 6.

Table 4.9 Fabrication process of the generic steps in a bilayer lift of process.

Process step	Diagram
<p>A. Substrate preparation in the form of surface cleaning is highly dependent on the substrates that are used. Solvents, including Opticlear (National Diagnostics, USA), acetone, methanol and isopropanol, and reverse osmosis (RO) water, in addition with sonication are used in different combinations to clean the surfaces of Si wafers. In contrast, wiping with a sponge immersed in solvent is required for both epoxy and composite substrates since sonication may damage the pillars in the composite. After solvent cleaning, Si wafers must be dehydrated in an oven at 150 °C for 20 min. The dehydration step is not appropriate for epoxy and composite substrates because high temperature and holding for that long time may degrade the piezoelectric properties of the materials and deform of the epoxy. However, composite substrates must be blown dry with N<sub>2</sub> to ensure that any particulates are removed before photoresist coating.</p>	 <p>A 3D perspective diagram of a rectangular substrate block. The word "Substrate" is printed in black on the front face of the block.</p>
<p>B. Photoresist coating. A few ml of the positive photoresist are dropped onto the substrate surface and spin coated at a certain speed and time to establish a uniform layer of photoresist. Two types of positive photoresists are needed to create the undercut. The LOR3A and 10A (Microchem Corp, Newton, Massachusetts, USA) resists are employed as the primary photoresist applied on the substrate. The photoresist thickness is determined by the spin speed. Generally, the LOR3A provides a thin film in the range 200 – 600 nm whilst LOR10A offers an intermediate film thicknesses from 650 – 1500 nm [155], [157]. The second photoresist is S1818, providing a standard thickness of 1.8 μm (Rohm &amp; Haas Electronic Materials LLC, Marlborough, USA).</p>	 <p>A 3D perspective diagram showing a substrate with two layers of photoresist. The bottom layer is yellow and the top layer is red. A legend below the diagram shows a yellow rectangle labeled "1<sup>st</sup> Resist" and a red rectangle labeled "2<sup>nd</sup> Resist".</p>
<p>C. Photoresist Baking. After the primary (LOR) resist coating on Si wafers, each of the LOR photoresists is baked at 150 °C on a hot plate as recommended in [182] with various times from 5-8 min. Then the secondary (S1818) resist is spin coated, and it is baked at 115 °C for 3 min [149], [183]. Owing to the insolubility of the photoresist solvents in the LOR resists, they do not intermix with the S1818 layer when it is baked properly [16].</p>	 <p>A 3D perspective diagram showing the substrate with the bilayer photoresist on a blue "Hot Plate". Wavy lines above the substrate represent heat being applied during the baking process.</p>
<p>D. Photoresist Exposure. The pattern from the photomask is then transferred to the coated substrate via UV exposure by a mask aligner (MA6, Karl SUSS, Germany). The exposure time varies with the resist thickness. A thicker resist requires longer exposure time to ensure that the photoresist becomes soluble. Thus, exposure times ranging from 6-10 sec have been used for the present works.</p>	 <p>A 3D perspective diagram showing the substrate with bilayer photoresist. A "Photomask" is positioned above it. Green arrows labeled "UV Light Source" point downwards through the photomask onto the substrate.</p>

Process step	Diagram
<p>E. Development of resist. After exposure, the substrate is then immersed in a beaker of MF319 (Metal-Ion-Free) developer (Micro hem Corp., USA). The exposed resist is dissolved and the resist profile, including the array element pattern is developed on the substrate. It should be noted that the beaker must be mildly agitated by hand for a few times to ensure that the resist is completely dissolved.</p>	 <p style="text-align: center;">Substrate</p>
<p>F. Metallisation. Prior to metal deposition, surface cleaning using a plasma etcher (PlasmaFab 505 Barrel Asher, UK) at 150 watts for 1 min is needed to ensure that the exposed region is sufficiently clean and to promote good adhesion of the deposited metal to the surface. Metal deposition is carried out using a Plassys MEB 550S electron beam evaporator with a high vacuum, beyond <math>1 \times 10^{-6}</math> mbar to deposit thin films of Ti and Au across the substrate.</p>	 <p style="text-align: center;">Substrate</p> <div style="display: flex; align-items: center; margin-top: 10px;"> <div style="width: 20px; height: 10px; background-color: red; margin-right: 5px;"></div> <span><b>Ti/Au</b></span> </div>
<p>G. Lift-off process. The substrate is immersed in resist remover to complete the resist strip off. These wafers are immersed in either 1165 or SVC-14 removers (Rohm and Haas, Philadelphia, USA), depending on the type of the substrates. In the final step, a plastic pipette is used to gently blow the stripped resist and residual metal from the surface to ensure that they are no longer present in the vicinity of the array element.</p>	 <p style="text-align: center;">Substrate</p>

## 4.5. Thinning, Releasing and Wax Removal

The composite with the array elements on one surface was lapped to achieve the required thickness ( $\sim 50 \mu\text{m}$ ) for operating at 30 MHz. The surface with the elements must be against the glass carrier to reduce the thickness and expose the pillars from the opposite side. Quartz wax was melted at  $60 \text{ }^\circ\text{C}$  onto the glass carrier sitting on a hot plate. The melted wax was evenly spread to become a thin layer using a steel scraper. The carrier was removed from the hotplate and allowed to cool down for a few seconds before adhering the sample to minimise the epoxy deformation. The thinning step was again achieved with a PM5 lapping machine using the process steps 1-3 as previously presented in Table 4.8. When the sample thickness approaches  $20 \mu\text{m}$  before achieving the required thickness, gradual lapping with  $3\text{-}\mu\text{m}$  abrasive and the slow speed are necessary to relieve the stress in the thin composite and to prevent it peeling off. After achieving the desired thickness, the release and wax removal steps were completed by melting the wax and immersing the sample it in solvent, e.g., IPA and Ecoclear (Logitech, Glasgow, UK) as shown in Table 4.10.

Table 4.10 Parameters for composite release and wax removal after lapping.

	Wax melting	Solvent immersion		
Process	1	2	3	4
Temperature (°C)	65	50	$T_R$	$T_R$
Time (min)	3	50	15	Overnight
Solvent	IPA needed for wax removal	Ecoclear	Ecoclear	Ecoclear

## 4.6. Poling

Unpoled piezoelectric materials must undergo a poling process to orientate dipole moments before they can be used. Whilst poling, the dipoles are aligned along the direction of an applied electric field. Once the field is removed, the dipoles are retained approximately in the direction of the applied field. Consequently, the material obtains a permanent polarization and exhibits piezoelectricity.

Before poling, the surface of the composite array opposite that of the array element was coated with Ti/Au (20/180 nm and 30/470 nm) via the Plassys MEB 550S electron beam evaporator to form the ground connection for this process.

Contact poling was used to pole bulk gel cast material. Prior to poling, the sample must have electrodes deposited on both sides using a Peltier cooled sputter coater (Emitech K575, Emitech Ltd., UK) for gold coating at 80 mA for 1 min. This process provided a gold electrode 100 nm thick. This conventional poling process is generally performed in an oil bath to distribute the heat which aids the reorientation of the dipoles and also provide an insulating medium to minimise dielectric breakdown and electrical shorting as, shown in Figure 4.6. The sample was preheated in the oil bath at 100 °C, and voltage of 10kV/mm was applied to the samples for 30 min.

The composite materials were poled using a custom corona poling equipment (AFM Ltd, University of Birmingham, Birmingham, UK) to prevent scratching of the composite of electrode surfaces which may have occurred with a contact poling pin [50], [95]. Each sample to be poled was flattened and held in place with a silica ring and copper plate as shown in Figure 4.7 (a), then placed at the center of an enclosed chamber as displayed in Figure 4.7 (b).

In the case of composite for a SET, a temperature of 110 °C was employed to aid the alignment of the dipoles. This high temperature was not used for the composite arrays since it had the potential to damage the electrical connectivity of the array elements by deforming the epoxy. A high voltage of 30 kV applied at a rate of 1 kV/min was slowly applied to prevent electric shock to the material. At a certain voltage, a corona discharge was created from the corona tip and impinged onto the surface of the sample. The voltage was held at this value for 15 min.



Figure 4.6 Equipment set-up for contact poling using a power supply of 5 kV and silicone oil heated by a hotplate. A guard was used in front of the hotplate during the poling process.

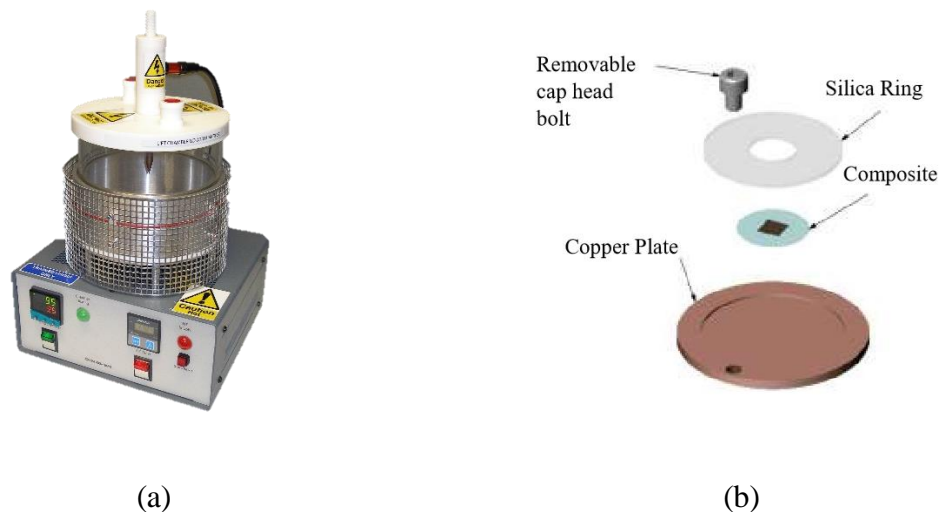


Figure 4.7. (a) The custom corona poling equipment for non-contact poling of 1-3 composites (b) the assembly for holding a sample in place using a silica ring and copper plate. (reprinted from Ref. [50]).

## 4.7. Characterisation Techniques

### 4.7.1. Characterisation of Gel-Cast Material

As described in Section 4.2.1, the 1-3 randomised composite is a material fabricated in-house using gel casting. Prior to forming the composite structure, the powders, rheology of slurry,

and the physical, mechanical, functional, structural and microstructural properties of bulk gel cast samples were investigated.

Particle size distribution and specific surface area of as-received and milled PZT powders from both batches were characterised by a particle size analyser, and a Brunauer–Emmett–Teller (BET) analyser, respectively. The crystallinity of as received and milled PZT powders from batch 2008 was only characterised using X-ray diffraction, XRD, due to an availability of the XRD. These steps are necessary to ensure that the crystalline material does not change after prolonged milling and the particle size of the milled powder is sufficiently fine and suitable for casting into the mould cavities. The rheology of the gel-cast slurries prepared from the PZT powder batch 2002 was determined by using an AR 500 rotational rheometer (TA Instruments, DE, UK) to observe the viscosity and gelation of the slurries before casting. Ten specimens of a bulk gel cast material were also tested to investigate the physical properties, including drying and sintering shrinkage, density, and green strength.

### **X-ray Diffraction Analysis**

The milled powder and sintered bulk samples were placed in a sample holder. An X-ray diffractometer (ARL Equinox 3000, Thermo Fisher Scientific, UK) was used to examine the phase, composition and crystallinity of a sample using Cu-K $\alpha$ 1 radiation with a wavelength of 1.54056 Å at incident and reflection angles ( $2\theta$ ) of 15° - 90°. The intensity spectra were analysed to match the ICDD (International Centre for Diffraction Data, Newton Square, USA) PDF-2 database.

### **Particle Size Analysis**

Particle size measurement of the PZT powders was carried out using a laser diffraction particle size analyser (Sympatec, Bury, UK) integrated with sonication via an ultrasonic bath. Suspensions of 0.5 g of as-received PZT and milled PZT powders were mixed with 3 g of distilled water and two drops of Na<sub>4</sub>P<sub>2</sub>O<sub>7</sub> dispersing agent (Merck, Dorset, UK) in a Vycor glass container. After dropping the suspension into the bath, sonication worked automatically for 15 seconds to break down any particle agglomerates. The instrument uses a laser beam which is scattered and diffracted by the particles distributed in the water. The angle of scattered light is detected by a series of detectors, the angle being inversely proportional to particle size, indicating that the smaller the particle size, the larger the angle of light scattering.

## Specific Surface Area

The specific surface area (SSA) of milled PZT powder (TRS Technologies, PA, USA) was measured. SSAs of all the milled powders from both studies were characterised by the same equipment which is a BET single point nitrogen absorption analyzer (Micromeritics Area ASAP2010c, Norcross, USA).

## Viscosity Measurement

The rheology behaviour of a 1.2- $\mu\text{m}$  PZT slurry derived from the batch no. 2008 and the effect of dispersant concentrations and quantity of resin on the flowability of the slurries was well studied previously [50]. Thus, the optimised slurry preparation from the previous work was used again in the present study. However, the viscosity and gelation time of the milled PZT slurries derived from the batch no. 2002 were also observed directly to ensure that the slurries had good flowability before casting into the complex cavities of the randomised PDMS mould.

The viscosity and gelation time of the milled PZT slurries derived from the second batch were measured using an AR 500 rotational rheometer (TA Instruments, DE, UK). This was carried out using a cone and plate geometry with a 40 mm diameter cone, a cone angle  $2^\circ$  and a gap of 55  $\mu\text{m}$ , uniformly rotating against a flat measuring plate. The slurries were dropped onto the centre of the measuring stage, then the cone was lowered down until reaching the required gap. The slurries were presheared for 10 sec before measurement in the shear mode with a shear rate in the range  $0.1\text{-}600\text{ s}^{-1}$  at  $22\text{ }^\circ\text{C}$ . The gelation time of the slurries was investigated by measuring the viscosity behavior as a function of time at a shear rate of  $0.1\text{ s}^{-1}$  at  $22\text{ }^\circ\text{C}$ .

## Drying and Sintering Shrinkage

Ten specimens of the green samples with diameters of  $\sim 12\text{ mm}$  and thickness  $\sim 3\text{ mm}$  were used by digital Vernier caliper (Absolute, Mitutoyo, range  $0\text{-}160\text{ mm}$ , resolution  $0.01\text{ mm}$ ) to measure the linear shrinkage before and after sintering as follows:

- Drying shrinkage measurement (LD)

$$\text{LD} = \frac{D_M - D_d}{D_M} \times 100 \quad \text{Eq. 4.1}$$

where  $D_M$  is diameter of the soft mould;  $0.013\text{ (m)}$   
 $D_d$  is the diameter of the dried gel-cast bulk sample  $(\text{m})$

- Sintering shrinkage measurement (LS)

$$L_s = \frac{D_d - D_s}{D_d} \times 100 \quad \text{Eq. 4.2}$$

where  $D_d$  is diameter of the dried gel-cast bulk sample (m)  
 $D_s$  is diameter of the sintered sample (m)

### Density Measurement

The density of ten sintered bulk samples of PZT was measured with an analytical balance (ABS 320-4N, Kern, SciQuip Ltd., Shropshire, UK, measure range 300 g, readability  $\pm 0.1$  mg) using the Archimedes principle [184] described as follows:

$$\rho = \frac{W_1}{W_2 - W_3} \quad \text{g.cm}^{-3} \quad \text{Eq. 4.3}$$

where  $W_1$  is dry weight of sample (g)  
 $W_2$  is the weight of sample after fluid impregnation (g)  
 $W_3$  is the weight of sample after fluid impregnation while immersed in DI water (g)

### Green Strength

Twenty specimens of the green gel cast were cast into rectangular bar with dimension of 45 mm length  $\times$  4 mm width  $\times$  3 mm thickness and used to investigate the green strength. This measurement was carried out using an Instron testing machine (Instron, Buckinghamshire, UK) with a three-point bending technique. All the measurements used a 1 N load cell, a span length of a specimen of 30 mm, and crosshead speed of 1 mm/min. The flexural strength,  $\sigma_f$ , was determined by a following equation:

$$\sigma_f = \frac{3PL}{2bd^2} \quad \text{MPa} \quad \text{Eq. 4.4}$$

where  $P$  is fracture load (N)  
 $L$  is the span length (m)  
 $b$  is the width of sample bar (m)  
 $d$  is the thickness of sample bar (m)

## 4.7.2. Surface Characterisation

### Thickness Variation using Contact Profiler Dektak XT

In the manufacturing of piezocomposite, thickness variation caused by epoxy bumps is often found, particularly at the interface between the composite and fan-out epoxy, because the composite is composed of two materials with different mechanical properties [177]. Thus, thickness variation across the composite surface and at the interface between the composite

and the surrounding epoxy was measured using a contact height profiler (Dektak XT, Bruker, Coventry, UK). This equipment provides vertical resolution in range of 0.01 – 6500 nm. A thickness profile measurement of a 2D scan in the x and y directions was obtained by applying a force of 3 mg to a 2- $\mu\text{m}$  stylus tip with a scan length of 500 and 1500  $\mu\text{m}$ , providing resolutions of 0.1 and 0.02  $\mu\text{m}$ , respectively. In the composite region, one of each composite was used to explore the thickness variation, while three samples with two measurements for each composite were employed to examine the variation at the interface.

### **Surface Roughness using Optical Profiler Contour GT**

The surface roughness,  $R_a$ , of the composites was measured using a Contour GT-X 3D Optical Microscope (Bruker, Coventry, UK) with a maximum vertical resolution of 0.05 nm and a sample stage with automatic self-calibration. Five samples and three areas of 0.134 $\times$ 0.177 mm<sup>2</sup> across composite surface were employed to determine  $R_a$  of the composite.

### **4.7.3. Microstructure Characterisation**

#### **Optical Microscope**

During the microfabrication process in a clean room, James Watt Nanofabrication Centre, an optical microscope (Nikon Eclipse LV150, Nikon, Japan) was used to study resist profiles after development, and to observe the definition and deformation of the deposited metal on composite substrates.

#### **SEM**

For the 1-3 randomised composite, the morphology of the material powders and the bulk ceramic and the microstructure of the 1-3 composites were observed with a scanning electron microscope (SEM, JSM6060, Jeol, Tokyo, Japan). The samples were preheated in an oven at 60 °C for 30 min to remove humidity that can result in a poor resolution image. The samples were then placed into a Peltier cooled sputter coater (Emitech K575, Emitech Ltd., UK) for gold coating at 80 mA for 2 min before scanning images. Another SEM (S4700, Hitachi, Japan) was employed to observe the resist thickness and metal film on silicon wafers. The samples were coated using an automatic sputter coater (Agar Scientific, Essex, UK) for 30 sec before imaging.

## 4.8. Interconnect, Transducer Packaging, and Cabling

### Interconnect and Transducer Packaging

The composite array must be electrically interconnected and packaged for use. The design of the array elements with fan-out patterns proposed here allows the transducer packaging to be assembled in ways equivalent to designs used in commercial transducers, where the array elements are interconnected and secured at the rear of the transducer, while the ground side of the active element (composite) is facing forward, allowing direct contact with human tissue.

Details of the complete interconnects and transducer assembly procedures used in the present work are given in Table 4.11. A 42 awg micro-coaxial cable (9442 WH003 Alpha wire, Farnell, UK) 60 cm in length was connected to a 0.5 mm pitch trace on a Cabline<sup>®</sup>-VS plug (Figure 4.8) by soldering. The braided shield of each wire was split, and all the shields were bunched together for the ground connection. Owing to the difficulty in obtaining a delivery of the Cabline<sup>®</sup>-VS mating set during the global pandemic, there were only three example sets provided (I-PEX EUROPE SARL, Tremblay en France, France). Thus, three completed plugs with soldered 42 awg cables were assembled by an experienced staff member. The electrical joints and bunch of braided shields were secured with rapid curing adhesive (Araldite 90, Araldite, Glasgow, UK), producing a bulb of the adhesive over the soldered signal wires. For this reason, the pull bar normally used in the connector (Figure 4.8 (c)) was not assembled.

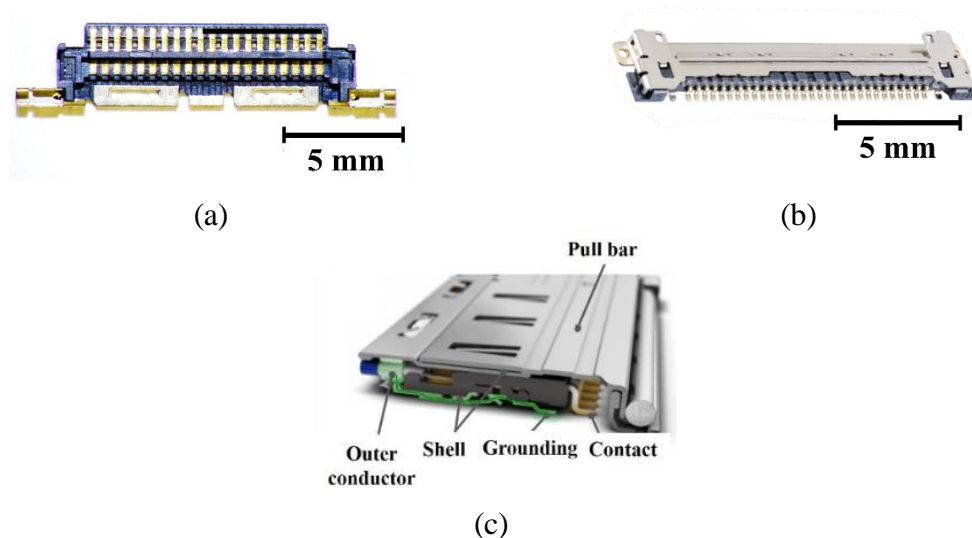


Figure 4.8 An overview of Cabline<sup>®</sup>-VS (a) plug (b) receptacle and (c) set (I-PEX Inc., Kyoto, Japan).

The other ends of the micro-coaxial cables were bunched together for insertion through a braided tinned Cu shield with a diameter of 7 mm, before stretching. In the prototypes, the

shield was used as a ground connection from the composite array to the plug, represented as an independent ground wire in Figure 4.9. Each micro-coaxial cable was trimmed to expose the signal wires using a scalpel and then connected to the individual element pads using a conductive Ag-epoxy (ICA) bump (MG Chemical, RS Component, Northants, UK). Further Araldite was employed to secure the electric joint to ensure it would not break while bending the cable up to  $90^\circ$  to put the housing in place and allow fabrication of the backing layer.

15 VF% W loaded epoxy was used as the backing layer to support the composite and reduce US reverberation. This composition does not reduce the sensitivity by too much because it possesses  $Z_a$  6.3 MRayl, which is lower than that of the active materials. However, axial spatial imaging resolution is sacrificed due to the production of a long wavelength, as described in Section 2.5.1. More importantly, the practical process was also considered, with the low W VF% providing good flowability for ease of casting and low agglomeration of W particles to prevent US reflections, which would cause image artifacts [43].

For the preparation of the backing material, Epofix resin and hardener were initially mixed before adding  $5\ \mu\text{m}$  W powder (Alpha Aesar, Heysham, UK). The mixture was degassed for 20 min prior to casting it in place in the housing. The entire assembly was cured at  $T_R$  overnight before completing the packaging. The final thickness of the backing layer was approximately 2 mm. A schematic diagram of a complete transducer assembly is shown in Figure 4.9 and complete  $\mu\text{US}$  arrays are presented in Figure 4.10.

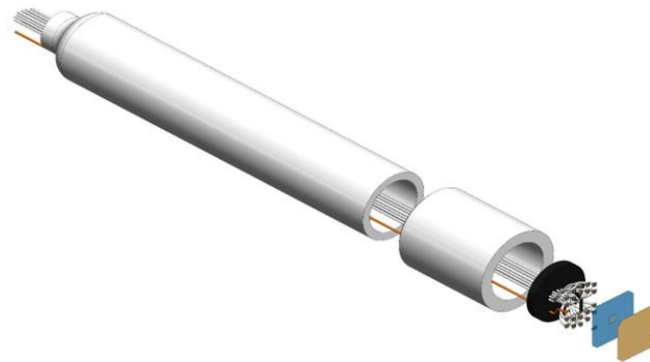
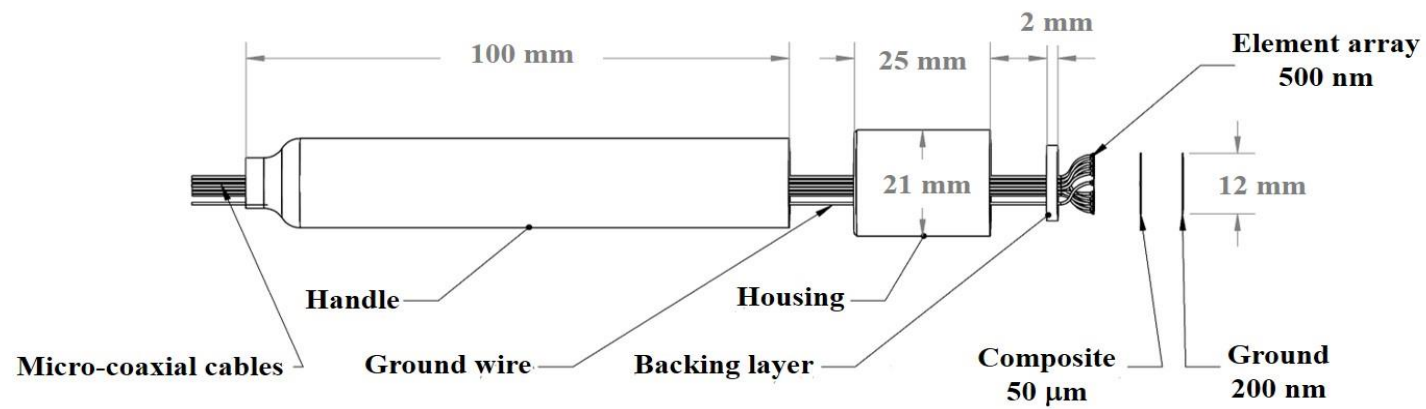
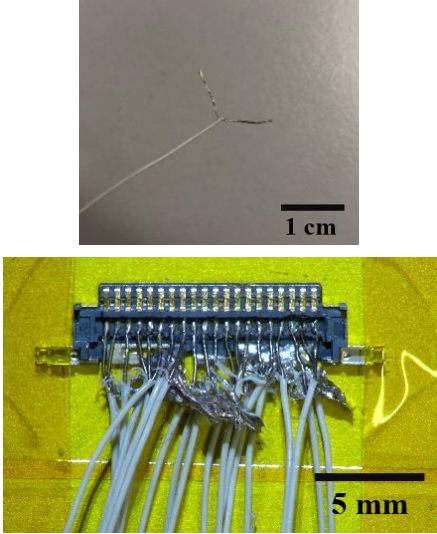
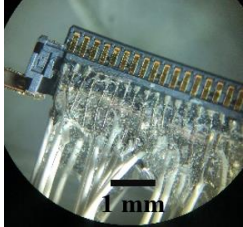
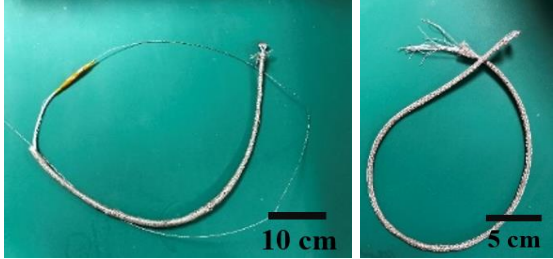
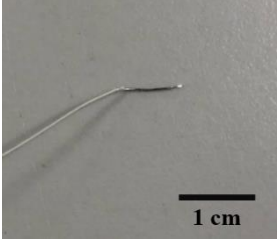
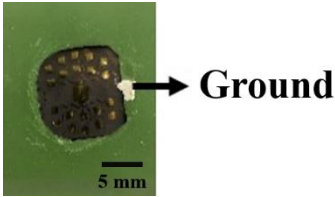
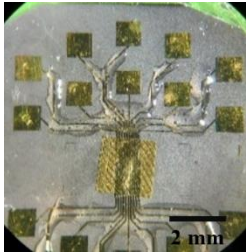
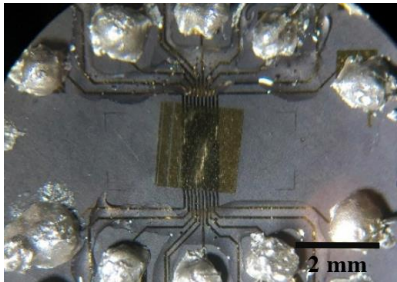
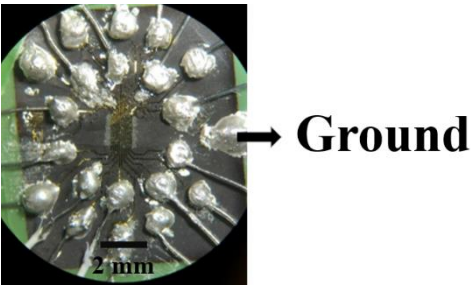
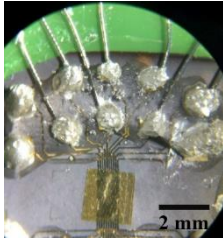
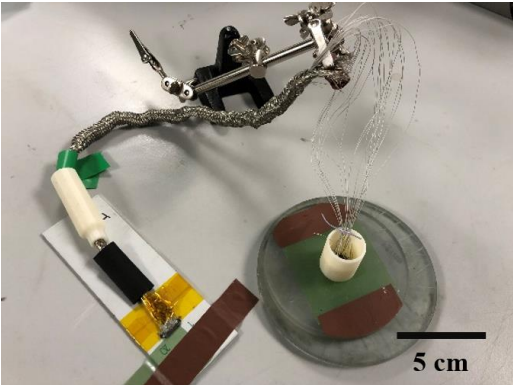
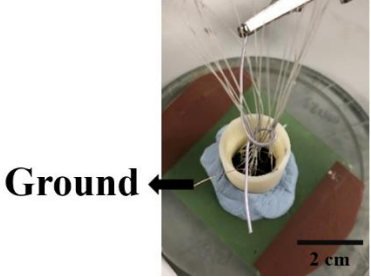
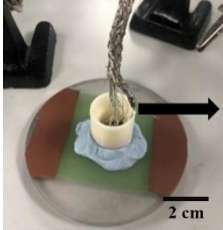
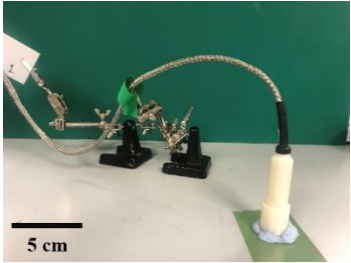
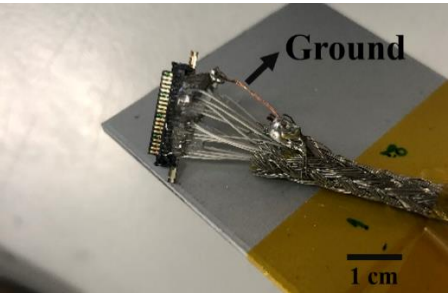


Figure 4.9 An expanded view of the complete composite transducer assembly and components, with an independent ground wire represented as a braided tinned Cu shield used in the final prototype.

Table 4.11 Process diagram of interconnect for  $\mu$ US composite transducer arrays.

Process	Diagram
<p>A. A number of signal conductor wires are split from a braided shield by a scalpel. Each signal wire is then individually soldered onto each element trace on a 0.5 mm pitch plug until 20 connections are completed. The braided shields of 20 micro-coaxial cables are bunched together by soldering and connected to the metal sheet on the plug to establish a good ground connection to the equipment.</p>	
<p>B. The electric joints are secured by Araldite which is cured within 90 sec.</p>	
<p>C. The other end of the micro-coaxial cables is bunched together with a robust wire by soldering in order to insert the group of cables through a braided shield. After insertion, the thicker support wire is then cut off, leaving the micro-coaxial cables in position.</p>	
<p>D. Heat shrink, the additively manufactured handle and the housing are inserted through the hose beforehand. Each cable is checked for electrical continuity and numbered.</p>	
<p>E. A group of signal conductors are split from the braided shield by a scalpel for connection to the element pad.</p>	

Process	Diagram
<p>F. The ground connection is created by painting a track of conductive Ag paint from the ground side of the substrate to the array side. After drying at <math>T_R</math>, the electric connection is then tested for continuity. The composite array is adhered onto green tape, then attached onto a glass carrier, facing upward for establishing the interconnects.</p>	
<p>G. Fan-out electrodes are secured by Araldite adhesive to prevent scratching from subsequent steps. The Araldite is cured at <math>T_R</math> for 1 hr to ensure that it is completely cured.</p>	
<p>H. Ag-epoxy part A and B (ICA) are mixed in a ratio of 1:1. An ICA bump is put on each element pad using a toothpick.</p>	
<p>I. The cables are attached to the 20 element pads via the conductive bumps and one ground connection is established.</p> <p>The entire assembly is cured overnight at room temperature.</p> <p>Note: After curing overnight, the electric connection of each element was electrically tested from the pad to the trace on the plug by a multimeter as well as between each bump to ensure that there were no short circuits.</p>	
<p>J. The ICA electrical joints are secured by Araldite adhesive to improve the strength for subsequent steps. The Araldite is cured at <math>T_R</math> for 1 hr to ensure that it is completely cured.</p>	
<p>K. The wires are gently lifted and bent by 90° before placing the housing in position. The housing is fixed in place by putty to prevent any leakage of the backing layer through to the front of the package assembly during casting.</p>	

Process	Diagram
<p>L. The backing layer mixture is cast into the housing by injection using a syringe and a needle. The entire assembly is cured at room temperature overnight.</p>	
<p>M. The ground wire is then connected to the shield by soldering to provide a ground connection from the front of transducer to the connection plug.</p>	
<p>N. An additively manufactured handle is joined to the housing using the Araldite adhesive, followed by a mixture of Epofix epoxy for additional bond strength. Heat shrink is then placed behind the handle to secure the wire braid in place.</p>	
<p>O. A wire is soldered from the braid to the ground connection on the plug.</p>	

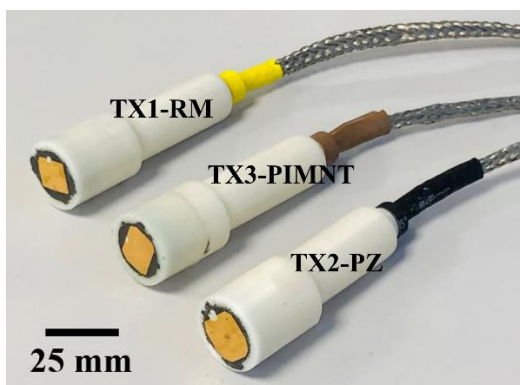


Figure 4.10 Photographs of the 20-element composite  $\mu$ US transducer array prototypes.

### Cabling

During functional testing, the transducer must be driven by a pulser-receiver for ultrasound imaging. In this study, a Vantage 128 High Frequency research US system (Verasonics, Kirkland, WA, USA) with 32 independent channels in both transmission and reception (UTA

160-DH/ 32 Lemo, Verasonics, Kirkland, WA, USA) was used to drive the transducer at a particular voltage amplitude and to receive signals. Thus, a break-out board with 20-channels and custom-made coaxial cables with Lemo connectors (Lemo UK Ltd., West Sussex, UK) was assembled in-house as show Figure 4.11 (a) for the electrical connection between the 20 array elements transducer and the Verasonics equipment. A braided shield was soldered onto one Lemo connector for the ground connection. A 20-way receptacle was soldered onto a breakout board as shown in Figure 4.11 (b), and the other side had 20 pins to plug in to the Verasonics cables.

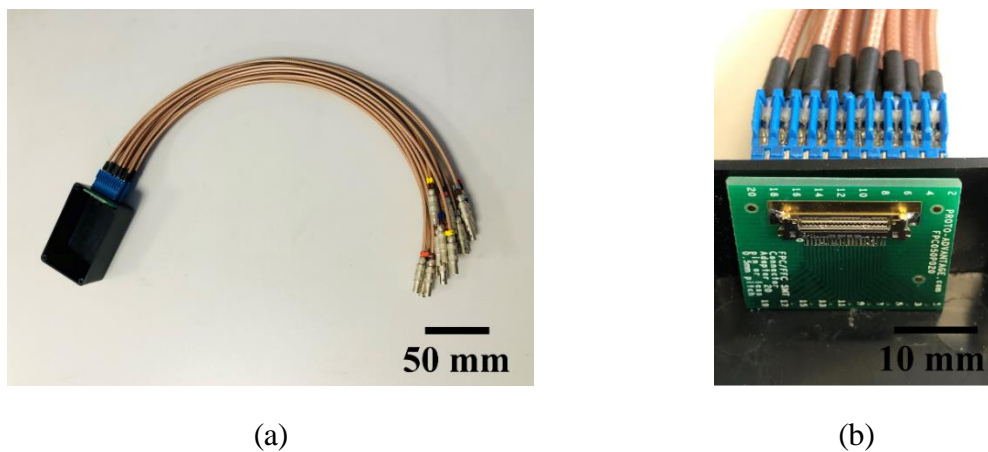


Figure 4.11 Photographs of (a) 20-channel custom-made cables (b) a 20-way receptacle soldered onto a breakout board.

## 4.9. Transducer Functional Testing

### 4.9.1. Dielectric Measurement

Capacitance and the dielectric loss of unpoled bulk and 1-3 randomised composite material fabricated from gel casting method and poled 1-3 diced piezocomposites were measured using an impedance analyser (4294A, Keysight, CA, USA) with frequency ranging from 40 Hz - 110 MHz. The capacitance,  $C$ , and dielectric loss were measured at 1 kHz and relative permittivity ( $\epsilon_r$ ) was then calculated by using Eq. 2.18. The unpoled material is usually employed to measure the capacitance for providing information on the intrinsic permittivity. The 1-3 diced piezocomposites made with the PZ54 ceramic and PIMNT single crystal piezoelectric materials were poled by the suppliers. For this reason, the measured capacitance and permittivity of the materials may be different to those of the unpoled material [185]–[187].

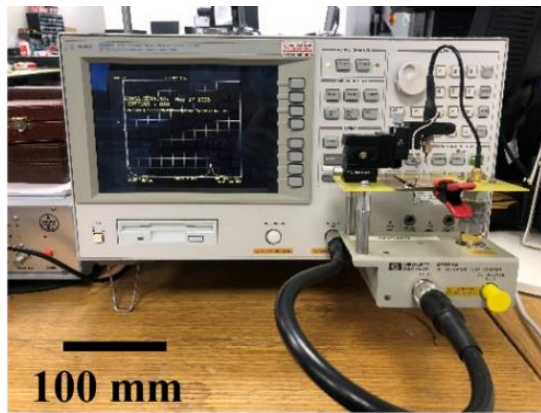
## 4.9.2. Electrical Impedance Spectroscopy

The impedance magnitude and phase of the composite arrays was measured by an Agilent 4395A impedance analyser (Keysight, CA, USA) with frequency ranging from 10 Hz - 500 MHz, Figure 4.12 (a). Before measurement, a ground connection electrode with a metal thickness of 200 nm was made on the front of the composite arrays by the Plassys IV evaporator. Each sample was placed face down against a bespoke Au-coated stage acting as a ground in the set-up as demonstrated in Figure 4.12 (b).

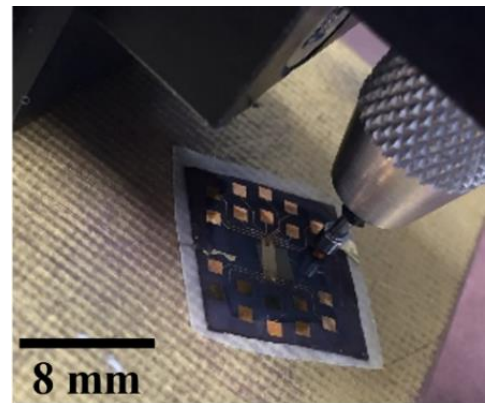
The electrical impedance spectra can be used to determine  $f_r$ ,  $f_a$  and  $k_{eff}$ , of the device, as expressed in Eq. 2.19. In addition, frequencies in range 200 – 300 kHz was also employed to determine the planar electromechanical coupling factor,  $k_p$ , for a disc material from the following equation:

$$k_p = \sqrt{2.51 \times \left(\frac{f_a - f_r}{f_r}\right) - \left(\frac{f_a - f_r}{f_r}\right)^2} \quad \text{Eq. 4.5}$$

where  $f_a$  is maximum impedance frequency (anti-resonance frequency) (Hz)  
 $f_r$  is minimum impedance frequency (resonance frequency) (Hz)



(a)



(b)

Figure 4.12 (a) Experimental set-up with an impedance analyser and (b) a probe measurement on a fanout pad.

## 4.9.3. Electrical Continuity

Current-voltage characteristic curves were obtained using a Summit 12000 probe station (Cascade Microtech, Oregon, USA) (Figure 4.13 (a)) to determine electrical continuity of individual elements. This method enables to identify which element is active or inactive element. The front of the composite array was placed face down on a glass plate. The plate was then placed onto a vacuum chuck before measurement. Microprobes were directed to the element pad and the end of the element (Figure 4.13 (b)), respectively, with applied drain

voltages of  $\pm 500$  mV to measure the continuity along the length of each element. In addition, this set-up could also identify discontinued or broken connections in elements, as illustrated in Figure 4.13 (c).

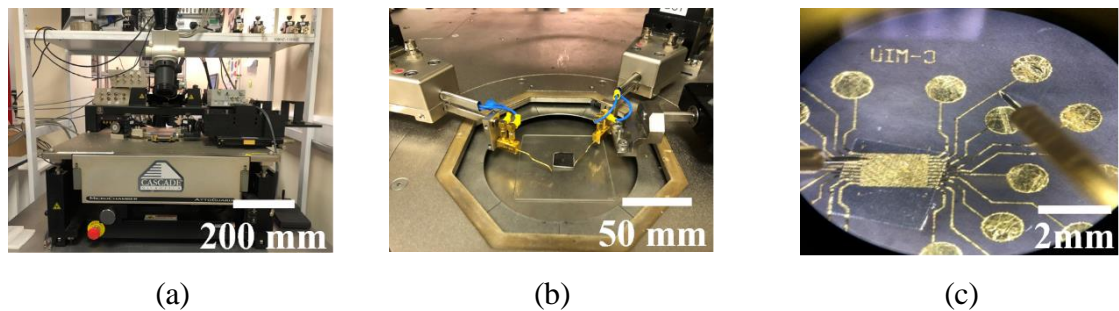


Figure 4.13 (a) A Summit 12000 probe station, (b) microprobes and (c) element measurement.

#### 4.9.4. Pulse-echo Response Measurement

The pulse echo response of the  $\mu$ US arrays was tested using a Vantage 128 High frequency research ultrasound system (Verasonics, Kirkland, WA, USA). The equipment set-up for pulse-echo response measurement is shown in Figure 4.14. A flat piece of quartz, 5 mm thick was employed as a target. The transducer and the quartz were submerged in a water bath filled with deionized water. The echo signal was measured for all 20 elements of each array individually at a distance of 5 mm because the array TX1-RM provides minimum focal length of 8.2 mm and the TX2-PZ and TZ3-PIMNT provide 20 and 17 mm, respectively, in accordance with Eq. 2.9. These relatively large distances are a function of the very short US wavelengths at their operating frequencies.



Figure 4.14 Experiment setup for measuring the pulse-echo response.

## 4.10. Finite Element Analysis

3D models of 1-3 piezocomposites and transducers were implemented by means of FEA using Onscale (CA, USA). These models were investigated as preliminary studies to gain better understanding of how spurious modes are generated in 1-3 composite with repetitive and symmetrical structure, and interfere with the resonance frequencies, and how the composite structures influence transducer performance. The 1-3 piezocomposite models were constructed, Figure 4.15 (a), to determine  $k_{eff}$  as previously described in Eq. 2.19, and to investigate the electrical impedance characteristics influenced by material displacement at certain frequencies. For the functional properties of the transducers, models were built up with water as the medium to analyse the axial resolution and bandwidth response from the voltage output in the frequency domain.

In practice, pillar geometry for dice-and-fill composites is dictated by the kerf of 13  $\mu\text{m}$ , which originates from and is limited by the nominal value of the smallest blade available, a 10  $\mu\text{m}$  blade. Therefore, the pillar geometry and spacing in the FEA model were set based on the piezocomposites manufactured in practice. The mesh (element) size defines the model resolution. The accuracy of results is increased by decreasing the element size. However, the computation time and memory requirements are also increased since a larger number of elements is required in the model if each element is smaller. Generally, 15 elements per wavelength is considered acceptable in FEA. The details of the FEA model for the 1-3 piezocomposites and the transducers, fabricated from PZ54 and PIMNT29 piezoelectric materials, in a water load are provided in Table 4.12.

Complete sets of material properties, including piezoelectric, dielectric, and mechanical properties, of semi hard PZ54 ceramic and PIMNT29 single crystal were used to implement the FEA model. These were provided by Meggitt Ferroperm (Kvistgaard, Denmark) and TRS Technologies Inc. (PA, USA) as given in Appendix II. For the 1-3 piezocomposite model, symmetry boundary conditions were applied to x and z axes to avoid edge effects. Boundaries in the thickness dimension (y axis) were set to be free, with no external forces in the composite model. For a transducer in water, the lateral sides were also set as symmetrical boundaries. The fixed boundary was used at the maximum coordinate in the y-axis to achieve a full reflection of the ultrasound waves. The back of the transducer was set as an absorbing boundary, so that acoustic waves passing through the boundary are not reflected.

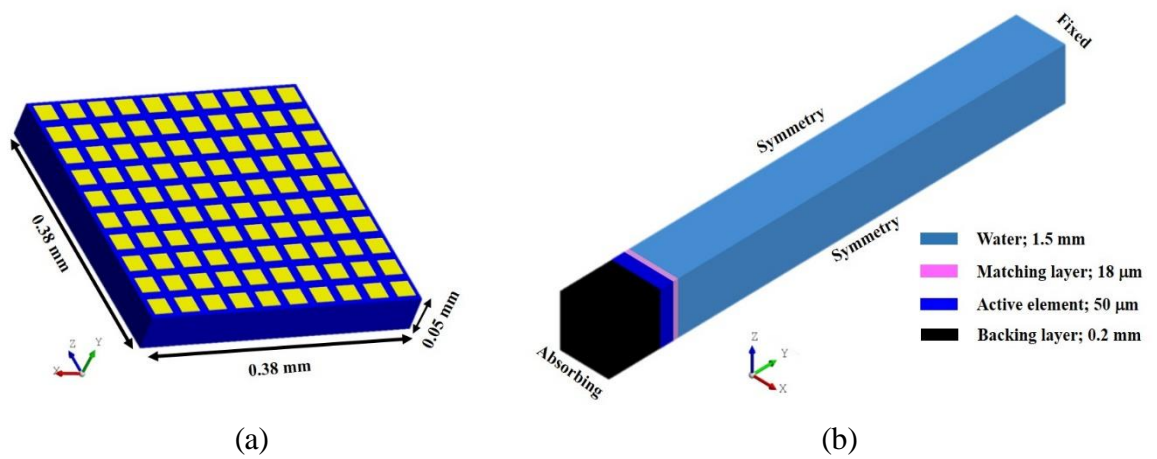


Figure 4.15 Onscale 3D models of (a) a sample of 1-3 piezocomposite material with pillar width of 25  $\mu\text{m}$  and (b) a miniaturised transducer with assigned components in a water load with boundary conditions as indicated.

Table 4.12 FEA model parameter set for 1-3 diced piezocomposite material made with the dice-and-fill technique for  $\mu\text{US}$  linear arrays.

<b>1-3 piezocomposite material</b>	
Operating frequency (MHz)	32 and 27 MHz
Active material	PZ54, PIN-PMN-29%PT (PIMNT)
Passive material	Epofix Sptruers
Size constraint	0.38 mm width $\times$ 0.38 mm length $\times$ 0.05 mm thick Pillar size: 25 x 25 x 50 $\mu\text{m}$
Composite structure	Kerf width: 13 $\mu\text{m}$ Volume fraction: 43% Aspect ratios: 1.92 and 2.2, respectively
Mesh size	15
Boundary	x minimum: symmetry x maximum: symmetry y minimum: free y maximum: free z minimum: symmetry z maximum: symmetry

Transducer Model	
Load material	Water
Backing layer	Thickness: 1.5 mm Material: Tungsten loaded epoxy with 15% VF Thickness: 0.2 mm $Z_a$ : 6.3 Mrayl
Mesh size	15
Boundary	x minimum: symmetry x maximum: symmetry y minimum: absorbing y maximum: fixed z minimum: symmetry z maximum: symmetry

#### 4.11. Summary

Chapter 4 has described the manufacturing processes used to produce three types of  $\mu$ US arrays, based on 1-3 connectivity randomised PZT ceramic, diced PZ54 ceramic, and diced PIMNT single crystal piezocomposites. The randomised piezocomposites were made by the combination of gel casting and micromoulding techniques, whilst the diced piezocomposites were made by modified dice-and-fill methods. In the gel casting process, numerous phases of characterisation were required to ensure that the final products fabricated using this method were relatively high quality, particularly, achieving a high green strength in order to withstand subsequent processes. Modified dice-and-fill methods which were suitable for the manufacture of 1-3 diced piezocomposites from PZ54 ceramic and PIMNT single crystal were demonstrated. In addition, FEA models based on practical works of the diced composites were described to investigate electrical impedance characteristics and spurious modes, the results of which are given in detail in Chapter 5.

In 1-3 piezocomposite fabrication, epoxy curing at elevated temperatures was highly recommended to enhance environmental resistance to the subsequent processes. Surface planarization was also necessary to improve the surface finish prior to patterning the fine array elements onto the composite substrate. Poor  $R_a$  and high thickness variation at the interface between the composite and the fan-out epoxy may cause element delamination in the subsequent processes if care is not taken. To improve  $R_a$ , the fan-out epoxy must be reduced in size in order to maximise the pressure applied onto the composite area, allowing it to be polished effectively.

Array elements were photolithographically defined on the composites by a bilayer lift-off process, which has advantages in facilitating resist dissolution and producing smooth edges of the metal film. The effect of different primary resist thicknesses on the yield of active elements and validated and optimised processes for each substrate are presented and discussed in Chapter 6. After the composite arrays were lapped to the required thickness, the means of sample releasing from a lapping glass carrier and wax removal as well as their results are also discussed in Chapter 6.

Prior to transducer packaging, electrical impedance spectroscopy and electrical continuity were used to identify both the active and inactive elements in the composite arrays. In addition, the former was used to observe the electrical impedance characteristics and the presence of spurious modes, and to determine  $k_{eff}$ . The devices have been designed in ways equivalent to commercial transducers. The design of array elements with fanout pads allows composite arrays to be interconnected and secured within an additively manufactured housing from the rear of the device and with the ground side facing forwards for direct contact with tissue. The devices were operated with a commercial research array controller through micro-coaxial cables attached with ICA bumps on fan-out pads and a break-out board to determine their performance through a basic measurement of pulse-echo response.

# Chapter 5 Composite Fabrication

## 5.1. Introduction

A key objective of the work described in this thesis was to fabricate 1-3 randomised piezocomposites with feature sizes of 2 - 50  $\mu\text{m}$  using the novel approach of gel casting associated with soft micromoulding processes for  $\mu\text{US}$  linear array transducers, and to compare them with other two piezocomposites made with more conventional approaches.

Piezoelectric materials used in this present work comprise PZT5H powder for the randomised ceramic composites, PZ54 ceramic and PIMNT single crystal wafers for manufacturing 1-3 diced composites with symmetrical square pillars and a pillar pitch of 38  $\mu\text{m}$  via modified dice-and-fill methods. In term of piezoceramic materials, the PZT5H provides higher  $\epsilon_r$ ,  $d_{33}$ , and  $k_t$  than those of the PZ54 (Section 2.7.2) since the former is categorised as a soft PZT material which is poled more easily than the semi-hard PZ54. So, the functional and acoustic properties of an US transducer made with the PZT5H are aimed to be a slightly greater than the one made with the PZ54. However, the PZ54 is selected for an investigation of the optimal parameters used in the dice-and-fill process prior to transferring to the single piezocrystal material because of a lack of availability of the material. Among piezoelectric materials used in this present work, the PIMNT possesses excellent properties, especially, highest  $k_{33}$  of 0.9 (Section 2.7.3), so it is expected that it can improve bandwidth and sensitivity of US transducers. Nonetheless, the overall performance of the transducers is not only affected by the electrical properties, but it is also dependent on physical characteristics such as  $VF$  of piezoelectric material and  $AR$ , as discussed in Section 2.7.7.

Regarding the randomised composite, Thongchai [50] previously studied the optimised condition of a PZT slurry with low viscosity, which is suitable for gel casting into a micromould. A 48 vol% of solid (PZT5H powder) loading in 30 wt% hydantoin resin with other additives and solvent was recommended to use, since it was shown that this condition produced low viscosity, which was less than 1 Pa.s, and high green strength of cast sample bodies. The low viscosity is required for fully filling into the micromould. The high green strength is desirable in order to prevent the green bodies of the bristle block samples being damaged during processing and handling. Thus, this condition was chosen to use throughout the present work.

Primary characterisation was carried out, including powder, rheological behaviour, green strength, density, and microstructure of plate and bar gel-cast samples. In addition, the microstructure and electrical impedance characteristics of 1-3 randomised composites measured as SETs were primarily investigated, as described in Section 5.2. Initial work reported in this thesis used the PZT5H powder with a batch no. 2008 as used in [50]. When this was exhausted, a second batch (batch no. 2002) of powder, nominally with the same specification, was utilised, with steps being taken to ensure that the characteristics, especially mean particle size and rheology behaviour, of the new powder were as close as possible to those of the original batch.

As mentioned previously, in order to compare the functional and acoustic properties of transducers made from different materials and methods, 1-3 piezocomposites including PZT (PZ54; semi-hard) ceramic and PIMNT single crystal piezoelectric materials were also fabricated using modified dice-and-fill methods. The optimum dicing parameters were investigated to effectively produce the 1-3 composites with a pillar pitch of 38  $\mu\text{m}$ . The preliminary investigation and measurements of the electrical impedance characteristics of the 1-3 diced piezocomposite SETs were studied, as shown in Section 5.3.

All three types of 1-3 piezocomposite were lapped and polished to achieve smooth and planar surfaces, before fine array elements were patterned directly on the composite surfaces. That work is presented in Chapter 6; thus, Section 5.4 provides only the results of the surface characteristics of the composites, including thickness variation in the composite region of the samples and at the interface between the composite and the additional epoxy region provided for fan out, as well as surface roughness measured by an optical profiler.

## **5.2. Material Characterisation for 1-3 Randomised Composites**

### **5.2.1. Powder Characterisation**

#### **Particle Size Analysis**

Particle size distribution, PSD, can be expressed either in density curves or cumulative curves. The density distribution,  $q_3(x)$ , represents the amount of each particle size by volume, whereas the cumulative curve,  $Q_3(x)$ , expresses the percentage of particles that are smaller or coarser than the specific sizes.

The density distribution curve of the as-received powder with batch no. 2008 in the present work showed a bimodal density distribution with the centre of primary and secondary peaks at 18 and 2.2  $\mu\text{m}$ , respectively, as shown in Figure 5.1 (a). The  $Q_3$  curve shows that 90%,

D90, of the particles were below 25  $\mu\text{m}$  in size, and 50%, D50, of the particles were smaller than 10  $\mu\text{m}$  in size. A slurry made with this powder would be unacceptable for casting into a micromould because the larger particles may hinder the slurry flowing into the tiniest mould cavities, which are approximately 2  $\mu\text{m}$ .

Figure 5.1 (b) displays the PSD curves of the PZT5H powder after vibro milling for 48 hr. The density curve of the milled particles shows a monomodal distribution, with a mean particle size of 1.24  $\mu\text{m}$ . In addition, over 90% of particles are below 3  $\mu\text{m}$  and 50% are smaller than 1.25  $\mu\text{m}$ . These results indicate that the mean particle size of the as-received powder was reduced significantly after milling, which is in accordance with SEM micrographs of both powders (Figure 5.2). According to the morphology observed by SEM, the as-received powder comprises doughnut-shaped granules which are indicative of spray-drying granulation. These soft agglomerates have a broad range of size, from 5 - 20  $\mu\text{m}$ , which is beneficial for the improvement of powder flowability in die filling of the dry pressing process [188]. Meanwhile, the milled powder did not have large agglomerates and gave a particle size of approximately 1  $\mu\text{m}$ , indicating that the primary source of the change in particle size was a result of the breaking-down of the powder agglomerates. This particle size was considered acceptable to prepare a slurry for gel casting into the micromould, with a broad range of feature sizes, 2 - 50  $\mu\text{m}$ .

The specific surface area, SSA, value of 2.11  $\text{m}^2/\text{g}$  measured by nitrogen absorption based on the BET technique for the milled powder was greater by 40.3% than the as-received value of 1.26  $\text{m}^2/\text{g}$  as reported in previous work [50], [95]. The correlation between the SSA and the PSD in this work showed inverse proportionality, in agreement with the literature [189]–[191].

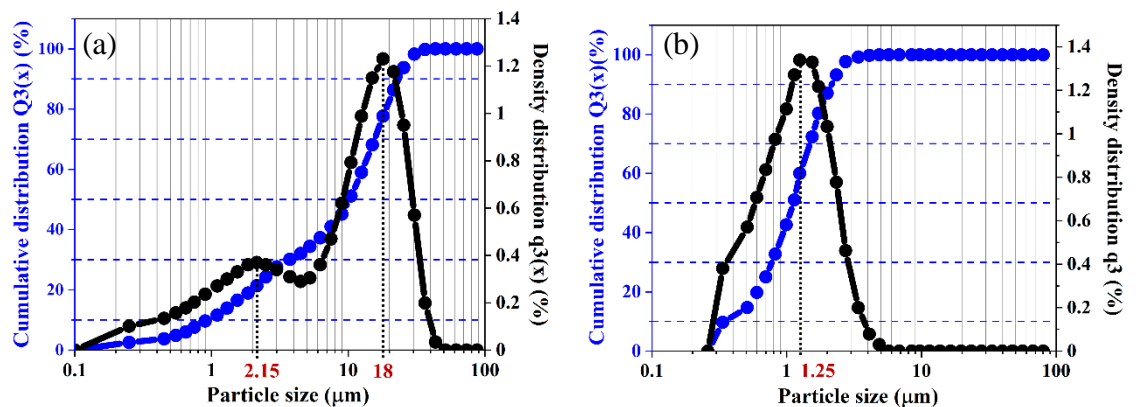


Figure 5.1 The particle size distribution curves of (a) as-received PZT powder (batch no. 2008) and (b) milled PZT powder after 48 hr vibro milling.

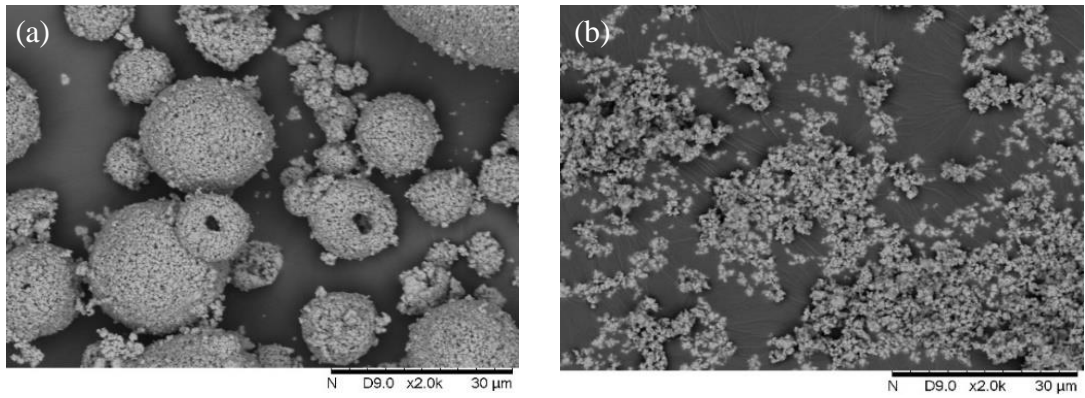


Figure 5.2 Microstructures of (a) as-received PZT powder with batch no.2008 and (b) the same powder after vibro milling for 48 hr.

During fabrication of the 1-3 randomised composites in this project, the batch no. 2008 of as-received powder was exhausted. Characterisation of the new batch with a batch no. 2002 was investigated to ensure that the mean particle size was as close as possible to that of the previous batch [50]. The PSD of the new batch also had a bimodal distribution, with the centres of the primary and secondary peaks at 2.15 and 15  $\mu\text{m}$  as shown in Figure 5.3 (a). Since the mean particle size at the first peak was close to the milled powder of the previous batch (1.24  $\mu\text{m}$ ) and the second one showed lower density distribution, the powder was first prepared using a range of different milling conditions: e.g., sieving, sonication and ball-milling. However, a bimodal distribution with a secondary peak of 14 – 40  $\mu\text{m}$  remained, as shown in Appendix III. Thus, the new batch was milled by the vibro-milling with different milling times, including 24, 36 and 39 hr.

It was found that a tendency of the density curves for all milled powders was to show a monomodal distribution, Figure 5.3 (b-d), with mean particle sizes of 1.61, 1.44 and 1.22  $\mu\text{m}$ , respectively. In addition, the D90, D50 and D10 values are listed in Table 5.2. The morphology of the as-received powder and 39-hr milled powder were extremely similar, with a primary particle size of approximately 1  $\mu\text{m}$  as illustrated in Figure 5.4. For this reason, the measured SSA of milled powders are only slightly changed since the primary particle has not changed with milling time, as listed in Table 5.1. These data indicate that the peak at 15  $\mu\text{m}$  in the PSD for the as-received powder of batch no. 2002 was due to much softer agglomerates than the 18  $\mu\text{m}$  peak observed in the batch no. 2008 powder. However, after vibro-milling, the powders from the two batches were very similar.

Table 5.1 Summary of particle size and specific surface area of the as-received and milled PZT powders.

PZT powder	D10 ( $\mu\text{m}$ )	D50 ( $\mu\text{m}$ )	D90 ( $\mu\text{m}$ )	Mean Particle Size ( $\mu\text{m}$ )	SSA ( $\text{m}^2/\text{g}$ )
As-received powder Batch no. 2008	0.9	10.5	25.5	10 (bimodal)	n/a
VB – 48 hr	0.33	1.14	2.38	1.25	2.11
As-received powder Batch no. 2002	0.65	1.85	6.25	8.57 (bimodal)	n/a
VB – 24 hr	0.36	1.6	4.2	1.61	1.81
VB – 36 hr	0.3	1.35	3.6	1.44	2.16
VB – 39 hr	0.3	1.2	3.3	1.22	2.09

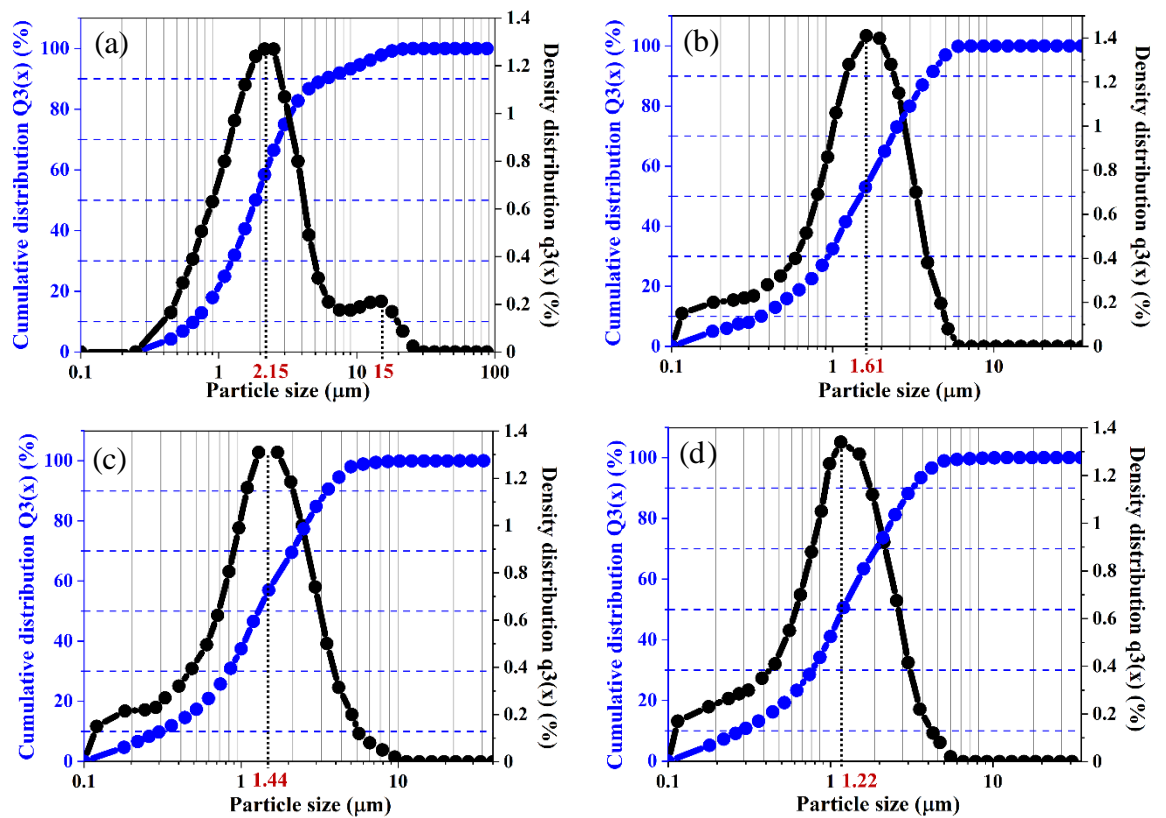


Figure 5.3 The particle size distribution curves of PZT powder with batch no. 2002 of (a) as-received powder and milled PZT powder after (b) 24 hr, (c) 36 hr and (d) 39 hr milling time.

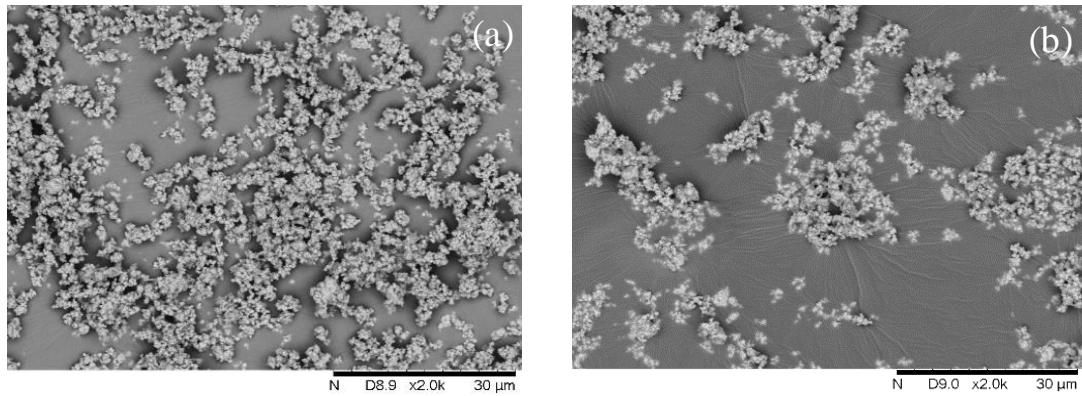


Figure 5.4 Microstructures of (a) as-received PZT powder with batch no.2002 and (b) milled PZT powder after 39 hr vibro-milling.

### Crystalline material structure

Figure 5.5 shows the XRD patterns of as-received powder from the batch no. 2008 and a ceramic disc sintered at 1200 °C, prepared from the 48-hr milled powder. These measurements were undertaken because that most of 1-3 randomised composites used in the present work were fabricated based on this powder and were required to ensure that the phase and crystal structure of the material did not change during processing. The patterns matched with ICSD 86136, in agreement with other literature [50], [192]. As a result, there was no phase transformation after the prolonged milling and sintering process since the XRD pattern of both samples were very similar.

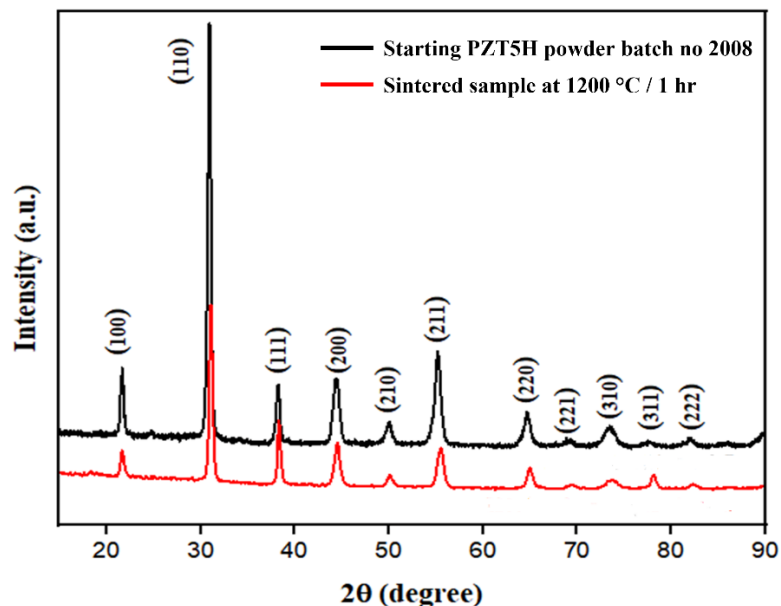


Figure 5.5 XRD patterns of as-received and sintered PZT disc at 1200°C, prepared from 1.24 μm powder from the batch no 2008.

### 5.2.2. Slurry Characterisation

All PZT slurries were prepared with the optimised conditions of a 48 vol% of solid loading in 30 wt% resin contents as described in Section 4.2.1. Rheological behaviour, viscosity,  $\eta$ , and gelation or idle time of slurries reported here are the results of the slurries made with 24, 36 and 39-milled powders. The rheology of the 48-hr milled powder is not provided here, since it was unavailable for measurement. Nonetheless, all the characterisation of the milled powder and slurry in this work showed that the rheological behaviour, viscosity and gelation time of the samples made from the new powder batch were very close to that of the previous study [50]. This is because the milled powder from the two batches had the same particle size and morphology.

Rheological behaviour of a suspension is usually attributed to the perturbation of the suspension or slurry structure [193], [194]. In the equilibrium state, without shear stress, the particles are held in the suspension with attractive interparticle forces, e.g., electrostatic, Van der Waals and hydrophobic forces [194], [195]. The agglomerates, the packing ability of particles and particle structure in the suspension, are dependent on the particle size and the PSD. A high degree of particle packing with random structure and separation between particles is usually found for coarser particles and broader PSD, since the smaller particles occupy the space created in the separation of the coarser particles. Highly hexagonal packing with smaller separations and an ordered structure tend to be found for smaller particles and narrower PSD, owing to the relatively mono-sized particles [194], [196].

At low shear rates, liquid is trapped in voids within flocs and the floc network, which are more likely to be found in suspensions made with coarser particles and broader PSD owing to the random particle structure influenced by the polysized particles [197]. As the shear rate,  $\dot{\gamma}$ , increases, the flocs are broken down by shear stress,  $\tau$ , and the entrapped liquid is released, producing more ordered particle structures being formed in the flow direction [194]. At higher shear rates, the magnitude of  $\tau$  pushing the particles becomes greater than the interparticle forces. While the particles are moved from their stable state, the slurry structure remains ordered during flow owing to the influence of the immobilised liquid and the polysized particles that are flowing as ordered layers of triangular particle packing. Hence, the suspension flows easily under  $\tau$ , indicating that the viscosity,  $\eta$ , is low. Furthermore, the relation between  $\eta$  and  $\dot{\gamma}$  shows linear proportionality. This action is well known as shear thinning behaviour [193], [198], [199].

On the other hand, as particles move from their stable state in a less ordered structure, they become jammed into each other, resulting in clusters of particles or flocculation precluding flowability of the suspension. These clusters, or the disordered structure, dissipate the extra energy to drive the suspension to flow, thereby causing a rise in  $\eta$  when  $\dot{\gamma}$  increases. This implies shear thickening behaviour. It usually occurs in systems composed of finer particles, with a narrow PSD, as they are very likely to re-agglomerate and form the particle clusters or flocculation in the fluid, owing to the larger interparticle interactions [194], [200]–[203].

In the present study, both shear thinning and thickening behaviours were observed in all suspensions, where they were made with three powders derived from various milling times (24, 36 and 39 hrs), as shown in Figure 5.6 (a). The shear thinning behaviour was exhibited at very low shear rates from 0 - 100 s<sup>-1</sup>, indicating that the suspensions flowed with ordered structure. At higher shear rates,  $\eta$  tended to gradually rise when  $\dot{\gamma}$  was increased from 100 to 600 s<sup>-1</sup>, which is in agreement with Thongchai [50]. This behaviour implies that the flocculation might gradually form during flow, as the slurry structure changes to the less ordered structure described above. Nevertheless,  $\eta$  for the two suspensions made with powders milled for 24 and 36 hrs was still lower than 1 Pa.s at the highest shear rate of 600 s<sup>-1</sup>, whereas the shear thickening behaviour was accentuated in the suspension made with powder milled for 39 hrs, showing  $\eta$  of ~1.5 Pa.s at the highest rate. This higher viscosity implies a resistance to the flow of the suspension, which was attributed to the formation of the flocculation caused by the cooperation of the finest particles in the milled 39-hr powder as listed in Table 5.1. More force was needed to break the interparticle forces of the flocculation, leading to the outcome of higher viscosity and accentuated shear thickening behaviour found in this suspension, which corresponds with other work [50], [193], [194], [196].

Slurry viscosity, however, is usually considered at a low shear rate of 100 s<sup>-1</sup> because that is close to the condition during casting [50], [198], [204]. For this reason, the highest slurry viscosity at the highest rate was still acceptable. In addition, the viscosity value at the highest rate was still lower than that of the previous work, i.e. 2 Pa.s measured at a shear rate of 100 s<sup>-1</sup>, which was used to fabricate the randomised composites [95]. At the low shear rate of 100 s<sup>-1</sup>, all slurries exhibited low  $\eta$ , <1 Pa.s (Table 5.2), indicating that the suspensions had good flowability to fill the mould cavities, as required for gel casting [141], [205]. Interestingly, the slurry made with powder from 39-hr milling had higher viscosity, 0.47 Pa.s, than the slurries made from the other two powders, 0.34 Pa.s. This is also attributed to

the influence of the finer particles that tend to produce flocculation, which needed more energy to push the slurry to flow, leading to higher viscosity as described previously.

Figure 5.6 (b) shows the viscosity curves as a function of time, from which the gelation time of the slurries can be identified. The start time was counted after the slurries were manually mixed with the hardener, in a process which lasted for approximately 3 min. All suspensions showed a period of constant viscosity, following which the viscosities rose gradually and then increased abruptly towards infinity. The constant period of the viscosity is known as the gelation time of the polymerisation process, which is the available time for mixing and casting [203]. It was found that all slurries showed a period of constant viscosity beyond 10 min (Table 5.2), indicating that the gelation time of all slurries was suitable for a gel casting process, in agreement with other literature [50], [203].

The correlation between the gelation time and the mean particle size showed linear proportionality. It is claimed that gelation time reduction is strongly influenced by a ‘container’ effect [203], [206]. Imagine a scenario, the smaller particles can fill into the interstices of the larger particles, and this creates the smaller container. For slurry gelation, polymer chain lines are needed to simultaneously connect the particles and fill the interstices of the particles at a certain period. The smaller the container, the shorter the polymer chain needed to connect the particles. For this reason, by reducing the particle size, the container was reduced, resulting in a decrease in gelation time.

Table 5.2 Measurement of viscosity and idle time of the slurries made with milled PZT powders.

<b>PZT powder Milling time; Mean particle size</b>	<b>Viscosity <sup>1</sup> (Pa.s)</b>	<b>gelation time <sup>2</sup> (min)</b>
<b>24 hr; 1.61 μm</b>	0.34	14
<b>36 hr; 1.44 μm</b>	0.34	12
<b>39 hr; 1.22 μm</b>	0.47	11

<sup>1</sup>At shearrate 100 s<sup>-1</sup>

<sup>2</sup>At viscosity of 600 Pa.s

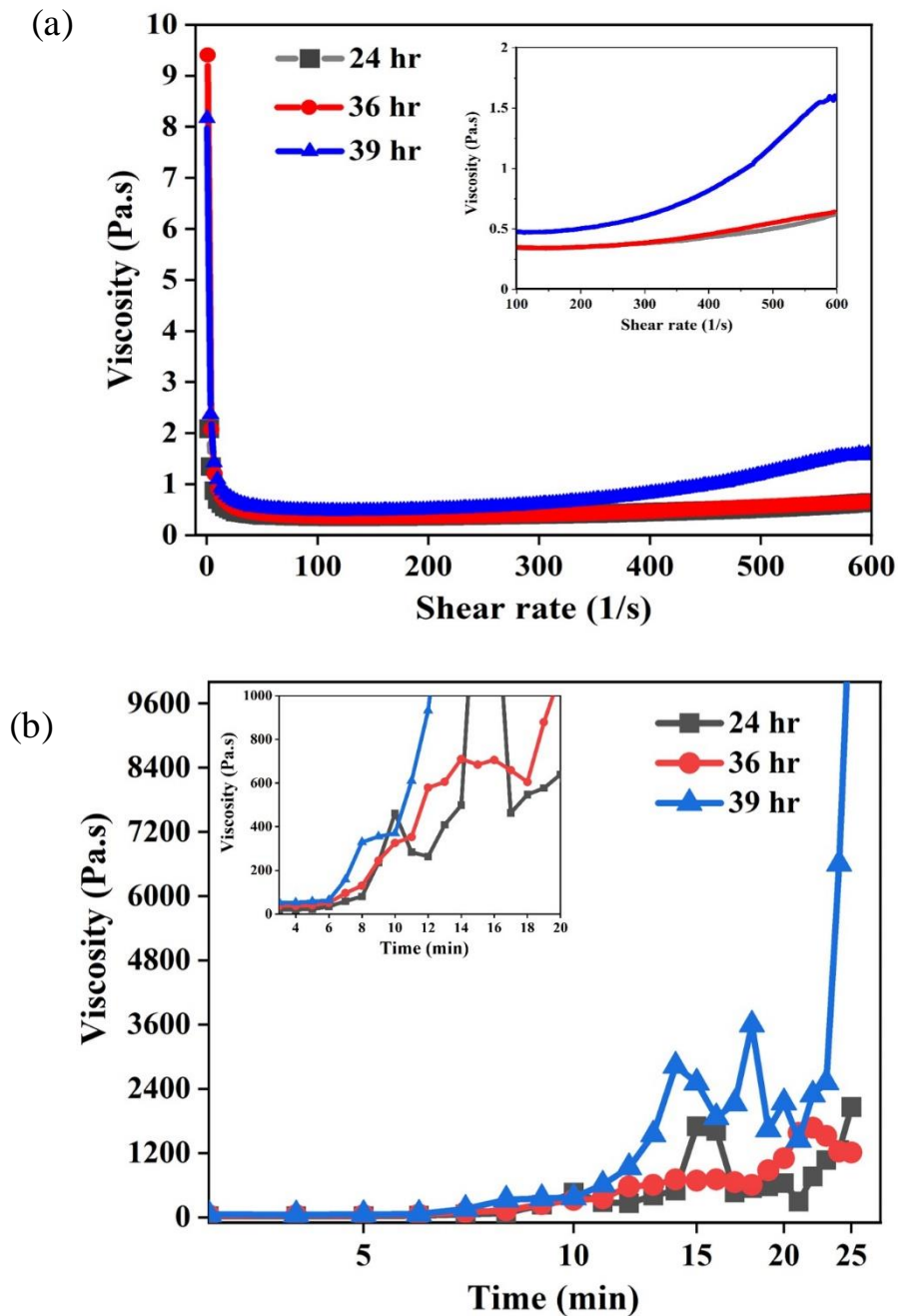


Figure 5.6 Variation of viscosity curves as (a) a function of shear rate and (b) a function of time of slurries comprising PZT5H powders milled for various times and with constant 48 vol% solid loading and 30 wt% resin content.

### 5.2.3. Characterisation of Green and Sintered Samples

#### Bulk Gel-cast Sample Characterisation

Green PZT samples made with powder with a mean particle size of 1.24- $\mu\text{m}$  (48 hr milling) were produced at room temperature,  $T_R$ , by using the optimum conditions of 48 vol% solid loading and 30 wt% resin contents. Figure 5.7 shows a green PZT sample of around 12 mm diameter and 1.5 mm thickness after demoulding and drying. The samples exhibited good geometrical replication and no cracks or bubbles were observed. The green properties,

including drying shrinkage, green density and green strength, were observed to be close to previous work [50], in the order of  $6.6 \pm 0.05\%$ ,  $4.79 \pm 0.11 \text{ g/cm}^3$  and  $49.7 \pm 2.49 \text{ MPa}$ , respectively. The green strength is the most important factor in gel casting used for fabricating the relatively small features of the 1-3 composites. High green strength is preferred because the tiny pillars of the green bodies must be able to withstand stresses during various processes, such as manual demoulding, holding, and transferring to sintering.

In addition, it was noticed that the green strength obtained for the samples produced in this work and elsewhere [50] was improved significantly compared to the work ( $\sim 38 \text{ MPa}$ ) reported by Jiang [95], who fabricated 1-3 randomised composites by using EGDGE resin with the gel casting method. This might be attributed to better water solubility of the hydantoin resin used in this work, to which a higher solid loading of 48 vol% could be added while maintaining a low viscosity; in Jiang's work, the solid loading was 45 vol%. The viscosity of the slurry in the present work,  $0.47 \text{ Pa}\cdot\text{s}$  at a shear rate of  $100 \text{ s}^{-1}$ , was 61.7% less than the slurry prepared by Jiang,  $1.23 \text{ Pa}\cdot\text{s}$ . Many studies suggest that the higher viscosity implies flocculation generation during flow [194], [201], [202]. The flocculation might adversely affect the homogeneous nature of the microstructure in the green bodies, which might lead to poor green strength.

The sintering shrinkage and density of  $17.96 \pm 1.42\%$  and  $7.50 \pm 0.62 \text{ g/cm}^3$ , achieved in the present work, providing a relative density of  $93.2 \pm 1.69 \%$ , were close to the results reported by Thongchai [50]. The microstructure of as sintered and fracture surfaces of the green samples exhibited non-uniform powder packing in some regions, as shown in Figure 5.8 (a). The microstructure of the surface of sintered samples showed a grain size of around 1 - 2  $\mu\text{m}$ , as illustrated in Figure 5.8 (c). Micropores were observed in the fracture surfaces of the sintered sample, as demonstrated in Figure 5.8 (d), which is similar to those from other work [50], [95], [141], [145]. According to Thongchai [50] and Jiang [95], the apparent porosity increased with increasing resin content, resulting in a decrease of the sintering shrinkage and sintered density.

It was believed that the porosity originated from resin decomposition during the burn-out step. The resin decomposition generated an accumulation of gases in the system and the gases could be released by flowing through the porous structure of the green bodies [207]. Thus, a sample with a higher resin content would cause more gas accumulation, as well as a lower gas permeation rate owing to the closer particle packing. This would increase the degree of internal stress, resulting in the formation of defects, such as cracks and voids. However, some pores were seemingly located at junctions of grains, as indicated by the red

circles (Figure 5.8 (c–d)). From a different viewpoint, therefore, the formation of pores at the junction may be attributed to non-uniform powder packing introduced by flocculation in the suspension with higher resin content, in relation with densification during the sintering process. As Jiang noted that ‘the presence of the non-absorbing epoxy resin in the slurry with higher resin content probably caused the flocculation of the PZT particles’ [2, p. [95]].

In the gelling system, the resin molecules interact with solvent and crosslinker molecules to create a 3D network to immobilise the particles and fill the particle interstices. In fact, the resins are absorbed on the surface of the PZT particles; consequently, the particles are dragged towards and approach each other. When the concentration of the non-absorbing polymer exceeds a critical value, the free polymer chains become the bulk solution. The concentration difference between the particle-particle approach zone and the bulk solution produces an osmotic pressure, resulting in attraction of the particles and leading to, e.g., flocculation [208], [209]. This introduces a non-uniform distribution of particles and interstices, which causes the formation of pores after the burn-out process.

In the sintering stage, if considering an ideal system where particles with a constant size are uniformly packed, the interstices are uniformly distributed. The pores or interstices are uniformly replaced by grain boundary diffusion, known as grain growth, leading to a uniform densification and homogeneous microstructure. However, the formation of pores presented at the grain junctions is shown in the present work. This might be attributable to non-uniform packing introduced differential densification between regions of different initial packing densities [210].



Figure 5.7 A green PZT sample, prepared by gel casting from 48 vol% solid loading in 30 wt% resin with 1 wt% Displex AA4040 and solvent, after demoulding and drying.

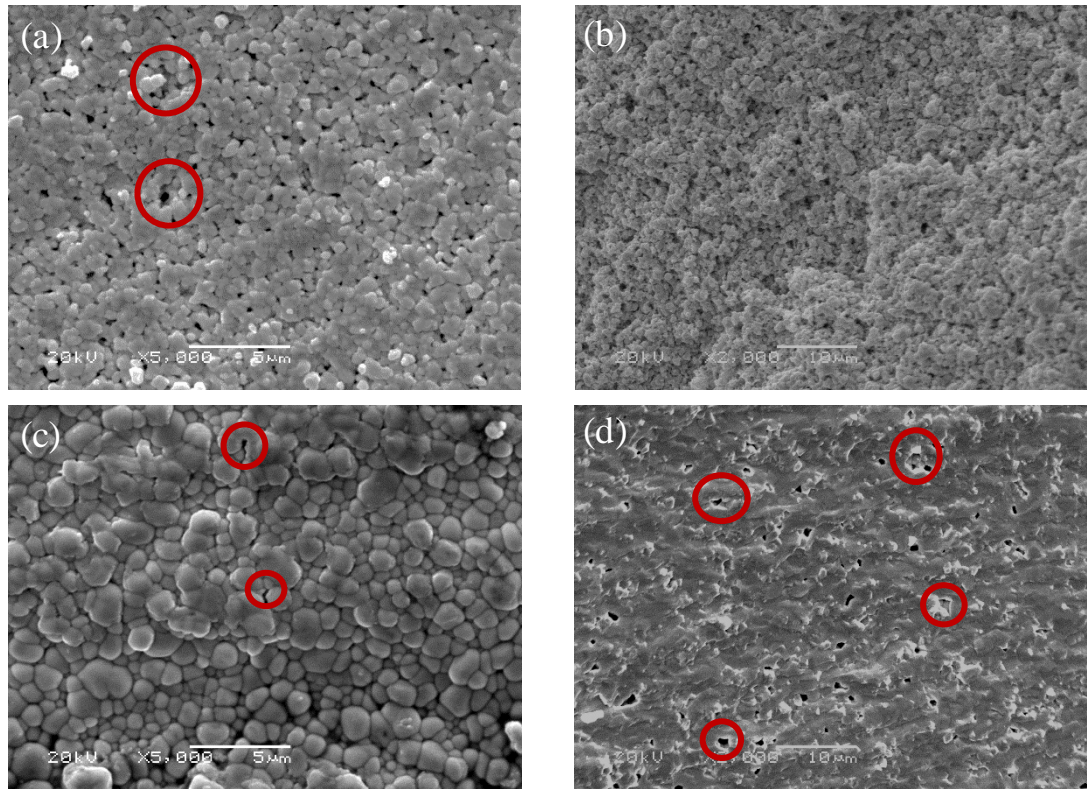


Figure 5.8 SEM images showing (a, c) surface and (b, d) fracture microstructures of (a, b) bulk-green body samples and (c, d) sintered samples obtained from milled PZT5H powder with 48 vol% solid loading and 30 wt% resin content.

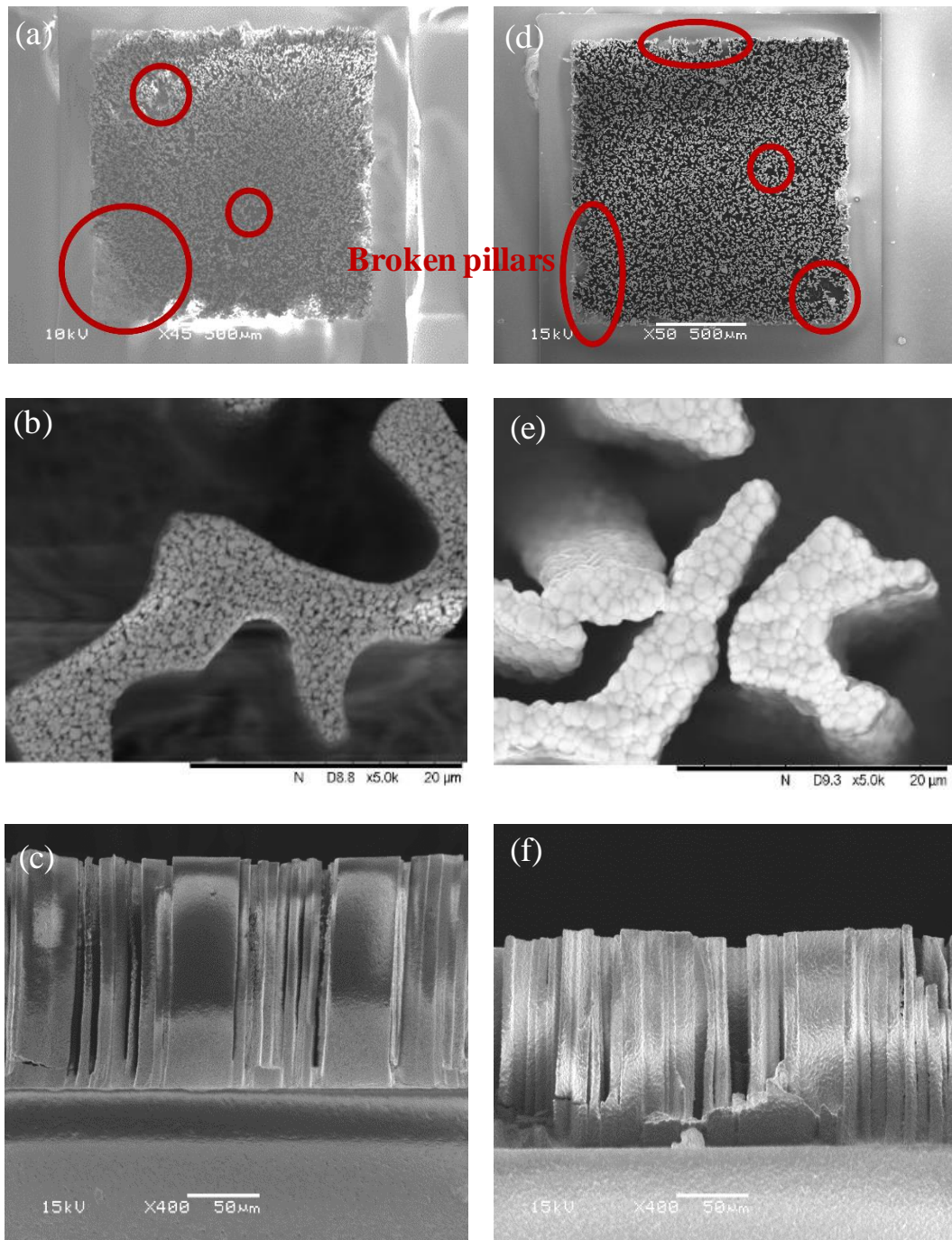
### Microstructure of Bristle Block Samples and Composites

The microstructure of typical PZT segments after demoulding (green samples) and sintering are presented in Figure 5.9 (a) and (b), respectively. Broken pillars were sometimes found at the centre and the edges of the patterns due to the reuse of the master mould and difficulty demoulding. This offered ~80% yield of survival pillars after demoulding. When used to make a composite, these broken regions will reduce the  $VF$  of piezoceramic which may influence  $k_{eff}$ , bandwidth and sensitivity of transducers. However, the completed areas could be used for SETs with an area of  $1.5 \times 1.5 \text{ mm}^2$  and for  $\mu\text{US}$  arrays with an area of array elements of  $1 \times 1.4 \text{ mm}^2$ .

It can be seen that the gel casting process had successfully filled the micromould cavities as shown in Figure 5.9 (b) and (e). The microstructure shows a homogenous and uniform grain size. Tilted pillars observed in the sintered samples (e) may have occurred during the transfer to the sintering process due to the presence of grain connections between the pillars. However, tilting at the tip of pillars can be eliminated when the composite surface is being exposed by lapping.

Five samples of green and sintered samples were used to measure a pillar height and a smallest lateral size. For the green samples, the height and lateral size were  $\sim 135.46 \pm 1.56 \text{ }\mu\text{m}$  and  $\sim 5.15 \pm 1.31 \text{ }\mu\text{m}$ , respectively, providing  $AR = 26$ . After sintering, the pillar height

was decreased to  $\sim 124.60 \pm 1.45 \mu\text{m}$ , with a smallest feature size of  $\sim 5.40 \pm 1.26 \mu\text{m}$  resulting in  $AR = 23$ . The microstructure shows a homogenous and uniform grain size.



Green body sample

Sintered sample

Figure 5.9 SEM micrographs of typical (a-c) green and (d-f) sintered bristle-block PZT samples derived from the gel casting technique with 48 vol% solid loading of (1.24- $\mu\text{m}$  powder) in 30 wt% resin content.

Figure 5.10 shows the microstructure of a randomised composite surface after encapsulation with epoxy and lapping with 3- $\mu\text{m}$  alumina abrasive to give pillar exposure. Pulled-out grain and pinholes can be seen. The former may be caused by chipping during the lapping process

[178] and the latter is likely to have originated from bubble entrapment in the epoxy during encapsulation.

In composite fabrication, vacuum degassing, centrifuge and heat are generally recommended as simple and efficient methods to remove bubbles from the epoxy before curing [211]. In the present fabrication of the randomised composites, two degassing steps were employed. The first was after mixing the epoxy resin with the epoxy hardener in order to remove bubbles that were introduced by mechanical mixing. The second degassing step was during infiltration of the epoxy into the kerfs in the mould to aid the process to fill microcavities and to remove the bubbles that might be generated during filling and fast flowing. The degassing steps should not last longer than 20 min, because the pot life, i.e., the gelation time of the epoxy mixture before it starts to harden, is approximately 30 min.

The presence of the pinholes indicated that the level of vacuum and time during degassing might not be sufficient to force the bubbles to flow through the liquid epoxy. In addition, the purpose of curing at elevated temperatures was to enhance the environmental resistance of the epoxy. Meanwhile, it also assisted the bubble removal by lowering the viscosity of the epoxy mixture, allowing the bubbles to flow up to the surface of the mixture. However, this method came with the expense of shortened pot life and limited the time for bubble removal [211], [212]. This may cause the bubbles to become trapped within the structure.

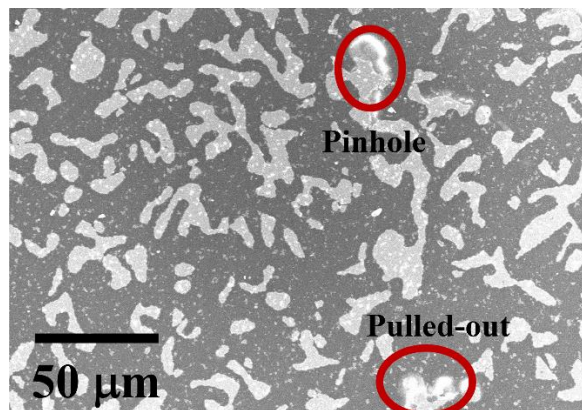


Figure 5.10 SEM micrograph showing exposed surfaces with defects in 1-3 randomised ceramic composites.

#### 5.2.4. Electrical Properties of Bulk Gel-cast PZT Ceramic and Randomised Composite

Five samples of unpoled bulk gel-cast PZT ceramic and unpoled 1-3 randomised composite were used to measure electrical properties as given in Table 5.3. The  $\epsilon_r$  and  $d_{33}$  values of the ceramics are slightly lower than those from the supplier [213]. This is possibly caused from the different processing route, producing a lower density ( $7.5 \text{ g/cm}^3$  compared to  $7.95 \text{ g/cm}^3$

quoted by the manufacturer). However, they are similar to those reported in previous work [50]. For the 1-3 randomised PZT piezocomposites,  $\epsilon_r$  was relatively low compared to the bulk ceramic, being 87% lower, and the dielectric loss,  $\tan \delta$ , was increased. This is because of the inclusion of over 60 VF% epoxy, where the epoxy has small  $\epsilon_r$ , only 4.8 – 5 [214]. The  $d_{33}$  value of the composite could not be measured, due to the limited number of randomised piezocomposite samples available.

Electrical impedance characteristics of the composites are shown in Figure 5.11. The centre frequencies of ~30.3 and 36.2 MHz correspond to sample thicknesses of ~ 50 and 42  $\mu\text{m}$ , respectively, providing  $k_{eff}$  values of 0.58 and 0.59. The electrical impedance graphs show no presence of spurious modes observed at the frequencies of interest, which is in agreement with modelled electrical impedance characteristics [92]. This is attributed to a high AR and the random distribution of pillar geometry, orientation and spacing [41], [96], [99], [215], [216].

In the case of the randomised composite, the US waves propagate in this structure randomly because the periodicity of the pillars and parallel facing surfaces no longer exist in this composite structure. For this reason, the spurious modes mostly cancel each other out, while leaving pillars oscillating primarily along their length (the thickness direction of the composite). In addition, the random geometry pillars have AR in the range of 1 – 25, representing tall and thin pillars. This also enables pillars to vibrate along their length effectively. Thus, this results in magnitudes of thickness resonance frequencies greater than those of the spurious mode frequencies.

Table 5.3 Electrical properties of bulk gel cast samples and 1-3 randomised composites.

	$d_{33}$ (pC/N)	<i>Coupling factor</i>	$\epsilon_r$ at 1 kHz	$\tan \delta$
<b>Sintered bulk gel cast samples<sup>1</sup></b>	517 ± 1.6	0.57 ± 0.020 <sup>2</sup>	2913 ± 1.53	0.022 ± 0.32
<b>TRS ceramic</b>	750	0.75	4800	0.0018
<b>1-3 randomised composites<sup>1</sup></b>	-	0.58 ± 0.045 <sup>3</sup>	350 ± 2.17	0.035 ± 0.44

<sup>1</sup>Measured from unpoled materials

<sup>2</sup> $k_p$  = planar electromechanical coupling coefficient in planar mode

<sup>3</sup> $k_{eff}$  = effective electromechanical coupling coefficient

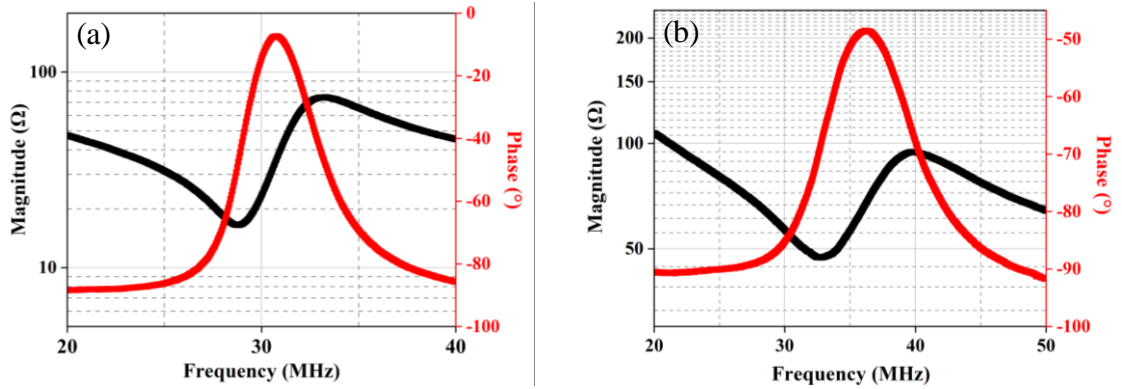


Figure 5.11 The electrical impedance magnitude and phase of 1-3 randomised PZT piezocomposites with operating frequencies of (a) 30.3 MHz, and (b) 36.2 MHz.

### 5.3. Material Characterisation for 1-3 Diced Composites

#### 5.3.1. Single pitch dicing

As mentioned in Section 4.2, PZ54 piezoceramic material was one of the active materials for preliminary study in the dicing parameters, as it was less brittle than the single crystal material. To maintain volume fraction of ceramic up to 40% and  $AR$  greater than two, the first dicing series was studied using a pitch from 36 - 38  $\mu\text{m}$ . Spindle speed (blade rotation) was set to be 20,000 RPM because it was suitable for dicing single piezocrystal materials and reducing saw blade vibration as recommended from the literature [12].

In the first passes, piezoceramic samples were diced in one direction to produce a 2-2 geometry of rectangular slices. The cut depth was set to be 150  $\mu\text{m}$ , allowing sufficient pillar height for subsequent processes and the feed rate of a blade was varied between 0.2-0.5 mm/s. However, higher feed rates produce a larger stress applied to the sample than slower rates. Thus, the feed rate was reduced to be 0.2 mm/s and a water coolant with a flow rate was also adjusted to be 0.5 L/min to minimise pillar breakages. The pillar pitch of 36 and 37- $\mu\text{m}$  pitches were accompanied by 65% and 80% yield of surviving pillars, respectively, as displayed in Figure 5.12 (a-b). Most collapsed slices were found in positions corresponding to the end of the dicing direction. This may be related to the effect of the blade vibration caused by looseness of the blade attachment [12]. More importantly, the small slices are very fragile and prone to collapse easily when faced with vibration.

However, a 38- $\mu\text{m}$  pitch provided 90% yield with some breakages at the end of cutting passes as shown in Figure 5.12 (c). Thus, this condition was chosen for further processes. Prior to the second series of cuts perpendicular to the first series, the kerfs must be filled with epoxy to secure the pillars from the stresses generated during second dicing procedure. In this regard, it also allowed a deeper cut depth than the first passes by 11.7% due to thin

slices being supported by the epoxy. Thus, yield of survival pillars was much better than the first passes. Nonetheless, this increased process time due to multiple steps in encapsulation and lapping to expose pillar surface as given in Table 4.6. Figure 5.13 shows the 1-3 ceramic composite with 38- $\mu\text{m}$  pillar pitch manufactured from a single pitch dicing method after separation into  $2 \times 2 \text{ mm}^2$ .

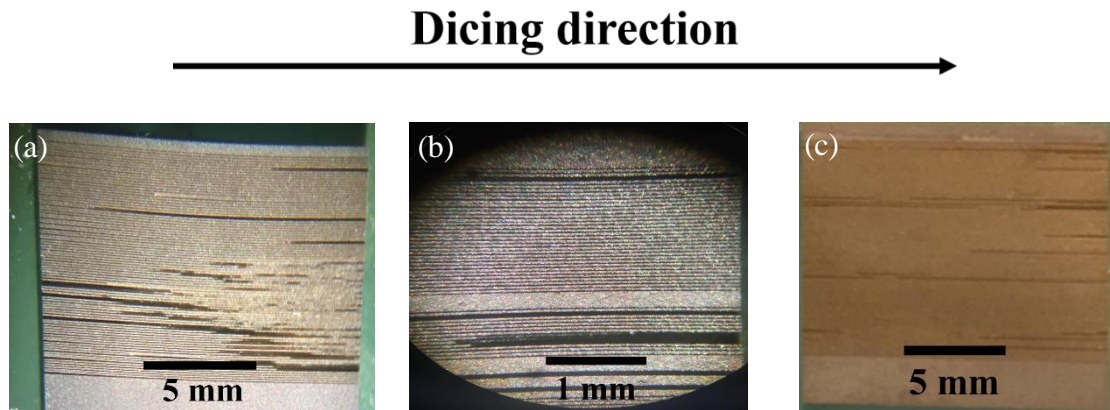


Figure 5.12 Optical micrographs showing examples of collapsed pillars in the PZT ceramic diced at (a) 36  $\mu\text{m}$ , (b) 37  $\mu\text{m}$  and (c) 38  $\mu\text{m}$  pitches.

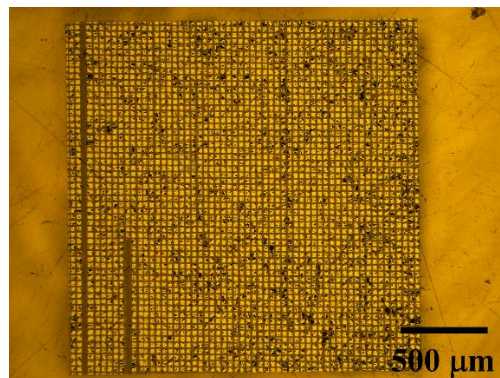


Figure 5.13 Optical micrograph showing a top view of a test sample of diced PZT ceramic piezocomposite (after pillar exposure) made with single pitch dicing to produce 38  $\mu\text{m}$  pillar pitch.

### 5.3.2. Double pitch dicing

The PZ54 piezoceramic was also used in another preliminary study, using the double pitch dicing method before tuning to suit the more fragile single crystal material. The first series of cuts in orthogonal directions was similar to the dicing parameters for the piezoceramic, as shown in Table 4.5, except for the pillar pitch, which was 76  $\mu\text{m}$ ; a 99.5% yield of surviving pillars was attained with this condition. However, there were missing pillars at the centre of the sample, as illustrated in Figure 5.14 (a). For this reason, cut depth and feed rate of the blade were reduced by 26 and 50%, respectively, to achieve as close to 100% yield in dicing

the PIMNT single piezocrystal material as possible. With the reduced cut depth, it also reduced the height of pillars, hence, the lapping steps for pillar exposure must be very carefully monitored to maintain sufficient height for subsequent processes until the final lapping step to achieve the required thickness of 50  $\mu\text{m}$ . After the first cuts in two orthogonal directions were completed, the pillars were also secured with the epoxy to prevent the collapse while dicing the second cuts and followed by lapping to expose pillar surfaces. The second series of cuts were diced at the centre of the interpillar regions of the first series of cuts to produce a 38  $\mu\text{m}$  pillar pitch.

Figure 5.14 (b) shows optical microscope images of 1-3 diced PIMNT single crystal piezocomposite with a 38  $\mu\text{m}$  pitch, made using the double pitch dicing method. Some rows of pillars were uneven compared to their neighbours due to misalignment in the second cuts. The blade was aligned based on the kerfs from the first cuts, while the first cuts were aligned from the edge of the sample piece. Alignment with the kerf may be unreliable because pillar rows at the edges were slightly tilted after the first cuts due to the forces from the blade and water coolant pushing them. Thus, it is suggested that the first line of the first series should be 2-3 mm away from the edge of the sample to withstand the dicing forces and to use this first cut as a base line for the first and second series of cuts.

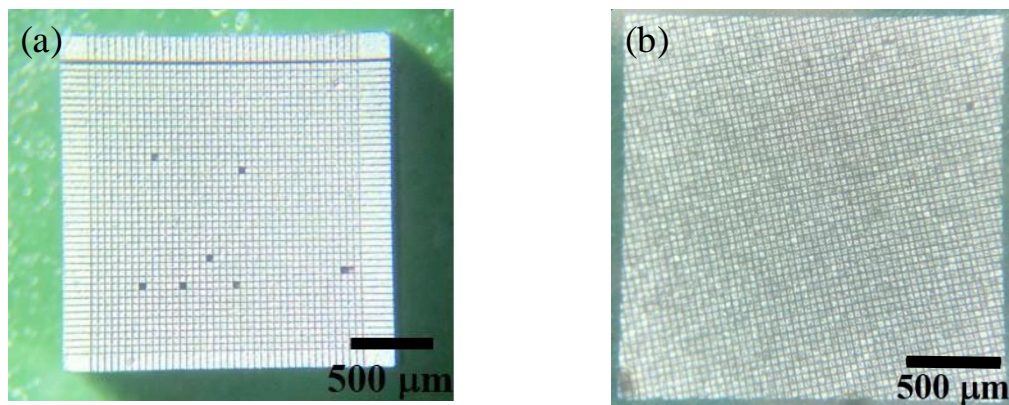


Figure 5.14 Optical micrographs showing top views of (a) diced ceramic sample and (b) diced single crystal composite (after pillar exposure) made with a double pitch dicing method to produce 38- $\mu\text{m}$  pillar pitch.

### 5.3.3. Electrical properties of diced composites

In this measurement, one sample for each composite was used to observe electrical properties and electrical impedance characteristics. It is found that the electrical properties of the diced PIMNT single crystal piezocomposite are better than those of the diced ceramic composite, as shown in Table 5.4. This is because of the superior properties of the single crystal itself, e.g.,  $d_{33}$ ,  $k_t$  and  $k_{33}$  [67], [68], [217]. However, the polymer inclusion of over 50 VF% in the

composite strongly influenced the dielectric properties, which showed relatively low values compared to the bulk piezoelectric materials [217], [218].

Figure 5.15 shows the electrical impedance characteristics of both ceramic and single crystal composites. Spurious modes present near the resonance frequencies in both cases. This is attributed to the periodicity of the square pillars and low  $AR \sim 2$ . As described in Section 2.7.6, spurious modes arise from periodicity of the pillars because US waves propagate pillar-to-pillar and reflect at the pillar faces and the diagonal directions, hence, lateral vibrations or spurious modes are generated as shown in Figure 5.16. Their resonances become prominent and interfere with the fundamental thickness resonances when the thickness of the pillars is close to the pillar width, representing low  $AR$ .

According to lateral vibration shown in Figure 5.16, its magnitude in the diced ceramic composite was much greater than that of the diced single crystal. This may be related to the elastic stiffness constant, which determines the response of the crystal structure of materials to externally applied inputs and its stability. The PZ54 piezoceramic has lower elastic stiffness constants in all lateral directions than the single piezocrystal by around 10-50%, as listed in Appendix II. For this reason, the PZ54 piezoceramic was more sensitive to the inputs. This resulted in lateral vibrations of greater amplitude produced and coupled to the thickness resonance frequencies.

Table 5.4 Electrical properties of 1-3 diced piezocomposites.

1-3 diced piezocomposite	$k_{eff}$	$\epsilon_r^*$ at 1 kHz	$\tan \delta$
PZ54 Ceramic <sup>1</sup>	0.73 <sup>2</sup> , 0.406 <sup>3</sup>	259	0.015
PIMNT Single crystal <sup>1</sup>	0.835 <sup>2</sup> , 0.675 <sup>3</sup>	337	0.033

<sup>1</sup> Poled piezoelectric material

<sup>2</sup> FEA Model

<sup>3</sup> Experiment

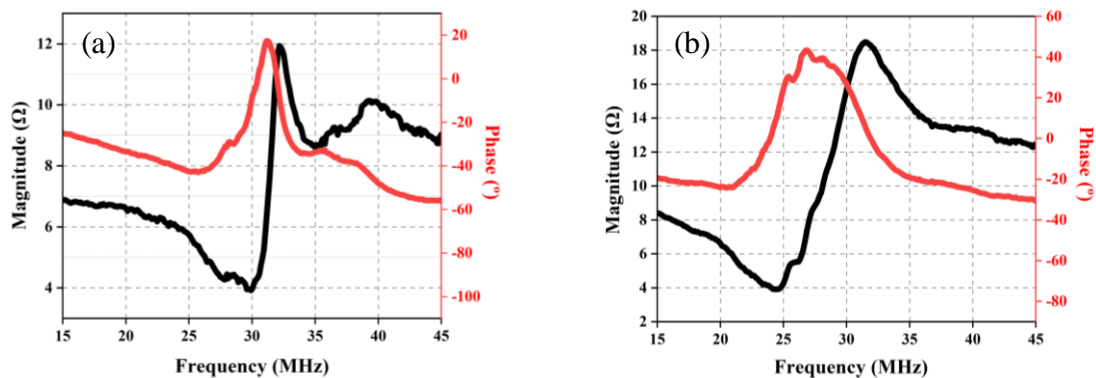
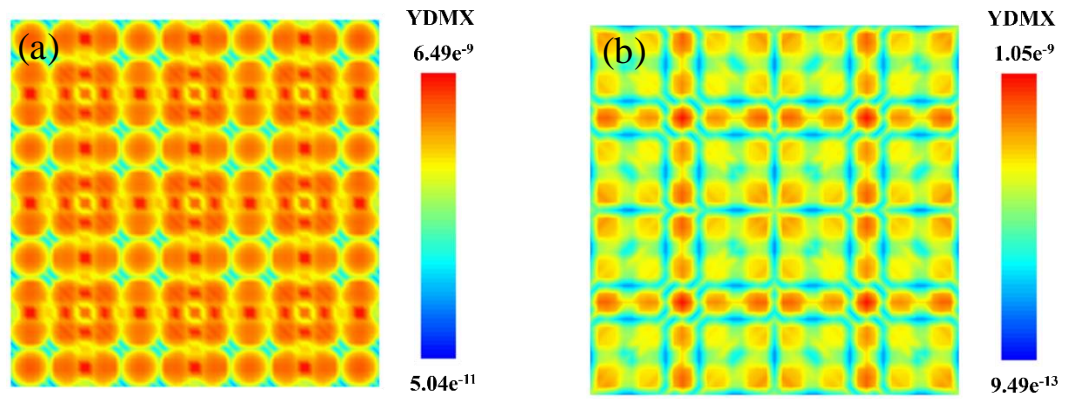


Figure 5.15 Experimental electrical impedance magnitude and phase of 1-3 (a) diced ceramic and (b) diced single crystal composites.



YDMX: Maximum displacement in Y-axis (unitless)

Figure 5.16 Maximum displacement in Y-axis (YDMX) showing lateral vibration of spurious modes observed in (a) diced ceramic and (b) diced single crystal composites with the composite structure of 38  $\mu\text{m}$  pitch.

## 5.4. Surface characterisation

As discussed in Section 3.3, the difference in the elastic properties of the two materials in the composite creates the epoxy bumps and thickness variation, causing poor surface roughness,  $R_a$  [44], [149]. Thus, surface polishing is required after lapping in order to improve the  $R_a$  of the composite surfaces. After pillar exposure by three lapping steps, the samples were polished on the polyurethane plate (Logitech, Glasgow UK) at a speed of 40 rpm, for a total duration of 1 hr and a load of 750 g, as previously discussed in Section 4.3. This polishing condition provided the removal rate of approximately 15  $\mu\text{m}/\text{hr}$ .

### 5.4.1. Surface Profile

Height non-uniformity of the 1-3 piezocomposites and at the interface between the composite area and the fan-out epoxy were characterised using a Dektak XT (Bruker, Coventry, UK). A scanning resolution of 0.02  $\mu\text{m}$ , based on the scan length and measurement duration, was used throughout these measurements.

Figure 5.17 shows surface profiles measured in the composite area. Pillar and epoxy regions in the randomised composite are difficult to identify owing to the arbitrary geometry and dimensions of the pillars, whereas pillar edges in the diced composites are more visible due to the square geometry and repetition of the pillars. The height variation between the ceramic and single crystal pillars and the polymer is limited to be less than 120 nm, which corresponds to the previous work [149].

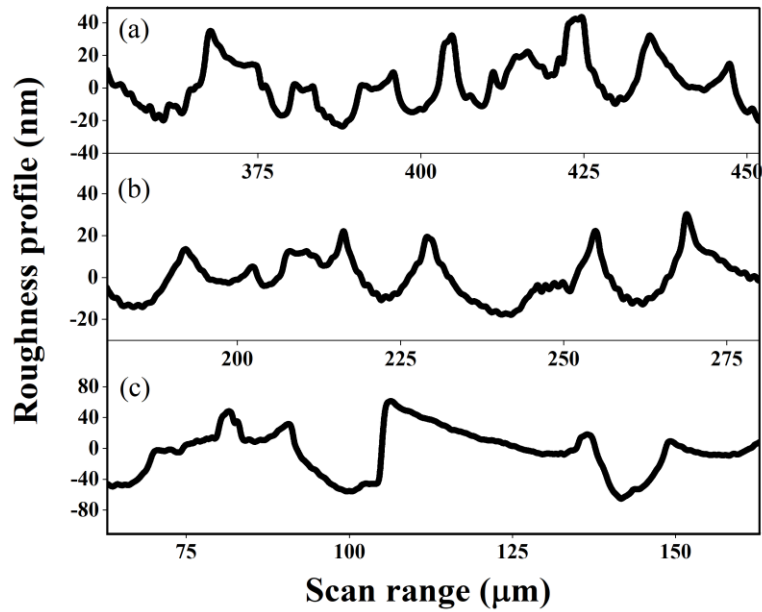


Figure 5.17 Surface profiles in the composite area of (a) randomised ceramic, (b) diced ceramic and (c) diced single crystal piezocomposites measured after polishing.

A concern about the height differences in the composites is that the large variation might initiate the delamination of a deposited electrode in the subsequent processes. Thus, the characteristics of the interface between the composite region and the fan-out epoxy region were also explored from three samples and measured two sides of the interfaces.

Figure 5.18 shows examples of the height differences at the interface for all three composites. It was found that the fan-out epoxy was higher than the composite regions with the difference at the interfaces for the randomised composite, diced ceramic and diced single crystal composite of  $\sim 2.42 \pm 0.6$ ,  $2.27 \pm 1.35$  and  $2.54 \pm 1.15 \mu\text{m}$ , respectively. This indicated the presence of the bumps surrounding the composite regions as a bowl shape because of the differences in the elastic properties of the two materials, as mentioned previously.

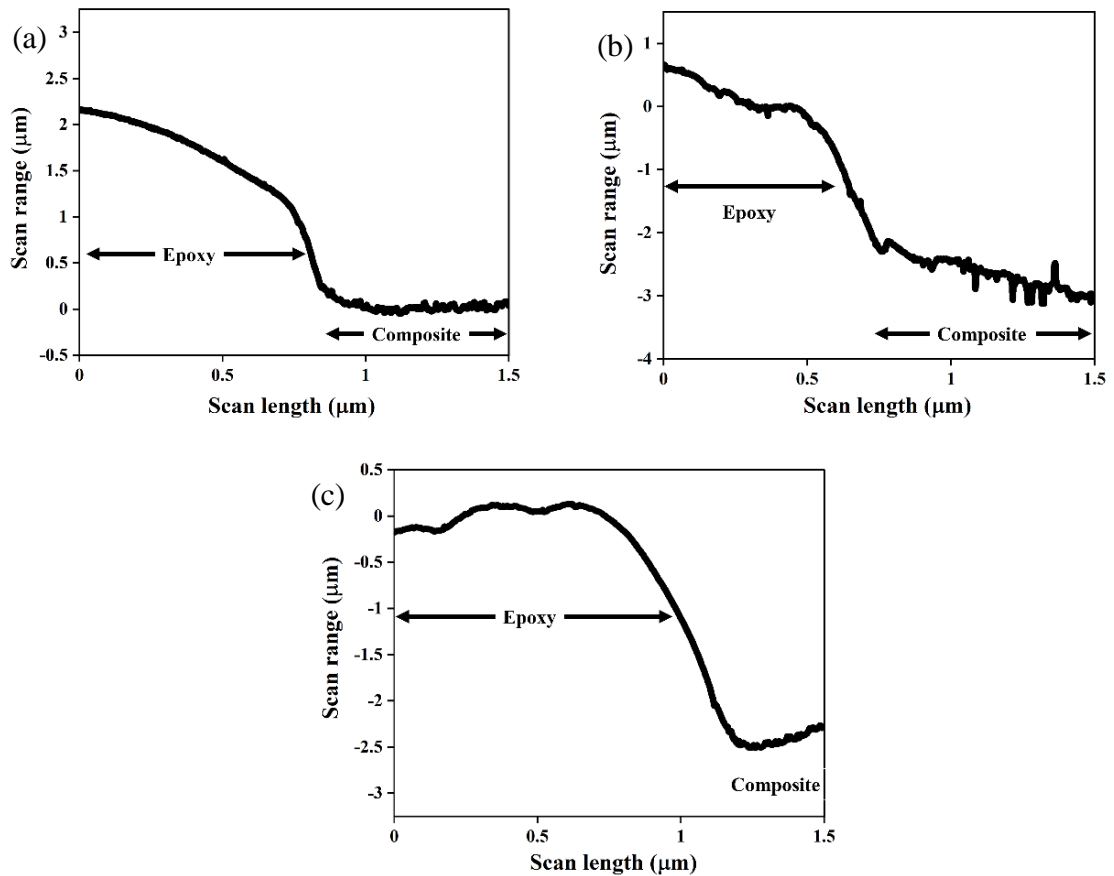


Figure 5.18 Surface profiles at the interfaces between the composite area and the fan-out epoxy of (a) randomised ceramic, (b) diced ceramic and (c) diced single crystal piezocomposites measured after polishing.

## 5.4.2. Surface Roughness

Optical microscope images of composite surfaces after polishing are presented in Figure 5.19. The randomised composite has pinholes in the fan-out epoxy and composite region due to the trapped bubbles generated during insufficient degassing conditions and curing at the elevated temperatures as previously described in Section 5.2.3. Missing ceramic grains were found in the diced ceramic composite because the grains may be partially detached after dicing due to the stresses generated and then be removed during lapping and polishing [149]. The diced single crystal composite, however, possessed a much smoother surface than the other composites because it has no grains to be pulled out. However, the edges of the pillars remained chipped. These features were possibly created during the dicing process, since the single crystal material is more fragile than ceramic [12], [70], [116].

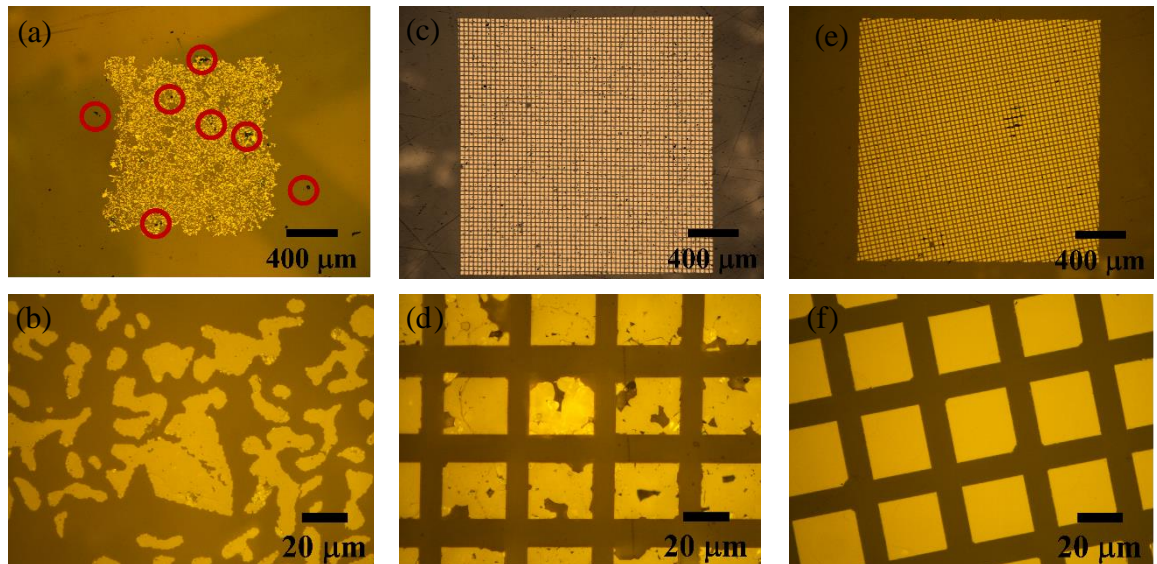


Figure 5.19 Optical micrographs of surfaces after polishing of 1-3 (a-b) randomised composite, (c-d) diced ceramic composite and (e-f) diced single crystal composite.

Figure 5.20 shows 3D optical profiler images of 1-3 piezocomposites. The average surface roughness values measured by the optical profiler of five samples for the randomised, diced ceramic and diced single crystal composites were around  $23.18 \pm 1.03$ ,  $27.61 \pm 1.26$ , and  $21.66 \pm 0.94$  nm, respectively. The surface roughness values of the ceramic composites were larger due to the influence of the pinholes, cracks and pulled-out grains, as illustrated in Figure 5.20 (a–b). The single crystal composite was relatively smoother than the ceramic composite, by 21.5%, owing to no grains being pulled out, which corresponds to the microscope and 3D images.

It can be seen that cracks and clefts were found in the diced composites, corresponding with published evidence [149], (Figure 5.20 (b) and (c)). These defects could initiate material breakdown during the poling due to short-circuit through channels in the defects. The formation of cracks, attributed to residual stresses, occurred in the process of curing the epoxy [219]–[221]. In this thesis, one cure-cycle at  $60^{\circ}\text{C}$  for 2 hr with the heating ramp rate from  $40 - 60^{\circ}\text{C}$  of  $1^{\circ}\text{C}/\text{min}$  was used to avoid prolonging the process, which might cause depoling of the piezoelectric materials. More importantly, the slow heating rate minimised residual stresses by increasing time of stress relaxation [220]. In addition, it extended the period of thermal expansion until the end of the cure cycle, resulting in the thermal expansion being more effective in the curing cycle. This meant that the compressive stresses originated from the crosslinking shrinkage during curing and thermal shrinkage during cooldown was minimised by compensation of the tensile stresses in the cure cycle[220]. Nevertheless, some residual stresses remained, leading to cracks existing in the composites. In addition, the formation of cracks is potentially attributed to the influence of thermal mismatch between

the epoxy and ceramic pillars. The epoxy has a higher thermal expansion coefficient,  $\alpha_{\text{epoxy}}$ :  $45 - 65 \times 10^{-6} (\text{°C})^{-1}$  than that of the ceramic,  $\alpha_{\text{ceramic}}$ :  $0.5 - 15 \times 10^{-6} (\text{°C})^{-1}$ , leading to greater epoxy deformation during cooldown [101].

Regarding the presence of clefts, their shape seemed identical to the dimensions of kerfs. A possible reason is due to trapped bubbles blocked in the microchannels, thereby inhibiting fluid flow [199], [222]–[224]. As a result, incomplete filling was observed, as shown in Figure 5.20 (f). A double cure cycle is therefore recommended because the first dwell time at a low temperature allows the entrapped bubbles to flow up to the surface of the epoxy mixture and subsequently disappear while polymer crosslinking is carried out at a higher temperature in the second dwell time [219]. However, this cycle is longer, which may provide adverse effects with the depoling of the piezoelectric materials and economic issues.

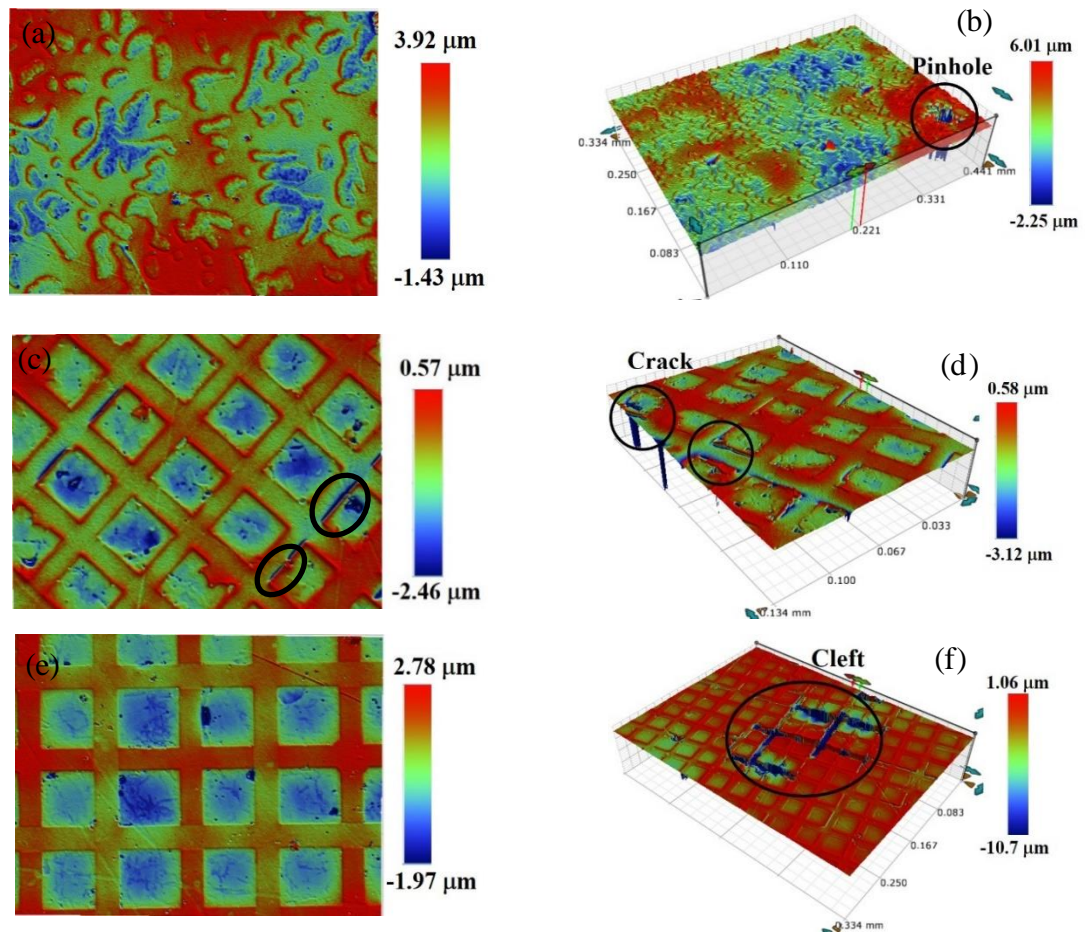


Figure 5.20 Three-dimensional optical profiler images of (a – b) randomised ceramic, (c – d) diced ceramic and (e – f) diced single crystal piezocomposite surfaces (magnification 50 x). Images (a, c, and e) are the composite surfaces, images (b, d and f) are the interface regions between the composite area and the fan-out epoxy.

## 5.5. Summary

This chapter focused on the fabrication of 1-3 piezocomposites made by gel-casting and modified dice-and-fill methods. The study of the gel casting process was conducted by investigating the influence of the particle size distribution on the rheological behaviour of the PZT slurries, the physical and mechanical properties of green bodies and sintered samples, and the electrical properties of bulk gel-cast samples and 1-3 randomised composites. Furthermore, the study of dicing parameters that are suitable for PZT piezoceramic and PIMNT single crystals was investigated. The electrical properties of the 1-3 diced piezocomposites were observed and the surface characteristics of all three composites were also studied to ensure that the composites were sufficiently smooth and planar before electrode patterning.

The results obtained can be summarised as follows:

- The soft agglomerates of the as-received PZT powders were broken down by the vibro-milling method with different milling times. The particle size distribution curves of the milled powder showed a monomodal distribution, with a mean particle size in the range 1.22 - 1.61  $\mu\text{m}$ , with respect to the milling time.
- The viscosity of the slurries increased with the decrease of the mean particle size. All slurries possessed both shear thinning and thickening behaviour, due to the influence of the flocculation generated at higher shear rates. However, the shear thickening behaviour was more accentuated in the slurry made with the finest powder, mean particle size 1.22  $\mu\text{m}$ , since the fine powder is most likely to re-agglomerate and form flocculation, owing to the more attractive interparticle interactions.
- The green body samples prepared with the hydantoin resin had physical properties close to those published in previous work. A higher green strength of  $49.7 \pm 2.49$  MPa was achieved, compared to the work using the EGDGE resin ( $\sim 38$  MPa). This was attributed to the better water solubility of the hydantoin resin, and the higher solid loading achieved.
- The density of the sintered samples was approximately  $7.50 \pm 0.62$  g/cm<sup>3</sup>, providing relative density of  $93.2 \pm 1.69\%$ . Porosity was found in the microstructure of the sintered samples. It possibly caused by the internal stresses generated from gas accumulation of resin decomposition. However, the presence of some pores was located at junctions between grains. This was attributed to the effect of flocculation

of the excess resin. It introduced non-uniform packing of particles in some regions and subsequently caused pores after the burn-out process. This produced an inhomogeneous microstructure, resulting in the differential densification. For this reason, pores at the junctions were observed.

- 1-3 connectivity randomised composites with feature dimensions of 2 - 50  $\mu\text{m}$  were fabricated via the combination of gel casting and micromoulding. The powders milled for 39 and 48 hrs were used to prepare the slurries for gel casting. A high  $AR$  of 23 could be achieved, which was beneficial for the subsequent process steps.
- The electrical impedance characteristics of the 1-3 randomised piezocomposites showed a smooth profile. This was attributed to the randomised pattern and the high  $AR$  of 1 – 25, which simultaneously cancelled the spurious modes and raised the thickness resonance frequencies to be dominant over the other modes.
- The diced composite materials were achieved through the use of a modified dicing method to produce the structure of a 1-3 piezocomposite of 38  $\mu\text{m}$  pitch, providing an  $AR \sim 2$ . Diced ceramic piezocomposites were produced by a single pitch dicing method, with 90% yield of the surviving pillars. Diced single-crystal piezocomposites were manufactured through the double pitch dicing method, providing over 99% yield; however, this method produced uneven pillar geometries because of misalignment of the second series of cuts. In addition, the pillar height is restricted in order to maximise yield of the survival pillars.
- The electrical impedance characteristics of the 1-3 diced piezocomposites showed spurious modes coupled in at their resonance frequencies. This was attributed to the periodicity of the square pillars and low  $AR$ . The  $k_{eff}$  value of the diced single crystal piezocomposites were greater than the diced ceramic and the randomised piezocomposites, owing to the superior properties of the single crystal material itself. However, the dielectric properties of all three composites were lower than their parent piezoelectric materials, as expected, due to the inclusion of the epoxy.
- Height variation was usually found in the composites, owing to the effects of dissimilarity in the elastic properties of the two materials on the mechanical processing. The average surface roughness values for the randomised, diced ceramic and diced single crystal composites were measured to be  $23.18 \pm 1.03$ ,  $27.61 \pm 1.26$ ,

and  $21.66 \pm 0.94$  nm, respectively. The single crystal composite was relatively smoother than the ceramic composites (by 21.5%), owing to no grain pull-out.

- Defects were found in composites. The formation of pinholes and clefs caused by insufficient vacuum conditions during epoxy impregnation and the constrained time during heating to allow bubbles to escape led to bubble entrapment. The presence of the bubbles inhibited fluid flow into the microchannels, resulting in the clefs between pillars. In addition, cracking originated from the residual stresses developed during the curing process, which was difficult to avoid due to the influence of thermal mismatch between the epoxy and ceramic pillars.

# Chapter 6 Microfabrication

## 6.1. Introduction

This chapter starts by describing, in Section 6.2, the microfabrication of array elements patterned on different substrates to obtain a kerfless structure using a photolithographic process based on a bilayer lift-off (BLO) process. This process has been extended considerably from the basic process outline provided in Chapter 4. Si wafer and epoxy substrates were used as preliminary samples prior to work with the composite substrates. The developed BLO processes are examined in this chapter in order to achieve a high yield of active elements patterned directly on composite surfaces and to validate the reliability of the process. In the array patterning on the diced composites, the arrays were aligned at an oblique angle relative to the lines of pillars in order to avoid misalignment of the element and to reduce the spurious modes. However, this mean did not adopt to the randomised composites due to the random distribution of pillars and spacing in the composite itself.

The process is followed by lapping to achieve the required thickness, which is suitable for ~30 MHz  $\mu$ US array transducers. Once the required substrate thickness of approximately 50  $\mu$ m is achieved, the composite is very fragile. The sample must be released from its glass carrier very carefully to avoid tearing it, destroying the continuity of the array elements. An effective method for removing the material from the carrier is described in Section 6.3.

## 6.2. Microfabrication of Array Element Patterning

A photolithography process based on a bilayer lift-off process was developed to create array elements with an element pitch of 50 -  $\mu$ m (35 -  $\mu$ m element trace and 15 -  $\mu$ m kerf) on 1-3 piezocomposites. Two processes with different primary resists, including LOR3A and LOR10A, were explored. The baking temperature and time controls the undercut rate of the primary resist and improve the resist adhesion, as mentioned in Section 3.3.2. In this study, a temperature of 150 °C was used throughout, although a baking temperature of 150 - 190 °C is typically recommended for the LOR resists [182]. However, the temperature stability of the piezoelectric materials must be considered, since they will depole at sustained high temperatures, leading to poor functional properties of the transducer devices. For example, the PIMNT single crystal material must not be processed at a temperature beyond its  $T_C$  (200 °C) because the material will lose its piezoelectric and electromechanical properties, e.g.,  $d_{33}$  and  $k_t$ , at the  $T_C$ . The S1818 photoresist was used as the secondary resist coated on top of the

primary one. Its recommended spinning speed and baking conditions are shown in the literature [183], [225].

### 6.2.1. Development Process I: LOR3A

This section describes the processes using the LOR3A/S1818 resists to establish a bilayer resist profile on different substrates. The process was initially studied and validated on the Si wafers and epoxy substrates, prior to patterning the fine array elements on the 1-3 composite surfaces. The process optimisation adopted for each substrate is summarised in Table 6.1 and the rationale for the parameters defined in it are described in the next three subsections.

Table 6.1 Process flow of bilayer lift-off process for Si, epoxy and composite substrates based on LOR3A/S1818 resist.

Parameter	Si wafer	Epoxy	Composite
<b>Surface cleaning</b>	Sonication	Wiping	Wiping
<b>Solvent</b>	Opticlear, Acetone, IPA, RO	IPA, RO	IPA, RO
<b>Dehydration (°C / min)</b>	150/20	-	-
<b>Primary resist</b>	LOR3A	LOR3A	LOR3A
<b>Spin speed (rpm / sec)</b>	4000/30	4000/30	4000/30
<b>Bake (°C / min)</b>	150/5	150/5	150/5
<b>Secondary resist</b>	S1818	S1818	S1818
<b>Spin speed (rpm / sec)</b>	4000/30	4000/30	4000/30
<b>Bake (°C / min)</b>	115/3	115/3	115/3
<b>Exposure time (sec)</b>	6	6	6
<b>Development time in MIF319 developer (sec)</b>	160	160	160
<b>Oxygen plasma treatment (Watt/min)</b>	150 /1	150 /1	150 /1
<b>Metallisation (Ti/Au; nm)</b>	20/180	20/180	20/180
<b>Lift-off in strippers</b>	1165	1165	1165
<b>Time (hr)</b>	1	1.30	1.30

Opticlear, National Diagnostics, Scientific Laboratory Supplies Ltd, Nottingham, UK RO: reverse osmosis water

### 6.2.1.1. Si wafer Substrates

For the Si wafers, substrate preparation, including chemically cleaning via sonication and dehydration, is necessary to remove any contamination and dry any moisture on the substrates prior to resist spinning. Contamination and moisture cause poor adhesion between a resist and the substrate, resulting in delamination of the resist [16]. The bilayer resist of LOR3A/S1818 was spun at 4000 rpm for 30 sec. To study the influence of time of baking at 150 °C on the undercut and cleanliness of the resist profile after the development step, the baking time of the LOR3A was tested at 5, 6, 7 and 8 min. Then, the coated substrate was subjected to UV exposure for 6 sec, followed by development in MIF319 developer for 160 sec.

Figure 6.1 shows a high magnification SEM micrograph of the cross section of bilayer resist profiles established on Si wafers. The LOR3A and S1818 resist thicknesses of  $0.23 \pm 0.02$  and  $1.83 \pm 0.04$   $\mu\text{m}$  were obtained. Undercuts on the order of  $0.65 \pm 0.04$ ,  $0.55 \pm 0.01$ ,  $0.45 \pm 0.05$ , and  $0.29 \pm 0.02$   $\mu\text{m}$  were achieved with respect to baking times of 5, 6, 7 and 8 min, respectively. The undercut decreases linearly as the baking time is increased as shown in Figure 6.2, in agreement with the literature [226]–[228].

Views of the surface of the bilayer resist profile for each baking time are demonstrated in Figure 6.3. The light color represents the exposed resist, and the darker region represents the sacrificial photoresist mask, as labelled in Figure 6.3 (b). At a constant development time, the straight linewidth of the exposed resist in the middle part of the pattern for all conditions is approximately  $34.8 \pm 0.18$   $\mu\text{m}$ . This value is calculated based on mark references alongside the array pattern as given in Section 4.4. More importantly, the resist profiles of the first three baking times provide a relatively wide undercut and a clean exposed surface. However, the profile for the baking time at 8 min shows residual resist as displayed in Figure 6.3 (d). This may cause shape uniformity and delamination of the particular element during the lift-off process, since the residual resist underneath the element film will be dissolved by resist removers.

Owing to the possibility of depoling the piezoelectric material, a shorter period of baking time is more desirable. Thus, the baking condition of 150 °C/5 min was chosen for further processes. The cross-section of the bilayer resist shows that the undercut and pattern were developed without distortion with an average S1818 width of  $14.46 \pm 0.06$   $\mu\text{m}$ , as demonstrated in Figure 6.4. Prior to metallisation, surface modification via oxygen plasma treatment is necessary to promote good adhesion of film and substrate by removing any

residual resist and particles, which may occur after the development step. Thin films of Ti /Au with a total thickness of 200 nm were deposited on the wafers, followed by lift-off in a 1165 remover for 1 hr at  $T_R \sim 22$  °C. Solvent blowing for a few seconds using a pipette was required to remove the metals that was stripped out from the element pattern for few seconds before finishing the lift-off process. The resulting high quality of array elements with an average trace width of  $34.52 \pm 0.56$   $\mu\text{m}$  is shown in Figure 6.5. Thus, this recipe was further used for the epoxy substrate.

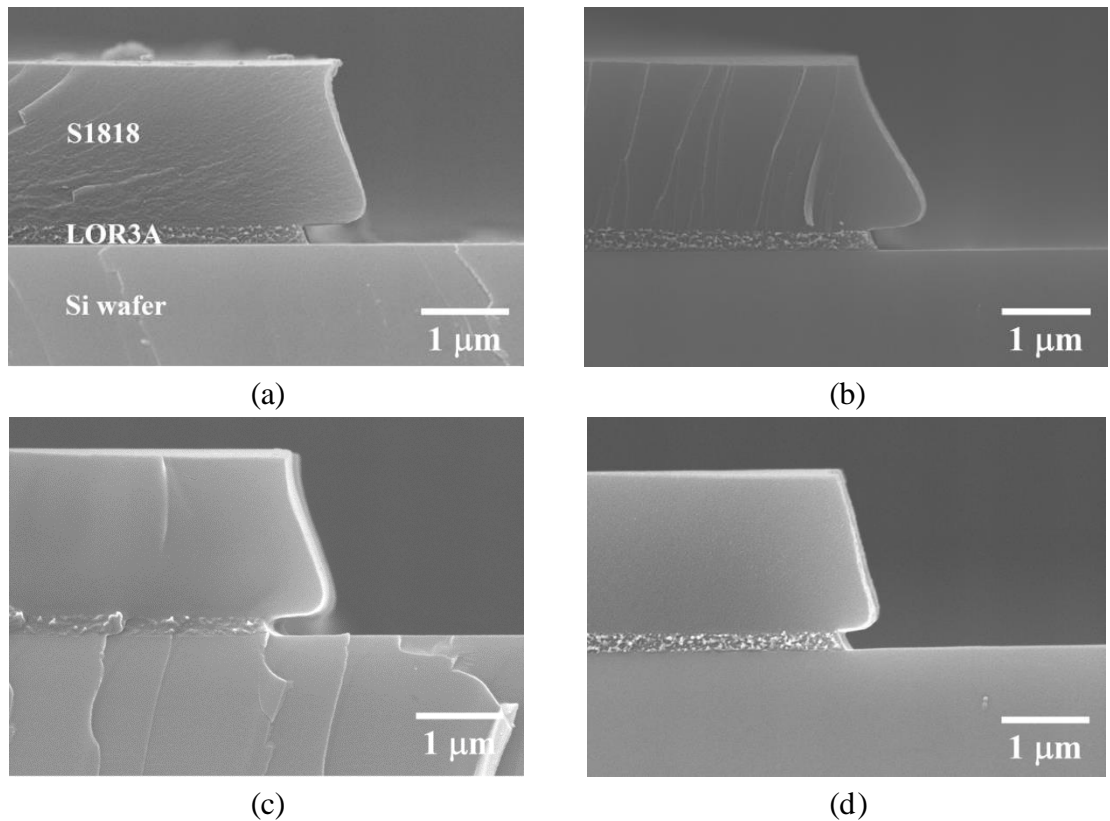


Figure 6.1 SEM micrographs showing the undercut geometry of the LOR3A/S1818 bilayer resist profiles on Si substrates baked on a hot plate with varying baking time (a) 5, (b) 6, (c) 7, and (d) 8 min.

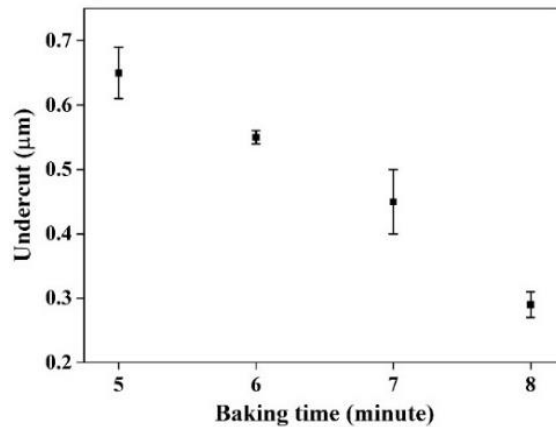


Figure 6.2 Undercut width generated with a constant developing time of 160 sec as a function of baking time.

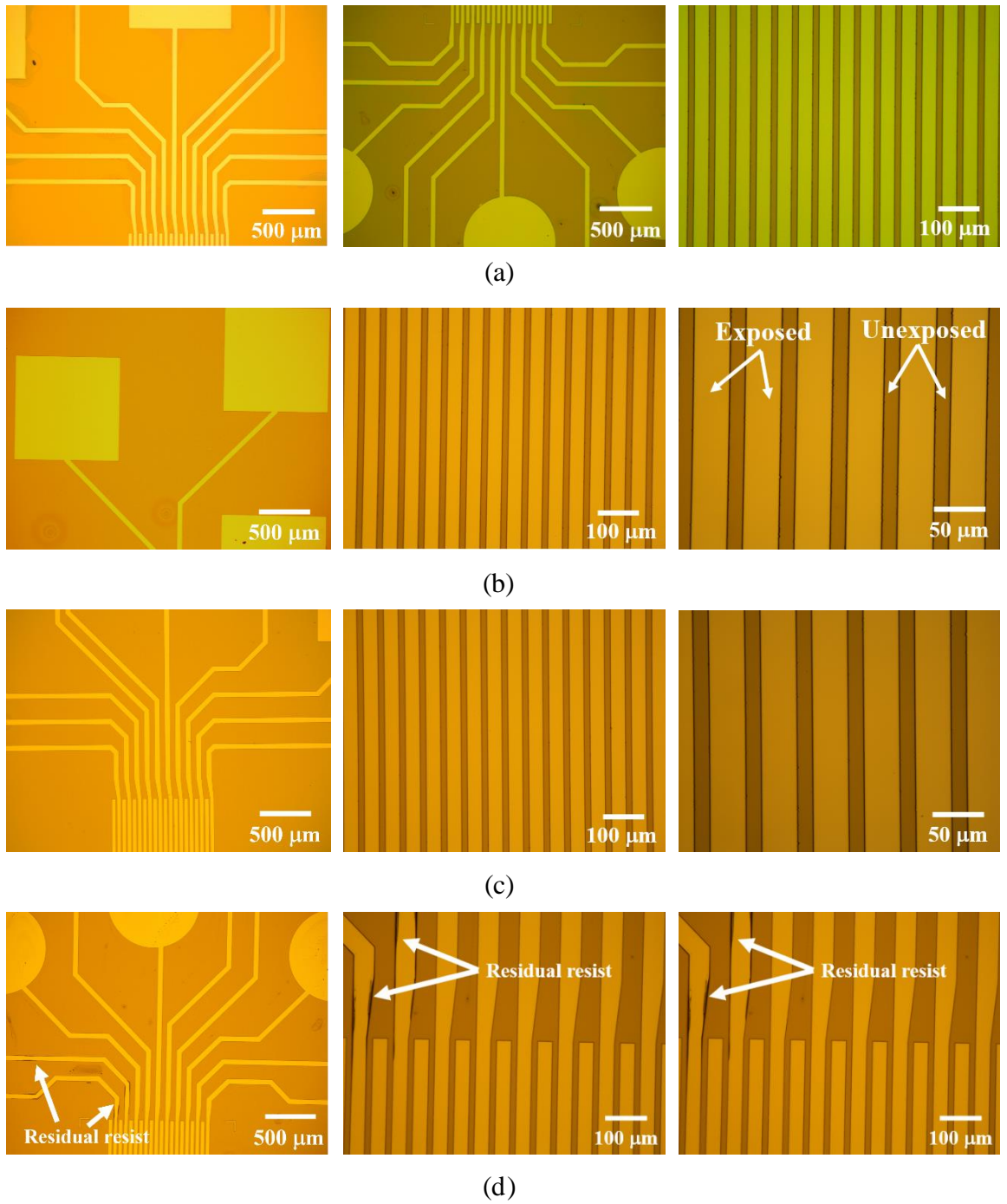


Figure 6.3 Optical micrographs of bilayer LOR3A/S1818 resists on Si substrates with varying LOR3A baking time at (a) 5, (b) 6, (c) 7, and (d) 8 min.

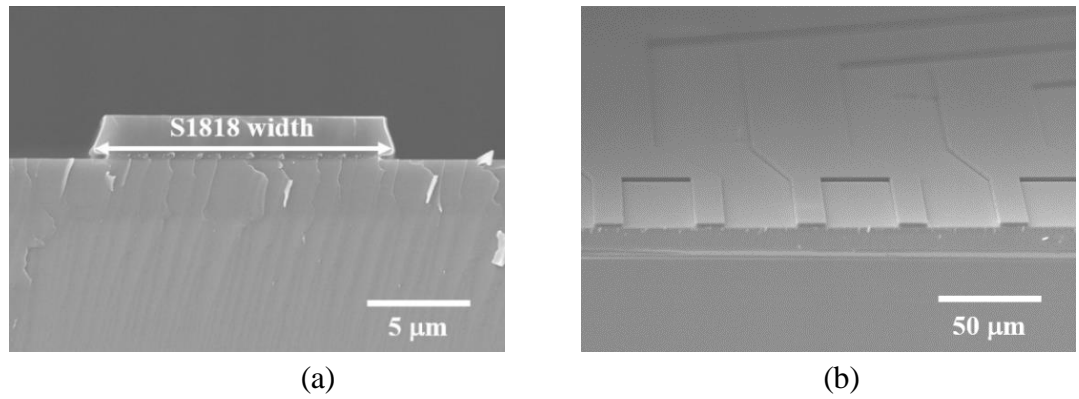


Figure 6.4 SEM micrographs showing bilayer LOR3A/S1818 resists on Si substrates (a) a cross-section with an average S1818 width of  $14.46 \pm 0.06 \mu\text{m}$  and (b) overview of bilayer resist profiles baked at  $150 \text{ }^\circ\text{C}$  for 5 min.

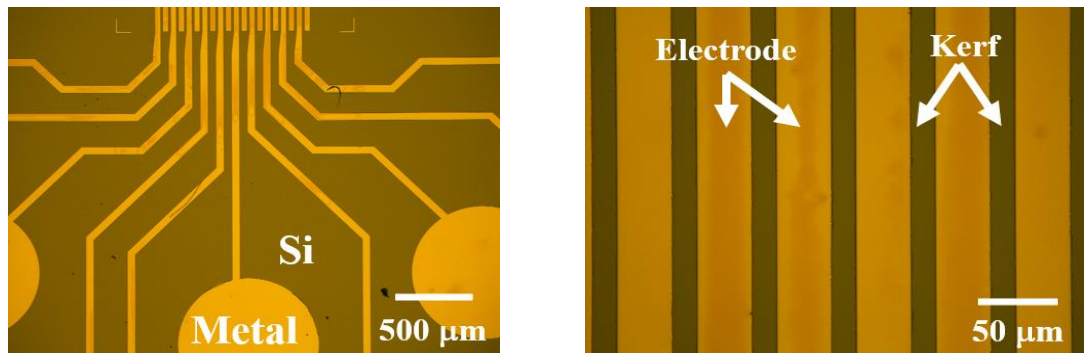


Figure 6.5 Optical micrographs of the 50- $\mu\text{m}$  array elements with fan-out patterned on a Si substrate with the baking conditions of  $150 \text{ }^\circ\text{C} / 5 \text{ min}$ . Linewidth after development:  $35.04 \pm 0.56 \mu\text{m}$ ; element traces after lift-off:  $34.52 \pm 0.56 \mu\text{m}$ .

### 6.2.1.2. Epoxy Substrates

The optimised conditions identified on the Si wafer were then applied to the epoxy substrates. The surface roughness of the epoxy measured by the optical profiler was approximately  $50 \pm 1.41 \text{ nm}$ . In this case, the sonication and dehydration steps are unnecessary because the former might break the pillars in the composite and, the latter may cause degradation in the piezoelectric properties.

It was previously reported that a clean resist profile could be achieved on this material [178], [183]. Thus, the epoxy surface was cleaned by solvent wiping with a sponge and subsequently dried by blowing with a nitrogen gun prior to applying the resist. Figure 6.6 (a-b) shows the temporary photoresist mask with a high quality, of the narrow linewidth created on the epoxy surface. The exposed area reveals the true status of the epoxy surface with scratches produced from the abrasive in the lapping process. Moreover, no residual resist remains on the exposed area.

The sample was subjected to metallisation to produce 200 nm Ti/Au films and the lift-off process was applied by immersion in a 1165 stripper for 1 hr and 30 min in  $T_R$ , followed by

the solvent blowing for a few seconds. The lift-off process of the epoxy required longer stripping than the Si wafer due to the good adhesion of the epoxy. Figure 6.6 (c-d) shows the array elements with fan-out elements patterned on the epoxy substrate. Although the wrinkles of the thin film were observed, straight and uniform traces of widths of  $34.3 \pm 0.17 \mu\text{m}$  were established.

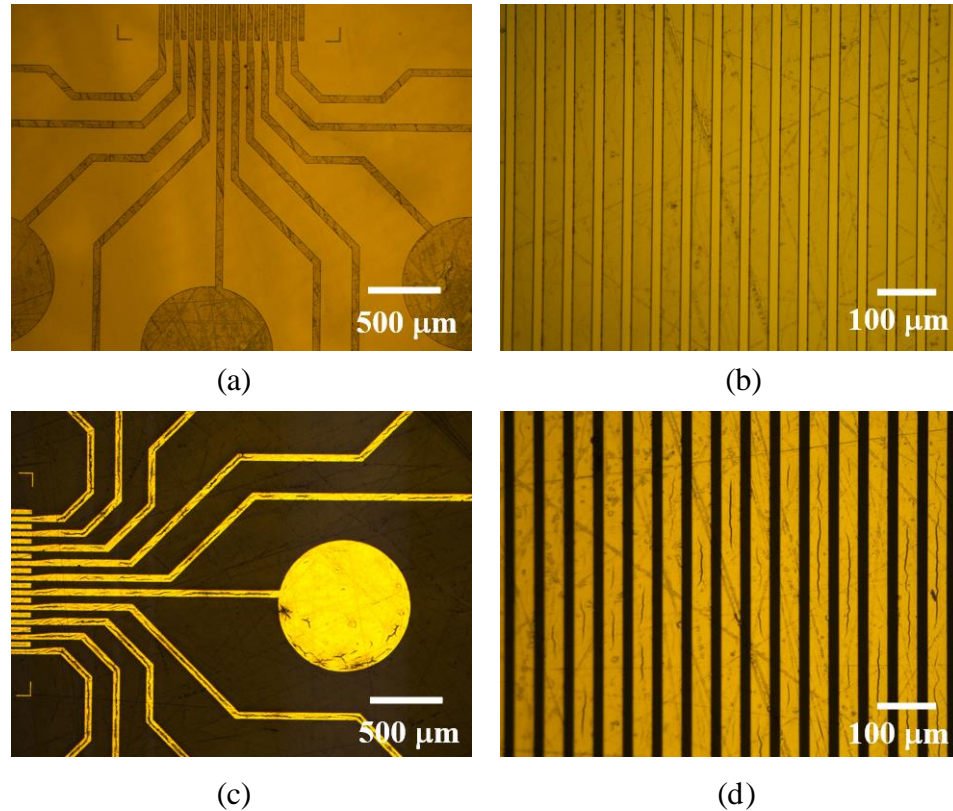


Figure 6.6 Optical micrographs of (a-b) bilayer LOR3A/S1818 resist profiles on epoxy substrates made with the LOR3A baking condition at 150 °C for 5 min and (c-d) the 50- $\mu\text{m}$  element pitch patterned Ti/Au array elements with fan-out after lift-off in 1165 stripper.

### 6.2.1.3. Composite Substrates

After the process validation for the epoxy substrates, the same parameters were then adopted for the 1-3 piezocomposite substrates. The samples were subjected to bilayer photoresist spinning, baking, exposure, and development processes as detailed in Table 6.1. Figure 6.7 shows the pattern of the sacrificial mask on a composite substrate. The exposed areas present the true status of the composite surface with scratches produced during the lapping process, as illustrated in Figure 6.7 (a). Meanwhile, dull regions represent spaces between array elements when the metal is deposited. A straight linewidth and cleanliness of the mask were achieved on all composites. Then the samples were subjected to metallisation to deposit the thin film; this was then followed by a lift-off process for 1 hr and 30 min at  $T_R$  and the solvent

blowing for 2 min to ensure that the stripped metals were blown away from the element pattern, with particular care being taken in the composite region.

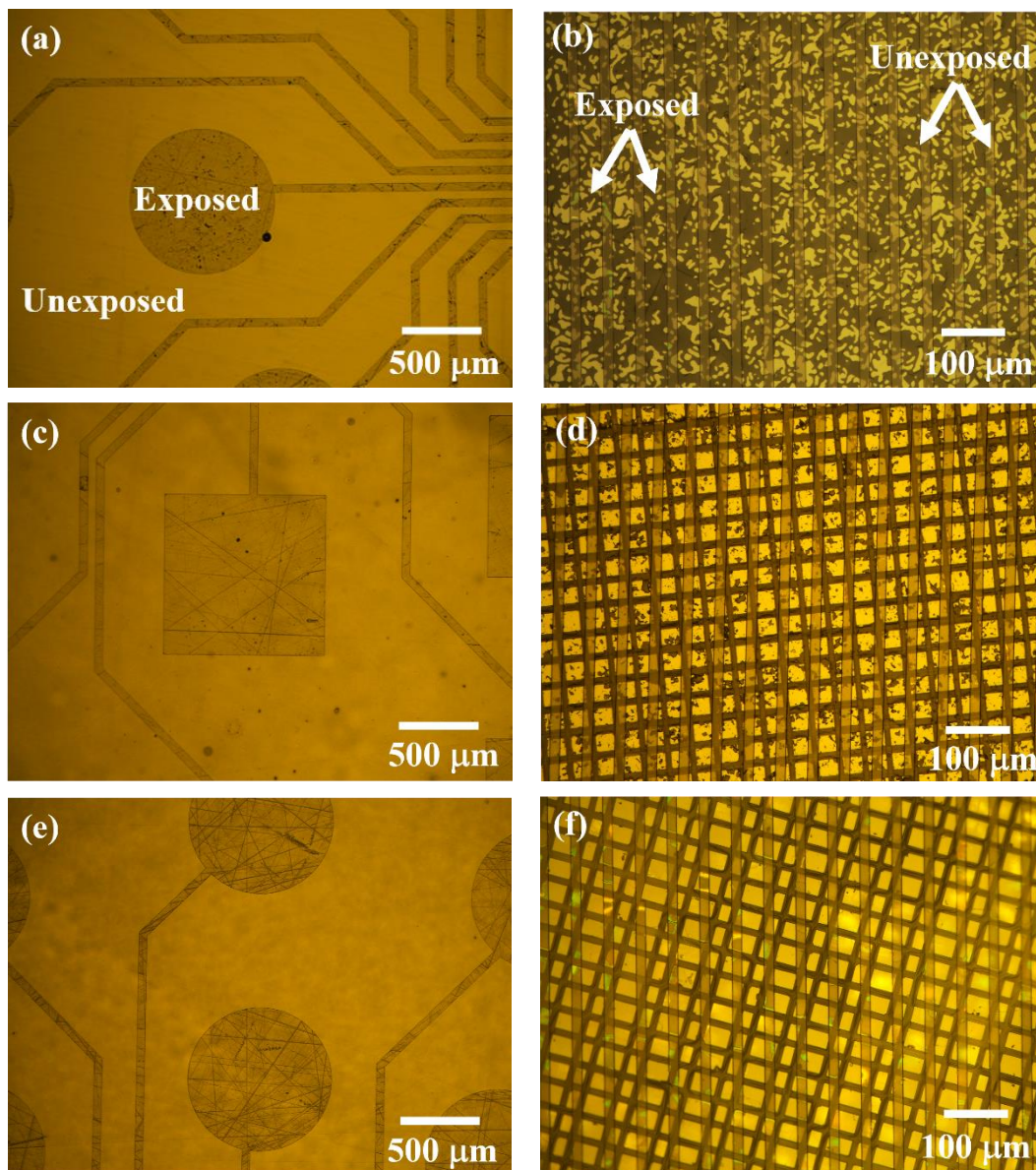


Figure 6.7 Optical images of bilayer LOR3A/S1818 resist profiles established on surfaces of 1-3 (a) randomised ceramic (b) diced ceramic and (c) diced single crystal composites.

Measurement of the traces demonstrated an average width of  $34.4 \pm 0.17 \mu\text{m}$  was attainable on the composite surfaces, as presented in Figure 6.8. The diced composites show traces with relatively straight edges, whereas shape deformation of the traces is seen in the randomised composite, as demonstrated in Figure 6.8 (a). This is because the trace shape varied along with the irregularly shaped pillars in the composite region. In addition, the discontinuities of some elements are evident in the diced single crystal composite (Figure 6.8 (c)), which corresponds to the cracks previously described in Section 5.4.2. 75% yield of high-quality traces was achieved by this process, determined by electrical continuity and electrical impedance characteristics, and by lack of delamination. The former measurements are given

in Section 7.2- 7.3.1, while the latter was observed under an optical microscope. This indicates that the yield does not only depend on the efficient productivity, but also relies on the quality and perfection of the composite substrates. For example, yield is affected by the cleavages and cracks at the interface of the pillar and epoxy, and pinholes as exhibited in Figure 6.8 (c)

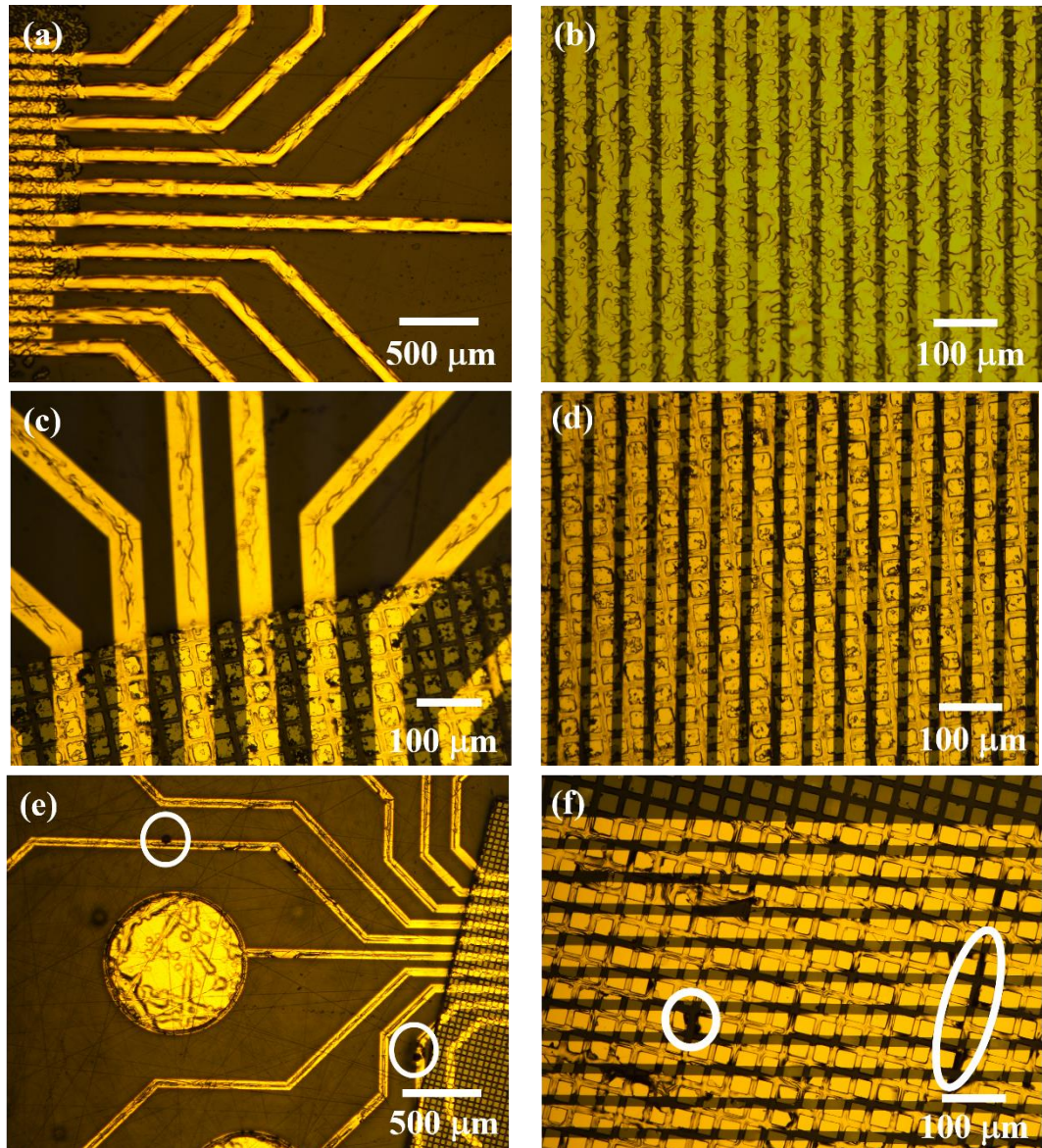


Figure 6.8 Optical micrographs of 50-μm pitch Ti/Au array elements with fan-out patterned on surfaces of 1-3 (a) randomised ceramic (b) diced ceramic and (c) diced single crystal piezocomposites using a LOR3A/S1818 bilayer resist profile with the LOR3A baking conditions of 150 °C/5 min.

Interestingly, shape deformation and wrinkles are only observed on the metal films deposited on the fan-out epoxy. This can be explained by solvent permeation into the epoxy surface: most of the lift-off solvents are categorised as polar liquids which greatly permeate into most of the polymers [179].

Although, a curing process of the epoxy at elevated temperatures was suggested to enhance the environmental resistance of the epoxy, e.g., chemical and heat resistance, by increasing its glass transition temperature,  $T_g$ , to be 100-120 °C [149]. Where,  $T_g$  refers the temperature at which polymers change from a hard condition to a rubbery condition. However, with the present processes, the samples are exposed to cycles of elevated temperatures, including wax melting in the lapping and polishing steps (60 °C) and baking of the resist in the microfabrication process (115-150 °C), and high vacuum in metallisation ( $8 \times 10^{-9}$  mbar). These cyclic environments have the potential to accelerate the degradation of its  $T_g$  by breaking down the crosslink bonds in the epoxy, leading to chemical decomposition and deterioration of the epoxy properties e.g., cohesive strength and chemical and heat resistances [179], [229]. Thus, when the entire sample was immersed for 1 hr and 30 min, the solvent penetrated through the re-entrants in the bilayer resist profile to cause bottom-up resist dissolution. Once the resist dissolved, the solvent permeated into the exposed epoxy surface and the surface underneath the metal fan-out easily, resulting in the metal swelling and subsequent deformation. In addition, the use of solvent blowing for 2 min was used in the composite substrates to ensure that any residual metals were completely removed from the composite region, whereas this mean did not adopt for the pure epoxy substrates. This potentially accelerated the solvent permeation into the epoxy region due to repulsive force during blowing, resulting in a higher degree of the metal deformation in the epoxy region of the composite substrates

### **6.2.2. Development Process II: LOR10A**

In an attempt to overcome some of the problems discussed in the previous section in the fabrication of suitable electrode element structures on the composite surfaces using the LOR3A/S1818 resist system, an alternative system incorporating LOR10A resist was investigated. This section describes the study of the optimisation for the LOR10A resist established on Si, epoxy, and composite substrates. LOR10A has the advantage that it allows an increase in the thickness of the metal film. Typically, the primary resist should be thicker than the thin film by around 33% for a clean lift-off process and good edge definition [155], [157]. The aim of the thicker element film is to ensure uniformity and increase element continuity of the traces over the composite region. In addition, it is essential when using high power devices because it provides increased current capability [230].

As a result of the previous development process (I), the baking condition of the LOR10A of 150/5 °C/min was maintained throughout the process. The other control parameters were set as given in Table 6.1. Si substrates was also used as a preliminary sample in this process to

investigate influence of spinning conditions on LOR10A thickness. Because the exposure time of 6 sec was successfully used for all substrates in the previous process, hence, the development time in this development process II was not fixed in order to allow the thick resist of LOR10A to be completely dissolved. The optimised parameters used for each substrate are summarised in Table 6.2.

Table 6.2 Process flow of bilayer lift-off process for Si, epoxy and composite substrates based on LOR10A/S1818 resist.

<b>Parameter</b>	<b>Si wafer</b>	<b>Epoxy</b>	<b>Composite</b>
<b>Surface cleaning</b>	Sonication	Wiping	Wiping
<b>Solvent</b>	Opticlear, Acetone, IPA, RO	IPA, RO	IPA, RO
<b>Dehydration (°C/min)</b>	150/20	-	-
<b>Primary resist</b>	LOR10A	LOR10A	LOR10A
<b>Spin speed (rpm / sec)</b>	4000/30	4000/30	4000/30
<b>Soft bake (°C/min)</b>	150/5	150/5	150/5
<b>Secondary resist</b>	S1818	S1818	S1818
<b>Spin speed (rpm/sec)</b>	4000/30	4000/30	4000/30
<b>Soft bake (°C/min)</b>	115/3	115/3	115/3
<b>Exposure time (s)</b>	6	10	10
<b>Development time in MIF319 developer (s)</b>	300	180	180
<b>Oxygen plasma treatment (Watt/min)</b>	150 /1	150 /1	150 /1
<b>Metallization (Ti/Au; nm)</b>	30/470	30/470	30/470
<b>Lift-off in strippers</b>	1165	SVC14	SVC14
<b>Time (hr)</b>	1	1	1

Opticlear, National Diagnostics, Scientific Laboratory Supplies Ltd, Nottingham, UK RO: reverse osmosis water

#### 6.2.2.1. Si Wafer Substrates

The LOR10A resist was spun at speeds of 3000/30, 4000/30, and 6000/30 rpm/sec. Top views of the outcome of each spinning condition are demonstrated in Figure 6.9. The linewidth of the exposed resist at the middle part of the pattern for all conditions was approximately  $34.1 \pm 0.36 \mu\text{m}$ . The resist profile of all conditions provides a relatively clean

exposed surface. Figure 6.10 shows cross sections of a bilayer resist spun at different conditions, as mentioned above, on a Si substrate at high magnification. These conditions provide primary (LOR10A) resist thicknesses of  $1.02 \pm 0.01$ ,  $0.86 \pm 0.02$ , and  $0.51 \pm 0.01$   $\mu\text{m}$ , respectively. As expected, the resist thickness decreases as the spinning speed is increased as described in the literature [155]. Thus, the spinning speed of 4000/30 rpm/sec was chosen for metallisation with the Ti/Au film thickness of 30/470 nm and lift-off process. As a result, the primary LOR10A resist thickness is higher than that of the metal films by 41.8%, as demonstrated in Figure 6.11. In addition, it shows the discontinuity of the resists and the metal films, which will aid the lift-off process.

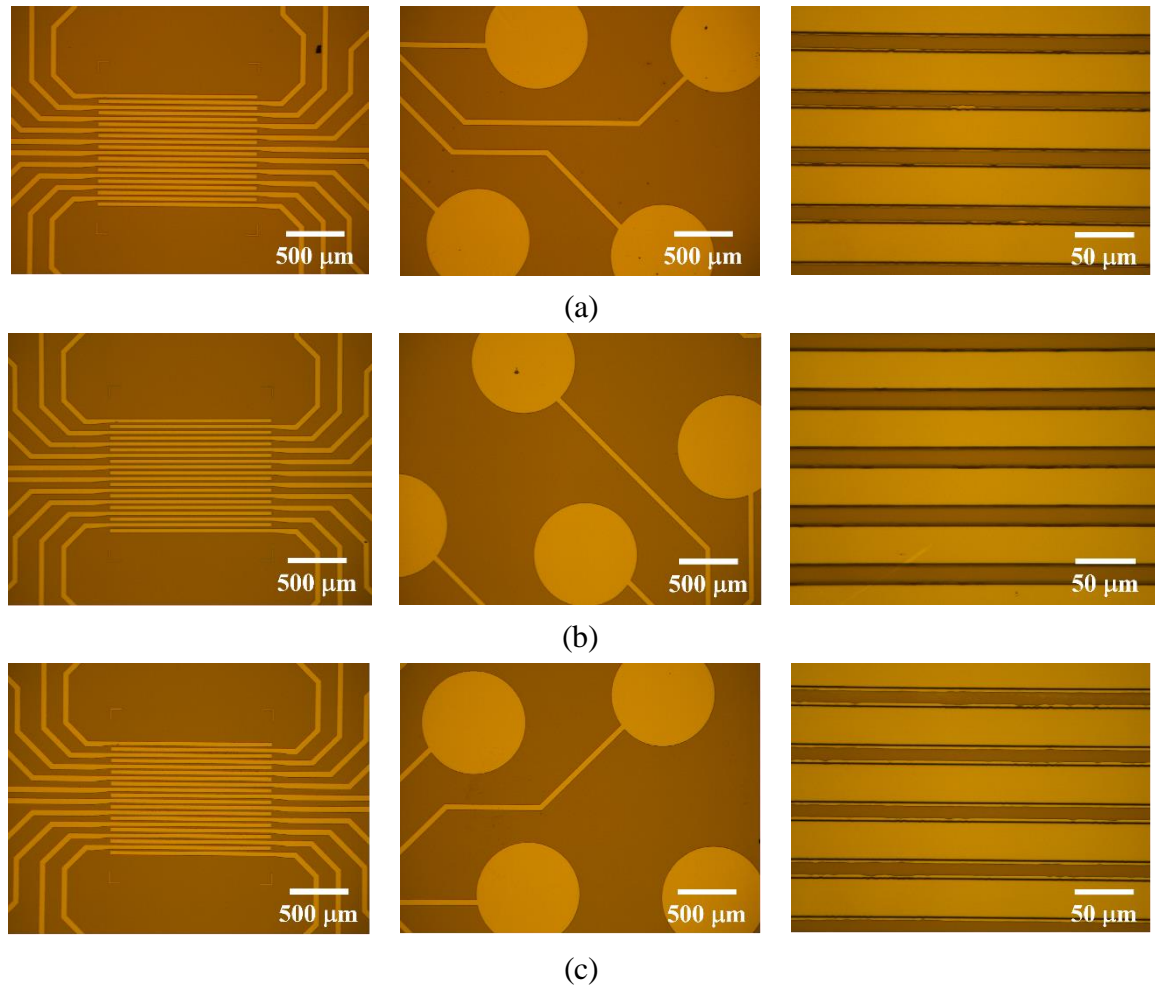


Figure 6.9 Optical micrographs of LOR10A/S1818 bilayer resist profiles established on Si substrates with LOR10A spin speeds of (a) 3000, (b) 4000, and (c) 6000 rpm.

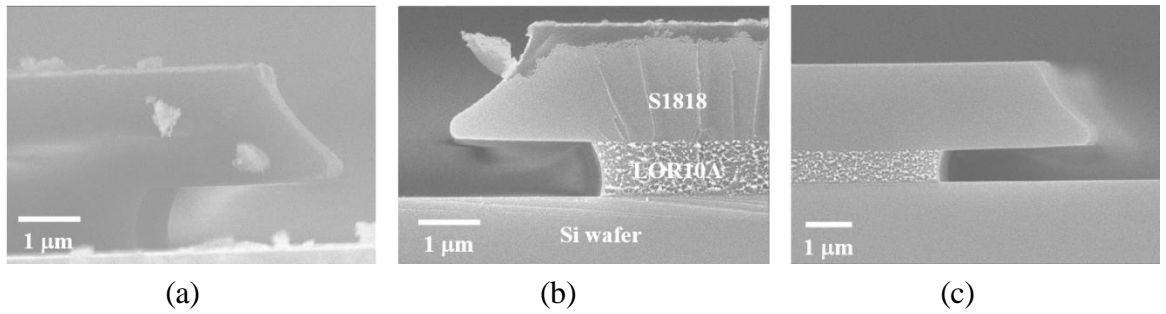


Figure 6.10 SEM micrographs showing thickness of LOR10A as a function of spinning speed of (a) 3000, (b) 4000, and (c) 6000 rpm.

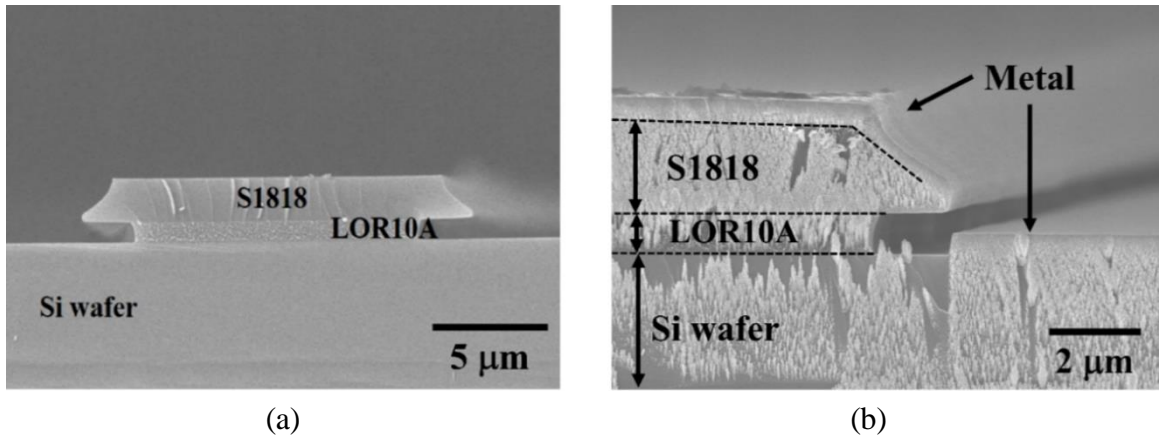


Figure 6.11 SEM micrographs showing a cross-section of (a) bilayer LOR10A/S1818 resist profile with the spin condition of 4000 rpm for 30 sec and (b) 500 nm metal film deposited on the bilayer resist pattern.

#### 6.2.2.2. Epoxy Substrates

The optimised spinning conditions for the LOR10A with 4000 rpm for 30 sec observed on the Si wafer substrate was applied further to the epoxy substrate. Owing to the prolonged development process observed in the previous study, the exposure time was increased to 10 sec to increase the solubility of the S1818 top resist, which accelerates its development rate and opens the channel to the underlying resist, allowing it to develop faster. The development time for the epoxy substrate was found to be 180 sec. Figure 6.12 shows the sacrificial mask with high quality straight linewidths created on the epoxy surfaces. Following this, the samples were subjected to metallisation to produce thin films of Ti/Au of 30/470 nm, followed by lift-off at  $T_R$ .

Regarding the wrinkles on the metal traces observed in the previous processes (Section 6.2.1.2-6.2.1.3), two groups of samples with epoxy substrates underwent lift-off processes using different removers. One group was immersed in 1165 remover, while the other was immersed in an SVC-14 remover. It was found that the average trace width of the sample using 1165 was  $\sim 33.8 \pm 0.68 \mu\text{m}$ , whereas the SVC-14 produced the trace width of  $\sim 34.5 \pm 0.12 \mu\text{m}$ .

During the experiments, solvent blowing was used, with the sample immersed in the 1165 remover for 1 hr and blowing for 30 min to completely remove the resist. Comparing the samples lifted-off with the SVC-14 remover, the blowing was needed for only 2 min to ensure that the stripped metals were spread away from the element pattern. For this reason, the samples lifted-off with the 1165 remover show a higher level of metal deformation than the samples dissolved by SVC-14 (Figure 6.13), resulting in narrower traces with higher variation in trace width. This study also confirmed that the solvent blowing via a pipette accelerated the solvent permeation into the epoxy region, causing more metal deformation in the epoxy region, as previously observed in the epoxies and composites in Section 6.2.1.2 - 6.2.1.3. In the cases with shortened lift-off times, a possible reason for this lies in the high capabilities of the SVC-14 remover. It is regarded as a highly effective and excellent positive photoresist stripper for metal lift-off, because it includes Dimethyl Sulfoxide, DMSO, which is a non-toxic and a polar solvent that can effectively dissolve both polar and non-polar [231], [232]. A shorter duration for the solvent immersion process step and better dissolution decreases the possibility of solvent permeation into the epoxy region. In addition, the 1165 remover contains 90-99% of NMP which is categorized as a toxic solvent [233]. As discussed in Section 6.2.1.3, the sample was previously exposed to harsh environmental cycling and it was immersed in this toxic solvent for long time, hence, the cohesive strength of the epoxy might deteriorate. For this reason, the traces on the samples immersed in the SVC-14 remover show less deformation and it was the preferred option to adopt for the processing of the composite substrates.

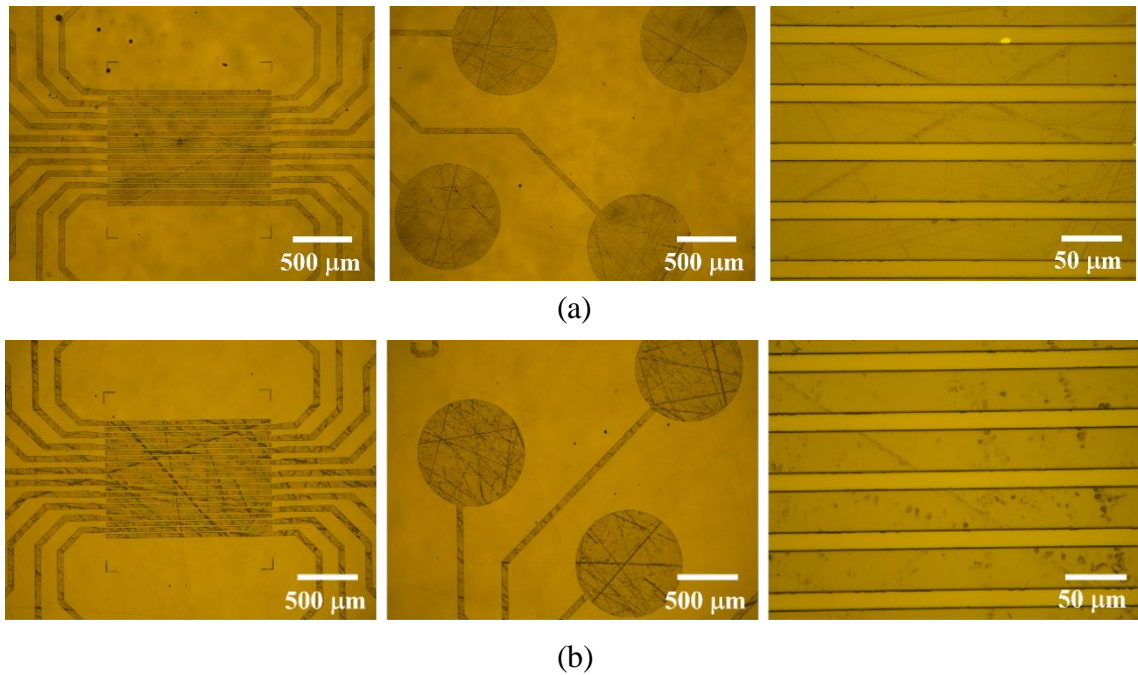


Figure 6.12 Microscopic images of epoxy substrates with a bilayer resist spun at 4000 rpm for 30  $\mu\text{m}$ .

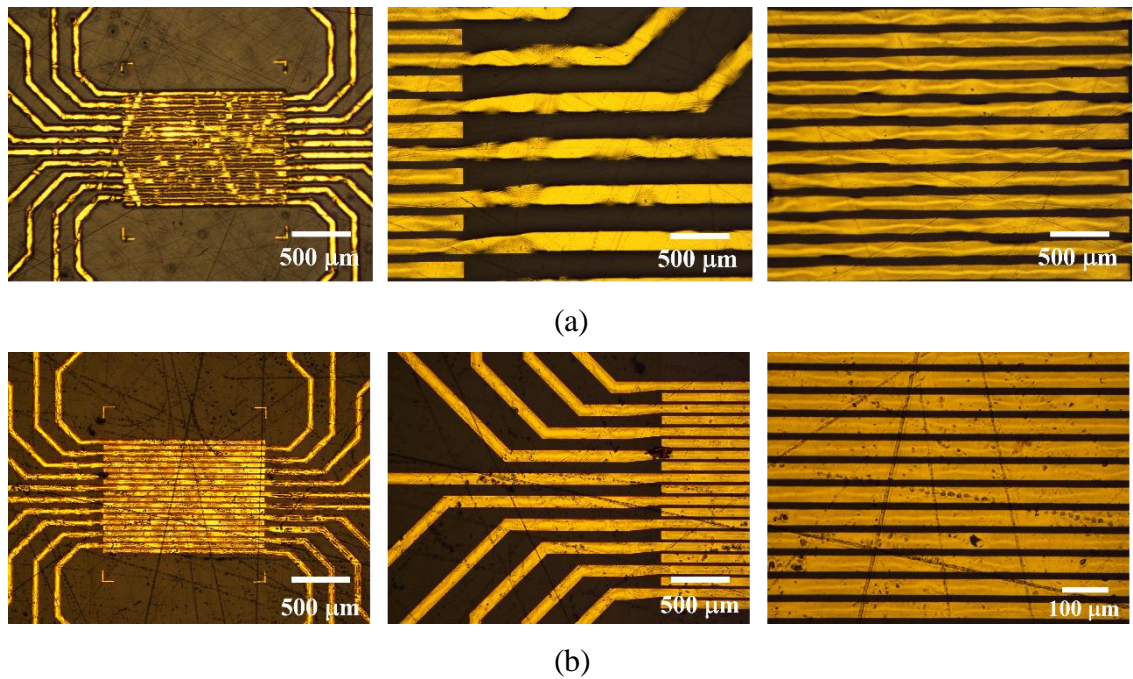


Figure 6.13 Optical micrographs of 20 array 500 nm thick Ti/Au elements established on epoxy surfaces using a LOR10A/S1818 bilayer resist process with lift-off carried out in (a) 1165 and (b) SVC-14 removers.

### 6.2.2.3. Composite Substrate

After completing the process validation on the epoxy substrates, the recipe was then applied to the 1-3 piezocomposite substrates. The samples were subjected to the bilayer photoresist spinning, baking, exposure, and development processes as illustrated in Table 6.2. Figure 6.14 shows photoresist masks on the different composite substrates. A satisfactory linewidth and mask cleanliness were achieved in all composite samples.

However, epoxy swelling (Figure 6.14 (a)) was found in randomised composites when they were subjected to resist baking at high temperatures. Owing to the presence of pinholes found in the randomised composite as previously discussed in Section 5.4.2, these defects might initiate the epoxy swelling. This is attributed to the stock layer in the randomised composites. When lapping to expose the pillar region, the distance between the exposed surface and the stock layer is  $\sim 100 \mu\text{m}$  or less as a result of the net shape gel casting fabrication process and the limited depth of the moulds. When the resist was spun on imperfect surfaces of randomised composites, there was a possibility of the resist penetrating through these defects and approaching to the stock layer. This possibly introduced clefs at an interface between the stock layer and epoxy, hence, the epoxy started deforming and swelling easily when baking at high temperatures.

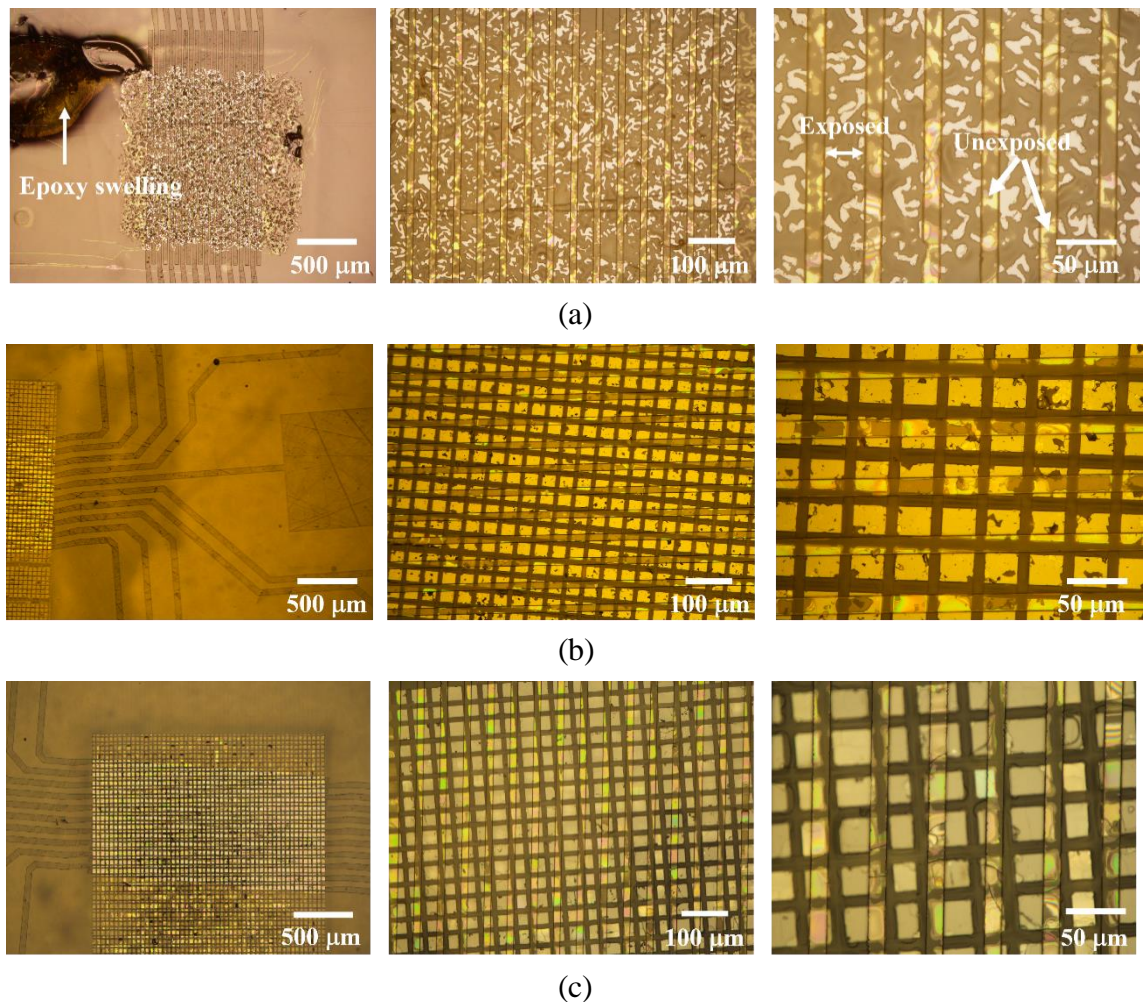


Figure 6.14 Optical micrographs of LOR10A/S1818 bilayer resist profiles established on the surfaces of 1-3 (a) randomised composite (b) diced ceramic composite and (c) diced single crystal composite.

After improving surface adhesion via  $\text{O}_2$  plasma treatment, the samples were then subjected to metallisation to deposit the metal films, followed by immersion in SVC-14 remover for 1 hr at  $T_R$ . Straight, neat and continuous element traces were accomplished on the composite

surfaces as demonstrated in Figure 6.15 with almost 98% yield of traces. In one case however, in the diced ceramic composite, there was a broken trace due to a missing pillar, as illustrated in Figure 6.15 (b).

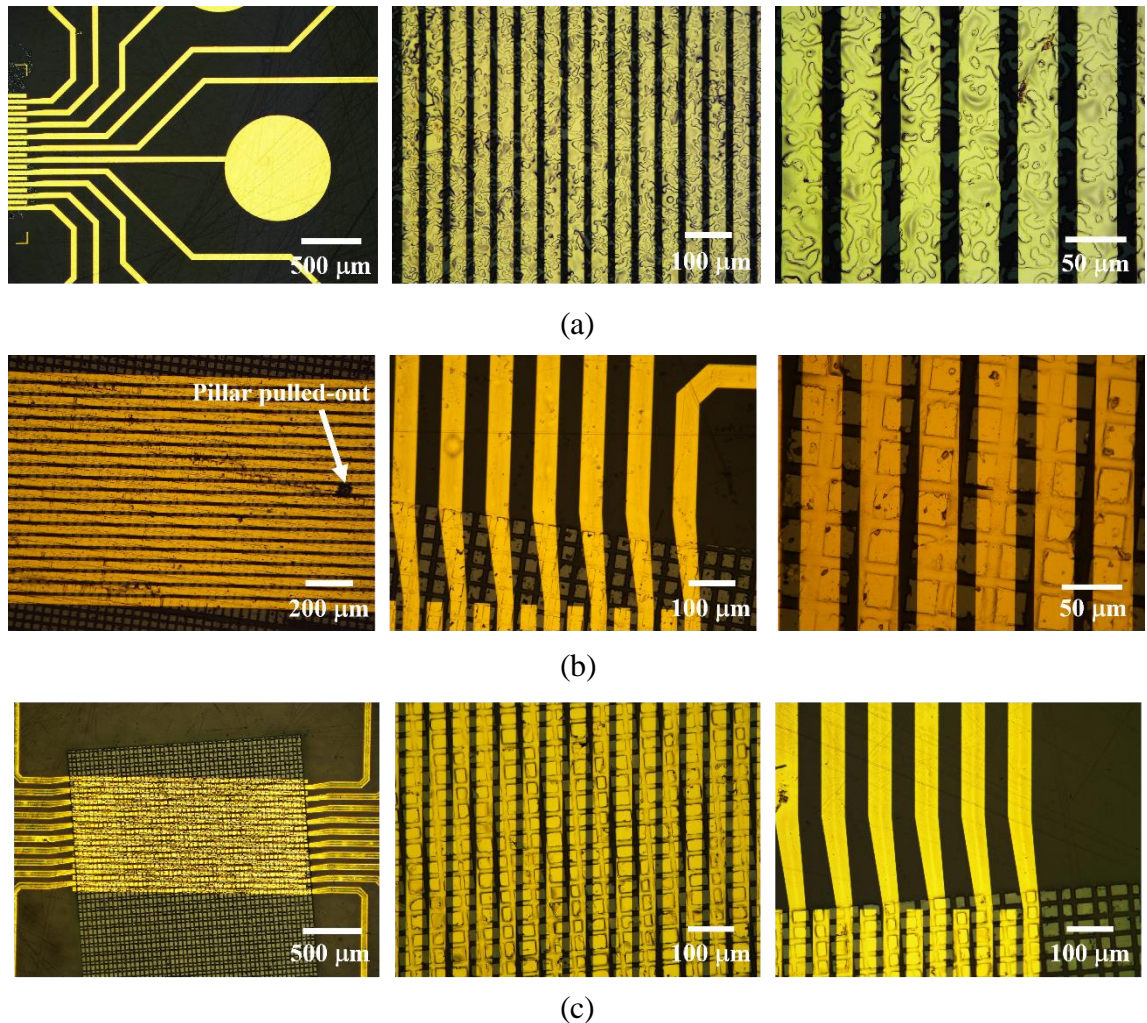


Figure 6.15 Optical micrographs of 20 array 500 nm thick Ti/Au electrodes established using a LOR10/S1818 bilayer resist process metal established on surfaces of 1-3 (a) randomised composite (b) diced ceramic composite and (c) diced single crystal composite.

### 6.3. Releasing and Wax Removal

Whilst they might seem simple ancillary processes, releasing of substrates from their carriers and wax removal proved to be the most challenging steps in the fabrication process for the  $\mu$ US transducer arrays.

The electrical continuity of the electrical traces is dependent on the effectiveness of the methods used to release the thin composite array from its glass carrier. In the process of composite fabrication for SETs, a high temperature (100 °C) was usually used to melt the wax to release the composites after lapping them to the desired thickness [50], [95]. The high

temperature increases the rate of wax melting due to the low melting point of the wax itself (65-69 °C) [234]. The sample was held from one corner by tweezers, and subsequently peeled from the carrier following the wax melting. This process proved an effective means to release the thin SET composites, with continuous electrode layers from the glass carrier with no reports of any damage to the material using this process in the previous works [50], [95]. However, for the composite arrays, the electrodes could be easily damaged, so a number of process modifications were investigated as described below.

Process 1: Due to the relatively harsh environmental cycling involved in the fabrication of the composite arrays, a lower temperature of 65 °C was used to melt the wax. After releasing the sample, the wax on the array side must be cleaned from the surface. Wiping using lint free wipes immersed with IPA or Acetone cannot be used as the arrays might be scratched. Instead, the sample was immersed in IPA for 2 hr to completely dissolve the wax from the array surface. However, the presence of ruptures was observed on the elements patterned on the fan-out epoxy, as shown in Figure 6.16. The array elements were sectionally split along the element length and these cracks had affected the electrical continuity.

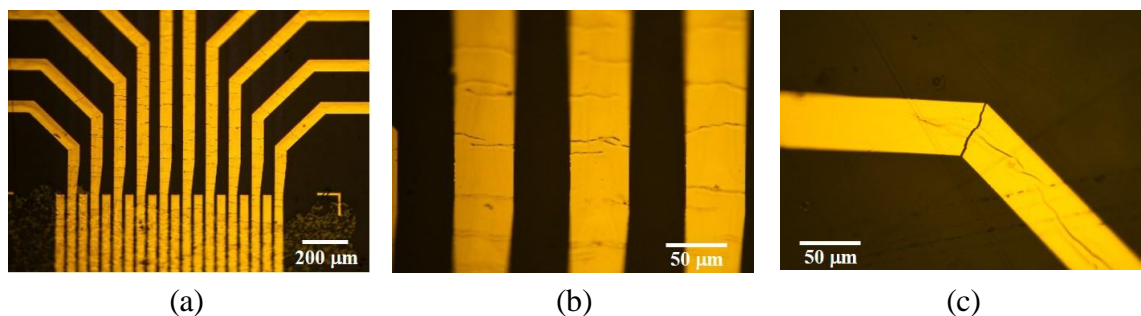


Figure 6.16 Optical micrographs of composite array samples derived from process 1, showing (a-b) cracking on array elements and (c) a discontinuous trace.

Process 2: As recommended by Logitech (Logitech, Glasgow, UK), Ecoclear was used to remove the wax from the substrates since it is suitable for many types of material, e.g., glass, ceramic, metal, electrical components, epoxies, etc. The composite sample adhered on a glass carrier with wax was immersed in Ecoclear heated to 50 ° for 50 min to simultaneously release the sample and dissolve the wax. Unfortunately, the continuity of the arrays was still found to be broken, particularly at the corners, as displayed in Figure 6.17. This was due to the sharp discontinuities at these corners, which are potential points where cracks can initiate due to high stress concentration at these corners when loads or energy are applied [235], [236]. In addition, it should be noted that the heat was involved in these two studies. Therefore, it was thought that heat may be a contributing factor to the creation of the cracks and ruptures on the element traces.

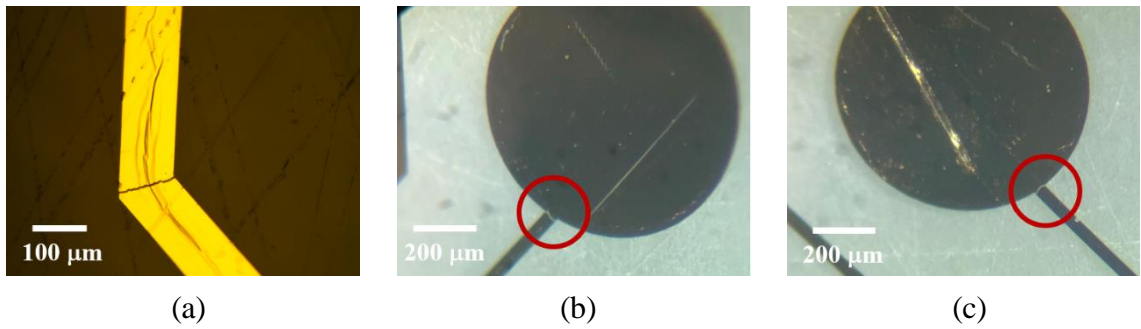


Figure 6.17 Optical microscopes of composite array samples derived from process 2, illustrating (a) cracking at a corner of an element trace, and (b-c) discontinuous traces at interfaces between fan-out pads and traces.

Process 3: This process was carried out at  $T_R$ . As a first step, the entire assembly was soaked in the Ecoclear solvent for 15 min. During immersion, a scraper was used to gradually lift the edge of the thin composite in order to increase the rate of wax dissolution. Unfortunately, the sample suddenly peeled from the carrier via acceleration of the scraper. As a result, most of the traces were broken, as demonstrated in Figure 6.18. However, it should be noted that cracks or ruptures along the trace length and at the corner are not exhibited.

Process 4: As a result of these previous studies, another group of composites was immersed in the Ecoclear at room temperature and left overnight. It was found that almost 100% yield of flawless traces were achieved using this method as demonstrated in Figure 6.19.

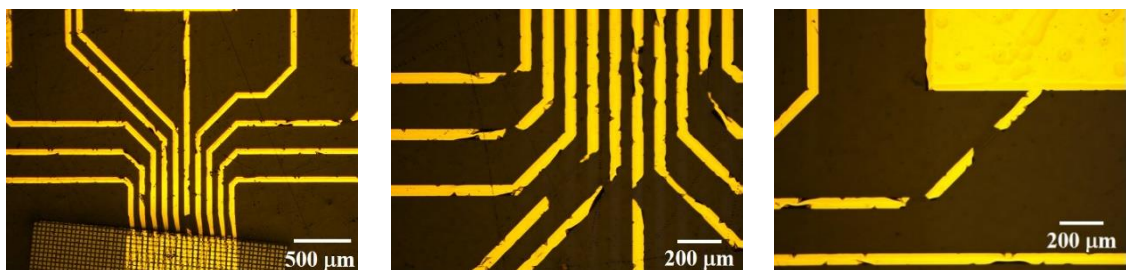


Figure 6.18 Optical micrographs of composite samples, presenting discontinuous traces caused from peeling in Process 3.



Figure 6.19 Optical micrographs composite samples with flawless array elements derived from Process 4.

Due to the harsh environmental cycling involved in the fabrication of the composite arrays, the thin film array elements patterned on the underlying substrate separated easily due to

thermal expansion mismatch between the epoxy ( $\alpha$ :  $45 - 65 \times 10^{-6}$  m/m. °C) and Ti/Au metal ( $\alpha$ :  $9-14 \times 10^{-6}$  m/m. °C) [101], [179]. This caused stretching and deformation of the fan-out epoxy, which may be responsible for producing the cracks observed in the array elements, resulting in discontinuity of the elements. Although the epoxy was cured at an elevated temperature to enhance its properties and provide chemical and heat resistance, the composite with the fan-out epoxy experienced harsh cycling as described in Section 6.2.1.3. This accelerated the degradation and is thought to have decreased the  $T_g$  by breaking down the polymerised bonds in the epoxy. This results in weakening of the epoxy. Therefore, high temperatures should be avoided in the release and wax removal processes.

## 6.4. Summary

Viable processes for fine array elements patterning on 1-3 composites for  $\mu$ US transducer arrays were developed. A variety of aspects for array fabrication were investigated and techniques to overcome challenging steps were also firstly established and reported here. The primary outputs of this work in the development process of a bilayer lift-off process for high quality composite arrays, and effective means of releasing substrates are summarised as follows:

- Development processes using a bilayer lift-off process for array element patterning on the composite substrates were studied. The elements defining 20 element arrays at 50 -  $\mu$ m pitch were directly patterned onto the polished surface of the composite substrates.
- Lift-off development processes I and II provided 75% and 98% yield of high-quality element traces, respectively. Process II (utilising LOR10A/S1818 resists) demonstrated it is highly capable of producing straight, neat, and continuous element traces in both composite and fan-out epoxy regions. It should be noted that the yield is not only dependent on a viable process, which is suitable for the composite surfaces, but also the perfection and characteristics of the composite itself.
- The pillar geometry influenced the variation of the metal deposited on the composite region, whereas the solvent permeation and the accretion of solvent blowing using a pipette resulted in a negative outcome by causing the deformation of the metal on the fan-out epoxy region.
- The process of releasing and wax removal after thinning the composites proved to be one of the most challenging steps in  $\mu$ US array transducer fabrication. High

temperatures should be avoided to prevent the electrical discontinuities in the traces due to the epoxy stretching, because the samples were exposed to harsh environmental cycling. A successful release process was developed involving the use of Ecoclear solvent at room temperature with almost 100% yield.

# Chapter 7 Functional Characterisation

## 7.1. Introduction

This chapter describes the results of characterisation measurements for the fabricated 1-3 piezocomposites, including randomised composite, diced ceramic composite, and diced single crystal composite, and the three completed  $\mu$ US array transducers. During the course of this project, approximately 60, 40, and 30 samples for the randomised, diced ceramic, and diced single crystal piezocomposites, respectively, have been produced in order to develop and refine the necessary process steps discussed in Chapter 5 and 6 that were required in order to produce successful functioning high frequency arrays. The composite arrays presented in this section have been selected based on a centre frequency,  $f_c$ , which is close to 30 MHz in order to compare functional, electrical and acoustic properties. The fine array elements patterned on the composites were fabricated using one of the bilayer lift-off (BLO) photolithographic processes (either Process I or II) as described in Chapter 6. All results presented in this chapter are analysed from the randomised and diced single crystal composite arrays fabricated from the BLO Process I, and the diced ceramic composite array fabricated using the BLO Process II.

Prior to transducer packaging, electrical continuity and impedance characteristics of each element were measured to ensure whether the element was functioning or not. These results are provided in Section 7.2 and 7.3.1. It should be noted that the results from single crystal composites presented in Section 7.2 and other Sections are analysed from two different samples. The single crystal composite 1 showed in Section 7.2. is used as an example to estimate functional elements via electrical continuity tests. The results in other Sections are derived from another single crystal composite 2 because it had a centre frequency,  $f_c$ , closer to the those of the other two composites. The electrical impedance characteristics of  $\mu$ US linear array transducer assemblies including micro-coaxial cables and backing layer were investigated and are given in Section 7.3.2. Finally, as the culmination of the project, the performance of the three completed transducer arrays was characterised and compared via their pulse-echo responses, creating simple images with a research ultrasound imaging system. This work is described in Section 7.4.

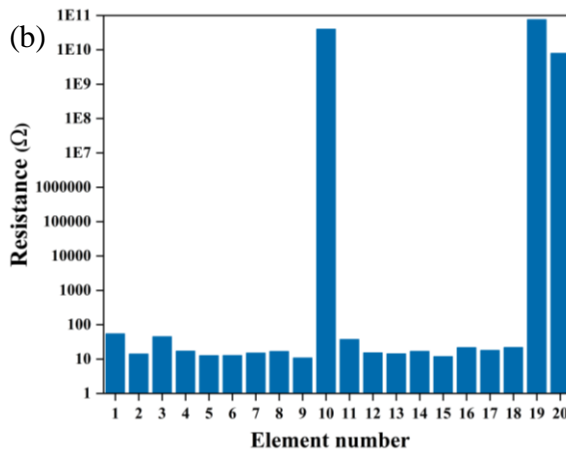
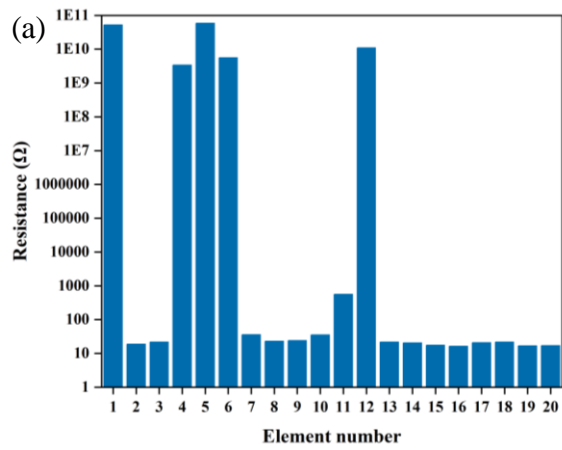
## 7.2. Electrical Continuity

The electrical continuity of each element is demonstrated as a resistance,  $R$ , where it was calculated from the current and voltage measured by a wafer probing system (Summit 12000, Cascade Microtech, Oregon, USA). Two microprobes were used. One probe contacted to the element pad and another probe directed to the end of the element, respectively, with applied drain voltages of  $\pm 500$  mV to measure the continuity along the length of each element. The array elements in randomised and diced single crystal composites were made by the BLO Process I with a total film thickness of 200 nm, whereas the elements in the diced ceramic composite were fabricated using BLO Process II with the thickness of 500 nm.

Figure 7.1 shows the results for all three arrays. Elements with low resistance ( $R < \sim 100 \Omega$ ) represent continuous elements, whereas the elements with intermediate resistance ( $\sim 100 < R < 10^6 \Omega$ ) and high resistance ( $R > 10^6 \Omega$ ) imply partially continuous elements and discontinuous elements, respectively. Examples of damaged elements in the composite region and fan-out epoxy for three composites, which correspond to those with partial continuities and discontinuities are shown in Figure 7.2.

The discontinuities originated from element delamination at the fan-out and element patterned at the interface between the composite and the fan-out epoxy regions, for instance: elements 1, 4 and 6 in the randomised array, and element 16 and 18 in the diced single crystal array as shown in Figure 7.2. (a-b), and (e), respectively. The partial continuity of the elements is thought to be caused from electrical short-circuits through the defects, e.g., pinholes, cracks, and clefts, during corona poling at 30 kV. This appears to have caused elements to be burnt and pulled apart, e.g., in the middle of element 11 in the randomised composite (Figure 7.2. (a)) and elements 10, 19, and 20 of the diced ceramic array (Figure 7.2. (c-d)). Another possible reason of the partial continuity may be element delamination in the composite region of the diced single crystal array as illustrated in Figure 7.2. (f). This delamination occurred during the improper release of the thin composite arrays from the glass carrier, as discussed in Section 6.3, and tended to be found more in the composite arrays patterned with a thin metal film of 200 nm using BLO Process I.

Thus, in the examples shown here, the number of functional elements in the randomised composite, diced ceramic composite, and diced single crystal composite determined from these continuity measurements are 15, 17, and 13, respectively, each from a potential total 20.



$R < 100 \Omega$  : Functioning element  
 $-100 < R < 10^6 \Omega$ : Partially functioning element  
 $R > 10^6 \Omega$  : Inactive element

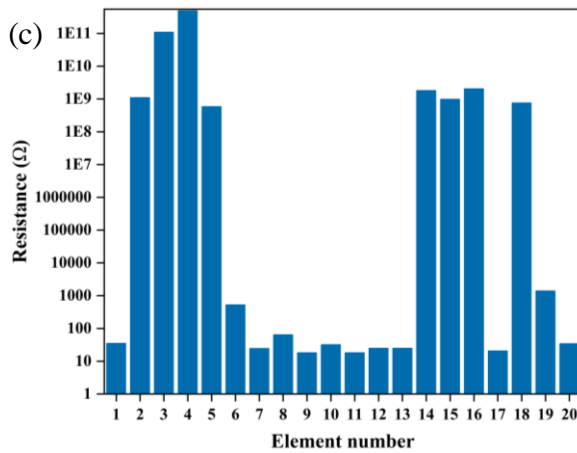


Figure 7.1 Calculated resistance,  $R$ , for individual elements of the (a) randomised composite, (b) diced ceramic composite, and (c) diced single crystal 1 composites; continuous element -  $R < 100 \Omega$ , partial continuity  $-100 < R < 10^6 \Omega$ , and discontinuous element -  $R > 10^6 \Omega$ .

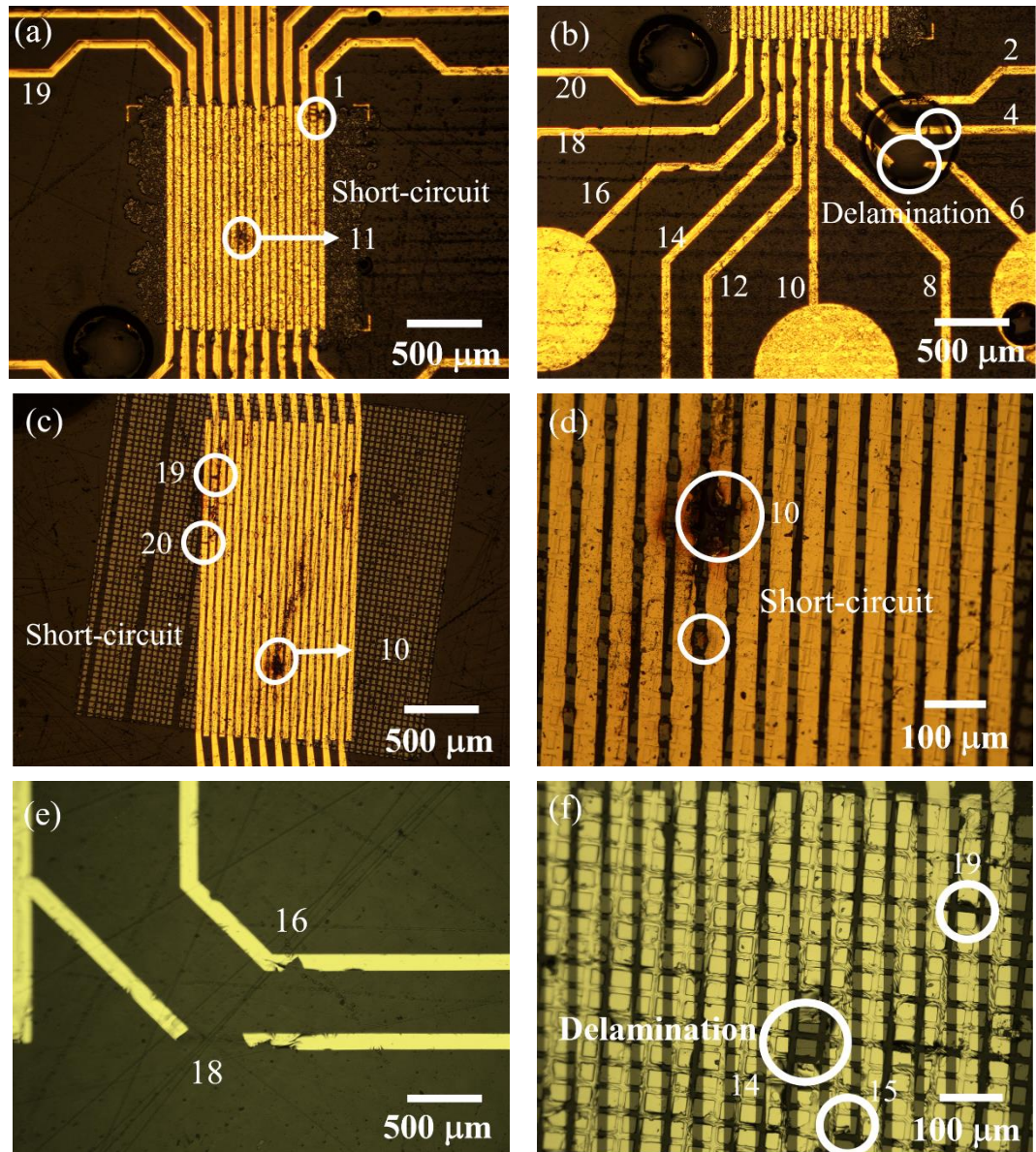


Figure 7.2 Optical microscope images of element arrays patterned on (a-b) randomised composite fabricated by the BLO Process I, (c-d) diced ceramic composite fabricated by the BLO Process II, and (e-f) diced single crystal composite 1 fabricated by the BLO Process I, illustrating typical examples of damages electrodes on each type of composite.

### 7.3. Electrical Impedance Measurements

#### 7.3.1. 1-3 Piezocomposite with 20 Array Elements

The broken elements at the fan-out could be repaired by careful application of small amounts of conductive Ag paint (Agar Scientific, Essex, UK), as shown in Figure 7.3, allowing the number of functional elements to be increased. However, elements broken within the composite regions were difficult to heal due to insufficient space given by adjacent elements. As mentioned previously, owing to a large difference of a centre frequency,  $f_c$ , between the single crystal composite shown in Section 7.2 and the other two composites, another sample of a single crystal composite 2 with  $f_c \sim 27$  MHz was used for subsequent measurements and

for the final transducers. Unfortunately, it was not possible to test the electrical conductivity of this second array at the time required due to the test equipment being broken.

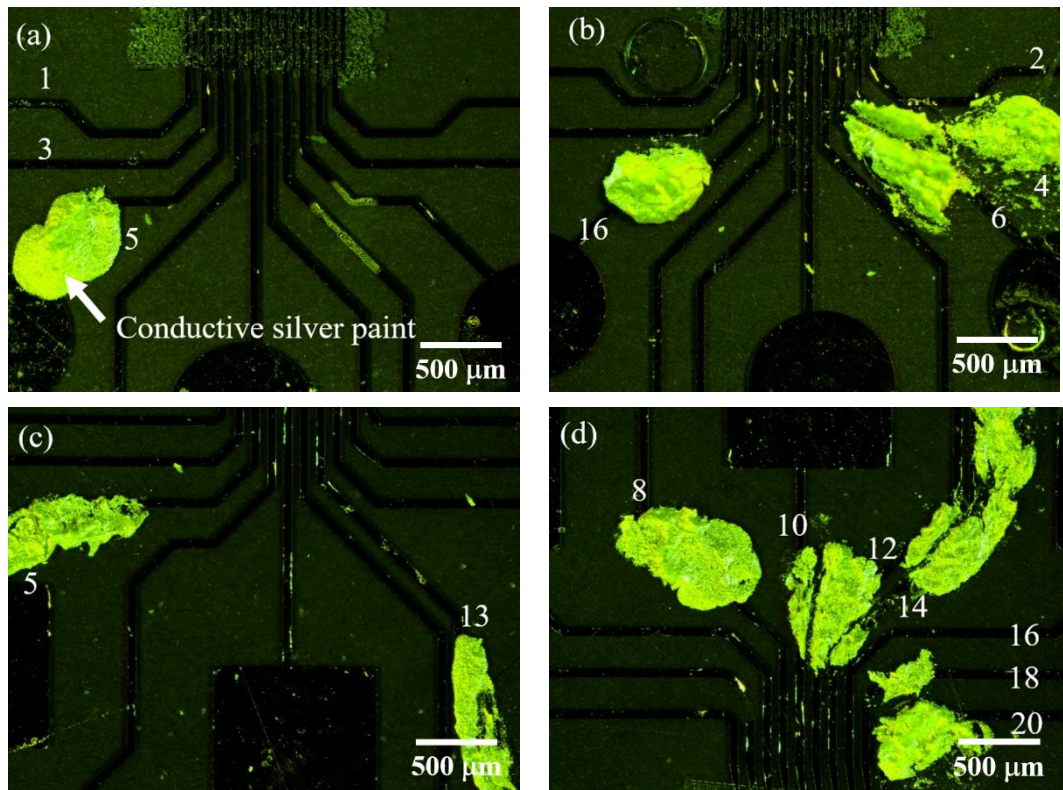


Figure 7.3 Repaired elements of (a) randomised composite and (b) diced single crystal composite 2.

Figure 7.4 shows the electrical impedance magnitude and phase measured from the 20 elements of the composites after all repairing processes were completed. The functional elements showed indications of  $f_r$  and  $f_a$ , representing typical characteristics of impedance magnitude spectra [62]. Meanwhile, the elements with featureless (straight line) and high impedance magnitudes approaching  $10\text{k } \Omega$  imply inactive elements. The numbers of functional elements after repairing of randomised composite, diced ceramic composite, and diced single crystal composite 2 presented in this section were 18, 19, and 15, respectively. The  $f_c$  and mean value of  $k_{eff}$ , of all piezocomposites are listed in Table 7.1, and the individual values of  $f_r$ ,  $f_a$  and  $k_{eff}$  for each element in all three composites are shown in Figure 7.5.

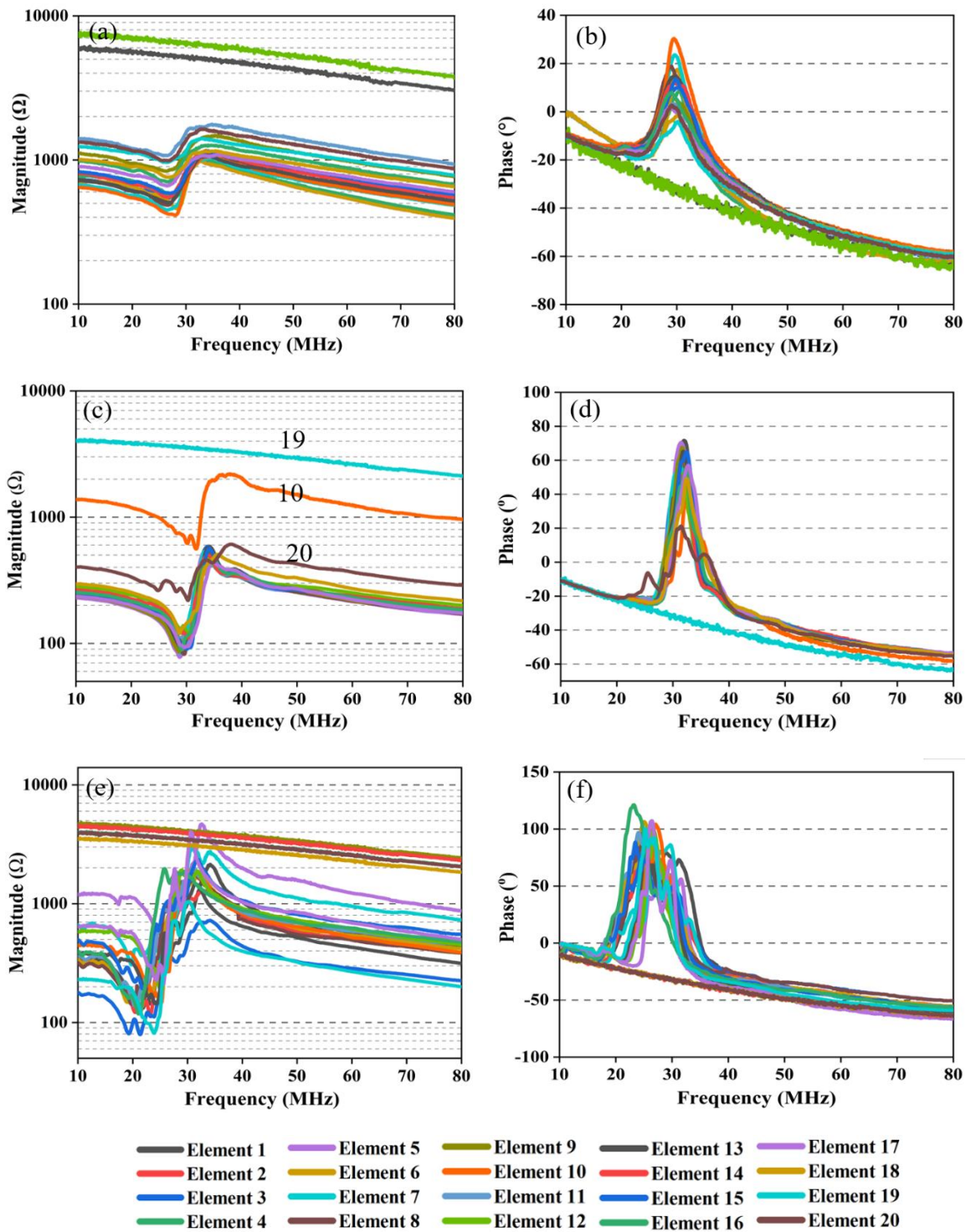


Figure 7.4 Experimental measurements of electrical impedance magnitude (left) and phase (right) of 20 array elements patterned on (a-b) randomised composite, (c-d) diced ceramic composite, (e-f) diced single crystal composite 2.

Table 7.1 Mean resonance and centre frequencies, and effective coupling coefficient of 1-3 piezocomposites.

	<b>Randomised Ceramic Composite (TX1-RM)</b>	<b>Diced Ceramic Composite (TX2-PZ)</b>	<b>Diced Single Crystal Composite (TX3-PIMNT)</b>
<b>Number of Functional Element</b>	18	19	15
$f_r$ (MHz) <sup>1</sup>	26.8 ± 0.45	29.5 ± 0.91	21.9 ± 1.2
$f_a$ (MHz) <sup>1</sup>	34.6 ± 0.97	34.7 ± 1.33	32.4 ± 1.5
<b>Centre frequency<sup>1</sup> (MHz)</b>	30.7	32.1	27.2
<b>Magnitude at <math>f_r</math><sup>1</sup> (<math>\Omega</math>)</b>	640 ± 202	101 ± 31	162 ± 75
$k_{eff}$ <sup>1</sup>	0.67 ± 0.02	0.56 ± 0.04	0.77 ± 0.02

<sup>1</sup>Functional element only

As expected, electrical impedance characteristics from the randomised composite array showed relatively smooth impedance characteristics, indicating that the spurious modes were reduced from the thickness mode, which is in agreement with the randomised composite performance, as previously described in Section 5.2.4. Key factors were strongly dependent on the random distribution of pillar geometry, spacing, and relatively high  $AR$ ,  $\sim 1$ -25. While the spurious modes were found in the diced composite arrays due to the periodicity of the square pillar and low  $AR$ , as discussed previously in Section 5.2.4 and 5.3.3, the previous results and those presented here prove that the random distribution of ceramic enables suppression of extraneous modes from near the fundamental thickness modes in  $\mu$ US composite arrays.

The discrepancies between impedance magnitude and phase (Figure 7.4) and  $k_{eff}$  (Figure 7.5) of each element in all three composites is dependent on the effective volume of piezoelectric material beneath the element [170]. The average impedance magnitudes of the functional elements at their resonant frequencies in each array are listed in Table 7.1. In the randomised composite array, the high electrical impedance and variation in impedance magnitude were caused by the small effective volume fraction of PZT (PZT5H) piezoceramic in each element. This is because its effective volume fraction was less than that of the other two piezocomposites by 3-8% due to broken pillars during composite processing, as previously shown in Section 5.2.3. For the diced composite arrays, the partial coverage was caused by an alignment of array element at an oblique angle relative to the lines of pillars and element delamination in the middle of some elements in the composite region. This results in a

variation in impedance characteristics and  $k_{eff}$ , as can be seen obviously in the elements 10 and 20, as shown in Figure 7.4 (c).

The diced single crystal composite array obtained the highest mean  $k_{eff}$ , compared with the other composite arrays, because of the ultrahigh  $k_{33}$  and  $d_{33}$ , of the PIMNT single crystal piezoelectric material [67]–[69]. Meanwhile, the diced PZT ceramic composites provided the lowest  $k_{eff}$  because the PZ54 piezoceramic (Maggit Ferroperm, Kvistgaard, Denmark) possesses low  $d_{33}$ , and  $k_t$  as shown in Table 2.3. In addition, it is categorised as a semi-hard piezoelectric material, as reported by the supplier [75]. It is well known that piezoelectrically-hard PZT piezoelectric material is difficult to pole because the domain reorientation is limited by the oxygen vacancies [55], [66]. Thus, the PZ54 piezoceramic might also be difficult to pole, leading to low  $k_{eff}$ . The randomised composite provided intermediate  $k_{eff}$ , with slightly higher electrical properties, as presented in Table 2.3, and the highest  $AR$  of  $\sim 1$ -25, compared with the diced composites with  $AR$  of 1.6-2. Furthermore, the randomised composite was made of piezoelectrically-soft PZT5H piezoceramic, which is likely to pole more easily than the PZ54 due to the ease of domain reorientation [55], [66] and also has higher values of  $k_t$ ,  $k_{33}$ , and  $d_{33}$  than the PZ54 (Table 2.3).

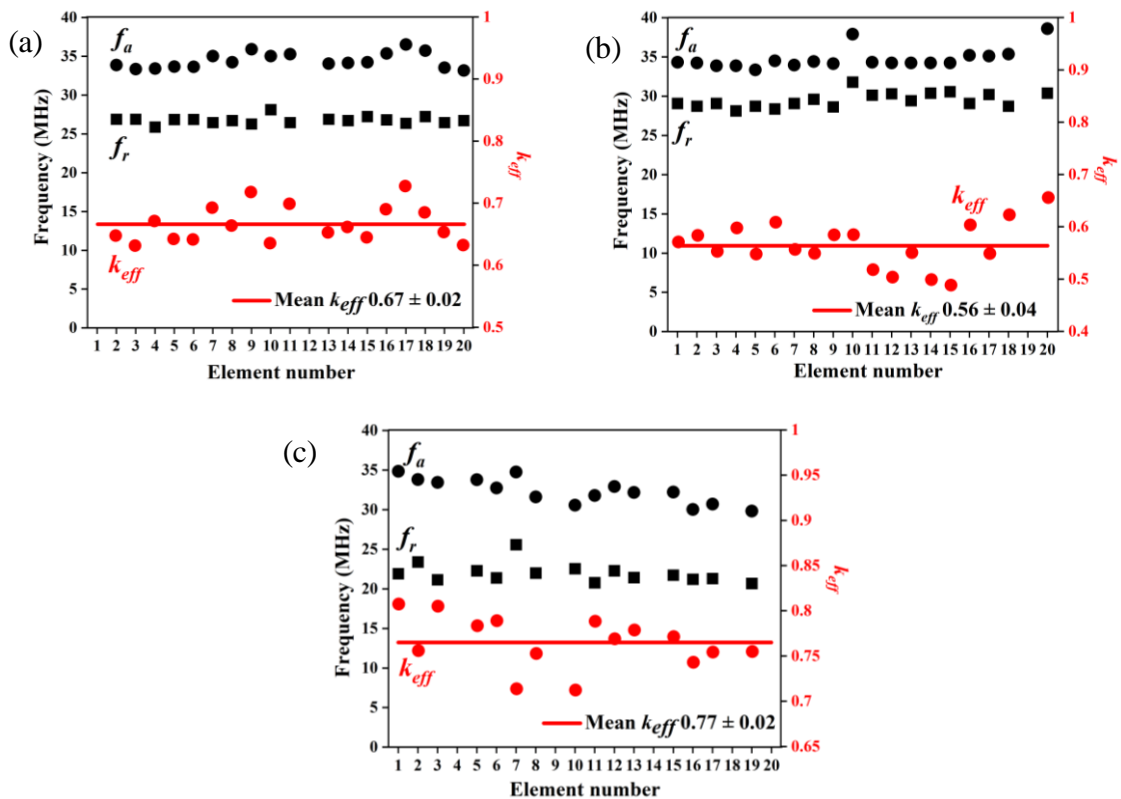


Figure 7.5 Measurements of the resonance ( $f_r$ ) and anti-resonance ( $f_a$ ) frequencies and  $k_{eff}$  for functional elements in (a) randomised composite, (b) diced ceramic composite, and (c) diced single crystal composite 2.

### 7.3.2. 20 Element $\mu$ US Array Transducers

The next stage of electrical impedance measurements was carried out with completed  $\mu$ US array devices. The composite arrays were connected to 0.6 m long microcoaxial cables and integrated with the backing layer as described in Section 4.8. The electrical impedance characteristics of the three  $\mu$ US arrays made with randomised composite, diced ceramic composite, and diced single crystal composite 2, namely as TX1-RM, TX2-PZ, and TX3-PIMNT, are presented in Figure 7.6. After transducer packaging the overall impedance magnitude at  $f_r$  was damped to be approximately 90  $\Omega$  and the impedance phase excursion was also shifted in all arrays, from positive to the maximum phase being negative not exceeding 0°. These changes are possibly attributed from the effect of damping by the backing layer and the addition of cables, in agreement with the literatures [12], [148]. These reductions cause adverse effects in the transducer performance, including the centre frequency, bandwidth, and the pulse-echo amplitude [237], [238]. A simple adjustment of instrument gain and the use of a preamplifier at the transducer end of the cable are recommended to solve this issue [237]–[239].

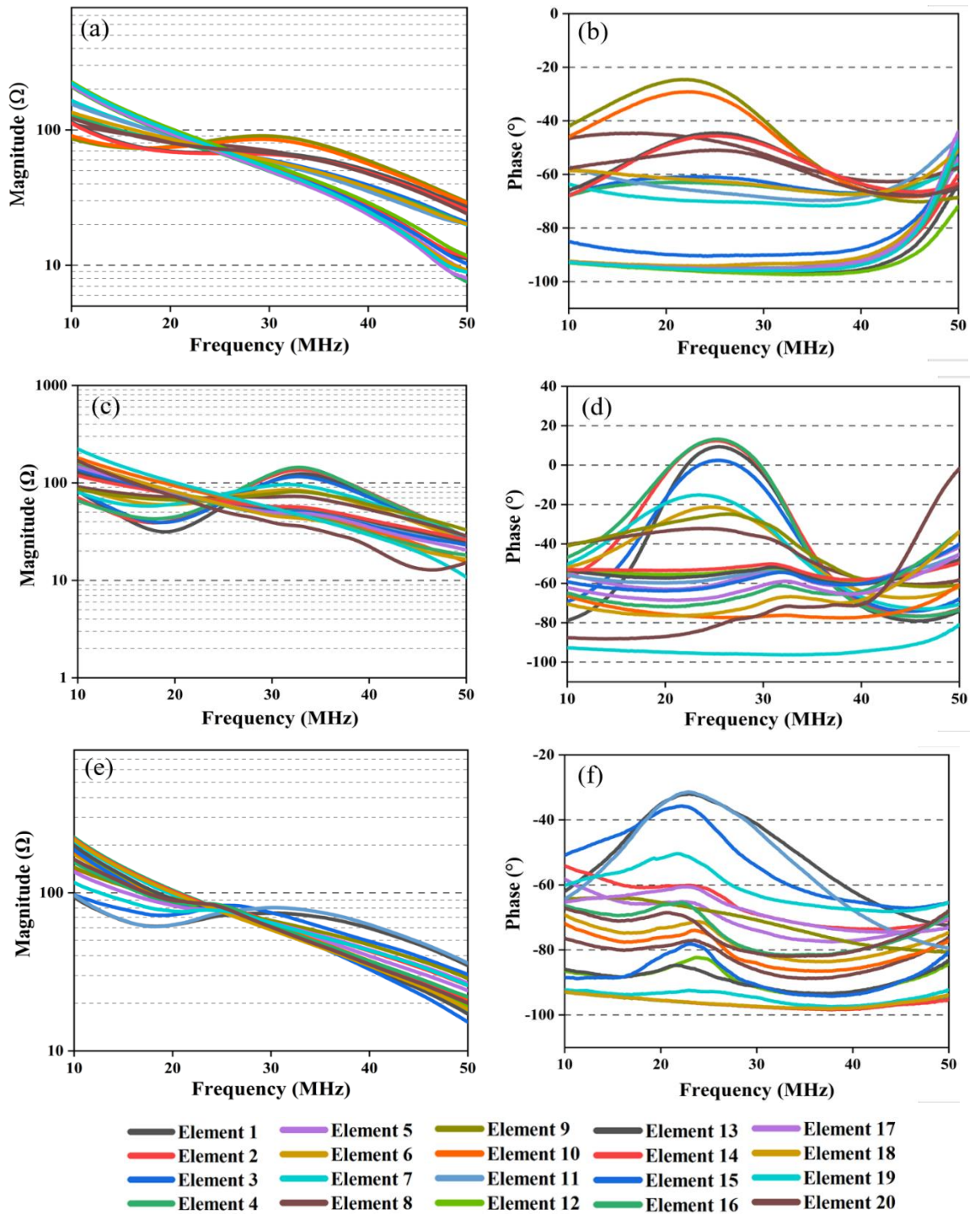


Figure 7.6 Experimental measurements of (left) electrical impedance magnitude and (right) phase measured from 20 elements connected to microcoaxial cable for (a-b) TX1-RM, (c-d) TX2-PZ, and (e-f) TX3-PIMNT  $\mu$ US array transducers.

## 7.4. Pulse-echo Response

The pulse-echo responses of each array transducer were measured individually, and the results compared. In addition, each transducer was used to produce a B-scan image. For the measurements, elements 1 through 20 of the transducers under test were simultaneously connected to the high-frequency Vantage 128 System (Verasonics, Kirkland, WA, USA) with the arrangement described in Section 4.8. Each element was excited and received line-

by-line to collect echo signal data and produce the B-scan. The spatial pulse length,  $PL$ , axial resolution,  $R_A$ , and other characteristics of all three US array transducers are presented in Table 7.2. The  $PLs$  (red lines in Figure 7.7- Figure 7.9) were employed to determine operating frequency or  $f_c$  and -6 dB fractional bandwidth, BW, of the devices with the following equations [69]:

$$f_c = \frac{1}{2}(f_1 + f_2) \quad \text{Eq. 7.1}$$

$$\text{BW} = \frac{f_2 - f_1}{f_c} \quad \text{Eq. 7.2}$$

Table 7.2 Characteristics and properties of  $\mu\text{US}$  array transducers made with 1-3 randomised ceramic, diced ceramic, and diced single crystal piezocomposites.

Transducer Array	TX1-RM	TX2-PZ	TX3-PIMNT
<b>Mean centre frequency<sup>1</sup> (<math>f_c</math>; MHz)</b>	27.1 $\pm$ 2.1	30.1 $\pm$ 2.9	23.3 $\pm$ 1.1
<b>-20 dB pulse length (<math>PL</math>; <math>\mu\text{s}</math>)</b>	0.26 $\pm$ 0.058	0.22 $\pm$ 0.054	0.24 $\pm$ 0.046
<b>Axial resolution (<math>R_A</math>; <math>\mu\text{m}</math>)</b>	200	169	184
<b>Mean fractional bandwidth (BW; %)</b>	33.7 $\pm$ 10.8	45.6 $\pm$ 16.3	31.8 $\pm$ 8.47
<b>Peak-to-peak (a.u.)</b>	75.7 $\pm$ 32.42	114.8 $\pm$ 45.3	1774 $\pm$ 1053

<sup>1</sup> Mean centre frequency ( $f_c$ ) equivalent to the operating frequency

The difference in the centre frequencies between the data measured from the electrical impedances and measured from the pulse-echo responses is possibly due to the change in measured conditions. The bear composites were tested with the electrical impedance analyser to analyse the resonant frequencies of the composites, whereas the composites with the addition of backing layer and cables were measured with the commercial array controller to determine the acoustic properties of the transducers. With these different conditions in measuring, the centre frequencies may have changed.

The pulse-echo responses and bandwidths of selected elements for all three  $\mu\text{US}$  array transducers are presented in Figure 7.7- Figure 7.9.  $R_A$  was defined as one half of the  $PL$  of the echo signal as mentioned in Section 2.4, Eq. 2.8, with a smaller value of  $PL$  resulting in an improvement in  $R_A$  [29], [35], [52]. The -20 dB pulse lengths of approximately 0.26, 0.22, and 0.24  $\mu\text{s}$  for TX1-RM, TX2-PZ, and TX3-PIMNT, respectively, correspond to  $R_A$  of approximately 200, 169, and 184  $\mu\text{m}$  respectively. These results are in agreement with the mean BW at -6 dB because the BW increases as  $PL$  decreases [29], [52]. As a result, TX2-

PZ obtained the smallest  $R_A$ , by 9–18%, and broadest bandwidth, by 26–30%, compared with the other two transducers. In fact, TX1-RM should provide the narrowest BW due to the widest  $PL$ . The possible reason lies in the variation of pillar geometry underneath elements. Surprisingly, TX3-PIMNT provided the narrowest bandwidth. This is potentially attributed to the uneven pillars that produce modes coupling the thickness resonance frequencies, leading to a degradation in the pulse shape of the transducer. This was confirmed with the FEA of a SET made with single crystal composite with the composite structure based on experimental observations of the combinations of two pillar dimensions. Figure 7.10 shows that the shapes of the frequency responses obtained by experimental measurements and FEA models are similar with a dip in the response in both diced composites.

The value for  $PL$  and BW obtained from the three transducers described here were similar but poorer than those of Cannata ( $f_c = 35$  MHz,  $PL = 0.094$   $\mu$ s, BW = 52%) [80] and Ritter ( $f_c = 30$  MHz,  $PL = 0.11$   $\mu$ s, BW = 58%) [81]. In the present work,  $PL$  is longer by 57.5% and the bandwidth is narrower by 32.6%. This is because that both Cannata and Ritter used matching layers and had better electrical matching between transducer and instruments. In addition, in the present work, electrical impedance mismatch causes energy reflection through an electrical transmission line of transducer – cable – instrument and the lack of a matching layer generates additional reflections at the interface between the transducer and the acoustic medium [53], [54], [69]. Consequently, the ringing is produced and then coupled with the transmission output, leading to an extension in the duration of both transmission pulse and the returning signal [54]. Owing to the inversely proportional relationship between  $PL$  and BW, the extended  $PL$  in all three transducers described here provides a narrower BW, corresponding with the literature [52], [54].

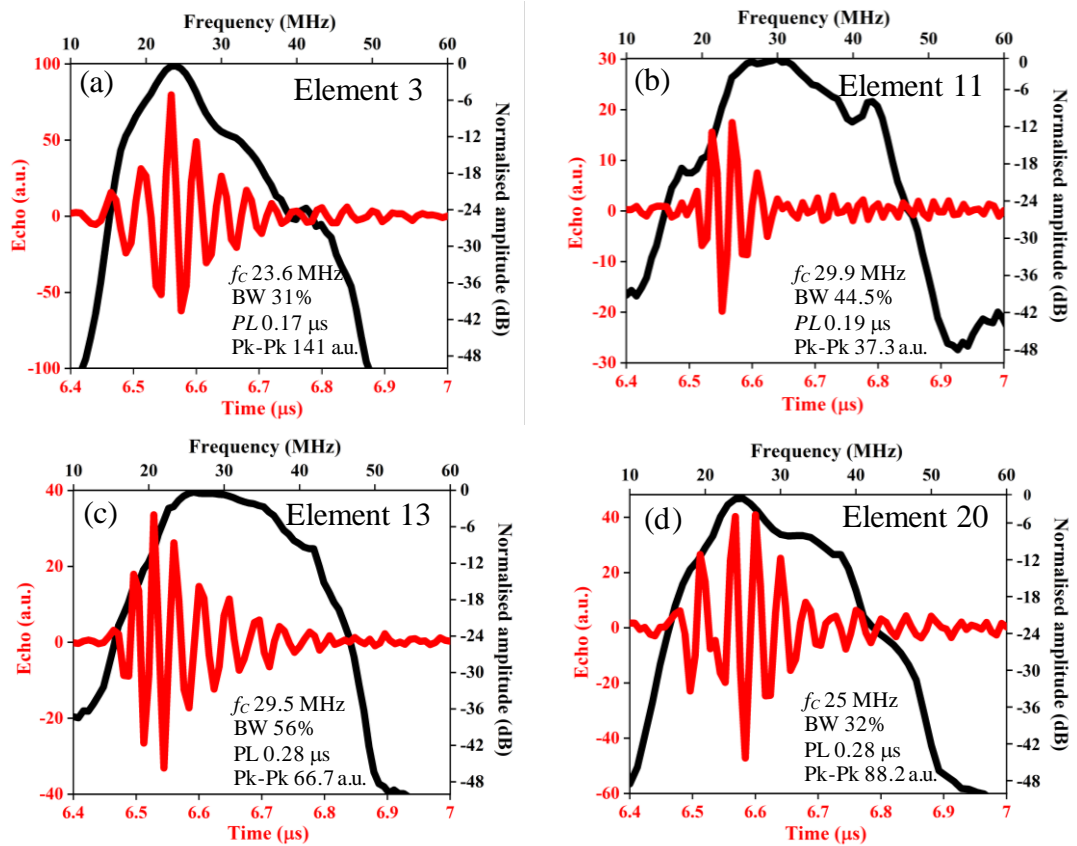


Figure 7.7 Pulse-echo response of elements (a) 3, (c) 11, (c) 13, and (d) 20 from TX1-RM with  $f_c$  of 27 MHz.

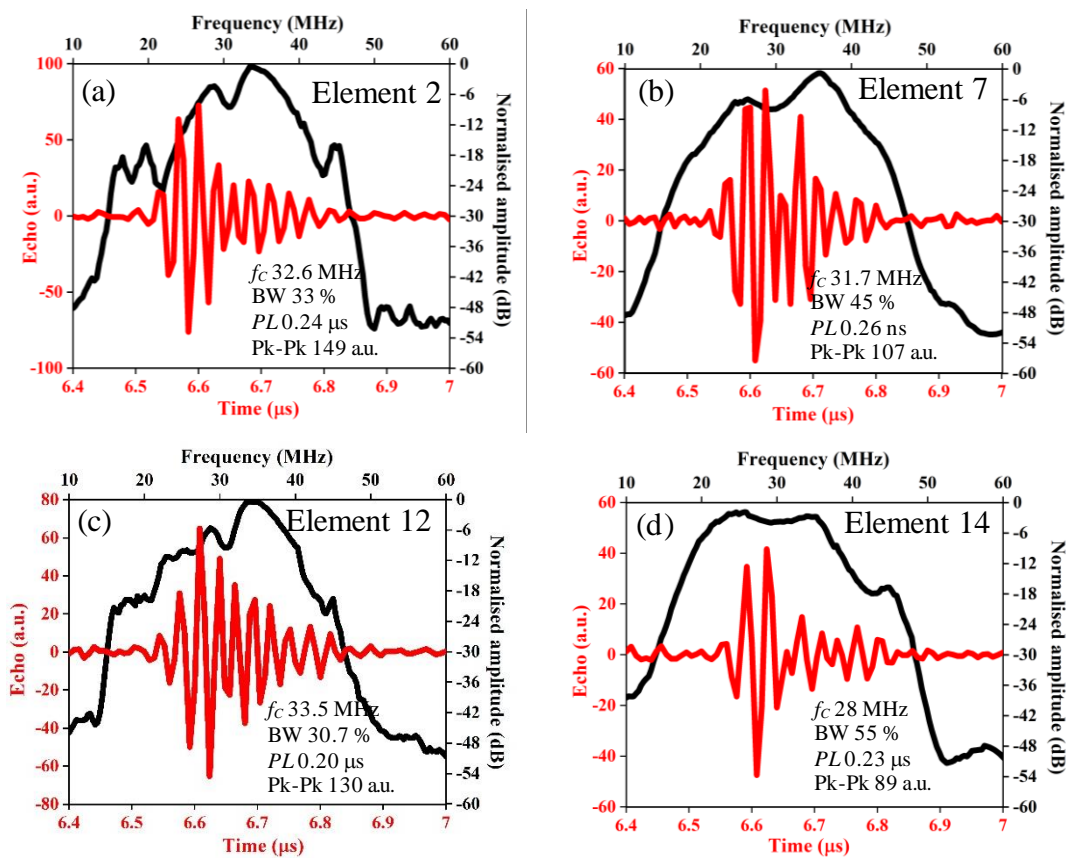


Figure 7.8 Pulse-echo response of elements (a) 2, (b) 7, (c) 12, and (d) 14 from TX2-PZ with  $f_c$  of 30 MHz.

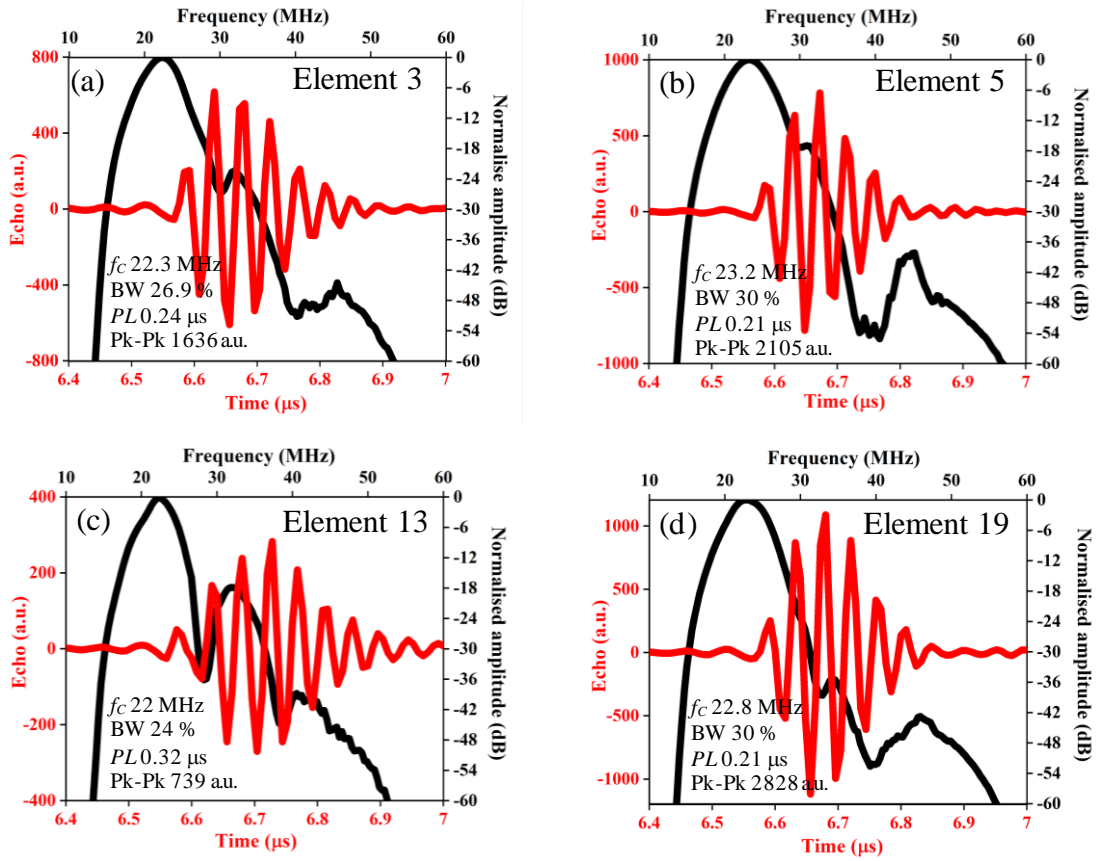


Figure 7.9 Pulse-echo response of elements (a) 3, (c) 5, (c) 13, and (d) 19 from TX3-PIMNT with  $f_c$  of 23 MHz.

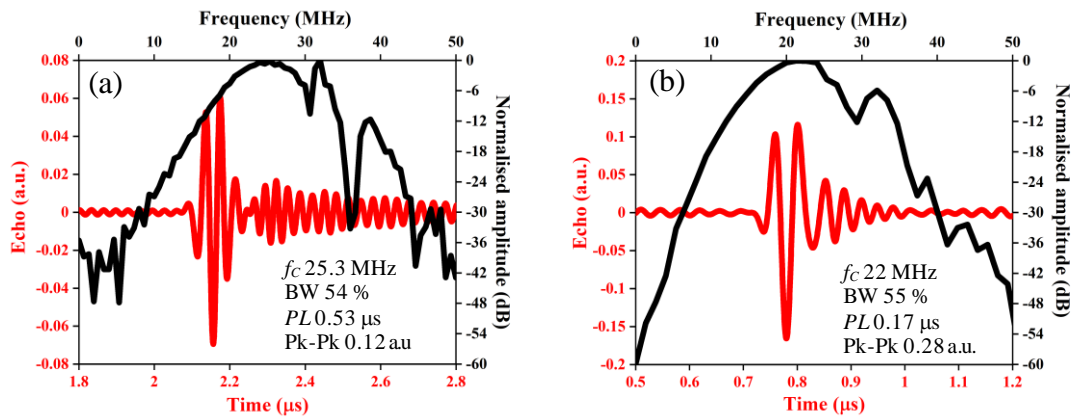


Figure 7.10 FEA modelled pulse-echo response of SETs made with (a) diced ceramic composite and (b) diced single crystal composite with structures identical to those made experimentally in the present works.

In contrast to BW, maximum sensitivity, determined from the peak-to-peak signal in the pulse-echo responses, was observed in TX3-PIMNT, as shown in Table 7.2. This is attributed to it having the highest  $k_{eff}$ . At the same time, the other two transducers had relative low sensitivity, attributed to their lower values of  $k_{eff}$ . Although  $k_{eff}$  potentially influences transducers performance, the  $VF$  of piezoelectric material in the composite also affects the overall output energy being transmitted to the target. It was suggested that a high  $VF$  is

desirable to increase the output energy, and, in turn, to gain strong echoes [170]. In the present work, the  $VF$  in the randomised composite was lower than the diced composites, as described in Section 7.3.1. Consequently, it provides the minimum sensitivity.

These results in term of sensitivity are in good agreement with the B-scan images produced by the Verasonics ultrasound research system as discussed in Section 4.9.4. The image generated by the TX3-PIMNT has a clearer feature in it than those of the other two transducers as presented in Figure 7.11; however, it is also the deepest feature from top to bottom, indicative of the smaller BW.

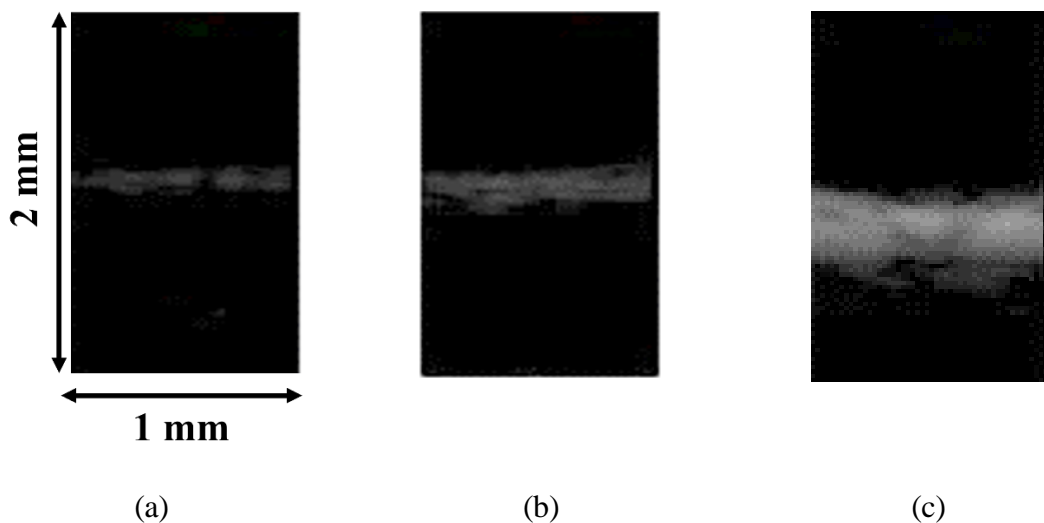


Figure 7.11 B-scan images of a quartz flat imaged by (a) TX1-RM, (b) TX2-PZ, and (c) TX3-PIMNT  $\mu$ US array transducers.

## 7.5. Summary

The results of characterisation of the 1-3 piezocomposite arrays and the  $\mu$ US array transducers made with them were described in this chapter. It has been shown that all three types of composite materials, including randomised ceramic, diced ceramic and diced single crystal composites have been successfully incorporated as the active materials to form three functional high frequency ultrasound array transducers. The variation in results for each device was reported, with the variations corresponding to issues met during the composite fabrication and microfabrication of the array element patterns.

The results of the characterisation can be summarised as follows:

- The number of working elements, measured via continuity, is potentially influenced by the array element qualities, depending on the thickness of the electrode elements and the effective processing in releasing the arrays from the glass carrier after

lapping. Some functioning elements showed partial continuity by presenting intermediate resistance because the electrode elements were broken in the middle, explained by electrical short-circuits during poling and element delamination in composite regions.

- Inactive elements with high resistance, broken in the fan-out patterns, were repaired by patches of conductive Ag paint, thus increasing the number of functional elements. After this stage of fabrication, the numbers of functioning elements, measured by electrical impedance spectroscopy, of the randomised composite, diced ceramic composite, and two diced single crystal composites were 18, 19, and 15, respectively, from a maximum of 20 in each case.
- The electrical impedance characteristics of the randomised composite array showed smooth impedance spectra due to the beneficial of the distribution in pillar geometry and high  $AR$ . This demonstrated that the random pattern enables suppression of the spurious modes from the fundamental thickness resonance modes in  $\mu$ US composite arrays effectively. In contrast, the spurious modes were seen in the diced composite arrays due to the periodicity of the square section pillars and low  $AR$ .
- The variations in electrical impedance characteristics,  $k_{eff}$ , pulse length, and bandwidth of each element are dependent on the effective volume of piezoelectric material and diverse pillar dimensions beneath the element. In the randomised composite  $\mu$ US array, they varied according to random pillar size distribution, whereas element array alignment at an oblique angle relative to the lines of pillars caused the variation in the diced composite  $\mu$ US arrays.
- The electrical impedances of  $\mu$ US array transducers were damped and shifted compared with those of the individual composite arrays because of the influence of a backing layer and the additional 0.6 m microcoaxial cable to each element. This cause electrical impedance mismatch with the arrays, which bring issues during transducer testing.
- Among the three completed  $\mu$ US arrays, TX2-PZ transducer obtained the best  $R_A$  (169  $\mu$ s) and broadest bandwidth (45.6%). TX3-PIMNT transducer provided the narrowest bandwidth, adversely influenced by the uneven pillars that produced the modes coupling to the thickness resonance frequencies. This resulted in the degradation of the overall performance of the transducer.

- The TX3-PIMNT transducer possessed the maximum sensitivity, compared with the other two transducers, corresponding with it having the highest  $k_{eff}$ . This result also corresponded with the B-scan imaging, where the image generated by TX3-PIMNT transducer was clearer, but with poorer spatial resolution than for the other two transducers.
- The sensitivity of a transducer, determined by the output energy, is dependent on the  $k_{eff}$  and the  $VF$  of piezoelectric material. High  $VF$  is required for greater transmitted power. In TX1-RM, made with randomised composite, the  $VF$  was lower than the diced composites by 3-5%, resulting in the lowest sensitivity and reducing the clarity of the ultrasound image.

# Chapter 8 Conclusion and Future work

## 8.1. Conclusions

The novel 1–3 connectivity piezoceramic-polymer composites with a random distribution of pillar cross-sections and spacing have demonstrated their advantages and pitfalls for applications in  $\mu$ US array transducers, with high operating frequencies, exceeding 25 MHz, compared with conventionally repetitive designs.

Piezocomposites with random structures have been researched and discussed in detail for high-frequency single-element ultrasound transducer applications. The main aim of the work presented in this thesis was to utilise randomised composite as the active material in  $\mu$ US arrays. Fabrication of complete  $\mu$ US arrays based on randomised composite and operated with a commercial array controller was established for the first time in this study.

In addition, microfabrication routes for  $\mu$ US arrays based on photolithography techniques were developed to define the fine 50  $\mu$ m element pitch directly on the surface of 1–3 piezocomposites. This is potentially important for small wafer-scale fabrication, which may reduce device costs.

In most previous research, the array elements and electrical connections were on the front face of the  $\mu$ US array transducers. However, this can potentially lead to poor acoustic coupling since the transducer cannot be placed in direct contact with human tissue, owing to the uneven surfaces produced by the adhesives used to secure the electrical joints. The array elements produced in this work allow electrical interconnects to be secured inside a housing, therefore facilitating the direct contact between the transducer and tissue. Additionally, having driven element electrodes on the front face is a potential safety hazard. The array design studied in this thesis instead included a continuous ground electrode on the front face.

### 8.1.1. Fabrication of 1–3 Piezocomposites

1–3 connectivity PZT randomised piezocomposites with feature dimensions of 2 – 50  $\mu$ m and pillar height-to-width aspect ratios in the range 1 – 25 were successfully fabricated by a combination of gel casting and micromoulding. A gel casting system based on an optimised composition of 48 vol% solid loading of PZT powder and 30 wt% resin was used to prepare PZT slurries with low viscosity,  $< 1$  Pa.s. at a shear rate of  $100 \text{ s}^{-1}$ . The study addressed how particle size influences viscosity behaviour and gelation time. The viscosity of the slurries increased when the mean particle size decreased since the fine powder agglomerated,

generating flocculation of the slurry. Conversely, a linear correlation was observed between the gelation time and the mean PZT particle size. The small particles create small interstices because polymer chains can fill the interstices between the larger particles. In this regard, the epoxy polymer chain rapidly links the particles through these small interstices, resulting in a decrease in gelation time. The maximum viscosity of the PZT slurries was 0.47 Pa.s. and gelation time exceeded 10 min, indicating that they were suitable for casting into a micromould. The PZT samples prepared from a slurry, comprising 48 vol% solid loading of PZT powder with a mean particle size  $\sim 1.2 \mu\text{m}$  PZT and 30 wt% resin, yielded samples with a green strength of 49.7 MPa.

Following gel casting, 80% yield of surviving pillars was achieved after demoulding. The loss of pillars demonstrated that the demoulding step is the most challenging in fabricating 1–3 piezocomposites via this method, since the survival of pillars during demoulding depends on the operator's skill and the cleanliness of the master mould. The absence of pillars leads to a reduction of the volume fraction of the piezoceramic, which has an adverse effect on the overall performance of the transducers made with these 1–3 randomised ceramic piezocomposites.

For comparison, 1–3 connectivity diced piezocomposites with square pillars on a  $38 \mu\text{m}$  pitch, were made from PZT piezoceramic and PIMNT piezoelectric single crystal using a modified dice-and-fill method. For any particular material thickness, the pillar aspect ratio produced with the dice-and-fill method is restricted by the smallest width of commercially available saw blades, which were shown to produce a  $13 \mu\text{m}$  kerf. As a result,  $50 \mu\text{m}$  thick 1–3 diced piezocomposite with  $38 \mu\text{m}$  pillar pitch resulted in a low aspect ratio of 2. The diced ceramic piezocomposites yielded only 90% pillar survival with the conventional single pitch dicing method, whereas the modified, double-pitch, dicing method yielded over 99% pillar survival in single crystal piezocomposites, through optimisation of the dicing parameters. The yield was achieved at the expense of a prolonged process and produced uneven pillars due to the misalignment of the second series of cuts. Nevertheless, these findings indicate that these modified fabrication processes can manufacture multiple active elements simultaneously, which can potentially be adapted to wafer-scale production with a relatively high yield of such materials.

Height variation observed in the composites is usually due to the dissimilarity between the elastic properties of the epoxy and piezoelectric materials. Therefore, surface modification is necessary to prepare the piezocomposite surfaces before creating fine array element electrodes, of  $35 \mu\text{m}$  element trace and  $15 \mu\text{m}$  kerf, since relatively smooth and planar

surfaces are required to achieve high-quality elements with photolithography. The surface roughness values achieved for the three types of piezocomposites studied, i.e., random composite, diced ceramic composite, and diced single crystal composite, were 23, 27, and 21 nm, respectively, after optimisation of the lapping process and polishing with a chemical solution.

### **8.1.2. Microfabrication based on Photolithography**

Two processes based on photolithography were developed, with different types of primary resists used in a bilayer lift-off process. The processes were validated primarily on Si wafers and epoxy substrates before transferring them to piezocomposite substrates. The findings from this study are significant in several regards.

Firstly, surface preparation before the resist coating, e.g., sonication and dehydration, is not required and should be avoided for the composite substrates since it can cause pillar breakage and depoling of the piezoelectric materials. Solvent wiping and blowing were sufficient to clean, dry and remove the contamination from the piezocomposite surface.

Secondly, deformation of the metal electrode films deposited on the extra epoxy regions provided for fan-out connections was caused by solvent permeation during the extended lift-off process. Although the epoxy was cured at elevated temperatures to enhance the chemical and heat resistance, the piezocomposites experienced harsh, cyclic environments during processing, which led to the deterioration of the epoxy properties and subsequent solvent absorption in the epoxy region. The effect of solvent absorption can be reduced by using a high-quality solvent, such as SVC-14 stripper, in the lift-off process because this solvent offers a shorter lift-off time.

Finally, the key factors to control the yield and quality of continuous electrode elements, e.g., smooth surfaces and clean edges, in the microfabrication process strongly depend on a process suitable for the non-uniform surface of the 1–3 piezocomposites and the imperfections and surface characteristics of the piezocomposite itself. This includes the use of LOR10A photoresist, as it allows thicker metal films which better survive subsequent processing.

The most challenging step in the  $\mu$ US array transducer fabrication is the process of releasing the piezocomposite arrays from the glass carriers after lapping to the required thickness of approximately 50  $\mu$ m, and the subsequent removal of wax from the array surface. Temperatures over 30 °C should not be used in this step, to maintain the electrical continuity

of the elements, because such temperatures accelerate epoxy stretching, leading to electrical discontinuity and a reduction in yield of intact elements.

### 8.1.3. Functional Properties of $\mu$ US Array Transducers

Fundamental characterisation of the 1–3 randomised PZT ceramic piezocomposite with array elements displayed their electromechanical properties and electrical impedance characteristics compared to the diced piezocomposite arrays made with the PZT piezoceramic and the PIMNT single crystal. The diced single crystal composite array provided the maximum  $k_{eff}$  of 0.77, compared with the other composite arrays, due to the ultrahigh  $k_{33}$  and  $d_{33}$  of the PIMNT single crystal piezoelectric material itself. The diced ceramic PZT composite array had the minimum  $k_{eff}$  of 0.56. This is because it is classified as a semi-hard piezoelectric material in which poling efficiency is limited by oxygen vacancies. The randomised composite array had an intermediate  $k_{eff}$  of 0.67. This is related to its high aspect ratio of pillar height-to-width,  $AR \sim 1-25$ . In addition, the randomised composite was fabricated from soft PZT piezoceramic, which can be poled more easily than the hard PZT piezoceramic.

Based on its smooth electrical impedance characteristics, a  $\mu$ US array transducer made with randomised composite is more desirable since the random geometry of the piezoelectric segments and the high  $AR$  effectively suppress the generation of spurious modes at frequencies close to the fundamental thickness modes. Spurious modes were, however, evident in the transducers made with the 1–3 diced piezocomposites due to the periodicity of the square pillars and their low  $AR$ s.

The prototype devices were designed in ways equivalent to commercial transducers. The design of array element with fan-out pads allows the interconnects to be secured within a housing from the rear of the devices, with the ground side facing forwards for direct contact with tissue. A 15 VF% tungsten loaded epoxy was used as the backing layer to reduce reverberation of the piezoelectric materials and secure the electrical joints of interconnects. The devices were operated with a commercial research ultrasound array controller (Verasonics Vantage 128 High Frequency system, Kirkland, WA, USA) through 42 awg micro-coaxial cables attached with ICA bumps on fan-out pads and a break-out board, to determine their performance through basic measurement of pulse-echo responses.

The performance of the arrays measured via pulse-echo response indicated that the diced ceramic composite array, TX2-PZ, provided the shortest  $PL$  and highest bandwidth of 45.6% among the three  $\mu$ US arrays that were fabricated. This was attributed to the substantial

effective volume fraction and uniformity of pillar dimension. Surprisingly, the transducer fabricated using the diced single crystal composite array, TX3-PIMNT, provided the narrowest bandwidth. This was adversely influenced by the uneven pillar dimensions in the composite that produced modes coupling into the thickness resonance frequencies and resulted in the degradation of the transducer's overall performance.

In determining the sensitivity of the transducers, the TX3-PIMNT transducer showed the maximum sensitivity, compared with the other two transducers, because it had the highest  $k_{eff}$ . This result corresponded with the B-scan images, where the image generated by the TX3-PIMNT transducer was better than those of the other two transducers. Conversely, the lowest sensitivity was observed in TX1-RM, the transducer incorporating the randomised composite array. This is because the volume fraction of the piezoelectric material was lower than the diced piezocomposites, resulting in the lowest sensitivity, and reducing the perceived quality of the US image. These results indicate that the  $k_{eff}$  value and the volume fraction of the piezoelectric material significantly influence the sensitivity of the transducer.

Overall, the results that have been presented suggest that the gel casting method associated with micromoulding is a promising means to fabricate 1–3 connectivity piezocomposites with sufficiently fine structures for  $\mu$ US array applications with operating frequencies above 25 MHz. Furthermore, the kerfless  $\mu$ US arrays produced by defining the elements photolithographically on piezocomposite substrates with randomised pillars and repetitive square pillar sections may provide a feasible route to wafer-scale fabrication with sufficiently high yield of functional elements for commercial manufacture.

## **8.2. Recommendations for Future Work**

The work described in this thesis focused particularly on materials and material processing techniques. Further work to lead to viable devices for potential clinical use is recommended in two areas.

### **8.2.1. $\mu$ US Array Transducers with the Addition of a Matching Layer**

The next step in array transducer fabrication beyond this study is to add matching layer to the front face of each transducer. It is interesting to anticipate how the matching layer will influence the performance of the transducers. Preliminary FEA modelling of a single element transducer, SET, with a structure based on a 1–3 connectivity diced PIMNT single crystal piezocomposite and utilising suitable available passive materials as the matching layer, indicated that the overall performance of the array, after adding 18  $\mu$ m PVDF sheet

(Precision Acoustic, Dorset, UK) would improve as shown in Figure 8.1. In particular, the  $R_A$  and sensitivity were significantly enhanced by 27.3% and 62.6%, respectively.

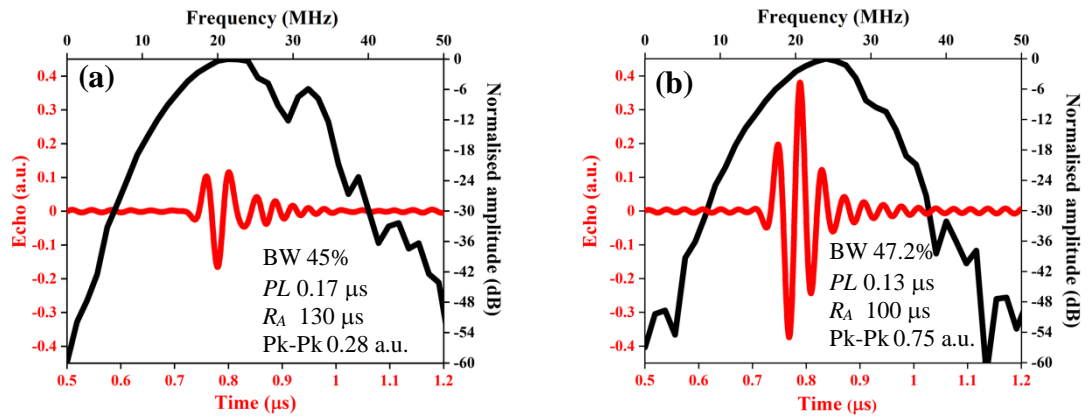


Figure 8.1 FEA modelled pulse-echo response of SETs made with the diced single crystal composites with an identical composite structure to the experimental structure in the present work (a) without a matching layer and (b) with a matching layer.

The primary factors improving the performance are the low  $Z_a$  and specific thickness of the matching layer. PVDF provides  $Z_a = 3.92$  MRayl, relatively close to that of tissue, with  $Z_a \sim 1.5$  MRayl [72]. This will effectively enhance the output energy transferred across the interface by reducing the acoustic impedance mismatch and wave reflection within the matching layer – piezocomposite - load combination. In addition, the calculation of the specific thickness of the PVDF material as  $18 \mu\text{m}$  was based on a quarter-wavelength at the transducer’s operating frequency. This indicates that the quarter-wavelength matching layer can enhance the overall output of the transmission pulses by cancelling the reflected waves within the piezocomposite-matching layer interface via destructive interference and combining the phase of the transmitted pulses at the front of the transducer via constructive interference. This results in an increase in energy transferred to and from the tissue [53], [54].

### 8.2.2. Miniaturising the $\mu\text{US}$ Array Transducer Probe

The other recommended focus of the study is to investigate a method to achieve a miniaturised  $\mu\text{US}$  array transducer probe.

One approach to this is to use composite arrays made with the BLO Process II based on the photolithographic technique reported in Section 6.2.2. The array used in the present study (Figure 8.2 (a)) should be cut into small pieces, e.g.,  $3 \times 2 \text{ mm}^2$  with a laser cutting technique, as shown in Figure 8.2 (b). The literature suggests that, to accomplish a miniaturised probe,

the composite arrays need to integrate with flexible circuits [5], [10]–[11], as shown in (c–d), and with US application-specific integrated circuits (ASICs) [5].

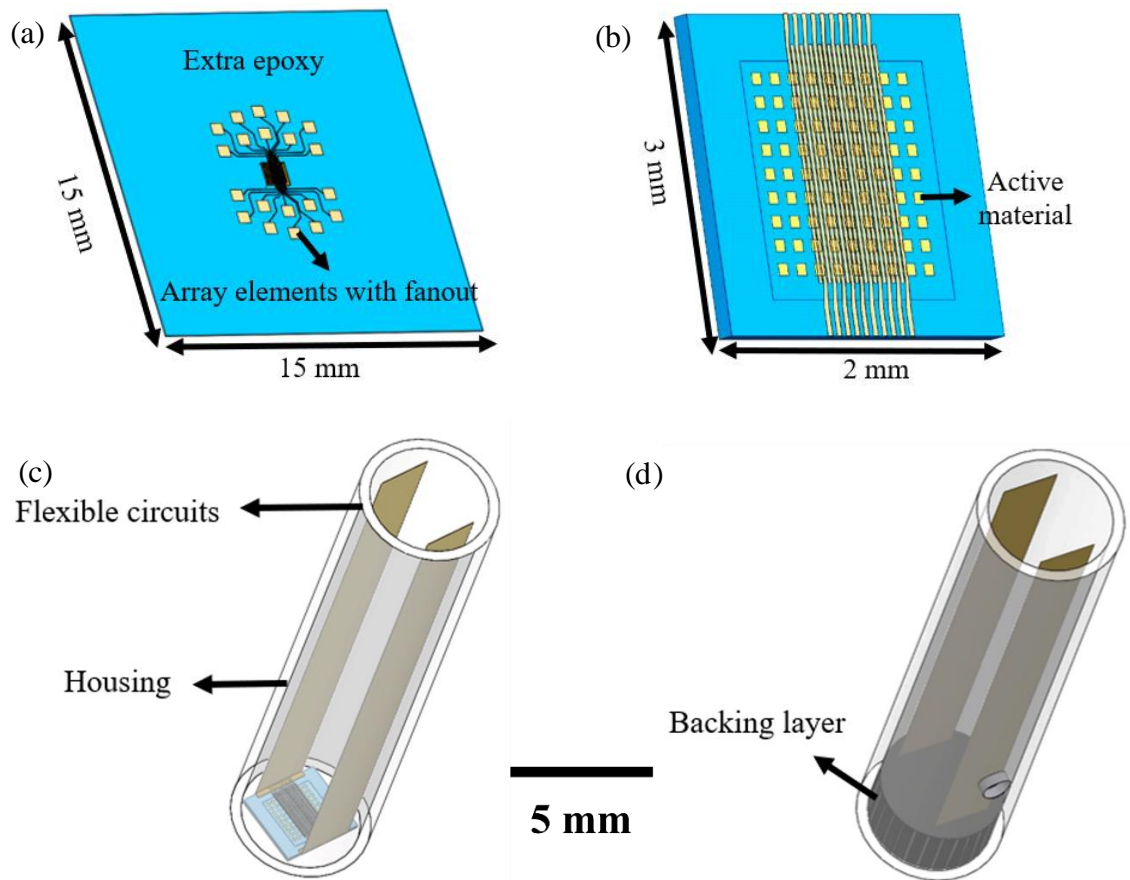


Figure 8.2 A virtual prototype of a proposed 30 MHz  $\mu$ US array with a probe with small cross-section. It comprises (a) the 1–3 piezocomposite with 20 array elements, (b) the extra epoxy, cut using the laser cutting technique, (c) flexible circuits aligned to match with the elements and connected with ACA, and (d) the addition of a backing layer cast in place to secure the electrical joints.

Establishing interconnection of the array elements with flexible circuits and ASICs can be achieved through using advanced technologies, e.g., flip-chip and wire bonding, or using an anisotropic conductive adhesive (ACA) described in Section 3.4.2. However, a cable is required for the electrical connection, which may create an issue with the electrical impedance mismatch, resulting in a loss of inherent performance of the transducer discussed in Section 7.3.2–7.4. Increased effective  $VF$  can reduce the electrical impedance magnitude enabling it to be closer to the cable, as discussed in Section 2.6.3, although a compromise would need to be reached so as not to adversely affect the acoustic match to tissue.

## References

- [1] T. L. Szabo, "Ultrasound imaging safety," in *Diagnostic ultrasound imaging: inside out*, Elsevier Academic Press, 2004, p. 20.
- [2] A. Carovac, F. Smajlovic, and D. Junuzovic, "Application of Ultrasound in Medicine," *Acta Inform. Medica*, vol. 19, no. 3, p. 168, 2011, doi: 10.5455/aim.2011.19.168-171.
- [3] G. R. Lockwood, D. Turnbull, D. Christopher, and F. Foster, "Beyond 30 MHz; Applications of high-frequency ultrasound imaging," *IEEE Eng. Med. Biol.*, vol. 15, pp. 60–71, 1996.
- [4] K. K. Shung, J. Cannata, Q. Zhou, and J. Lee, "High frequency ultrasound: A new frontier for ultrasound," *Proc. 31st Annu. Int. Conf. IEEE Eng. Med. Biol. Soc. Eng. Futur. Biomed. EMBC 2009*, pp. 1953–1955, 2009, doi: 10.1109/IEMBS.2009.5333463.
- [5] B. F. Cox *et al.*, "Ultrasound capsule endoscopy: Sounding out the future," *Ann. Transl. Med.*, vol. 5, no. 9, 2017, doi: 10.21037/atm.2017.04.21.
- [6] J. A. Brown, F. S. Foster, A. Needles, E. Cherin, and G. R. Lockwood, "Fabrication and performance of a 40-MHz linear array based on a 1-3 composite with geometric elevation focusing," *IEEE Trans. Ultrason. Ferroelectr. Freq. Control*, vol. 54, no. 9, pp. 1888–1894, 2007, doi: 10.1109/TUFFC.2007.473.
- [7] C. T. Chiu, B. Kang, P. Eliahoo, A. Theodore, and K. K. Shung, "Fabrication and Characterization of a 20 MHz Microlinear Phased Array Transducer for Intervention Guidance," *IEEE Trans. Ultrason. Ferroelectr. Freq. Control*, vol. 64, no. 8, pp. 1261–1268, 2017, doi: 10.1109/TUFFC.2017.2709623.
- [8] R. Liu, K. A. Harasiewicz, and F. Stuart Foster, "Interdigital pair bonding for high frequency (20-50 MHz) ultrasonic composite transducers," *IEEE Trans. Ultrason. Ferroelectr. Freq. Control*, vol. 48, no. 1, pp. 299–306, 2001, doi: 10.1109/58.896143.
- [9] M. Lukacs *et al.*, "Performance and characterization of high frequency linear arrays," *Proc. - IEEE Ultrason. Symp.*, vol. 1, no. 10, pp. 105–108, 2005, doi: 10.1109/ULTSYM.2005.1602807.
- [10] A. B. Lyse, "Micro-Engineering for High Frequency Ultrasound Arrays," University of Dundee, 2010.
- [11] A. Safari, V. F. Janas, and A. Bandyopadhyay, "Development of fine-scale piezoelectric composites for transducers," *J. Ceram. Process.*, vol. 43, no. 11 A, pp. 2849–2856, 1997, doi: 10.1002/aic.690431334.
- [12] R. McPhillips, "Fabrication of Ultrasound Transducers and Arrays Integrated within Needles for Imaging Guidance and Diagnosis," University of Dundee, 2017.
- [13] A. Abrar, D. Zhang, B. Su, T. W. Button, K. J. Kirk, and S. Cochran, "1-3 Connectivity piezoelectric ceramic-polymer composite transducers made with viscous polymer processing for high frequency ultrasound," *Ultrasonics*, vol. 42, no.

- 1–9, pp. 479–484, 2004, doi: 10.1016/j.ultras.2004.02.008.
- [14] A. Boonruang *et al.*, “Progress towards wafer-scale fabrication based on gel casting technique for 1-3 randomised piezocomposite microultrasound transducers,” *Eur. Ceram. Soc.*
- [15] A. Boonruang, T. Thongchai, T. Button, and S. Cochran, “Microfabrication of 1-3 Composites with Photolithographically Defined Electrode Patterns for Kerfless Microultrasound Arrays,” in *IEEE International Ultrasonics Symposium, IUS*, 2019, vol. 2019-Octob, pp. 1746–1749, doi: 10.1109/ULTSYM.2019.8925545.
- [16] Microchem, “Nano PMGI Resists,” 2002. Accessed: Nov. 01, 2020. [Online]. Available: <https://kayakuam.com/wp-content/uploads/2020/05/KAM-LOR-PMGI-Data-Sheet-51820.pdf>.
- [17] A. Boonruang, C. E. M. Demore, A. Moldovan, S. Neale, T. W. Button, and S. Cochran, “Fabrication of 30 MHz microultrasound linear arrays based on 1-3 randomised and diced piezocomposites,” *IEEE Trans. Ultrason. Ferroelectr. Freq. Control*.
- [18] A. Boonruang, A. Moldovan, T. W. Button, and S. Cochran, “Design and characterisation of a micro-US linear array based on randomised piezocomposite,” 2021.
- [19] H. Kasban, M. A. M. El-Bendary, and D. H. Salama, “A Comparative Study of Medical Imaging Techniques,” *Int. J. Inf. Sci. Intell. Syst.*, vol. 4, no. 2, pp. 37–58, 2015.
- [20] G. Sakas, “Trends in medical imaging: From 2D to 3D,” *Comput. Graph.*, vol. 26, no. 4, pp. 577–587, 2002, doi: 10.1016/S0097-8493(02)00103-6.
- [21] S. D. Waldman and R. S. D. Cambell, *Imaging of Pain*. Saunders Elsevier, 2011.
- [22] H. Azhari, *Basic of biomedical ultrasound for engineers*, 7th ed. A John Wiley & Sons, Inc., 2010.
- [23] G. ter Haar, “Ultrasound Ima.Pdf,” *Interface Focus*, vol. 1, no. May, pp. 686–697, 2011, [Online]. Available: <file:///C:/Users/ANIM-TIEKU/Downloads/Documents/rsfs20110029.pdf>.
- [24] L. F. Khilyuk, G. V. Chilingar, B. Endres, and J. O. Robertson, “Chapter 8 Magnitude and Intensity of Earthquakes,” in *Gas Migration. Event Preceding Earthquakes*, 1st ed., CBSPD, 2000.
- [25] P. Hoskins, K. Martin, and A. Thrush, *Diagnostic ultrasound physics and equipments*, 2nd ed. Cambridge Press, 2010.
- [26] V. I. Mikla and V. V. Mikla, “Ultrasound imaging,” in *Medical imaging technology*, Elsevier, 2014, pp. 114–128.
- [27] P. Hoskins, K. Martin, and A. Thrush, *Diagnositic ultrasound physics and equipment*, no. 2010. Cambridge University Press, 2010.
- [28] N. B. Smith and A. Webb, *Introduction to Medical Imaging: Physiscs, Engineering and Clinical Applications*. Cambridge University Press, 2011.

- [29] R. L. Goldberg and S. W. Smith, "Ultrasound Transducers," *Med. Devices Syst.*, vol. 27, pp. 14-1-14-16, 2006, doi: 10.1121/1.1526592.
- [30] J. E. Aldrich, "Basic physics of ultrasound imaging," *Crit. Care Med.*, vol. 35, no. 5 SUPPL., pp. 131-137, 2007, doi: 10.1097/01.CCM.0000260624.99430.22.
- [31] G. Kossoff, "Basic physics and imaging characteristics of ultrasound," *World J. Surg.*, vol. 24, no. 2, pp. 134-142, 2000, doi: 10.1007/s002689910026.
- [32] M. C. Ziskin, "Fundamental physics of ultrasound and its propagation in tissue.," *Radiographics*, vol. 13, no. 3, pp. 705-709, 1993, doi: 10.1148/radiographics.13.3.8316679.
- [33] R. S. C. Cobbold, *Foundation of Biomedical Ultrasound*. Oxford University Press, 2007.
- [34] S. N. Narouze, *Atlas of ultrasound-guided procedures in interventional pain management*. Springer, 2010.
- [35] A. Ng and J. Swanevelder, "Resolution in ultrasound imaging," *Contin. Educ. Anaesthesia, Crit. Care Pain*, vol. 11, no. 5, pp. 186-192, 2011, doi: 10.1093/bjaceaccp/mkr030.
- [36] B. A. Schrope and N. Goel, "Physical principles of Ultrasound," in *Abdominal Ultrasound for Surgeons*, 2014, pp. 7-17.
- [37] N. Tole, *Basic Physics of Ultrasonographic Imaging*. WHO Press, 2005.
- [38] W. R. Hedrick and D. L. Hykes, "Beam steering and focusing with linear phased arrays," *Journal of Diagnostic Medical Sonography*, vol. 12, no. 5, pp. 211-215, 1996, doi: 10.1177/875647939601200502.
- [39] D. MacLennan, "Fundamental characterisation and early functional testing of micromoulded piezocomposites," University of Strathclyde, 2010.
- [40] T. Ritter, "Design, fabrication, and testgin of high frequency (20 MHz) composite ultrasound imaging arrays," University of Paisley, 2000.
- [41] W. A. Smith and B. A. Auld, "Modeling 1-3 Composite Piezoelectrics: Thickness-Mode Oscillations," *IEEE Trans. Ultrason. Ferroelectr. Freq. Control*, vol. 38, no. 1, pp. 40-47, 1991, doi: 10.1109/58.67833.
- [42] K. K. Shung, J. M. Cannata, and Q. F. Zhou, "Piezoelectric materials for high frequency medical imaging applications: A review," *J. Electroceramics*, vol. 19, no. 1, pp. 139-145, 2007, doi: 10.1007/s10832-007-9044-3.
- [43] R. A. Webster, "Passive materials for high frequency piezocomposite ultrasonic transducers," *PhD Thesis Univ. Birmingham*, no. September, 2009, [Online]. Available: <http://etheses.bham.ac.uk/1311/>.
- [44] D. MacLennan, "Fundamental Characterisation and Early Functional Testing of Micromoulded Piezocomposites," University of Strathclyde, 2010.
- [45] O. T. Von Ramm and S. W. Smith, "Beam Steering with Linear Arrays," *IEEE Trans. Biomed. Eng.*, vol. BME-30, no. 8, pp. 438-452, 1983, doi:

10.1109/TBME.1983.325149.

- [46] K. K. Shung and Michael Zipparo, "Ultrasonic transducers and arrays," *IEEE Eng. Med. Biol.*, pp. 20–30, 1996.
- [47] J. M. Cannata and K. K. Shung, "Development of a high frequency (35-MHz) linear ultrasonic array," *Med. Imaging 2004 Ultrason. Imaging Signal Process.*, vol. 5373, no. May, p. 18, 2004, doi: 10.1117/12.537062.
- [48] M. G. Mooney and M. G. Wilson, "Linear array transducers with improved image quality for vascular ultrasonic imaging," *Hewlett-Packard J.*, vol. 45, no. 4, pp. 43–51, 1994.
- [49] D. Waller, J. Chen, and T. R. Gururaja, "Requirements of piezoelectric materials for medical ultrasound transducers," *IEEE Int. Symp. Appl. Ferroelectr.*, vol. 2, pp. 565–568, 1996, doi: 10.1109/isaf.1996.598040.
- [50] T. Thongchai, "Fabrication of Lead Free and Lead Based 1-3 Piezoelectric Composites for High Frequency Ultrasound Transducers," University of Birmingham, 2017.
- [51] M. G. Grewe, T. R. Gururaja, T. R. Shrouf, and R. E. Newnham, "Acoustic Properties of Particle/Polymer Composites for Ultrasonic Transducer Backing Applications," *IEEE Trans. Ultrason. Ferroelectr. Freq. Control*, vol. 37, no. 6, pp. 506–514, 1990, doi: 10.1109/58.63106.
- [52] R. H. Silverman, E. Vinarsky, S. M. Woods, F. L. Lizzi, and D. J. Coleman, "The effect of transducer bandwidth on ultrasonic image characteristics," *Retina*, vol. 15, no. 1, pp. 37–42, 1995, doi: 10.1097/00006982-199515010-00008.
- [53] J. Brown, S. Sharma, J. Leadbetter, S. Cochran, and R. Adamson, "Mass-spring matching layers for high-frequency ultrasound transducers: A new technique using vacuum deposition," *IEEE Trans. Ultrason. Ferroelectr. Freq. Control*, vol. 61, no. 11, pp. 1911–1921, 2014, doi: 10.1109/TUFFC.2014.006480.
- [54] T. A. Whittingham, "Broadband Transducers.," *Eur. Radiol.*, vol. 3, pp. 298–303, 1999.
- [55] G. H. Haertling, "Ferroelectric Ceramics: History and Technology," *Ferroelectr. Fundam. Collect.*, vol. 818, pp. 157–178, 2007, doi: 10.1002/9783527618002.ch6.
- [56] W. Massa, *Crystal structure determination*, 2nd ed. Springer-Verlag Berlin Heidelberg GmbH, 2004.
- [57] R. . Newnham, "Electroceramics," *Rep. Prog. Phys.*, vol. 52, pp. 123–156, 1989.
- [58] S. Cochran, "Piezoelectricity and basic configurations for piezoelectric ultrasonic transducers," in *Ultrasonic transducers ; Materials and design for sensors, actuators and medical applications*, 2012, pp. 3–35.
- [59] A. J. Moulson and J. M. Herbert, *Electroceramics: Materials, Properties, Application*, 2nd ed. John Wiley & Sons, Inc, 2003.
- [60] H. S. Hsu, F. Zheng, Y. Li, C. Lee, Q. Zhou, and K. K. Shung, "Focused high frequency needle transducer for ultrasonic imaging and trapping," *Appl. Phys. Lett.*,

vol. 101, no. 2, pp. 2–4, 2012, doi: 10.1063/1.4736731.

- [61] W. A. Smith, A. A. Shaulov, and B. M. Singer, “Properties of Composite Piezoelectric Materials for Ultrasonic Transducers,” *Proc. - IEEE Ultrason. Symp.*, vol. 1984-Novem, pp. 539–544, 1984, doi: 10.1109/ULTSYM.1984.198355.
- [62] IEEE Standard 177, “Standard 177: IEEE Standard Definitions and Methods of Measurement for Piezoelectric Vibrators,” *IEEE Std*, vol. 177, 1966, doi: 10.1109/IEEESTD.1966.120168.
- [63] IEEE Standard 176, “Publication and Proposed Revision of ANSI/IEEE Standard 176-1987 ‘ANSI/IEEE Standard on Piezoelectricity,’” *IEEE Trans. Ultrason. Ferroelectr. Freq. Control*, vol. 43, no. 5, p. 717, 1996, doi: 10.1109/TUFFC.1996.535477.
- [64] B. Jaffe and W. Cook, *Piezoelectric ceramics*. Academic Press London and New York, 1971.
- [65] P. Singh, L. S. Smith, M. Bezdecny, M. Cheverton, J. A. Brewer, and V. Venkataramani, “Additive manufacturing of PZT-5H piezoceramic for ultrasound transducer,” *IEEE Int. Ultrason. Symp.*, 2011, doi: 10.1109/ULTSYM.2011.0273.
- [66] K. Uchino, *Advanced piezoelectric materials*. Woodhead Publishing, 2010.
- [67] H. Fu and R. E. Cohen, “Polarization rotation mechanism for ultrahigh electromechanical response in single-crystal piezoelectrics,” *Lett. to Nat.*, vol. 403, no. 6767, pp. 281–283, 2000, doi: 10.1038/35002022.
- [68] S. E. Park and T. R. Shrout, “Characteristics of relaxor-based piezoelectric single crystals for ultrasonic transducers,” *IEEE Trans. Ultrason. Ferroelectr. Freq. Control*, vol. 44, no. 5, pp. 1140–1147, 1997, doi: 10.1109/58.655639.
- [69] D. Zhou *et al.*, “Broad-band and high-temperature ultrasonic transducer fabricated using a Pb(In<sub>12</sub>Nb<sub>12</sub>)-Pb(Mg<sub>13</sub>Nb<sub>23</sub>)-PbTiO<sub>3</sub> single crystal epoxy 1-3 composite,” *Rev. Sci. Instrum.*, vol. 82, no. 5, pp. 3–10, 2011, doi: 10.1063/1.3583746.
- [70] W. Zhang *et al.*, “Determination of the Mechanical Properties of PIN–PMN–PT Bulk Single Crystals by Nanoindentation,” *Crystals*, vol. 10, no. 1, pp. 1–11, 2020.
- [71] S. Zhang and F. Li, “High performance ferroelectric relaxor-PbTiO<sub>3</sub> single crystals: Status and perspective,” *J. Appl. Phys.*, vol. 111, no. 3, 2012, doi: 10.1063/1.3679521.
- [72] F. S. Foster, K. A. Harasiewicz, and M. D. Sherar, “A history of medical biological imaging with polyvinylidene fluoride (PVDF) transducers,” *IEEE Trans. Ultrason. Ferroelectr. Freq. Control*, vol. 47, no. 6, pp. 1363–1371, 2000, doi: 10.1109/58.883525.
- [73] M. A. O’Reilly and K. Hynynen, “A PVDF Receiver for Ultrasound Monitoring of Transcranial Focused Ultrasound Therapy,” *IEEE Trans Biomed Eng*, vol. 57, no. 9, pp. 2286–2294, 2010, doi: 10.1109/TBME.2010.2050483.A.
- [74] L. F. Brown, “Ferroelectric polymers: Current and future ultrasound applications,” *Proc. - IEEE Ultrason. Symp.*, vol. 1992-Octob, pp. 539–550, 1992, doi: 10.1109/ULTSYM.1992.275948.

- [75] Meggitt, “Ferroperm Piezoelectric Pz50 series,” *Meggitt*.  
[https://www.meggittferroperm.com/wp-content/uploads/2017/11/MSSDK\\_PZ50\\_Datasheet-201711.pdf](https://www.meggittferroperm.com/wp-content/uploads/2017/11/MSSDK_PZ50_Datasheet-201711.pdf).
- [76] S. Zhang and T. R. Shrout, “Relaxor-PT single crystals: Observations and developments,” *IEEE Trans. Ultrason. Ferroelectr. Freq. Control*, vol. 57, no. 10, pp. 2138–2146, 2010, doi: 10.1109/TUFFC.2010.1670.
- [77] G. Hayward and J. A. Hossack, “Unidimensional modeling of 1-3 composite transducers,” *J. Acoust. Soc. Am.*, vol. 88, no. 2, pp. 599–608, 1990, doi: 10.1121/1.399763.
- [78] R. E. Newnham, D. P. Skinner, and L. E. Cross, “Connectivity and piezoelectric-pyroelectric composites,” *Mat. Res. Bull.*, vol. 32, no. May, pp. 147–156, 1978.
- [79] Y. Zhang *et al.*, “Fine-scaled piezoelectric ceramic/polymer 2-2 composites for high-frequency transducer,” *J. Am. Ceram. Soc.*, vol. 97, no. 4, pp. 1060–1064, 2014, doi: 10.1111/jace.12859.
- [80] J. M. Cannata, J. A. Williams, Q. Zhou, T. A. Ritter, and K. Kirk Shung, “Development of a 35-MHz piezo-composite ultrasound array for medical imaging,” *IEEE Trans. Ultrason. Ferroelectr. Freq. Control*, vol. 53, no. 1, pp. 224–235, 2006, doi: 10.1109/TUFFC.2006.1588408.
- [81] T. A. Ritter, T. R. Shrout, R. Tutwiler, and K. K. Shung, “A 30-MHz piezo-composite ultrasound array for medical imaging applications,” *IEEE Trans. Ultrason. Ferroelectr. Freq. Control*, vol. 49, no. 2, pp. 217–230, 2002, doi: 10.1109/58.985706.
- [82] A. Abrar, D. Zhang, B. Su, T. W. Button, K. J. Kirk, and S. Cochran, “1-3 connectivity piezoelectric ceramic-polymer composite transducers made with viscous polymer processing for high frequency ultrasound,” *Ultrasonics*, vol. 42, no. 1–9, pp. 479–484, 2004, doi: <https://doi.org/10.1016/j.ultras.2004.02.008>.
- [83] E. K. Akdogan, M. Allahverdi, and A. Safari, “Piezoelectric composites for sensor and actuator applications,” *IEEE Trans. Ultrason. Ferroelectr. Freq. Control*, vol. 52, no. 5, pp. 746–775, 2005, doi: 10.1109/TUFFC.2005.1503962.
- [84] W. A. Smith, A. Shaulov, and B. A. Auld, “Tailoring the Properties of Composite Piezoelectric Materials for Medical Ultrasonic Transducers.,” *Ultrason. Symp. Proc.*, pp. 642–647, 1985, doi: 10.1109/ultsym.1985.198589.
- [85] H. J. Lee and S. Zhang, “Design of Low-Loss 1–3 Piezoelectric Composites for High Power Transducer Applications,” *IEEE Trans. Ultrason. Ferroelectr. Freq. Control*, vol. 59, no. 9, pp. 1969–1975, 2012.
- [86] P. Reynolds, J. Hyslop, and H. G., “Analysis of spurious resonances in single and multi-element piezocomposite ultrasonic transducers,” *IEEE Ultr.*, 2003.
- [87] J. Krautkramer, *Ultrasonic Testing of Materials*, 4th ed. Springer-Verlag Berlin Heidelberg GmbH, 1990.
- [88] G. Hayward, J. Bennett, and R. Hamilton, “A theoretical study on the influence of some constituent material properties on the behavior of 1-3 connectivity composite transducers,” *J. Acoust. Soc. Am.*, vol. 98, no. 4, pp. 2187–2196, 1995, doi:

10.1121/1.413333.

- [89] J. A. Brown, E. Chérin, J. Yin, and F. S. Foster, "Fabrication and Performance of High-Frequency Composite Transducers with Triangular-Pillar Geometry," vol. 56, no. 4, pp. 827–836, 2009.
- [90] J. Yin, M. Lee, J. Brown, E. Chérin, and F. S. Foster, "Effect of Triangular Pillar Geometry on High-Frequency Piezocomposite Transducers," *IEEE Trans. Ultrason. Ferroelectr. Freq. Control*, vol. 57, no. 4, 2010.
- [91] Jianhua Yin, M. Lee, E. Cherin, M. Lukacs, and F. S. Foster, "High-frequency piezo-composite transducer with hexagonal pillars," *IEEE Int. Ultrason. Symp.*, 2009, doi: 10.1109/ULTSYM.2009.5441815.
- [92] C. E. M. Démoré, L. Garcia-Gancedo, F. Dauchy, T. Button, J. C. Bamber, and S. Cochran, "1-3 Piezocomposite Design Optimised for High Frequency Kerfless Transducer Arrays," *IEEE Ultrason. Symp.*, 2009, doi: 10.1109/ULTSYM.2009.5442007.
- [93] C. E. M. Démoré, S. Cochran, L. Garcia-Gancedo, F. Dauchy, T. W. Button, and J. C. Bamber, "1-3 Piezocomposite design optimised for high frequency kerfless transducer arrays," *Proc. - IEEE Ultrason. Symp.*, 2009, doi: 10.1109/ULTSYM.2009.5442007.
- [94] Y. Jiang *et al.*, "Micro-moulded randomised piezocomposites for high frequency ultrasound imaging," *IEEE Int. Ultrason. Symp. IUS*, pp. 4–7, 2012, doi: 10.1109/ULTSYM.2012.0045.
- [95] Y. Jiang, "Fabrication and characterisation of novel ultrasound transducers," University of Birmingham, 2013.
- [96] C. E. M. Démoré, A. L. Bernassau, D. MacLennan, T. W. Button, and S. Cochran, "Investigation of Element Cross Talk in Arrays using 1-3 Piezocomposite Substrates," *IEEE Ultrasonics Symposium*, 2007. .
- [97] T. L. Szabo and P. A. Lewin, "Ultrasound transducer selection in clinical imaging practice," *J. Ultrasound Med.*, vol. 32, no. 4, pp. 573–582, 2013, doi: 10.7863/jum.2013.32.4.573.
- [98] G. Hayward and J. Bennett, "Assessing the influence of pillar aspect ratio on the behavior of 1-3 connectivity composite transducers," *IEEE Trans. Ultrason. Ferroelectr. Freq. Control*, vol. 43, no. 1, pp. 98–108, 1996, doi: 10.1109/58.484469.
- [99] J. A. Hossack, B. A. Auld, and H. D. Batha, "Techniques for suppressing spurious resonant modes in 1:3 composite transducers," *IEEE Int. Ultrason. Symp.*, pp. 651–655, 1991.
- [100] G. Harvey, A. Gachagan, J. W. Mackersie, and R. Banks, "Exploring the advantages of a random 1-3 connectivity piezocomposite structure incorporating piezoelectric fibres as the active element," *Proc. - IEEE Ultrason. Symp.*, vol. 1, pp. 1903–1906, 2006, doi: 10.1109/ULTSYM.2006.485.
- [101] W. D. Callister, *Materials Science and Engineering*. John Wiley & Sons, Inc., 2007.

- [102] Huntsman Advanced Materials, “Data sheet CY208/HY956,” 2003. 16113183022940.pdf (bag-distribution.com) (accessed Mar. 03, 2021).
- [103] Electrolube, “Technical Data Sheet UR5562 Polyurethane Resin,” 2000. Microsoft Word - UR5562 (rs-online.com) (accessed Mar. 03, 2021).
- [104] H. J. Lee, S. Zhang, Y. Bar-Cohen, and S. Sherrit, “High temperature, high power piezoelectric composite transducers,” *Sensors (Switzerland)*, vol. 14, no. 8, pp. 14526–14552, 2014, doi: 10.3390/s140814526.
- [105] Robnor, “Technical Data Sheet Epoxy Resin,” 2010. DATASHEET FOR ROBNOR EPOXY RESIN (farnell.com) (accessed Mar. 03, 2021).
- [106] S. Services, “Data Sheet Data Sheet Epofix,” 2012. EpoFix low viscosity epoxy resin (agarscientific.com) (accessed Mar. 03, 2021).
- [107] H.-C. Yang, J. Cannata, J. Williams, and K. K. Shung, “Crosstalk reduction for high-frequency linear array ultrasound transducers using 1-3 piezocomposites with pseudo-random pillars,” *IEEE Trans. Ultrasonics Ferroelectr. Freq. Control*, vol. 59, no. 10, pp. 2312–2321, 2012, doi: 10.1109/TUFFC.2012.2456.Hao-Chung.
- [108] M. Saleem, Q. Liu, T. Yasin, X. Qi, and J. Li, “Dice-and- fill processing and characterization of microscale composites,” *Ceram. Int.*, vol. 42, no. 9, pp. 10745–10750, 2016, doi: 10.1016/j.ceramint.2016.03.198.
- [109] C. T. Chiu, B. J. Kang, P. Eliahoo, T. Abraham, K. K. Shung, and L. Fellow, “Fabrication and Characterization of a 20-MHz Microlinear Phased-Array Transducer for Intervention Guidance,” vol. 64, no. 8, pp. 1261–1268, 2017.
- [110] R. Liu, K. A. Harasiewicz, D. Knapik, N. A. Freeman, and F. S. Foster, “2-2 Piezoelectric composites with high density and fine scale fabricated by interdigital pair bonding,” *Appl. Phys. Lett.*, vol. 75, no. 21, pp. 3390–3392, 1999, doi: 10.1063/1.125303.
- [111] H. R. Chabok, J. M. Cannata, H. H. Kim, J. A. Williams, J. Park, and K. K. Shung, “A high-frequency annular-array transducer using an interdigital bonded 1-3 composite,” *IEEE Trans. Ultrason. Ferroelectr. Freq. Control*, vol. 58, no. 1, pp. 206–214, 2011, doi: 10.1109/TUFFC.2011.1787.
- [112] F. S. Foster *et al.*, “A New 15-50 MHz Array-Based Micro-Ultrasound Scanner for Preclinical Imaging,” *Ultrasound Med. Biol.*, vol. 35, no. 10, pp. 1700–1708, 2009, doi: 10.1016/j.ultrasmedbio.2009.04.012.
- [113] K. A. Snook, C. H. Hu, T. R. ShROUT, and K. K. Shung, “High-Frequency Ultrasound Annular-Array Imaging. Part I: Array Design and Fabrication,” *IEEE Trans. Ultrason. Ferroelectr. Freq. Control*, vol. 53, no. 2, pp. 300–308, 2006, doi: 10.1109/TUFFC.2006.1593368.
- [114] V. F. Janas and A. Safari, “Overview of fine-scale piezoelectric ceramic-polymer composite processing,” *J. Am. Ceram. Soc.*, vol. 11, no. 78, pp. 2945–2955, 1995.
- [115] C. T. Chiu, B. J. Kang, P. Eliahoo, T. Abraham, and K. K. Shung, “Fabrication and Characterization of a 20-MHz Microlinear Phased-Array Transducer for Intervention Guidance,” *IEEE Trans. Ultrason. Ferroelectr. Freq. Control*, vol. 64, no. 8, pp. 1261–1268, 2017, doi: 10.1109/TUFFC.2017.2709623.

- [116] S. Zhang and F. Li, "High performance ferroelectric relaxor- PbTiO<sub>3</sub> single crystals : Status and perspective," *J. Appl. Phys.*, vol. 111, 2012, doi: 10.1063/1.3679521.
- [117] P. Zhao *et al.*, "The strength of PIN – PMN – PT single crystals under bending with a longitudinal electric field," 2011, doi: 10.1088/0964-1726/20/5/055006.
- [118] M. Kahrizi, *Micromachining techniques for fabrication of micro and nano structure*. InTech, 2012.
- [119] X. Jiang *et al.*, "Microfabrication of piezoelectric composite ultrasound transducers (PC-MUT)," *Proc. - IEEE Ultrason. Symp.*, vol. 1, pp. 922–925, 2006, doi: 10.1109/ULTSYM.2006.246.
- [120] B. Bahreyni, *Fabrication and design of resonant microdevices*. William Andrew Inc, 2008.
- [121] J. R. Yuan *et al.*, "High frequency piezo composites microfabricated ultrasound transducers for intravascular imaging," *Proc. - IEEE Ultrason. Symp.*, vol. 1, pp. 264–268, 2006, doi: 10.1109/ULTSYM.2006.83.
- [122] C. Liu, F. Djuth, X. Li, R. Chen, Q. Zhou, and K. Kirk Shung, "Micromachined high frequency PMN-PT/epoxy 1-3 composite ultrasonic annular array," *Ultrasonics*, vol. 52, no. 4, pp. 497–502, 2012, doi: 10.1016/j.ultras.2011.11.001.
- [123] J. Zhang, W. Ren, X. Jing, P. Shi, and X. Wu, "Deep reactive ion etching of PZT ceramics and PMN-PT single crystals for high frequency ultrasound transducers," *Ceram. Int.*, vol. 41, no. S1, pp. S656–S661, 2015, doi: 10.1016/j.ceramint.2015.03.258.
- [124] R. Fallow, W. Galbraith, M. Knowles, and G. Hayward, "Micromachining of a piezocomposite transducer using a copper vapor laser," *IEEE Trans. Ultrason. Ferroelectr. Freq. Control*, vol. 48, no. 3, pp. 639–640, 2001, doi: 10.1109/58.920684.
- [125] M. A. R.-B. Salvador Mendoza-Acevedo, J. A. M.-C. Edgar Norman Vázquez-Acosta<sup>1</sup>, and J. L. González-Vidal, "Release Optimization of Suspended Membranes in MEMS," in *Micromachining Techniques for Fabrication of Micro and Nano Structures*, InTech, 2012, pp. 183–204.
- [126] Z. Lei *et al.*, "Micromachining of high quality PMN-31%PT single crystals for high-frequency (>20 MHz) ultrasonic array transducer applications," *Micromachines*, vol. 11, no. 5, pp. 1–12, 2020, doi: 10.3390/mi11050512.
- [127] T. J. Clipsham and T. W. Button, "1-3 Piezocomposites realised from small feature size, high aspect ratio, hot embossed moulds. Part II: Piezocomposite fabrication," *Microsyst. Technol.*, vol. 16, no. 11, pp. 1983–1988, 2010, doi: 10.1007/s00542-010-1132-7.
- [128] S. Cochran *et al.*, "Net-shape ceramic processing as a route to ultrafine scale 1-3 connectivity piezoelectric ceramic-polymer composite transducers," *Proc. - IEEE Ultrason. Symp.*, vol. 3, no. c, pp. 1682–1685, 2004, doi: 10.1109/ULTSYM.2004.1418147.
- [129] S. Wang, J. F. Li, K. Wakabayashi, M. Esashi, and R. Watanabe, "Lost silicon mold

- process for PZT microstructures,” *Adv. Mater.*, vol. 11, no. 10, pp. 873–876, 1999, doi: 10.1002/(SICI)1521-4095(199907)11:10<873::AID-ADMA873>3.0.CO;2-F.
- [130] F. Laermer, S. Franssila, L. Sainiemi, and K. Kolari, “Deep Reactive Ion Etching,” in *Handbook of Silicon Based MEMS Materials and Technologies: Second Edition*, Elsevier Inc., 2015, pp. 444–469.
- [131] Y. Hirata, T. Numazawa, and H. Takada, “Effects of aspect ratio of lead zirconate titanate on 1-3 piezoelectric composite properties,” *Japanese J. Appl. Physics, Part 1 Regul. Pap. Short Notes Rev. Pap.*, vol. 36, no. 9 SUPPL. B, pp. 6062–6064, 1997, doi: 10.1143/jjap.36.6062.
- [132] B. Su, D. H. Pearce, and T. W. Button, “Routes to net shape electroceramic devices and thick films,” *J. Eur. Ceram. Soc.*, vol. 21, no. 10–11, pp. 2005–2009, 2001, doi: 10.1016/S0955-2219(01)00161-3.
- [133] T. W. Button *et al.*, “Net-shape ceramic manufacturing as an aid to realize ultrasonic transducers for high-resolution medical imaging,” *Proc. - IEEE Ultrason. Symp.*, vol. 3, no. August 2005, pp. 1625–1628, 2005, doi: 10.1109/ULTSYM.2005.1603173.
- [134] B. Su and T. W. Button, “A comparative study of viscous polymer processed ceramics based on aqueous and non-aqueous binder systems,” *J. Mater. Process. Technol.*, vol. 209, no. 1, pp. 153–157, 2009, doi: 10.1016/j.jmatprotec.2008.01.046.
- [135] D. MacLennan *et al.*, “Properties and application-oriented performance of high frequency piezocomposite ultrasonic transducers,” *Proc. - IEEE Ultrason. Symp.*, pp. 100–103, 2007, doi: 10.1109/ULTSYM.2007.38.
- [136] D. MacLennan *et al.*, “Fundamental performance characterisation of high frequency piezocomposites made with net-shape viscous polymer processing for medical ultrasound transducers,” *Proc. - IEEE Ultrason. Symp.*, pp. 58–61, 2008, doi: 10.1109/ULTSYM.2008.0015.
- [137] O. O. Omatete, M. A. Janney, and S. D. Nunn, “Gelcasting: From Laboratory Development Toward Industrial Production,” *J. Eur. Ceram. Soc.*, vol. 17, no. 2–3, pp. 407–413, 1997, doi: 10.1016/s0955-2219(96)00147-1.
- [138] A. C. Young, O. O. Omatete, M. A. Janney, and P. A. Menchhofer, “Gelcasting of Alumina,” *J. Am. Ceram. Soc.*, vol. 74, no. 3, pp. 612–618, 1991, doi: 10.1111/j.1151-2916.1991.tb04068.x.
- [139] L. J. Vandeperre, A. M. De Wilde, and J. Luyten, “Gelatin gelcasting of ceramic components,” *J. Mater. Process. Technol.*, vol. 135, no. 2–3, pp. 312–316, 2003, doi: 10.1016/S0924-0136(02)00862-2.
- [140] X. Mao, S. Shimai, M. Dong, and S. Wang, “Investigation of new epoxy resins for the gel casting of ceramics,” *J. Am. Ceram. Soc.*, vol. 91, no. 4, pp. 1354–1356, 2008, doi: 10.1111/j.1551-2916.2008.02278.x.
- [141] R. Xie, D. Zhang, X. Zhang, K. Zhou, and T. W. Button, “Gelcasting of alumina ceramics with improved green strength,” *Ceram. Int.*, vol. 38, no. 8, pp. 6923–6926, 2012, doi: 10.1016/j.ceramint.2012.05.027.
- [142] O. O. Omatete, R. U. S. A. Data, F. Precision, S. From, P. E. Derrington, and L.

Ivan, "METHOD FORMOLDING CERAMIC POWDERS USING AWATER-BASED GEL CASTING," 1991.

- [143] J. S. Ha, "Effect of atmosphere type on gelcasting behavior of Al<sub>2</sub>O<sub>3</sub> and evaluation of green strength," *Ceram. Int.*, vol. 26, no. 3, pp. 251–254, 2000, doi: 10.1016/S0272-8842(99)00050-4.
- [144] M. A. Janney, O. O. Omatete, C. A. Walls, S. D. Nunn, R. J. Ogle, and G. Westmoreland, "Development of low-toxicity gelcasting systems," *J. Am. Ceram. Soc.*, vol. 81, no. 3, pp. 581–591, 1998, doi: 10.1111/j.1151-2916.1998.tb02377.x.
- [145] X. Mao, S. Shimai, M. Dong, and S. Wang, "Gelcasting of alumina using epoxy resin as a gelling agent," *J. Am. Ceram. Soc.*, vol. 90, no. 3, pp. 986–988, 2007, doi: 10.1111/j.1551-2916.2007.01492.x.
- [146] V. F. and A. Valenza, "Epoxy resins as a matrix material in advanced fiber-reinforced polymer (FRP) composites," in *Advanced Fibre-Reinforced Polymer (FRP) Composites for Structural Applications*, 2013, pp. 88–121.
- [147] C. S. Desilets, A. R. Selfridge, and G. S. Kino, "Highly Efficient Transducer Arrays Useful in Nondestructive Testing Applications.," pp. 111–116, 1978, doi: 10.1109/ultsym.1978.197014.
- [148] A. Moldovan, "Development of a 1D Phased Ultrasonic Array for Intravascular Sonoporation," University of Strathclyde, 2021.
- [149] A. Bernassau, "Micro-Engineering for High Frequency Ultrasound Arrays," University of Dundee, 2009.
- [150] A. Bezanson, R. Adamson, and J. A. Brown, "Fabrication and Performance of a Miniaturized 64-Element High-Frequency Endoscopic Phased Array," *IEEE Trans. Ultrason. Ferroelectr. Freq. Control*, vol. 61, no. 1, pp. 33–43, 2014, doi: 10.1109/TUFFC.2014.6689774.
- [151] J. Yin, M. Lukacs, K. A. Harasiewics, and F. S. Foster, "Design and fabrication of ultrafine piezoelectric composites," *Ultrason. Imaging*, vol. 27, pp. 54–64, 2005.
- [152] R. C. Jaeger, *Introduction to microelectronic fabrication*, 2nd ed. Prentice Hall, 2002.
- [153] C. Mack, *Fundamental principles of optical lithography the science of microfabrication*. John Wiley & Sons Ltd, 2007.
- [154] J. Park *et al.*, "Bilayer processing for an enhanced organic-electrode contact in ultrathin bottom contact organic transistors," *Appl. Phys. Lett.*, vol. 92, no. 19, pp. 10–13, 2008, doi: 10.1063/1.2918121.
- [155] C. Koch and T. J. Rinke, *Photolithography: Basics of Microstructuring*, 2nd ed. Siegl Druck & Medien GmbH & Co. KG, Friedrichshafen, 2020.
- [156] E. Reichmanis and L. F. Thompson, "Polymer Materials for Microlithography," *Chem. Rev.*, vol. 89, no. 6, pp. 1273–1289, 1989, doi: 10.1021/cr00096a001.
- [157] Kayaku Advanced Materials, "Technical Data Sheet: LOR and PMGI Resists for Bilayer Lift-off Processing," 2019. <https://kayakuam.com/products/pmgi-lor-lift-off->

resists/ (accessed Mar. 14, 2020).

- [158] P. H. Holloway, "Gold/Chromium Metallizations for Electronic Devices.," *Solid State Technol.*, vol. 23, no. 2, pp. 109–115, 1980, doi: 10.1007/bf03215108.
- [159] B. Moazzez, S. M. O'Brien, and E. F. S. Merschrod, "Improved adhesion of gold thin films evaporated on polymer resin: Applications for sensing surfaces and MEMS," *Sensors (Switzerland)*, vol. 13, no. 6, pp. 7021–7032, 2013, doi: 10.3390/s130607021.
- [160] W. E. Martinez, G. Gregori, and T. Mates, "Titanium diffusion in gold thin films," *Thin Solid Films*, vol. 518, no. 10, pp. 2585–2591, 2010, doi: 10.1016/j.tsf.2009.07.187.
- [161] J. Pan, R. M. Pafchek, F. F. Judd, and J. B. Baxter, "Effect of Chromium – Gold and Titanium – Titanium," *IEEE Trans. Adv. Packag.*, vol. 29, no. 4, pp. 707–713, 2006.
- [162] M. Todeschini, A. Bastos Da Silva Fanta, F. Jensen, J. B. Wagner, and A. Han, "Influence of Ti and Cr Adhesion Layers on Ultrathin Au Films," *ACS Appl. Mater. Interfaces*, vol. 9, no. 42, pp. 37374–37385, 2017, doi: 10.1021/acsami.7b10136.
- [163] A. Jilani, M. S. Abdel-wahab, and A. H. Hammad, "Advance deposition techniques for thin film and coating," in *Modern Technologies for Creating the Thin-film Systems and Coatings two*, vol. 32, A. Jilani, M. S. Abdel-wahab, and A. H. Hammad, Eds. InTech, 1989, pp. 137–144.
- [164] D. M. Mattox, *Handbook of Physical Vapor Deposition (PVD) Processing*, 2nd ed. William Andrew Inc, 2010.
- [165] Shipley, "SVC-14 Technical Report." SVC-14-DATASHEET.PDF (kayakuam.com) (accessed Nov. 01, 2020).
- [166] Shipley Europe Ltd, "Microposit ® remover 1165." MICROPOSIT™ REMOVER 1165 (kayakuam.com) (accessed Nov. 01, 2020).
- [167] C. E. M. Demore *et al.*, "Functional characterisation of high frequency arrays based on micro-moulded 1–3 piezocomposites," *IEEE Int. Ultrason. Symp.*, pp. 1134–1137, 2009, doi: 10.1109/ultsym.2009.5441966.
- [168] J. Golden, H. Miller, D. Nawrocki, and J. Ross, "Optimization of Bi-layer Lift-Off Resist Processes," no. 617, 2009.
- [169] D. MacLennan, "Fundamental Characterisation and Early Functional Testing of Micromoulded Piezocomposites," pp. 1–264, 2010.
- [170] Q. Youngqiang, "Development of Ultrasonic Devices for Microparticle and Cell Manipulation," University of Dundee, 2014.
- [171] J. E. Morris, J. Lee, J. Liu, and P. O. Box, "Isotropic Conductive Adhesive Interconnect Technology in Electronics Packaging Applications Department of Electrical & Computer Engineering , Portland State University , SMIT Center & Department of Microtechnology and Nanoscience , Chalmers University of," *IEEE Polytronic*, pp. 1–8, 2005.
- [172] J. C. Bolger, J. M. Sylva, and J. F. McGovern, "Conductive epoxy adhesives to

- replace solder,” *Surf. Mt. Technol.*, vol. 6, no. 2, pp. 1–3, 1992.
- [173] C. Fei *et al.*, “Design of matching layers for high-frequency ultrasonic transducers,” *Appl. Phys. Lett.*, vol. 107, no. 12, 2015, doi: 10.1063/1.4931703.
- [174] J. Liu, “ACA bonding technology for low cost electronics packaging application - current status and remaining challenges,” 2000.
- [175] Y. C. Lin and J. Zhong, “A review of the influencing factors on anisotropic conductive adhesives joining technology in electrical applications,” *J. Mater. Sci.*, vol. 43, no. 9, pp. 3072–3093, 2008, doi: 10.1007/s10853-007-2320-4.
- [176] I. Mir and D. Kumar, “Recent advances in isotropic conductive adhesives for electronics packaging applications,” *Int. J. Adhes. Adhes.*, vol. 28, no. 7, pp. 362–371, 2008, doi: 10.1016/j.ijadhadh.2007.10.004.
- [177] D. MacLennan, S. Cochran, T. W. Button, H. Hughes, M. Ponting, and J. Sweet, “Ultra Precision Grinding in the Fabrication of High Frequency Piezocomposite Ultrasonic Transducers,” in *IEEE International Ultrasonics Symposium 2006*, 2006, pp. 2353–2356, doi: 10.1109/ULTSYM.2006.594.
- [178] A. Bernassau, “Micro-engineering for high frequency ultrasound arrays,” University of Dundee, 2009.
- [179] E. M. Petrie, *Epoxy Adhesive Formulations*. The McGraw-Hill Companies, 2006.
- [180] S. Zhang and F. Li, “High Performance Ferroelectric Relaxor-PbTiO<sub>3</sub> Single Crystals: Status and Perspective,” *J. Appl. Phys.*, vol. 111, no. 3, 2012.
- [181] D. E. Materials, “Micro resist technology.” <https://www.microresist.de/en/technical-sheet/> (accessed Jun. 14, 2020).
- [182] Microchem, “Lift-Off™ Resists,” 2002. [Online]. Available: [https://amolf.nl/wp-content/uploads/2016/09/datasheets\\_LOR\\_datasheet.pdf](https://amolf.nl/wp-content/uploads/2016/09/datasheets_LOR_datasheet.pdf).
- [183] Y. Jiang, “Photolithography procedures; AFM Private Communication,” 2010.
- [184] E. Bassoli and L. Denti, “Assay of secondary anisotropy in additively manufactured alloys for dental applications,” *Materials (Basel)*, vol. 11, no. 10, 2018, doi: 10.3390/ma11101831.
- [185] F. Cordero, “Quantitative evaluation of the piezoelectric response of unpoled ferroelectric ceramics from elastic and dielectric measurements: Tetragonal BaTiO<sub>3</sub>,” *J. Appl. Phys.*, vol. 123, no. 9, 2018, doi: 10.1063/1.5018746.
- [186] C. R. Bowen, A. C. Dent, R. Stevens, M. G. Cain, and A. Avent, “A new method to determine the un-poled elastic properties of ferroelectric materials,” *Sci. Technol. Adv. Mater.*, vol. 18, no. 1, pp. 264–272, 2017, doi: 10.1080/14686996.2017.1302274.
- [187] A. C. Dent, C. R. Bowen, R. Stevens, M. G. Cain, and M. Stewart, “Effective elastic properties for unpoled barium titanate,” *J. Eur. Ceram. Soc.*, vol. 27, no. 13–15, pp. 3739–3743, 2007, doi: 10.1016/j.jeurceramsoc.2007.02.031.
- [188] P. Höhne, B. Mieller, and T. Rabe, “Slurry development for spray granulation of

- ceramic multicomponent batches,” *J. Ceram. Sci. Technol.*, vol. 9, no. 3, pp. 327–336, 2018, doi: 10.4416/JCST2018-00022.
- [189] N. Gibson, P. Kuchenbecker, K. Rasmussen, V. D. Hodoroaba, and H. Rauscher, *Volume-specific surface area by gas adsorption analysis with the BET method*. Elsevier Inc., 2019.
- [190] M. P. Gómez-Tena, J. Gilabert, C. Machí, E. Zumaquero, and J. Toledo, “Relationship between the specific surface area parameters determined using different analytical techniques,” *Xii Foro Glob. Del Recubrimiento Cerámico. Qualicer*, no. 1, pp. 1–10, 2014.
- [191] I. E. Dubois, S. Holgersson, S. Allard, and M. E. Malmström, “Correlation between particle size and surface area for chlorite and K-feldspar,” *Water-Rock Interact. Birkle Torres-Alvarado*, pp. 717–720, 2010.
- [192] Y. Bai, “Vibrational energy harvesting using piezoelectric ceramics and free-standing thick-film structures,” University of Birmingham, 2015.
- [193] X. Xu, Z. Wen, X. Wu, J. Lin, and X. Wang, “Rheology and chemorheology of aqueous  $\gamma$ -LiAlO<sub>2</sub> slurries for gel-casting,” *Ceram. Int.*, vol. 35, no. 6, pp. 2191–2195, 2009, doi: 10.1016/j.ceramint.2008.11.033.
- [194] S. M. Olhero and J. M. F. Ferreira, “Influence of particle size distribution on rheology and particle packing of silica-based suspensions,” *Powder Technol.*, vol. 139, no. 1, pp. 69–75, 2004, doi: 10.1016/j.powtec.2003.10.004.
- [195] S. M. Olhero, L. Garcia-Gancedo, T. W. Button, F. J. Alves, and J. M. F. Ferreira, “Innovative fabrication of PZT pillar arrays by a colloidal approach,” *J. Eur. Ceram. Soc.*, vol. 32, no. 5, pp. 1067–1075, 2012, doi: 10.1016/j.jeurceramsoc.2011.11.016.
- [196] R. Hoffman, “Explanations for the cause of shear thickening in concentrated colloidal suspensions,” *J. Rheol. (N. Y. N. Y.)*, vol. 42, no. 1, pp. 111–123, 1998, doi: 10.1122/1.550884.
- [197] D. Guo, K. Cai, Y. Huang, L. Li, and Z. Gui, “Water based gelcasting of lead zirconate titanate,” *Mater. Res. Bull.*, vol. 38, no. 5, pp. 807–816, 2003, doi: 10.1016/S0025-5408(03)00044-8.
- [198] R. Xie, C. Liu, Y. Zhao, P. Jin, KechaoZhou, and D. Zhang, “Gelation behavior and mechanical properties of gelcast lead zirconate titanate ceramics,” *J. Eur. Ceram. Soc.*, vol. 35, no. 7, pp. 2051–2056, 2015, doi: 10.1016/j.jeurceramsoc.2015.01.009.
- [199] W. H. Boersma, “Shear thickening of concentrated dispersions,” Technische Universiteit Eindhoven, 1990.
- [200] T. P. D. S. Barros, D. G. D. L. Cavalcante, D. F. De Oliveira, R. E. Caluête, and S. J. G. De Lima, “Study of the surface properties of the epoxy/quasicrystal composite,” *J. Mater. Res. Technol.*, vol. 8, no. 1, pp. 590–598, 2019, doi: 10.1016/j.jmrt.2018.04.015.
- [201] R. Hoffman, “Discontinuous and Dilatant Viscosity Behavior in Concentrated Suspensions I. Observation of a Flow Instability.,” *Trans Soc Rheol*, vol. 16, no. 1, pp. 155–173, 1972, doi: 10.1122/1.549250.

- [202] R. Hoffman, “Discontinuous and dilatant viscosity behavior in concentrated suspensions III. Necessary conditions for their occurrence in viscometric flows,” *Adv. Colloid Interface Sci.*, vol. 17, pp. 161–184, 1982.
- [203] G. Liu, M. M. Attallah, Y. Jiang, and T. W. Button, “Rheological characterization and shape control in gel-casting of nano-sized zirconia powders,” *Ceram. Int.*, vol. 40, no. 9 PART A, pp. 14405–14412, 2014, doi: 10.1016/j.ceramint.2014.06.036.
- [204] R. Xie, Y. Zhao, K. Zhou, D. Zhang, Y. Wang, and H. L. W. Chan, “Fabrication of fine-scale 1-3 piezoelectric arrays by aqueous gelcasting,” *J. Am. Ceram. Soc.*, vol. 97, no. 8, pp. 2590–2595, 2014, doi: 10.1111/jace.13001.
- [205] C. Jiang, X. Gan, D. Zhang, R. Xie, and K. Zhou, “Gelcasting of aluminum nitride ceramics using hydantion epoxy resin as gelling agent,” *Ceram. Int.*, vol. 39, no. 8, pp. 9429–9433, 2013, doi: 10.1016/j.ceramint.2013.05.060.
- [206] M. Dong, X. Mao, Z. Zhang, and Q. Liu, “Gelcasting of SiC using epoxy resin as gel former,” *Ceram. Int.*, vol. 35, no. 4, pp. 1363–1366, 2009, doi: 10.1016/j.ceramint.2008.07.008.
- [207] D. -S Tsai, “Pressure buildup and internal stresses during binder burnout: Numerical analysis,” *AIChE J.*, vol. 37, no. 4, pp. 547–554, 1991, doi: 10.1002/aic.690370408.
- [208] P. Jenkins and M. Snowden, “Depletion flocculation in colloidal dispersions,” *Adv. Colloid Interface Sci.*, vol. 68, no. 1–3, pp. 57–96, 1996, doi: 10.1016/s0001-8686(96)90046-9.
- [209] Y. Otsubo, “Rheology Control of Suspensions by Soluble Polymers,” *Langmuir*, vol. 11, no. 6, pp. 1893–1898, 1995, doi: 10.1021/la00006a013.
- [210] S. L. Kang, *Sintering, Densification, Grain Growth and Microstructure*. Elsevier Butterworth-Heinemann, 2005.
- [211] Epoxy Technology, “Removing Bubbles from Epoxy,” 2009. [Online]. Available: [www.epotek.com](http://www.epotek.com).
- [212] M. Afendi, W. M. Banks, and D. Kirkwood, “Bubble free resin for infusion process,” *Compos. Part A Appl. Sci. Manuf.*, vol. 36, no. 6, pp. 739–746, 2005, doi: 10.1016/j.compositesa.2004.10.030.
- [213] T. Technologies, “High Sensitivity Soft Piezoelectric Ceramics.” <http://www.trstechnologies.com/Materials/High-Sensitivity-Soft-Piezoelectric-Ceramics>.
- [214] A. Bernassau, D. Hutson, C. E. M. Démoré, and S. Cochran, “Characterization of an epoxy filler for piezocomposites compatible with microfabrication processes,” *IEEE Trans. Ultrason. Ferroelectr. Freq. Control*, vol. 58, no. 12, pp. 2743–2748, 2011, doi: 10.1109/TUFFC.2011.2137.
- [215] J. A. Brown, E. Chérin, J. Yin, and F. Stuart Foster, “Fabrication and performance of high-frequency composite transducers with triangular-pillar geometry,” *IEEE Trans. Ultrason. Ferroelectr. Freq. Control*, vol. 56, no. 4, pp. 827–836, 2009, doi: 10.1109/TUFFC.2009.1106.
- [216] H. C. Yang, J. Cannata, J. Williams, and K. K. Shung, “A study of 1-3 pseudo-

- random pillar piezocomposites for ultrasound transducers,” *IEEE Int. Ultrason. Symp. IUS*, no. c, pp. 1743–1746, 2011, doi: 10.1109/ULTSYM.2011.0435.
- [217] D. Zhou *et al.*, “Broad-band and high-temperature ultrasonic transducer fabricated using a Pb(In<sub>1/2</sub>Nb<sub>1/2</sub>)-Pb(Mg<sub>1/3</sub>Nb<sub>2/3</sub>)-PbTiO<sub>3</sub> single crystal/epoxy 1-3 composite,” *Rev. Sci. Instrum.*, vol. 82, no. 5, pp. 3–10, 2011, doi: 10.1063/1.3583746.
- [218] Meggitt, “Ferroperm Piezoelectric Pz50 series,” *Meggitt*. .
- [219] S. R. White and H. T. Hahn, “Process Modeling of Composite Materials: Residual Stress Development during Cure. Part I. Model Formulation,” *J. Compos. Mater.*, vol. 26, no. 16, pp. 2402–2422, 1992, doi: 10.1177/002199839202601604.
- [220] M. S. Madhukar, M. S. Genidy, and J. D. Russell, “New method to reduce cure-induced stresses in thermoset polymer composites, Part I: test method,” *J. Compos. Mater.*, vol. 34, no. 22, pp. 1882–1904, 2000, doi: 10.1106/HUCY-DY2B-2N42-UJBX.
- [221] Y. Eom, L. BooGH, V. Michaud, P. Sunderland, and J. Manson, “Stress-Initiated Void Formation During Cure of a Three-Dimensionally Constrained Thermoset Resin,” *Polym. engineering Sci.*, vol. 41, no. 3, pp. 492–503, 2001.
- [222] C. Lochovsky, S. Yasotharan, and A. Günther, “Bubbles no more: In-plane trapping and removal of bubbles in microfluidic devices,” *Lab Chip*, vol. 12, no. 3, pp. 595–601, 2012, doi: 10.1039/c1lc20817a.
- [223] T. Christoforidis, C. Ng, and D. T. Eddington, “Bubble removal with the use of a vacuum pressure generated by a converging-diverging nozzle,” *Biomed. Microdevices*, vol. 19, no. 3, 2017, doi: 10.1007/s10544-017-0193-0.
- [224] M. Johnson, G. Liddiard, M. Eddings, and B. Gale, “Bubble inclusion and removal using PDMS membrane-based gas permeation for applications in pumping, valving and mixing in microfluidic devices,” *J. Micromechanics Microengineering*, vol. 19, no. 9, 2009, doi: 10.1088/0960-1317/19/9/095011.
- [225] W. R. T. Navaraj, “Inorganic micro/nanostructuresbased high-performance flexible electronics for electronic skin application,” University of Glasgow, 2019.
- [226] Y. Suh and G. P. Watson, “Optimization of Bilayer Lift-Off Process to Enable the Gap Size of 1  $\mu$ m Using LOR 3A and S1813,” pp. 2–5, 2020.
- [227] J. Golden, H. Miller, D. Nawrocki, and J. Ross, “Optimization of Bi-layer Lift-Off Resist Proces,” no. 617, 2009.
- [228] J. Liang, F. Kohsaka, T. Matsuo, X. Li, and T. Ueda, “Improved bi-layer lift-off process for MEMS applications,” *Microelectron. Eng.*, vol. 85, no. 5–6, pp. 1000–1003, 2008, doi: 10.1016/j.mee.2008.01.104.
- [229] V. Grumezescu and A. Grumezescu, *Materials for Biomedical Engineering: Thermoset and Thermoplastic Polymers*. Matthew Deans, 2019.
- [230] R. Serway and J. Jewett, *Physics for Scientists and Engineers with Modern Physics*, 9th ed. Physical Sciences: Mary Finch, 2014.

- [231] S. Sangon, N. Supanchaiyamat, J. Sherwood, C. R. McElroy, and A. J. Hunt, “Direct comparison of safer or sustainable alternative dipolar aprotic solvents for use in carbon-carbon bond formation,” *React. Chem. Eng.*, vol. 5, no. 9, pp. 1798–1804, 2020, doi: 10.1039/d0re00174k.
- [232] N. Ucar, N. Kizildag, A. Onen, I. Karacan, and O. Eren, “Polyacrylonitrile-polyaniline composite nanofiber webs: Effects of solvents, redoping process and dispersion technique,” *Fibers Polym.*, vol. 16, no. 10, pp. 2223–2236, 2015, doi: 10.1007/s12221-015-5426-3.
- [233] B. Åkesson, “N-methyl-2-pyrrolidone,” *IPCS Concise Int. Chem. Assess. Doc.*, no. 35, 2001.
- [234] Logitech Limited, “Ecoclear - Non Solvent Cleaning Fluid Ecoclear - Non Solvent Cleaning Fluid,” 2012. [Online]. Available: [https://logitech.uk.com/wp-content/uploads/Ecoclear-January-2012\\_OCON178.pdf](https://logitech.uk.com/wp-content/uploads/Ecoclear-January-2012_OCON178.pdf).
- [235] C. De Chen, “Singular stress analysis near sharp corners in anisotropic notched plates subjected to bending loads,” *Appl. Math. Model.*, vol. 55, pp. 183–204, 2018, doi: 10.1016/j.apm.2017.10.023.
- [236] W. Shen, N. Barltrop, R. Yan, E. Liu, K. Qin, and L. Song, “Stress field and fatigue strength analysis of 135-degree sharp corners based on notch stress strength theory,” *Ocean Eng.*, vol. 107, pp. 32–44, 2015, doi: 10.1016/j.oceaneng.2015.07.029.
- [237] X. Jian *et al.*, “The Study of Cable Effect on High-Frequency Ultrasound Transducer Performance,” *IEEE Sens. J.*, vol. 18, no. 13, pp. 5265–5271, 2018, doi: 10.1109/JSEN.2018.2838142.
- [238] Y. Yang, X. Wei, L. Zhang, and W. Yao, “The effect of electrical impedance matching on the electromechanical characteristics of sandwiched piezoelectric ultrasonic transducers,” *Sensors (Switzerland)*, vol. 17, no. 12, 2017, doi: 10.3390/s17122832.
- [239] V. T. Rathod, “A review of electric impedance matching techniques for piezoelectric sensors, actuators and transducers,” *Electron.*, vol. 8, no. 2, 2019, doi: 10.3390/electronics8020169.
- [240] N. E. Cabrera-Munoz *et al.*, “Forward-looking 30-MHz phased-array transducer for peripheral intravascular imaging,” *Sensors Actuators, A Phys.*, vol. 280, pp. 145–163, 2018, doi: 10.1016/j.sna.2018.07.035.
- [241] TRSTechnologies, “PIN-PMN-29%PT datasheet.”

# Appendix I

## Determination of material properties from independent parameters

Properties	Formula	Eq.
Density (g/cm <sup>3</sup> )	$\bar{\rho} = v\rho^c + v\rho^p$	Eq. I- 1
Acoustic impedance, $Z_a$ (Rayl)	$Z_a = \sqrt{\bar{C}_{33}^D \bar{\rho}}$	Eq. I- 2
Longitudinal velocity (m/s)	$V_L = \sqrt{\frac{\bar{C}_{33}^D}{\bar{\rho}}}$	Eq. I- 3
Elastic stiffness constant, $\bar{C}_{33}^E$ (N/m <sup>2</sup> )	$\bar{C}_{33}^E = V_c \left[ c_{33}^E - \frac{2V_p(c_{13}^E - c_{12})^2}{V_c(c_{11} + c_{12}) + V_p(c_{11}^E + c_{12}^E)} \right] + V_p c_{11}$	Eq. I- 4
Static dielectric constant, $\bar{\epsilon}_{33}^S$ (N/m <sup>2</sup> )	$\bar{\epsilon}_{33}^S = V_c \left[ \epsilon_{33}^S + \frac{2V_p(e_{31})^2}{V_c(c_{11} + c_{12}) + V_p(c_{11}^E + c_{12}^E)} \right] + V_p \epsilon_{11}$	Eq. I- 5
Piezoelectric stress constant, $\bar{e}_{33}$ (C/m <sup>2</sup> )	$\bar{e}_{33} = V_c \left[ e_{33} + \frac{2V_p e_{31}(c_{13}^E - c_{12})}{V_c(c_{11} + c_{12}) + V_p(c_{11}^E + c_{12}^E)} \right]$	Eq. I- 6
Elastic stiffness constant at constant electric displacement, $\bar{C}_{33}^D$ (N/m <sup>2</sup> )	$\bar{C}_{33}^D = \bar{C}_{33}^E + \frac{(\bar{e}_{33})^2}{\bar{\epsilon}_{33}^S}$	Eq. I- 7
Thickness coupling coefficient, $k_t$	$k_t = \sqrt{\frac{(\bar{e}_{33})^2}{\bar{C}_{33}^D \bar{\epsilon}_{33}^S}}$	Eq. I- 8

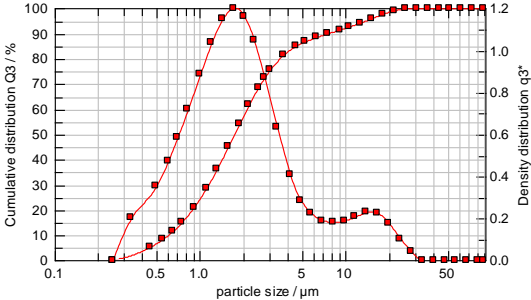
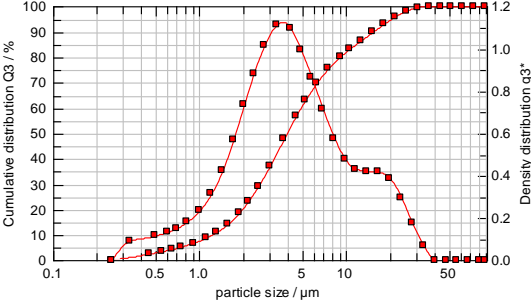
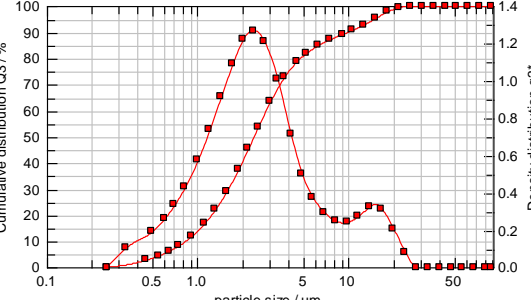
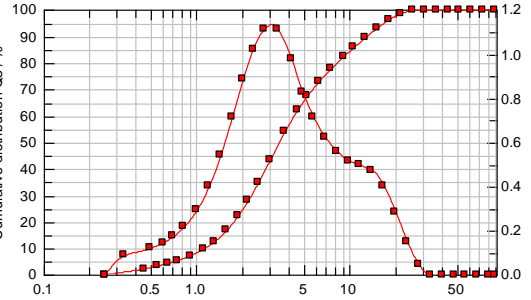
## Appendix II

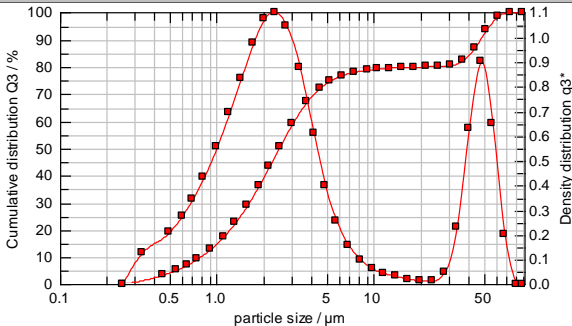
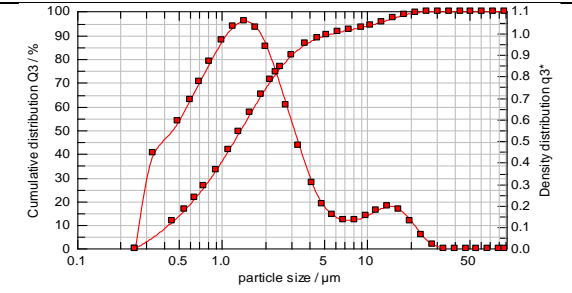
### Elastic, piezoelectric and dielectric properties of the piezoelectric materials used for FEA models

Material Properties	PZ54	PIMNT29	PZT5H
<b>Density (kg/cm<sup>3</sup>)</b>	7760	8198	7950
<b>Elastic stiffness constants: <math>c_{ij}</math> (10<sup>10</sup> N/m<sup>2</sup>)</b>			
$c_{11}^E = c_{22}^E$	14.6	16.3	12.3
$c_{12}^E$	9.15	14.7	7.4
$c_{13}^E = c_{23}^E$	8.82	12.1	8.5
$c_{33}^E$	11.9	11.5	12
$c_{44}^E = c_{55}^E$	2.57	6.6	0.1
$c_{66}^E$	2.75	3	-
<b>Dielectric constant: <math>\epsilon_{ij}^S</math></b>			
$\epsilon_{11} = \epsilon_{33}$	1460	965	-
$\epsilon_{22}$	1440	733	-
<b>Piezoelectric coupling coefficients: <math>e_{ij}</math> (C/m<sup>2</sup>)</b>			
$e_{15} = e_{24}$	14.9	6.2	-
$e_{31} = e_{32}$	-5.61	-7.7	-8.3
$e_{33}$	21.6	17.8	25
<b>Bulk &amp; shear attenuation</b>	3200	600	65
Reference	[75]	[241]	[95]

# Appendix III

## Investigation of particle size distribution of the PZT5H powder batch no.2002

Method	Particle size distribution
<p>Ultrasonic bath: 5 min – 50 g PZT powder</p>	 <p>Mean PSD ~ 8.4 <math>\mu\text{m}</math> with bimodal distribution</p>
<p>Ball-milling 30 min</p>	 <p>Mean PSD ~ 3.79 <math>\mu\text{m}</math> with bimodal distribution</p>
<p>Ball-milling 30 min + Sieving at 63, 36 microns</p>	 <p>Mean PSD ~ 9.07 <math>\mu\text{m}</math> with bimodal distribution</p>
<p>Ball-milling 1 hr</p>	 <p>Mean PSD ~ 8.59 <math>\mu\text{m}</math> with bimodal distribution (~ 14 <math>\mu\text{m}</math>)</p>

Method	Particle size distribution
<p style="text-align: center;">Ball-milling 7 hr</p>	 <p style="text-align: center;">Mean PSD ~ 21.63 <math>\mu\text{m}</math> with bimodal distribution</p>
<p style="text-align: center;">Ball-milling 15 min + freeze drying + Sieving</p>	 <p style="text-align: center;">Mean PSD ~ 9.25 <math>\mu\text{m}</math> with bimodal distribution</p>